University of Southampton

Faculty of Engineering and the Environment
Thesis Report

Investigation of Ballast Flight under Aerodynamic Flow using Computational Fluid Dynamics

---

Author:
Lee Anthony PARDOE

Supervisors:
Prof. William POWRIE
Dr. Zhiwei HU

A thesis submitted in fulfilment of the requirements for the Degree of Engineering Doctorate
in the
Infrastructure Group
Faculty of Engineering and the Environment
October 31, 2018

EPSRC
Engineering and Physical Sciences Research Council

UNIVERSITY OF Southampton
Engineering Doctorate (EngD)

hs2 engine for growth

UNIVERSITY OF SOUTHAMPTON

ABSTRACT

FACULTY OF ENGINEERING AND THE ENVIRONMENT

DEPARTMENT OF APPLIED FLUID MECHANICS

Doctor of Engineering

by Lee Anthony Pardoe

This study focuses on the aerodynamics underneath a passing High-Speed Train that can cause ballast flight. Numerical studies have been carried out on simplified particles at different orientations and elevations (levels), to observe changes in aerodynamic forces. A cube and a hemisphere (0.06 m in diameter) were simulated at inlet flow speed up to 120 m/s. Studies using moving wall techniques were also carried out, to observe changes in aerodynamic forces on isolated ballast grains and different track sections. Results demonstrated that URANS has produced meaningful results but not as detailed as DDES at a higher computational cost. Certain ballast characteristics are identified that can trigger ballast movements such as the particle shape, its orientation and the mass of the ballast grain. It was determined that shapes with flatter surfaces (i.e. cube) facing the flow are more likely to move than smoothly shaped ballast (i.e. hemisphere) and ballast of smaller mass is also prone to ballast movement. Further studies included some simple wind tunnel experiments, in which the critical velocities for ballast were measured. CFD studies of different sleeper blocks were also conducted using periodic and moving wall boundary conditions, to determine the risk of ballast movement at various locations across the track at certain ballast depths. Aerodynamic forces and flow behaviour are presented for each case study isolating it from mechanical vibrations caused by the passing High-Speed Trains. These numerical studies show that be lowering the ballast bed depth and having a rough ballast bed surface can provide benefits by reducing the aerodynamic load on the ballast bed. These computational studies suggest that improper use of aerodynamic sleepers can increase the likelihood of ballast movement due to reduced flow separation, which is why new sleeper shapes should be considered to not only prevent ballast from settling on top of sleeper blocks but also increase the flow separation.

Contents

List of Figures

List of Tables

Declaration of Authorship

I, *Lee Anthony Pardoe*, declare that the thesis entitled *Investigation of Ballast Flight under Aerodynamic Flow using Computational Fluid Dynamics* and the work presented in the thesis are both my own, and have been generated by me as the result of my own original research. I confirm that:

- This work was done wholly or mainly while in candidature for a research degree at this University;
- Where any part of this thesis has previously been submitted for a degree or any other qualifications at this University or any other institution. This has been clearly stated;
- Where I have consulted the published work of others, this is always clearly attributed;
- Where I have quoted from the work of others, the source is always given. With the exception of such quotations, this thesis is entirely my own work;
- I have acknowledged all main sources of help;
- Where the thesis is based on work done by myself jointly with others, I have made clear exactly what was done by others and what I have contributed myself;
- None of this work has been published before submission;

Signed:. . . . .

Date: . . . .

Acknowledgements

This research was carried out under the guidance and supervision of Prof. W. Powrie and Dr Z. Hu. I am very grateful for their knowledge, understanding and guidance throughout the completion of this project.

Would also like to extend my gratitude to those from the EngD and AFM groups, the industry supervisors from HS2 including Niall Fagan and the support from Dr Z. Xie and Dr R. De Kat. This project has provided me with the opportunity to explore areas of interest in Aerospace and Civil Engineering into greater depths.

The research is funded by the Engineering and Physical Sciences Research Council (ESPRC) grant EP/G036896/1 and High Speed 2 (HS2). The financial support is gratefully acknowledged to allow me to participate in the Engineering Doctorate program for Engineering Transport and the Environment at Southampton University.

Nomenclature

Symbols	**Definition**	**Units**
A	Area	m^2
a	Acceleration	ms^{-2}
C_{fb}	Consequence of event after ballast flight	
C_D	Drag coefficient	
C_L	Lift coefficient	
C_M	Pitching moment coefficient	
C_p	Pressure coefficient	
c	Speed of sound	ms^{-1}
D	Drag Force	N
G	Generation of energy	J
G_P	Specific gravity of the particle	
h	Height	m
I	Intermediate dimension of a ballast particle	m
I	Turbulent intensity	
k	Turbulent kinetic energy	m^2s^{-2}
L	Characteristic length	m
L	Lift Force	N
L	Longest dimension of a ballast particle	m
M	Mach Number	
M	Moment	kgm
m	Mass	kg
p	Pressure	$kgm^{-1}s^{-2}$
$P_{fb\|d}$	Probability of ballast particle flight after displacement	
P_d	Probability of ballast particle displacement	
P_e	Perimeter of equivalent area ellipse	m
P_o	Perimeter of the particle	m
Q	Q-Criterion	
R	Universal gas constant	$Jkg^{-1}K^{-1}$

R_c	Roughness constant	
R_{fb}	Risk of flying ballast	
R_h	Roughness height	m
S	Shortest dimension of a ballast particle	m
t	Time	s
T	Temperature of flow	$^{\circ}$C
U	Velocity	ms^{-1}
U^+	Velocity ratio	
U_∞	Freestream velocity	ms^{-1}
U_C	Critical velocity	ms^{-1}
u_i	Instantaneous velocity	ms^{-1}
u_i'	Fluctuation velocity	ms^{-1}
U_r	Radial velocity	ms^{-1}
W	Weight	N
x, y, z	Rectangular Cartesian coordinates	m
y^+	Wall normal distance	m
y_1^+	y^+ at first grid point	m
α	Angle of attack	$^{\circ}$
$\bar{u}_i$	Mean velocity	ms^{-1}
Δt	Change in time	s
Δx	Change in spatial	m
δ	Boundary layer thickness	m
γ	Ratio of specific heats	
κ	Wave number	
μ	Molecular dynamic viscosity	$kgm^{-1}s^{-1}$
μ_t	Eddy viscosity	m^2s^{-1}
ν	Kinematic viscosity	m^2s^{-1}
ω	Specified dissipation rate	s^{-1}
ρ	Density	kgm^{-3}
ρ_w	Density of water	kg/m^3
p_∞	Reference pressure	kgm^{-3}
p_s	Static pressure	Pa
τ	Stress tensor	Pa
ε	Turbulent dissipation rate	m^2s^{-3}

Abbreviations

APG	Adverse Pressure Gradient
CFD	Computational Fluid Dynamics
CFL	Courant Number
DES	Detached Eddy Simulation
HSR	High Speed Rail
HST	High Speed Train
LES	Large Eddy Simulation
RANS	Reynolds Averaged Navier Stokes
URANS	Unsteady Reynolds Averaged Navier Stokes

Chapter 1

Introduction

1.1 Background

The rail network is a principal mode of public and goods transportation. Rail systems worldwide have made consistent efforts to raise maximum and average running speeds over the past eighty years, providing people with better opportunities in reaching their destination. In the mid-sixties, Japan introduced High-Speed Trains (HSTs) that exceeded the performance of all other existing trains.

The train body structure was altered to create a smoother aerodynamic profile to reduce the aerodynamic drag and to achieve greater operational speed. After its success, the high-speed rail expanded globally to give people faster transport with improved capacity. The track was redesigned, to support this new variant of rail transport.

There are two track types; one is ballasted track that uses granular particles to support the track and the other is concrete slab track that uses a concrete foundation. Ballast is cheap to produce, and the track is maintained by regularly cleaning and adjusting the distribution of ballast particles depending on the usage frequency (Indraratna, 2011).

Slab track is a concrete track base system with a smaller depth than ballast, which is ideal for tracks in regular use. However, careful design and precision during installation are required to minimise future maintenance. Installation costs for slab track are greater than for ballasted track but its use can reduce maintenance costs over time.

There are some major issues of using ballasted track. First, the ballast support can become misaligned due to lateral loading by the train. Another is damage to particles over time due to additional loads and weathering, weakening the ballast support. Thus, regular maintenance is required to reduce any hazards (i.e. track buckling) or passenger discomfort during travel. Slab track does not require maintenance as frequently as ballasted track.

High-Speed Rail (HSR) firms in the United Kingdom, including HS1 and National Rail, currently use ballasted track. However, increasing the train speed can potentially increase the possibly of ballast movement/flight, which may collide with the speeding train, causing structural damage. This project is focused on ballasted tracks, since slab tracks do not experience these aerodynamic issues.

1.2 Project description and motivation

Previous research by Quinn et al. (2009) and others have indicated the probable cause of ballast flight is a combination of aerodynamic forces from the passing train and mechanical vibrations of the track. Therefore, this research has focused on the effects of turbulent flow on individual ballast particles underneath the train, since aerodynamic forces contribute towards ballast motion.

The investigation was carried out numerically by using Computational Fluid Dynamics (CFD) techniques. Using simulation tools, the flow field around the particle including flow separation and vortices can be visualised and quantified.

The shapes of ballast stones are complicated as they are irregular and vary in size. So initially, flow behaviour and aerodynamic forces on cubes and hemispheres were investigated, which were benchmarked using published experimental and numerical results. Different methods were examined to find an accurate solution not entailing excessive computational time.

Additional investigations were carried out on different sleepers at different ballast levels. Velocity profiles are measured across the track, and individual particles placed in various locations on the track to observe changes in aerodynamic forces.

For better confidence in the CFD results, experimental studies are carried out using wind tunnel facilities and other resources at Southampton University. An illustration of the result strategy is highlighted on Figure 1.1:

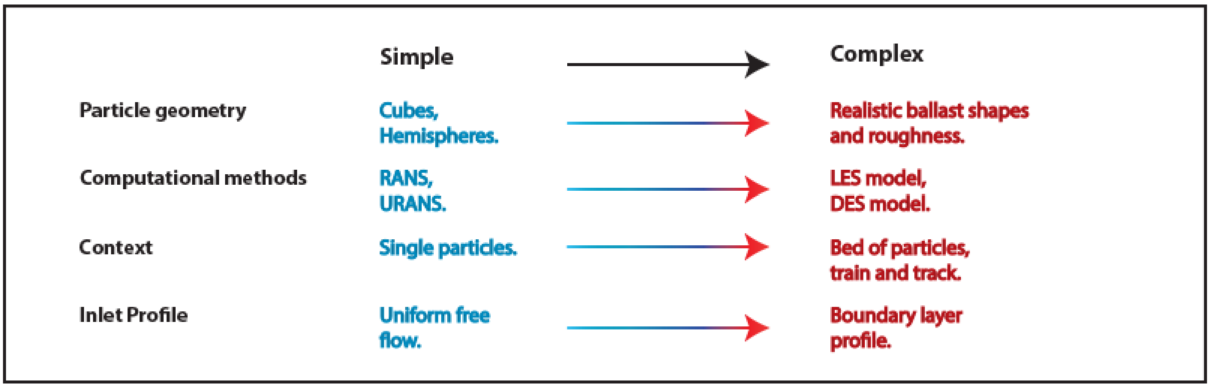

Figure 1.1: Research strategy for this investigation.

1.3 Aim and objectives

The aim of this study is to improve the understanding of the effects of air movement underneath a moving train on ballasted track using CFD and experimental methods, to propose a solution that can minimise the risk of ballast flight. This is carried out by isolating specific elements of the event where no gust or mechanical forces take place but instead a continuous air flow generated by the moving train. By breaking down these elements can provide a better understanding of what is happening rather than analyse the overall outcome without knowing which force is the biggest contribution towards ballast flight and how these factors can be reduced individually. Therefore, this analysis closely describes what is happening underneath the train between the bogies where the flow becomes less turbulent and the mechanical vibrations are reduced. These elements are described in greater detail in Chapter 2 from previous work conducted by other researchers.

Referring to the strategy in Figure 1.1, the following objectives are set for the project.

1. Isolated particles: Studies are carried out on isolated particles, such as a wall-mounted cube and hemisphere, to compare with published experimental data. Furthermore, realistic ballast shapes will be introduced to calculate changes in aerodynamic forces at different orientations. The ballast shapes are characterised along with its aerodynamic performance, to find which type of particles are more prone to flight. Their force coefficients are later compared with the cube and hemisphere. Some simple wind tunnel studies are also performed to validate some studies and approaches.
2. Track section studies: The second CFD study involves turbulent flow across track sections where the sleeper shapes and ballast levels are varied. Track study is important as the ballast depth is not consistent throughout the entire journey due to maintenance. Cubes are placed at various locations on the track to determine at which position(s) that isolated particle(s) are prone to movement. The effect of sleeper shapes and ballast level studies could influence the High-Speed Rail standards to minimise ballast flight.

For each analysis, both steady and unsteady turbulence models were used. The effects of wall roughness and wall movement were also compared to see the changes in aerodynamics. Numerical results revealed how the flow speed from the HST would contribute towards the lift and drag forces of these particles that are highly sensitive to its shape and the full-scale Reynolds number.

1.4 Ballastless (slab) tracks

Slab tracks are considered by some authors to be more suitable than ballast for high-speed rail lines (Chandra & Agarwal, 2013) but compared with ballasted track, its trade-off includes the difficulty of maintenance that could disrupt the rail service. However, compared with ballasted tracks, the frequency of required maintenance is low, providing a potentially attractive solution for track operators.

Figure 1.2: Slab track inside the tunnel at the Kyushu Shinkansen line (Yokoyama, 2000).

The Japanese Shinkansen Network is one of many high-speed rail lines that run on mostly slab track at higher average speeds of approximately 300 km/h (Yokoyama, 2000). Another example is the Chinese high-speed rail line, which is the world's longest network high-speed network (19,000 km) at January 2016, which operates at speeds between 200 to 350 km/h (Reuters, 2016).

The cross-section of a reinforced concrete slab track is shown in Figure 1.3 (Indraratna, 2011) where the foundation is supported by soil with high permeability including sand to avoid soil saturation, weakening the support strength (Powrie, 2013).

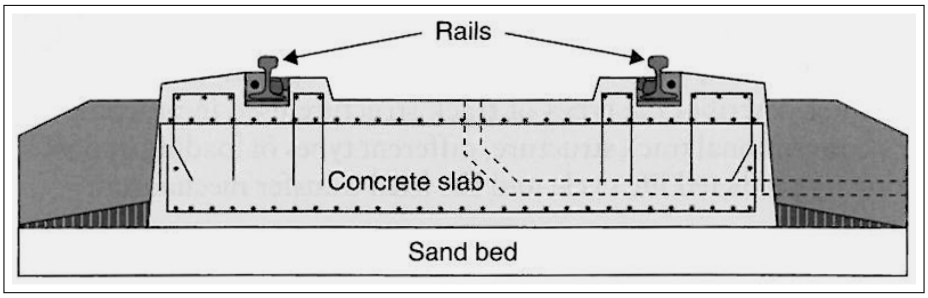

Figure 1.3: Cross-section of a slab track.

Using a slab track of ballast instead can potentially reduce the frequency of maintenance with a better service life. However, complexity and construction costs would be greater with time-consuming repairs during maintenance. Therefore, ballasted tracks remain popular in countries that regularly use HST at speeds over 300 km/h.

1.5 Ballasted tracks

Ballasted tracks consist of four major components; sleeper blocks to align the rail and distribute loads from the train, rails to support the train, and ballast as the supporting foundation, which is placed on top of sub-ballast.

1.5.1 Ballast particles

Ballast plays a vital role in transmitting and distributing train loads (Figure 1.4) to the underlying sub-ballast and sub-grade layer. The track is stabilised through the interlocking of ballast grains, which affects the permissible train speed and passenger ride comfort.

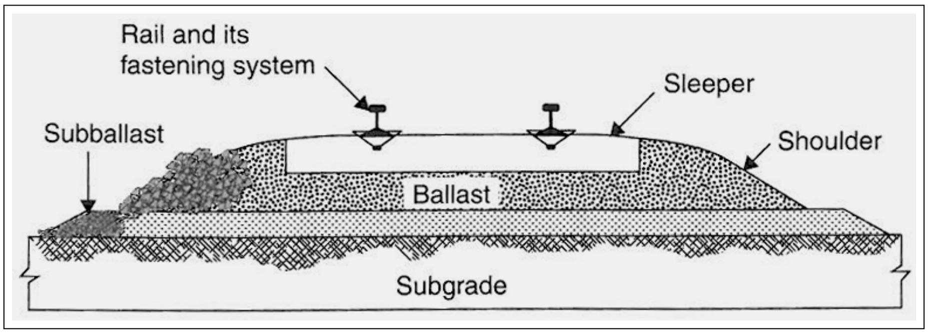

Figure 1.4: Cross-sectional layout of the ballast track, displaying ballast and formation layers (Indraratna, 2011).

Ballasted track can also provide better drainage, inhibits vegetation growth, is easier to clean and is resistant to deformation providing a suitable foundation for the track.

Many types of ballast are used on rail tracks. Sand ballast was used for tracks with a low traffic density supported by wooden sleepers. Sand ballast has good drainage properties but can easily be blown away due to its low grain weight, thus is not suitable for high-speed tracks.

Broken stone ballast is used on most railways including high-speed tracks with concrete sleepers. The initial costs are greater than other ballast types, but it provides a more economical option over time. Ballast stones are produced by crushing hard stones (i.e. granite) to sizes between 15 mm and 65 mm diameter using heavy machinery. The ballast particles need to be hard and durable with angular edges and free from impurities. Granite is preferred to limestone, as granite does not degrade as much when wet and has a larger density to resist external forces (Indraratna, 2011).

The shape of a ballast grain should be close to cubic with flat faces and or up to two rounded faces (Chandra & Agarwal, 2013). When the proportion of smaller particles is greater, the void size and drainage will decrease. But if the ballast grains are too big, the loads on the track ties would be improperly distributed that could cause the track to buckle. Therefore, smaller ballast grains are usually used as sub-ballast to support the ballast layer supporting the track and may be mixed in with larger ballast to improve interlocking between grains (Figure 1.4).

The material densities of different ballasts are summarised in Table 1.1:

Table 1.1: Material properties of ballast stones.

Material	**Density** kgm^{-3}
Limestone	2,300
Granite	2,600 to 2,800
Graphite	2,300 to 2,700

The ballast specifications in Canada and Australian rail tracks (Indraratna, 2011) states that the density of ballast stone should not be less than 2,500 kgm^{-3}, which suggests Limestone is unsuitable for high-speed rail systems. The ballast stones are distributed below, between and around the tracks shown in Figure 1.5.

Figure 1.5: Railway track supported by rail ballast (left). Ballast particles at different shapes and sizes (right).

The depth of the ballast layer depends on how regularly the track is used, the spacing between the track ties and the properties of the underlying soil. For HSTs, the ballast bed depth needs to be at least 300 mm, otherwise the train load could cause the ballast to overload the soil, causing settlement.

Ballasted track requires regular maintenance to avoid damage from future loads. This can be done by cleaning the ballast particles until it needs replacement due to excessive fouling or damage. The frequency of maintenance is dependent on the ground conditions and the track loads. Compacting the ballast particles would benefit the trackbed, but would also slightly lower the drainage. Thus an optimal choice is needed.

HSTs running on ballasted tracks could be subject to an additional issue, ballast flight due to mechanical and aerodynamic forces causing ballast grain(s) to roll and bounce off the ballast bed, which could lead to severe consequences. If a ballast stone lands on the railhead and is crushed by the train bogie, the stone can deform the rail and bogie surfaces, causing a defect that will propagate over time due to additional loading (Baker, 2014a).

Ballast flight can also be triggered when blocks of ice are formed on the train in cold weather conditions, which then plunges onto the track when the train is at high speed causing the ballast stones to move and possibly hit the moving train Premoli et al. (2015).

1.5.2 Sleepers

Sleepers are used to align and support the rails, transmitting and distributing loads across the ballast bed. Sleepers provide lateral resistance to sliding using the surrounding ballast to hold the track in place. Sleepers are designed to be durable even when ballast packing takes place with low installation and maintenance costs. Due to the large bearing area of sleepers, the load exerted on the ballast is distributed.

For this study, only concrete sleepers are considered as concrete sleepers are used in many railway systems including high-speed lines due to its low cost of maintenance and longer service life compared with wood, steel and cast iron sleepers (Chandra & Agarwal, 2013).

Firms including CEMEX and TARMAC manufacture pre-stressed concrete sleepers for both high speed and conventional railway lines. When designing sleepers, the designers would need to consider what rail system the sleeper is being used for and its purpose whether it is for goods or public transportation. Hence the designers would need to consider the forces acting on the sleeper, the geometric effect of the sleeper and provisions of failure against derailments. Therefore, the two most important variables would be the trains' expected operational speed and the vertical loads exerted onto the track. For this study, there are three different types of sleepers discussed that suit different loading conditions, including modern and traditional mono-block sleepers (Tarmac, 2016) and aerodynamic sleepers (Adif, 2012).

Traditional block sleepers are simple longitudinal beams that were introduced in the early 1800s to support the rails. The block sleeper dimensions are approximately $0.25\ m \times 0.125\ m \times 2.4\ m$. The main advantage of this design is their uniform cross-section hence low production and maintenance costs and increased stability. But due to poor traction between the wheel and the track on inclines and in wet conditions, new sleeper designs were considered.

Modern reinforced concrete mono-block sleepers were introduced to replace the traditional block sleepers due to their better performance regardless of condition. The shape of these sleepers prevents crack propagation to avoid complete failure. In the UK, the rail network uses mono-block sleepers including the G44 (Tarmac, 2016), which has a trapezoidal cross-section with varying sizes throughout the sleeper. The cross-section is at its smallest in the middle of the sleeper.

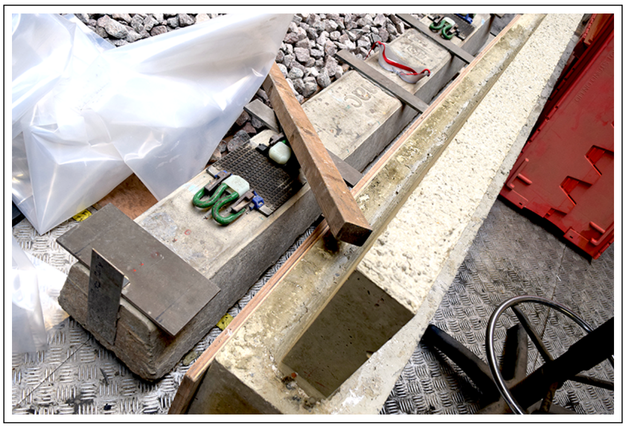

Figure 1.6: G44 mono-block concrete sleeper by Tarmac (2016). Photo taken at Civil Engineering Lab, Southampton University.

The length is between 2.4 m and 3.0 m. A sample G44 sleeper by TARMAC was measured geometrically in the Civil Engineering Lab at Southampton University (Figure 1.6) to be modelled computationally in a later chapter.

In further developments, Stanton-Bonna designed the Consolis sleeper, which is a mono-block sleeper that was used to support the track during the SNCF world record speed run (Consolis, 2016), (Stanton-Bonna, 2016).

The third sleeper considered was the aerodynamic sleeper, designed specifically for high-speed rail lines to prevent ballast flight by altering the shape of the upper surface. This sleeper was tested by a private engineering and technology group SENAR in Spain to characterise the physical effects of the phenomenon (Bazen, 2012).

Pressure and velocity were measured across a 400-meter section of the Madrid-Barcelona line to see which area was mostly affected by the train's (type 100, 102 and 103) movement running over 300 km/h (Figure 1.7):

Figure 1.7: Pitot tubes and hot-wire anemometers installed on the track.

Computational analysis was carried out by modelling a 2D cross-section of the sleeper with a moving wall representing the high-speed train in an attempt to compute the risk of ballast flight for different train and track characteristics (Adif, 2012). Simulations were conducted to determine the distribution where the individual stones reach the most probable heights of the ballast bed and to study the impact and rebound of ballast underneath the train. Based on the results shown in Figure 1.8, conditions were modified to reduce the risk of ballast flight while maintaining the lateral stability of the track by lowering the velocities near in the ballast bed between the sleeper blocks.

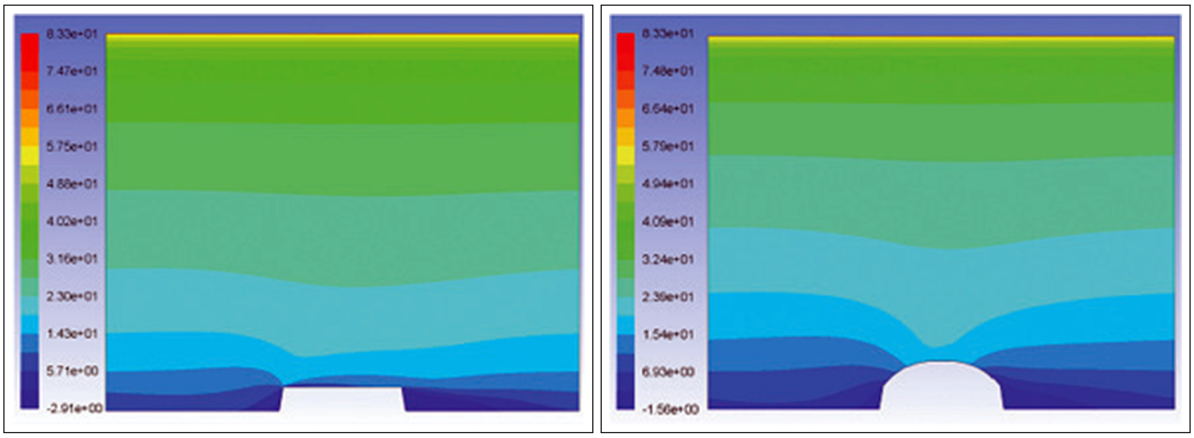

Figure 1.8: Velocity contour plot across track sections using CFD. Outcome using a mono-block sleeper (left) and using the aerodynamic sleeper (right) (Bazen, 2012).

It was found that by changing the sleeper shape, the aerodynamic load on the ballast bed was reduced, which reduces the number of ballast particles settling onto the sleeper without significant additional costs. This sleeper, known as the Aerotraveisa sleeper (Bazen, 2012) (Figure 1.9), has been adopted in new high-speed rail projects including the Mecca-Medina line in Saudi Arabia.

Figure 1.9: Final product of the aerodynamic sleeper (Bazen, 2012).

Having a smoother upper surface also prevents ballast particles from resting on the sleeper and reduces the aerodynamic load (by 21%) on the ballast bed, which can allow greater operational train speeds. The revealed dimensions of this sleeper from Bazen (2012) were noted for modelling.

1.6 Layout of the report

Essential aerodynamic and turbulence theory will be presented in Chapter 2 including basic aerodynamics and comparisons between different turbulence modelling approaches, which were used in the numerical study chapters.

In Chapter 3, a literature review of numerical and experimental studies was carried out, focusing on aerodynamics underneath HSTs, granular particle properties and obstacles undergoing turbulent flow.

Chapters 4 and 5 reported the numerical results for isolated particles and periodic channels under high-speed flow. Initial studies were benchmarked, while further studies required new experimental data. Simple experimental wind tunnel studies were carried out where its results were summarised.

Finally, conclusions of current findings and recommended future research are summarised in Chapter 6.

Chapter 2

CFD and Turbulence Theory

2.1 Introduction

Investigations in aerodynamics comprise three elements of theory, CFD simulation and experimental testing. CFD software capabilities have evolved rapidly in recent years owing to better hardware and development in numerical techniques, enabling engineers and researchers to solve more complicated problems efficiently.

The current capabilities of commercial CFD codes for wind engineering suggest that turbulence can be resolved numerically providing reasonable results that are deemed useful. However, it is still crucial to perform wind tunnel experiments to gain better confidence in CFD results, as they have not yet reached the desired accuracy in turbulence (Blocken, 2014).

2.2 Fundamentals of Fluid Mechanics

In fluid mechanics, as a fluid flow passes around an object, the air molecules near the object are disturbed and move around it generating aerodynamic forces between the flow and the object. The magnitude of these effects depends on the speed of the flow/object, the shape of the object, the mass of the flow, the viscosity and compressibility of the fluid. Aerodynamicists use parameters including the Reynolds number and Mach number to describe a flowing fluid.

2.2.1 Reynolds Number and Mach Number

The Reynolds number of the flow is the ratio of inertia forces (which resist changes in motion) and viscous forces (which are based on fluid *thickness*). The Reynolds number characterises whether the flow is inertia or viscosity dominated, and hence whether the flow is laminar or turbulent.

$$Re = \frac{\text{Inertia Forces}}{\text{Viscous Forces}} \qquad \text{Inertial Force} \propto \frac{\rho U^2}{L} \qquad \text{Viscous Force} \propto \frac{\mu U}{L^2} \tag{2.1}$$

where U is the velocity of the flow, L is the characteristic length such as the chord of an aerofoil, ρ is the fluid density and the μ is the dynamic viscosity. $\nu = \frac{\mu}{\rho}$ is the kinematic viscosity. Therefore, the Reynolds number can be written as:

$$Re = \frac{\rho U L}{\mu} = \frac{UL}{\nu} \tag{2.2}$$

At low Reynolds number, viscous forces are dominant, and the flow is laminar with the flow motions parallel and minimal disruption. As the Reynolds number increases, the flow reaches a transition at which it becomes turbulent. In turbulent flow, inertial forces are dominant and the flow motion is chaotic and randomised, with the instantaneous velocity and pressure changing over time within each region of flow.

The Mach number is the ratio between the speed of a body (U) and the local speed of sound ($c \approx$ 340 ms^{-1}) for air at atmospheric condition in its surrounding medium (e.g. gas or liquid). The Mach number is defined as:

$$M = \frac{U}{c} \qquad\qquad c = \sqrt{\gamma R T} \tag{2.3}$$

where γ is the ratio of specific heats (c_p/c_v), R is the universal gas constant (287 $Jkg^{-1}K^{-1}$) and T is the temperature of the fluid measured in Kelvin.

2.2.2 Compressible and Incompressible Flow

Compressible flow occurs where the change in pressure influences the fluid density. The mass of the fluid remains constant, but the volume changes due to the pressure. Compressible flow occurs when the fluid experiences significant changes in pressure or when the Mach number M is greater than above 0.3. When $M \leq$ 0.3, changes can be neglected, fluid is considered to be incompressible.

In incompressible flow, the density ρ remains constant, thermodynamics can be separated from aerodynamics. To study the flow aerodynamics only conservation of mass and momentum need be considered along with the flow temperature for applied thermodynamics, the energy conservation can be considered afterwards.

For HSTs, current speeds do not exceed M = 0.3, making the flow effectively incompressible.

2.3 Essential Turbulence Theory

The majority of flows in engineering applications are turbulent, which because of its unsteady nature, turbulence can be difficult to measure. Aerodynamicists dealing with fluid flow use statistical tools to evaluate the effects of turbulence alongside specialised equipment to measure it experimentally.

Figure 2.1 shows a turbulent quantity being measured at a single point, where the mean and instantaneous values have been quantified:

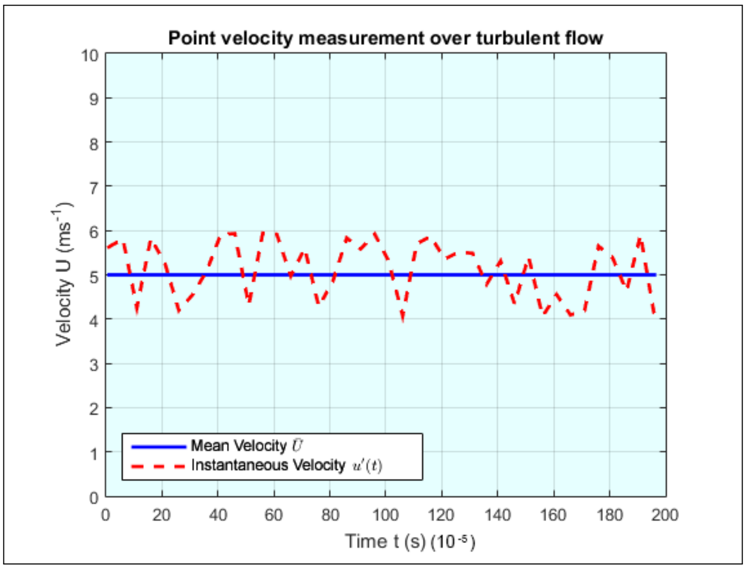

Figure 2.1: Point velocity measurement undergoing unsteady turbulent flow.

Turbulent flow is indeterministic, thus the instantaneous flow is difficult to quantify. Therefore, any flow quantity is subjected to *Reynolds decomposition* into the steady mean and fluctuating components. For example, the velocity at this point can be expressed as:

$$u(t) = \bar{U} + u'(t) \tag{2.4}$$

The same applies to scalar values associated with turbulent flow including pressure. Visualisations of turbulent flow can reveal rotational structures known as turbulent eddies with a range of length scales, which can change the overall flow characteristics. For example, if particles of a fluid are initially separated, vortex motions can bring them back together, exchanging mass and momentum.

The characteristic velocity and length of the larger eddies are of the same order as the velocity scale and length scale of the mean flow. Hence a 'large eddy' Reynolds number can be formed by combining these eddy scales with the kinematic viscosity. This will be large in all turbulent flows with different sized eddies, and similar as the flow Reynolds number. This would imply that these large eddies are dominated by inertia effects, whereas viscous effects dominate at small scales.

Another property of the turbulence fluctuations would be the turbulent kinetic energy per unit mass given by:

$$k = \frac{1}{2}(\overline{u'u'} + \overline{v'v'} + \overline{w'w'}) \tag{2.5}$$

In incompressible flow, the density is omitted.

By Fourier transformation, the fluctuations can be represented as a one-dimensional energy spectrum $E(\kappa)$ (Figure 2.2):

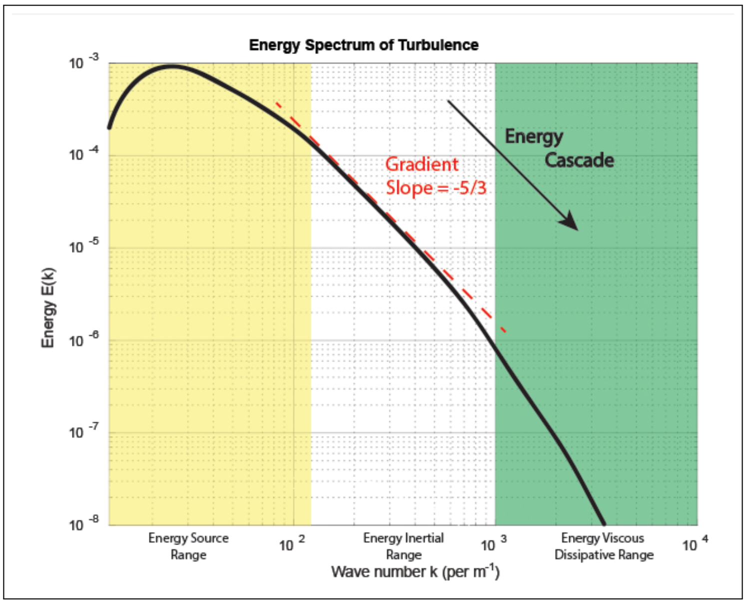

Figure 2.2: Energy spectrum of turbulence.

where the wavenumber $\kappa = 2\pi f/U$ represents the fluctuating properties of turbulence flow measured in cycles per unit distance. Figure 2.2 would suggest that the larger eddies in turbulent flow are more energetic with a lower wave number whereas smaller eddies are the opposite.

2.3.1 Boundary Layer

As the flow passes an object, its molecules interact with the surface, creating a boundary layer or viscous flow region near the surface (Figure 2.3). This causes the flow speed to decrease freestream velocity towards zero near the surface, within a thin layer, which is called a boundary layer.

The boundary layer plays an important part in aerodynamics for example in determining the frictional drag on an object. Figure 2.3 shows the streamwise velocity variation from freestream to the surface as the flow progresses from laminar to turbulent.

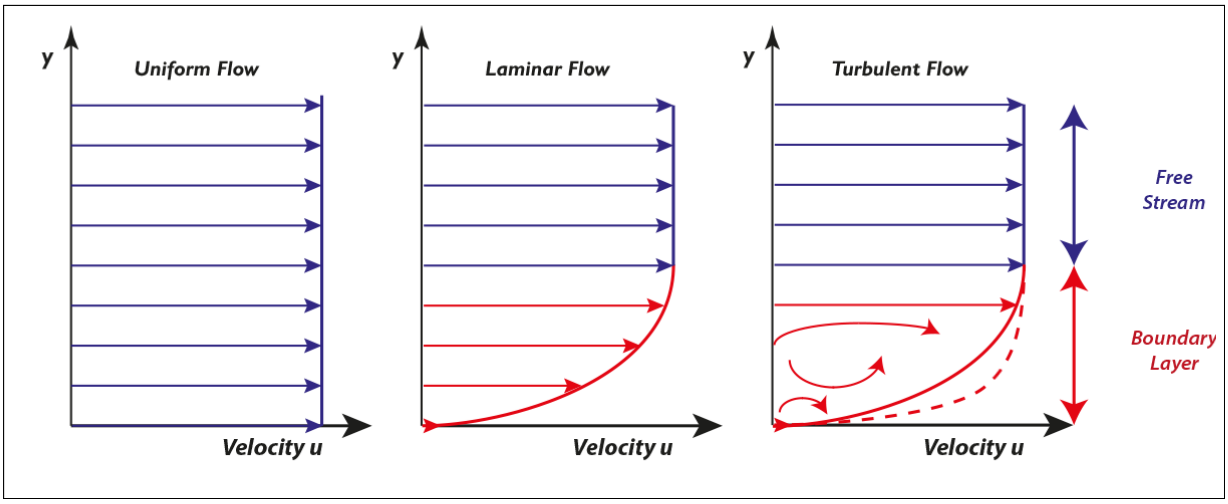

Figure 2.3: Changes of velocity profile from the wall surface. Laminar to turbulent profile with unsteady recirculation in the boundary layer. Dashed line represents boundary layer with higher τ_w.

Boundary layer effects are three dimensional. The boundary layer thickness (δ) is dependent on the Reynolds number that describes the flow characteristics.

Laminar flow and turbulent flow both can be described by Navier-Stokes and continuity equations, which can be solved analytically for simple cases or numerically for more complex flows.

In turbulent thin shear layer flows, the velocity gradient normal to the surface (du/dy) is large so by Newton's law of viscosity (Equation 2.6) the shear stress τ is also large.

$$\tau = \mu \frac{du}{dy} \tag{2.6}$$

The drag force on the fluid close to the surface does not depend on freestream parameters. As the distance from the wall y increases, the velocity gradient becomes smaller thus the viscous drag decreases. The mean flow velocity depends on the distance from the wall y, the fluid density ρ and the viscosity μ and the wall shear stress τ_w thus:

$$U = f(y, \rho, \mu, \tau_w) \tag{2.7}$$

Dimensional analysis (Versteeg & Malalasekera, 2007) shows that:

$$u^+ = \frac{U}{u_\tau} = f\left(\frac{\rho u_\tau y}{\mu}\right) = f(y^+) \tag{2.8}$$

which is known as **law of the wall** containing two important dimensionless variables u^+ and y^+, which is defined on Equation 2.8. The frictional velocity u_τ is determined by the skin wall friction τ_w and fluid density ρ such that:

$$u_\tau = \sqrt{\frac{\tau_w}{\rho}} \tag{2.9}$$

The law of the wall is illustrated in Figure 2.4, which shows the velocity distribution near a solid wall.

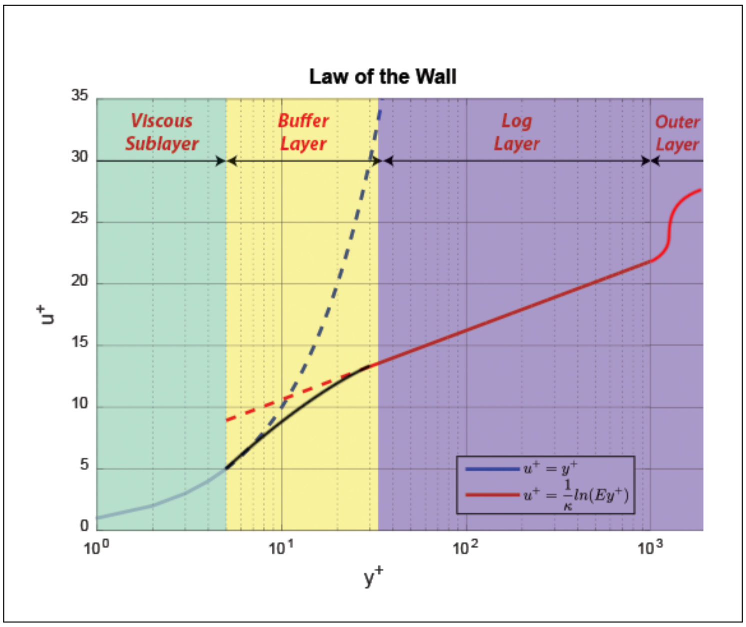

Figure 2.4: Dimensionless velocity against the dimensionless wall distance. Law of the wall.

Near the smooth wall, there is a viscous sub-layer where the fluid is close to stationary at the solid surface due to viscous effects. The viscous sub-layer is very thin such that $y^+ < 8$ and the shear stress may be assumed constant throughout. Thus the definitions of u^+ and y^+, lead to:

$$u^+ = y^+ \tag{2.10}$$

due to the linear relationship between the velocity and distance to the wall.

Outside the viscous sub-layer and the buffer layer $(30 < y^+ < 500)$ is the log layer, where the shear stress τ varies slowly with distance from the wall. The mixing length $l_m = \kappa y$, which provides a functional relationship between u^+ and y^+ such that:

$$u^+ = \frac{1}{\kappa} ln(y^+) + B \tag{2.11}$$

where $\kappa = 0.4$ is von Karman's constant and the additive constant $B \approx 5$ for smooth walls (with increasing wall roughness, B decreases). Owing to the logarithmic relationship between u^+ and y^+, it is referred to as the log-law layer or the wake region.

2.4 Introduction to Computational Fluid Dynamics

CFD is the computational analysis of fluid flow and heat transfer for a given system. The technique solves the governing Navier-Stokes equations of mass, momentum and energy conservation, and has become increasingly popular for industrial and non-industrial applications.

CFD techniques have been used in design, research and development procedures in aerospace projects since the 1960s and in later years have been applied to more complex systems such as combustion engines. Furthermore, automotive manufacturers use CFD to evaluate the aerodynamic performance of their designs. Thus CFD has become a vital component in the development process.

However, high-performance computing hardware is required for complex flows, which makes it difficult for industries to access. Although CFD is expensive, only it is still cheaper than a high-quality experimental lab and CFD does have some advantages over experimental approaches such as:

- Reduction in time between the initiation and completion of a production process and in costs for new designs.
- Ability to study complex systems, which are difficult to implement experimentally in detail.
- Ability to study systems that are exposed to hazardous environments at and beyond the normal performance limits (e.g. safety studies and destructive or accidental situational scenarios).
- A potentially high level of detail of results, depending on the user requirements and available resources.

In more recent developments, CFD packages now include animation for effective visualisation. Targeted solution data can be exported into many formats for further data manipulation.

In contrast, CFD can produce large quantities of data with no added expense and parametric studies can be performed more cheaply. CFD codes follow a structure around numerical algorithms suitable for analysing fluid flow problems. However, sufficient experience in using CFD is required to produce useful and reliable results.

The remainder of this chapter will discuss CFD solvers and turbulence models utilised in later chapters.

2.5 Turbulence Models

This section introduces the governing Navier-Stokes equations followed by a range of turbulence models and solution algorithms used in commercial software.

2.5.1 Navier-Stokes equation

Fluid flow is governed by the nature law of conservation. The first is the mass conservation continuity equation, which is based on the requirement that for any closed system, the mass is constant over time as mass cannot be created nor destroyed. With the unsteady component in red, the continuity equation is represented as:

$$\frac{\partial \rho}{\partial t} + \frac{\partial (\rho u_i)}{\partial x_i} = 0 \tag{2.12}$$

where ρ is the fluid density, $\mathbf{u}$ is the velocity vector with components in three dimensions u, v, w and t is time. The upper velocity limit throughout this project is approximately 83.3 ms^{-1}, which would imply that the Mach number is:

$$\frac{\text{Speed of Object/Flow}}{\text{Speed of Sound}} = \frac{83.3\ \ ms^{-1}}{340.3\ \ ms^{-1}} \approx 0.2448 \tag{2.13}$$

thus the flow can be treated as incompressible (ρ is constant), meaning Equation 2.12 can be reduced to:

$$\nabla \cdot (\rho \mathbf{u}) = 0 \implies \nabla \cdot \mathbf{u} = 0 \tag{2.14}$$

Momentum

Momentum is the product of mass and velocity. The momentum equation describes how the velocity, pressure, and density of a moving fluid are related by applying Newton's second law to fluid element motion.

$$\frac{\partial(\rho u_i)}{\partial t} + \frac{\partial(\rho u_i u_j)}{\partial x_j} = -\frac{\partial p}{\partial x_i} + \frac{\partial \tau_{ij}}{\partial x_j} \tag{2.15}$$

where the viscous stress tensor τ_{ij} is defined by:

$$\tau_{ij} = 2\mu\left(S_{ij} - \frac{1}{3}\frac{\partial u_k}{\partial x_k}\right) \tag{2.16}$$

where S_{ij} is the rate-of-strain tensor by distance.

$$s_{xy} = s_{yx} = \frac{1}{2}\left(\frac{\partial u}{\partial y} + \frac{\partial v}{\partial x}\right) \qquad s_{xz} = s_{zx} = \frac{1}{2}\left(\frac{\partial u}{\partial z} + \frac{\partial w}{\partial x}\right) \qquad s_{yz} = s_{zy} = \frac{1}{2}\left(\frac{\partial v}{\partial z} + \frac{\partial w}{\partial y}\right)$$

for incompressible flow.

Energy Equation

The energy equation is derived from the conservation of energy:

$$\frac{\partial(\rho E_T)}{\partial t} + \frac{\partial(\rho u_i E_T)}{\partial x_j} = \dot{q} + \left[\frac{\partial}{\partial x_j}\left(k\frac{\partial T}{\partial x_j}\right) - \frac{\partial(u_i p)}{\partial x_j} + \frac{\partial(u_i \tau_{ij})}{\partial x_i}\right] \tag{2.17}$$

where T is the temperature, k is thermal conductivity and E_T is the total energy.

$$E_T = e + \frac{1}{2}\mu_i u_i \tag{2.18}$$

Since the flow Mach number is lower than 0.3 and the flow can be considered as incompressible, thermodynamics is not part of this project. Also energy is not required.

2.5.2 Reynolds-Averaged Navier Stokes (RANS)

The RANS turbulence model transport equation models including Spalart-Allmaras (SA), $k-\varepsilon$ and $k-\omega$. RANS models the aerodynamic effects of turbulence in its calculations. Most industries use the two-equation models in CFD calculations that omit certain physics in turbulence, providing an approximate solution.

Steady RANS will provide a solution by using the local time-step for each cell. This will not make it time accurate, but will provide a faster solution which is ideal for initial studies.

The RANS equations are closed by assuming Reynolds stresses $(\overline{-u_i' u_j'})$ satisfying the Boussinesq approximation:

$$-\overline{u_i'u_j'} + \frac{1}{3}\overline{u_l'u_l'}\delta_{ij} = \nu_T\left(\frac{\partial U_i}{\partial x_j} + \frac{\partial U_j}{\partial x_i}\right) \tag{2.19}$$

where ν_T is the scalar eddy viscosity, which is determined from the turbulence velocity q and turbulence length scale l such that $\nu_T = Cql$ where C is a constant.

With algebraic zero equation models, the Boussinesq approximation is used where $\nu_T \approx ql$ and both velocity q and length l scales are assigned. For one equation models, the Boussinesq approximation is used with an additional partial differential equation known as the transport equation introduced, which is solved for kinetic energy $k = \frac{1}{2}q^2 = \overline{u_i'u_i'}$ and an algebraic relation for length scale l with $\nu_T \approx ql$.

For two equation models, the Boussinesq approximation is made with $\nu_T \approx ql$ with two additional transport partial differential equations for q and l. The velocity scale q is determined from the solution of the transport equation for kinetic energy k and $q = \sqrt{2k}$ (Sandberg, 2014).

Turbulent Kinetic Energy

The kinetic energy of turbulent fluctuations per unit mass k can be calculated using Equation 2.20:

$$k = \frac{1}{2}(\overline{u_x'^2} + \overline{u_y'^2} + \overline{u_z'^2}) \tag{2.20}$$

When estimating the turbulence intensity of the CFD inlet, it is necessary to have a value in the form of measurements or past examples to base the estimate on.

For a low turbulence intensity case ($\leq 1\%$), the flow is laminar for example where the flow originates from a static fluid like external flow across cars, aircraft and submarines. High-quality wind tunnels with reduced noise can reach low turbulence levels. Flow across non-complex channels such as ventilation ducts and pipes or low-speed flows are classified as medium turbulence cases with a turbulence intensity between 1% and 5%. Finally, for high turbulence intensity cases, the flow is at a high Reynolds Number for example inside complex geometries such as turbines and compressors. The turbulence intensity is between 5% and 20%.

Dissipation Rate

The turbulent dissipation rate ε, which is the conversion of turbulent kinetic energy into thermal internal energy due to large velocity gradients created by eddies at different scales. The turbulent dissipation rate ε is calculated by using the turbulence length scale or from the eddy viscosity ratio.

Turbulence length scale

$$\varepsilon = C_\mu \propto \frac{k^{\frac{3}{2}}}{l} \tag{2.21}$$

where the turbulence model constant $C_\mu = 0.09$. For specific CFD codes including AnSys Fluent, the turbulence length scale is different to the mixing-length:

Eddy viscosity ratio

$$\varepsilon = C_\mu \frac{\rho k^2}{\mu}\left(\frac{\mu_t}{\mu}\right)^{-1} \tag{2.22}$$

Specific Dissipation Rate

The turbulent specific dissipation rate ω is the turbulence kinetic energy converted into thermal internal energy per unit volume and time which can be computed following these approaches:

Turbulence length scale

$$\omega = \frac{\sqrt{k}}{l} \tag{2.23}$$

where the turbulence model constant $C_\mu = 0.09$ (Versteeg & Malalasekera, 2007). Again, for CFD codes, the turbulence length scale length is different based on the mixing-length:

$$\omega = C_\mu^{-\frac{1}{4}} \frac{\sqrt{k}}{l} \tag{2.24}$$

Eddy viscosity ratio

Similar to the turbulent dissipation rate ε, ω is computed using the following expression (Versteeg & Malalasekera, 2007):

$$\omega = \frac{\rho k}{\mu} \left(\frac{\mu_t}{\mu} \right)^{-1} \tag{2.25}$$

2.5.3 Two equation model $k - \varepsilon$

For this project, two-equation turbulence models were used using the $k - \varepsilon$ and $k - \omega$ equations commonly used in engineering problems.

The benefit of using a two-equation model is to determine the length and time scale of turbulence by solving two separate transport equations derive the kinetic energy of turbulence and the time/spatial scale of turbulence.

Standard $k - \varepsilon$ turbulence model

Engineering industries widely use the standard $k - \varepsilon$ model because of its robustness and reasonable accuracy for a range of turbulent flows. The $k - \varepsilon$ model is based on model transport equations for the turbulence kinetic energy k with units $m^2 s^{-2}$ and the dissipation rate ε of units $m^2 s^{-3}$.

The turbulent dissipation rate results in the velocity fluctuations dissipating over time towards a steady state. The eddy viscosity is determined by the length scale so the turbulent diffusion is calculated, which occurs only at a specified scale. However, in reality, all scales of motion contribute to turbulent diffusion.

With the use of gradient diffusion, the $k - \varepsilon$ model can relate the Reynolds stress to the mean velocity gradients and turbulent viscosity. The standard $k - \varepsilon$ model is valid for fully turbulent flows only.

Realisable $k - \varepsilon$ model

Once the strengths and weaknesses of the standard $k - \varepsilon$ model had been identified, additional variants of the model were created by modifying the model to improve its performance.

One is the RNG $k-\varepsilon$ model and another the Realisable $k-\varepsilon$ model that satisfies certain mathematical constraints that are in this study. The Realisable $k-\varepsilon$ model uses an alternative equation to calculate the turbulent viscosity and the dissipation rate that was derived from the exact equation for transport of the mean-square vorticity fluctuation.

Overall, the advantages of using $k-\varepsilon$ include the model being (Versteeg & Malalasekera, 2007):

- More robust.
- Easier to implement.
- Computationally cheaper than most two-equation models.
- Broadly validated by previous research.

The $k-\varepsilon$ should only be considered for fully turbulent flows. Different model variants and constants are suited for certain range of flow applications. However, its drawbacks include (Versteeg & Malalasekera, 2007):

- Being valid for fully turbulent and non-separated flows.
- Producing poor results for complex flows involving separations, severe pressure gradients and sharp streamline curvatures (e.g. swirling flows).
- Having a low sensitivity towards Adverse Pressure Gradients (APG).

2.5.4 Two equation model $k-\omega$

Standard $k-\omega$ turbulence model

The $k-\omega$ model is extended the $k-\varepsilon$ model, solving the kinetic energy the same way together with the specified dissipation rate ω with unit s^{-1}, which is also known as the turbulent frequency. This model allows near wall treatment for accuracy by providing a switch between the wall function and low Reynolds number correction based on the grid spacing. Therefore, $k-\omega$ demonstrated superior performance for wall-bounded flows and flows at low Reynolds number by using a correction function to damp the turbulent viscosity.

The $k-\omega$ model can potentially calculate transitional flows, and gives additional options to take into account compressible and free shear flows. The $k-\varepsilon$ element of the model can use gradient diffusion to relate the Reynolds stress to the mean velocity gradients and turbulent viscosity. Another benefit this model provides is that it works better under Adverse Pressure Gradient (APG) conditions but can under-predict the separation if the APG is too high.

To summarise, the overall advantages of standard $k-\omega$ include (Versteeg & Malalasekera, 2007):

- Better performance for wall-bounded layer, free shear and low Reynolds number flows.
- Suitably for complex flows under APG and separation.
- Ability to predict transitional flow.

The disadvantages include:

- Requiring mesh refinement near the wall.
- Early and excessive calculation of flow separation.

Shear Stress Transport (SST) $k-\omega$

The Shear Stress Transport $k-\omega$ model is a variant of the $k-\omega$ model, which has become popular since it combines the advantages of two models.

The first is the $k-\omega$ at the viscous sub-layer of the boundary layer where $y^+ \leq 5$. At the viscous sub-layer, the boundary layer is resolved by using low Reynolds Number without any extra damping functions, which would require a refined boundary layer mesh with the first cell normal to the wall with $y^+ \leq 1$. The growth rate of the cells from the solid boundaries should not exceed 1.25.

In the log layer of the boundary layer $y^+ \geq 30$ in the freestream flow, the model switches to Standard $k-\varepsilon$. Therefore, the SST $k-\omega$ model is useful all the way down to the wall. The model avoids the sensitivity problem, which Standard $k-\omega$ experiences with the inlet freestream turbulence properties including turbulent kinetic energy k, dissipation rate ε and specific dissipation rate ω. These values are determined by either the turbulence length scale or from the eddy viscosity ratio.

2.5.5 Unsteady RANS and Detached Eddy Simulation

Unsteady RANS

Steady RANS approaches the solution with a locally optimised time step for each cell, which is a faster solution but it is not time accurate. Whereas RANS is steady state and time-averaged, URANS takes the time-advancement approach by solving the flow for each time step. The difference between RANS and URANS would be the additional unsteady term in Equation 2.12 for Mass and Equations 2.15 for Momentum conservation. The global time step would need to be small enough to capture velocity fluctuations and unsteady mean quantities to make it time-accurate.

Detached Eddy Simulation (DES)

Detached Eddy Simulation (DES) is a popular hybrid that combines RANS/LES methods. The motivation was due to difficulties linked to the use of LES, particularly near solid walls. DES was introduced by Spalart et al. (1997) as a cost-effective procedure that treats the largest eddies by using LES, but using RANS within the attached boundary layer. Thus, the two methods are blended to eliminate each other's weaknesses.

The DES approach can be utilised with any turbulence model (i.e. Spalart-Allmaras, Realisable $k-\varepsilon$ or SST $k-\omega$) that has the appropriate turbulence length scale and is a sufficiently localised model. The SST $k-\omega$ model is a good example as it uses a turbulence length scale obtained from the model equations and compares it with the grid length scale to switch between LES and RANS by using a blending function, which was originally used to make the $k-\omega$. For RANS, the effective turbulence length scale is implied by the model l_{RANS} (Wilcox, 2006):

$$l_{RANS} = \frac{\sqrt{k}}{\omega} \tag{2.26}$$

For LES, the local finite-difference cell size Δ is used:

$$l_{LES} = \Delta \tag{2.27}$$

Cells are treated as part of the sub-grid and are deemed unresolvable when $l_{RANS} < l_{LES}$. Its applications range from research orientated problems to complicated industrial or military defence projects. DES is capable of reproducing results around complex shapes including a cylinder undergoing flow at Mach 2.5 whereas RANS was unable to do so accurately (Wilcox, 2006).

A performance study between URANS and LES was carried out by Salim et al. (2011) to assess whether URANS could perform equally well at a fraction of the computational cost. It was concluded that URANS fails to account for unsteady fluctuations, which makes it not as detailed as DES/LES.

2.5.6 Large Eddy Simulation (LES)

The LES method utilises a spatial filter that removes the smaller spatial scales of turbulence that cannot be resolved by the grid and introduces a sub-grid scale model in an attempt to emulate the effect of the unresolved small scales on the resolved larger ones.

LES is more computationally expensive than DES, URANS and RANS although produces the most accurate and reliable results since it resolves the mixing process in the flow field, LES will not be used in this project.

2.6 Solution Algorithms for Pressure-Velocity Coupling in Steady Flows

There are several solution algorithms used for pressure-based coupled solver. One is the SIMPLE (Semi-Implicit Method for Pressure-Linked Equations) solver and the other two are SIMPLEC and PISO, which are adopted on AnSys Fluent and OpenFOAM.

2.6.1 SIMPLE Algorithm

SIMPLE uses a relationship between the velocity and pressure corrections to enforce mass conservation and obtain a pressure field. This method follows an iterative approach, in which other scales are coupled into the momentum equation where calculations are executed sequentially. Figure 2.5 shows a flow chart of the SIMPLE algorithm where the pressure and velocities are calculated iteratively.

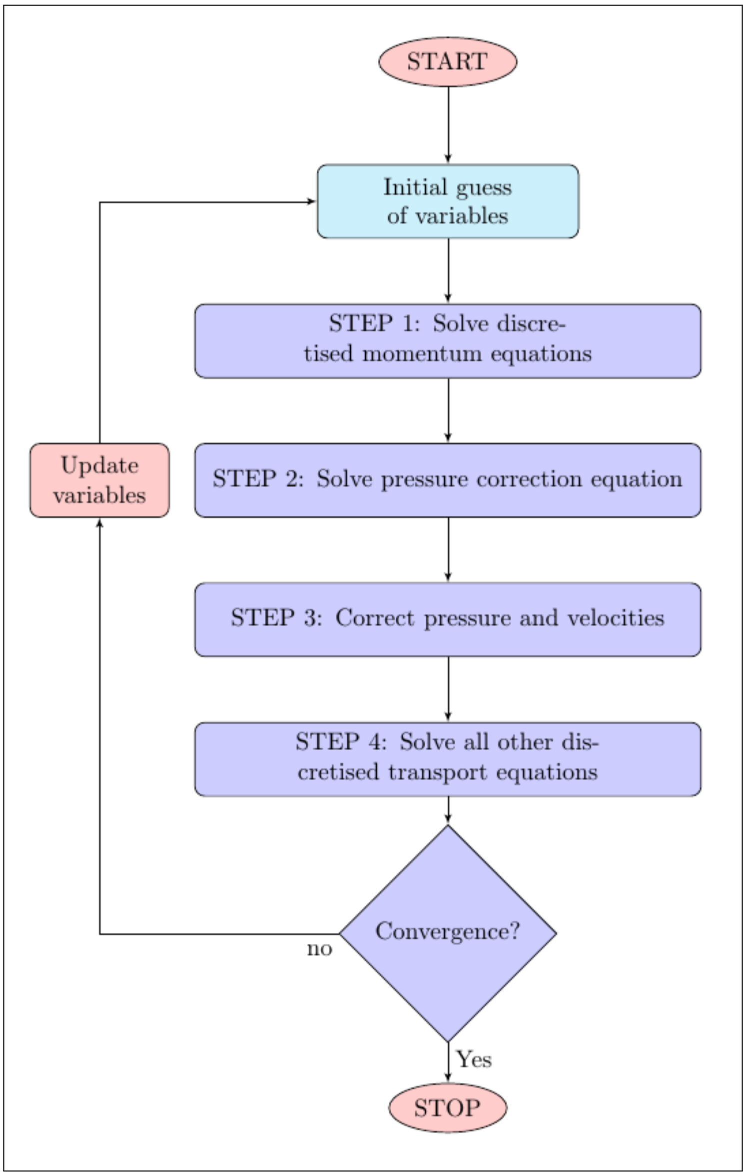

Figure 2.5: Flow chart of SIMPLE Algorithm.

2.6.2 SIMPLEC Algorithm

The SIMPLEC (SIMPLE Consistent) algorithm follows similar steps as the SIMPLE algorithm except the momentum equations are manipulated such that the SIMPLEC velocity correction omits terms that are less significant than those in SIMPLE.

2.6.3 PISO Algorithm

The PISO (Pressure Implicit with Splitting of Operators) algorithm is a pressure-velocity induced procedure that is originally developed for non-iterative computation of unsteady compressible flows. PISO uses one predictor and two corrector steps that can be seen as an extension of the SIMPLE algorithm but with an additional corrector step to enhance it (Figure 2.6).

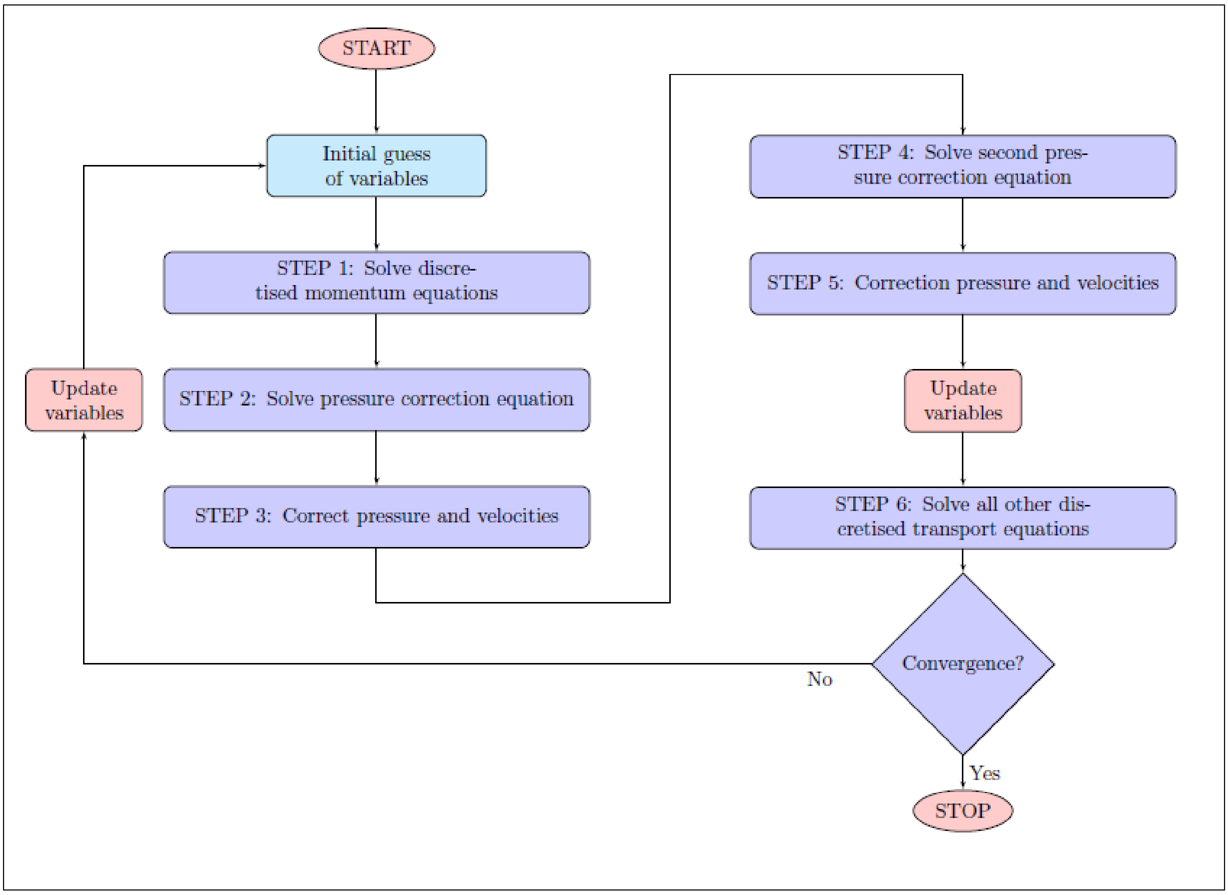

Figure 2.6: Flow chart of PISO Algorithm.

PISO is recommended with neighbouring correction for all transient flow calculations, especially for simulations with large time steps. This normally applies to LES or DES models that require smaller time steps. Using PISO may increase computational expense, meaning that SIMPLE or SIMPLEC may be more beneficial. PISO potentially can maintain a stable calculation with a larger time-step with momentum and pressure under-relaxation factors set to 1.0. However, for steady-state problems PISO does not provide any advantage over SIMPLE or SIMPLEC with optimal under-relaxation factors. A more detailed description of these algorithms can be found in Versteeg & Malalasekera (2007).

SIMPLE vs. SIMPLEC vs. PISO

In AnSys Fluent, all algorithms are available. SIMPLE is the default algorithm choice but in most cases, SIMPLEC is more beneficial due to the increased under-relaxation values used to speed up convergence depending on flow conditions. However, the solution can become unstable if the mesh skewness is too high. For skewed mesh cases, it would be advised to use a lower under-relaxation value (up to 0.7) or use the SIMPLE algorithm.

A comprehensive comparison (PISO, SIMPLE and SIMPLEC) using steady flow by Jang et al. (1986) suggests that for problems where momentum equations are not coupled with scalar variables, PISO showed a robust convergence compared to SIMPLE and SIMPLEC.

However, the scalar variables are closely linked to velocity in which PISO has no advantage over other methods and the iterative methods SIMPLE and SIMPLEC have robust convergence characteristics for strongly coupled problems (AnSys, 2009). Therefore in the computational chapters, SIMPLEC will be used as the pressure solver in AnSys Fluent to provide rapid convergence.

2.7 Errors and Uncertainty in CFD Modelling

This section discloses the importance of errors and uncertainties when performing CFD calculations, how are they are caused and what are the best practices to achieve the best possible level of confidence in CFD results from available resources.

2.7.1 Errors and uncertainty in CFD

CFD is perceived as good value for money if performed correctly. However, if the results are incorrect then time, money and effort would be wasted and can be disastrous if components or structures fail by using these incorrect results. In academic research, CFD development focuses on new functionality and better understanding whereas for the industry has an intention in making things work with limited knowledge and confidence in their results.

Experimental uncertainties calculation is a well-established practice, which should also be applied to numerical modelling. In the context of trust and confidence in CFD modelling, the following definitions of error and uncertainty have been defined as the following (Versteeg & Malalasekera, 2007):

Potential sources of errors

- Numerical error: iterative convergence errors, round off errors or discretisation errors.
- User error: human errors through incorrect usage of the software.
- Coding error: incorrect input or bugs in the software.

Uncertainty

- Input uncertainty: incorrect input due to misinterpretation of information or approximated representation of geometry and boundary conditions.
- Physical modelling uncertainty: discrepancies between real and CFD flows due to inadequate representation of physical processes due to simplifying assumptions in modelling process (e.g. incompressible flow, steady flow.)

2.7.2 Validation and verification

Thus, it is common practice to perform verification and validation between results to gain confidence in its accuracy. CFD results can be verified by comparing CFD results at different sizes of the absolute criteria for residuals or by performing a grid comparative study.

When it comes to validating the results, it is essential to make comparisons with other experimental/numerical data, which would need to have similar conditions for the data to be comparable (Versteeg & Malalasekera, 2007).

Chapter 3

Literature Review

3.1 Introduction

Many high-speed trains are operating in different countries including the high-speed rail network in China, the Inter City Express (ICE) in Germany, the Japanese Shinkansen and other countries that are adopting the use of the high-speed rail network.

The aerodynamic problems for high-speed trains are closely related to the flows occurring around the train. There exists many train aerodynamic research where its greater focus was to improve the speed and power of the train rather than understanding the flow behaviour, which has led to a loss in performance as a result of drag forces caused by turbulence. In the past, the main focus was to improve performance by reducing drag forces to reduce fuel consumption.

Baker (2014a) has described the main flow features around a train where the aerodynamic effects of the train became a concern when the passenger train speed has exceeded 100 km/h ($\approx 27.7ms^{-1}$). At greater speeds, ballast movement was triggered, which is why understanding the train aerodynamics is essential to resolve these engineering problems. To understand ballast flight better, each situation should be assessed to determine the relative importance of each potential drive.

Limited aerodynamic studies have already been conducted underneath the train in comparison to the roof and sides. The under-body has increasingly become a subject of interest due to ballast flight occurrences, causing damage to the train, track and nearby structures. Aerodynamic ballast flight was not an issue for conventional trains as they were not fast enough to trigger ballast motion.

3.2 Ballast flight

In train aerodynamics, ballast flight was detected in the 1980's but was avoided by using ballasted track for modern trains and slab track for high-speed trains. However, as high-speed rail expanded worldwide, countries including the United Kingdom chose to use the ballasted track in its development.

Figure 3.1 demonstrates one of the consequences of ballast flight occurrence where an individual ballast grain was crushed on the rail, causing damage that can lead to additional problems if not repaired.

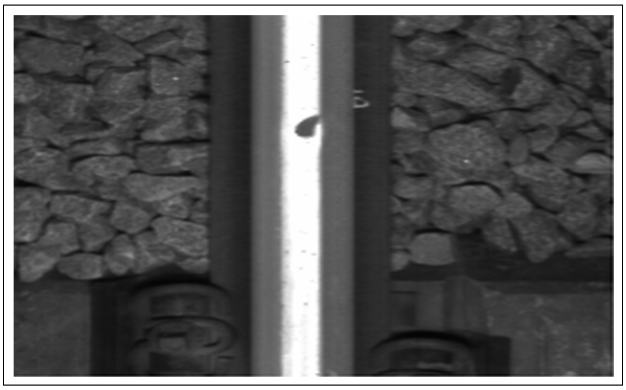

Figure 3.1: Rail tie surface deformation caused by ballast grain being crushed by speeding train (Baker, 2014a).

Ballast projection was also encountered during ICE 3 test runs, which is now becoming an issue for high-speed trains running on ballasted track including the ICE line from Madrid to Barcelona.

3.2.1 Incidents linked to ballast flight

A summary of reported cases of ballast flight occurrences (Kaltenbach, 2008) can be found in Table 3.1. The HSTs mentioned operated at travel speeds between 230 to 320 km/h (63.8 to 88.8 ms^{-1}).

Table 3.1: Selection of reported cases of ballast flight (Kaltenbach, 2008).

Date	**Train Type**	**Location**	**Speed**	**Track Type**	**Weather Conditions**	**Remarks**
2001	ICE 3	Fulda-Göttingen Germany	230 km/h	Monoblock sleeper lowered ballast	Winter conditions, snow	
2003	KTX	S. Korea	300 km/h	Monoblock	No snow	
2003	ICE 3	Lille-Calais, France	320 km/h	Bi-block sleepers	Winter conditions, snow	
2003	ICE 3	Belgium	300 km/h	Monoblock sleepers	No snow	Speeds up to 275 km/h did not cause problems on track.
2004	ICE 3	France	320 km/h	Bi-block sleepers	No snow	During homologation test runs.
2004	ICE 3	Mannheim-Stuttgart, Germany	250 km/h	Monoblock sleepers, lowered ballast	Winter conditions, snow	Foreign parts in the ballast have been found.
2004	ETR 500	Rome-Naples, Italy	300 km/h	Monoblock sleepers, ballast not lowered	No snow	New track with ballast above the sleepers
2006	ICE-T	Hamburg-Berlin	230 km/h	Monoblock sleepers, lowered ballast	Winter conditions, snow	

(Kaltenbach, 2008) suggested events that trigger ballast flight phenomenon varies in different environments in different countries. In Europe, ballast flight has occurred in normal weather conditions, causing extensive pitting of train under bodies on French (2004) and Belgian (2003) lines in Table 3.1. In other regions of France and in the Far East, the phenomenon was caused by ice particles falling from the trains, which cause the ballast to become airborne and hit the train. Unpublished reports include Siemens Velaro in Spain, which described ballast projection on the Madrid-Barcelona line running at 350 km/h.

3.2.2 Aerodynamic characteristics of individual ballast particles

The ballast flight phenomenon was investigated by Jacobini et al. (2013) who concluded that there are several possible causes. One is mechanical vibrations and forces, causing vertical movement of the track as the train passes. If a ballast stone was resting on top of the sleeper, the load would transmit to the particle, causing the particle to displace if the load overcomes the weight of the particle. Another reason could be the aerodynamic loads from the speeding train due to the initial gust and turbulence as the ballasted track enters the train's boundary layer. However, it can be the case of a combination of both. When the train is running at high speed, a strong turbulent flow is generated due to the boundary layer from the train surface and the rough geometry underneath the train including its bogies and cavity of the inter-car. At train speeds between 200 km/h ($\approx$ 55 ms^{-1}) and 300 km/h ($\approx$ 83.3 ms^{-1}), the strong airflow between the train and track can vary between 20 ms^{-1} and 50 ms^{-1} near the ballast surface. Due to the air flow, the ballast motion could initialise by rolling across the track, which would then roll away (Yoshida et al., 1992).

The concept of risk flying ballast risk R_{fb} was described by Jacobini et al. (2013) with the expression:

$$R_{fb} = P_d \times P_{fb|d} \times C_{fb} \tag{3.1}$$

where P_d is the probability that the ballast particle will displace from its original position, $P_{fb|d}$ is the probability of the particle flying after displacement and C_{fb} would be the consequence of the event of the flying ballast.

The train design itself can influence ballast movement due to the nose and length configuration, which initialises gust and a build up of vortices and pressure. Jing et al. (2014) describe the ballast flying mechanism with Equation 3.2, describing the forces acting on an individual particle using d'Alembert's principle:

$$F_w + F_a > mg + ma_T + F_i \tag{3.2}$$

where F_i is the particle interlocking force, F_a is the ballast force due to ballast bed vibration, F_w is the wind force acting on the ballast effective surface due to the high-speed train motion, mg is the gravitational force on its mass and a_T is the acceleration of the ballast grain relative to the ballast bed. These forces are illustrated in Figure 3.2:

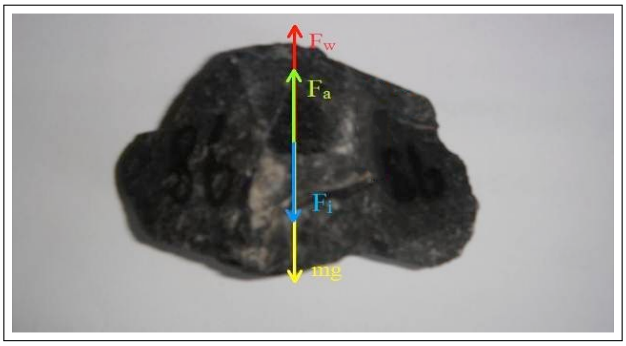

Figure 3.2: Forces that are acting on the ballast (Jing et al., 2014).

As pointed out in Jing et al. (2014), the viscous force on the ballast surface is hard to measure due to the ballast irregular shape. When the aerodynamic loads are applied onto the ballast bed, the ballast begins to accelerate in the same direction as the train along the streamwise direction.

It was noted that the wall shear stress of the ballast particle was the dominant parameter. To initialise the aerodynamics of ballast flight, the aerodynamic load must counteract the gravity and the reactions that are exerted by the ballast bed around the specific particle (Dantec, 2015). If the particle is on top of a sleeper, the distance between the stone and the train would be smaller, a larger aerodynamic load and local flow acceleration will be applied to the stone due to flow separation. Therefore, the stone on top of the sleeper could roll across the track, and could upward and hit the speeding train. If the particle is between the sleepers, the aerodynamic load is lower, and the downstream flow is partly shielded by the sleeper, within the wake region.

If the ballast particle is exposed, the stagnation pressure in the flow would be the most significant parameter influencing parameters of ballast flight. However, if the ballast particle was lying on the track bed, then the tangential force would likely be the cause of ballast movement.

Tests carried out by Deutsche Bahn (DB) have indicated that the ballast level would need to be lowered if the operational train speed of the vehicle was to exceed 160 km/h. Thus, ballast flight can be prevented in most cases except in certain conditions such as improper ballast conditions or foreign objects on the track. Ballast levels would need to be regularly monitored (Hoefener, 2012).

Kwon & Park (2006) described field tests to examine flow near the track surface using a 16-channel Kiel-probe and compared the results with wind tunnel results. With G7 and KTX high speed trains running at 300 km/h, 25 ms^{-1} gusts were produced above the track tie and the probability that ballast weighing under 50 g would fly was at least 50%. When the G7 was running at 350 km/h, the wind gusts increased to 30 ms^{-1}, thus a countermeasure would be needed to prevent ballast flight (Kwon & Park, 2006).

Previous studies involved the use of wind tunnel and large-scale field testing to verify these causes. However, it was pointed out by Jacobini et al. (2013) that the operating conditions vary for different High-Speed Railways. The key aerodynamic factor is speed related, since the events of ballast flight occurred at speeds greater than 260 km/h ($\approx$ 72.2 ms^{-1}).

Experiments conducted by Kwon & Park (2006) used transducers, which measured the pressure and displacement distribution of ballast particles of different shapes and masses. Two case studies were used to establish a link between the two parameters and the wind velocities. The first case study had the wall-mounted particles to record the pressure distributions and in the second case study the particles could move freely to determine the critical velocity. Numerical CFD studies were validated using the experimental data. However, the study did not consider the wind boundary effect and the platform was not elevated to reduce the boundary effects.

A similar study by Jing et al. (2014) used a combination of wind tunnel experiments and CFD simulations to determine the physical characteristics and the nature of the flow around individual ballast particles. The ballast particles were classified according to their shape and mass, similar to Kwon & Park (2006), and the influence of the wind velocity, pressure and other parameters on particle movement. Again, two experimental configurations were used with the particle able to move freely and then fixed.

Due to the boundary layer effect, the airflow at the bottom was slow but unsteady. The ballast was placed on a platform away from the lower part of the wind tunnel, to reproduce conditions in the ballast bedding in Jing et al. (2014).

The ballast samples used by Jing et al. (2014) were made of granite, similar to the ballast used in the UK. Each ballast grain was grouped by its shape (i.e. spherical, half-spherical and flat) and the surface area and mass were measured. Each ballast grain was fixed to the platform, and small holes punched through the stone to insert pressure taps to monitor the surface pressure.

When the ballast grains were fixed in place, they were placed adjacent to each other with spaces in-between on a smooth platform at a fixed height of 350 mm in front of the wind tunnel. During the test, the air pressure transducers were recorded at a wind speeds from 10 ms^{-1} to 30 ms^{-1} at intervals of 3 ms^{-1}.

For the second study, three rows of ballast were placed on the platform without constraints and the study was repeated. The critical velocities (U_C) of the ballast were recorded when the ballast displaced from its original position. Due to safety considerations, the speed increased until 30 ms^{-1} was reached. The displacement of ballast was then measured after the test.

A plot of the wind pressure against the velocity is shown in Figure 3.3. This clearly indicates that the wind pressure on the ballast surface is proportional to the wind velocity.

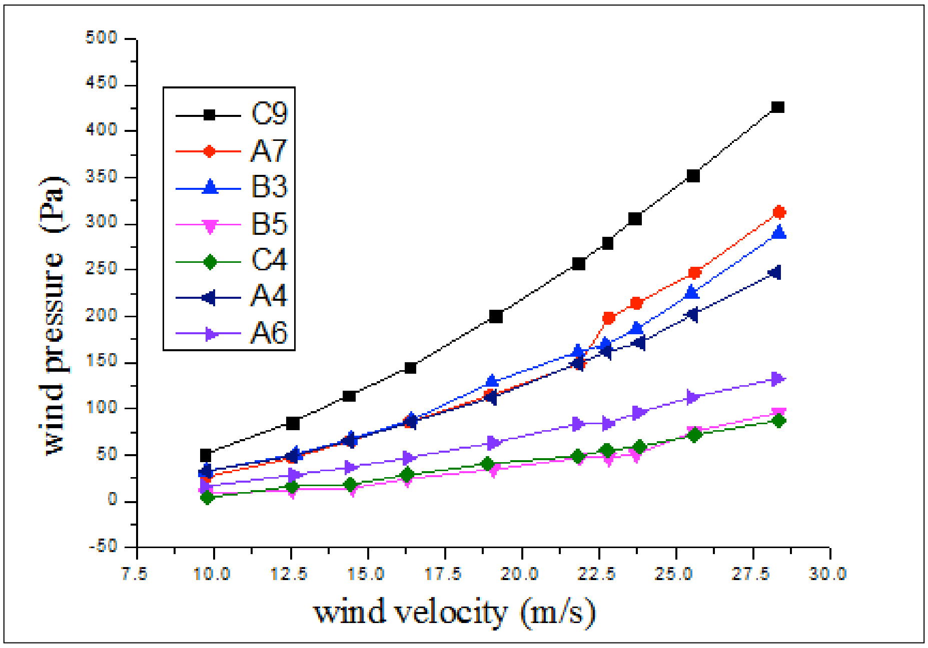

Figure 3.3: Measured wind pressure against wind velocity (Jing et al., 2014).

Most particles begin to move once the wind velocity approached 25 ms^{-1}, which implies that HST aerodynamics would lead to ballast particle motion. For the particle labelled ‘A7’ the air pressure suddenly increased in air pressure at around 22 ms^{-1}. This was likely due to the friction and concave-convex shape of the ballast, which reflects the uncertainty of flying ballast thus additional study is required.

Results in Jing et al. (2014) showed that for spherical ballast, particles of a smaller mass are more prone to movement than heavier particles. However, for flatter particles, the relation of particle mass and flow velocity is inverted, owing to the larger surface area. Therefore, particles with extended flat surfaces and smaller masses are more prone to displacement.

Jing et al. (2014) then conducted a numerical study, using similar conditions to the wind tunnel using an unstructured mesh. The windward sides were simplified and the inlet freestream velocity was set from 10 ms^{-1} to 30 ms^{-1} inclusive with increments of 5 ms^{-1} in-between. An implicit pressure solver was used with a steady solver with absolute velocity. The one equation Spalart Allmaras model was used for resolving turbulence. The computed results indicated that additional wind pressure was required to move the ballast stone. This was only applied to the spherical and half-spherical ballast grains as these shapes resisted some wind pressure. The wind pressure distribution was dependent on the geometry of the particle, and if the pressure difference was large enough, ballast movement would likely occur.

Thus Jing et al. (2014) concluded from wind tunnel testing that the wind pressure is proportional to the critical wind velocity when less than 22 ms^{-1}. The critical wind velocity is defined as the flow speed required to trigger ballast movement. This is a very low speed for a High-Speed Train but realistically, the flow velocity between the tracks would be lower than the train itself. Further investigations would be required to establish a clearer idea of ballast characteristics. Therefore, the mass and shape of the ballast were related to the critical wind velocity but not too relevant to the contact area with the platform surface. The displacement of the ballast motion was compared to the mass of the ballast particle and any other form of resistance but there was no consideration of interlocking forces.

Experiments from the Systra report (Systra, 2013) involved use of a ballast gun to determining the number of ejected particles linked towards the incident ballast characteristics such as kinetic energy transfer. These results were compared with numerical results of the collision process using discrete element models. As the train speed and length increase, the flow turbulence intensity increases increasing the chance of ballast movement.

Saussine et al. (2009) proposed a probabilistic model for ballast projection based on flow underneath the train. This model uses a stress-strength interference analysis to take into account the probabilistic character of turbulent flow beneath the car body and the probability of ballast particles to become airborne.

Movement between the vehicle body and the ballast bed was measured by a series of Pitot-tube sensors that were placed in the track. The results obtained varied depending on the speed and train type. The strength characteristics of the ballast bed defined by the grain ejection under exposure to the turbulent flow field whose velocity was measured by the Pitot tubes for a large number of trains at different running speeds. The results showed a good correlation was achieved between the number of ejected stones with a displacement of 0.1 m or more and the global signal power, which is related to measured air flow (Figure 3.4):

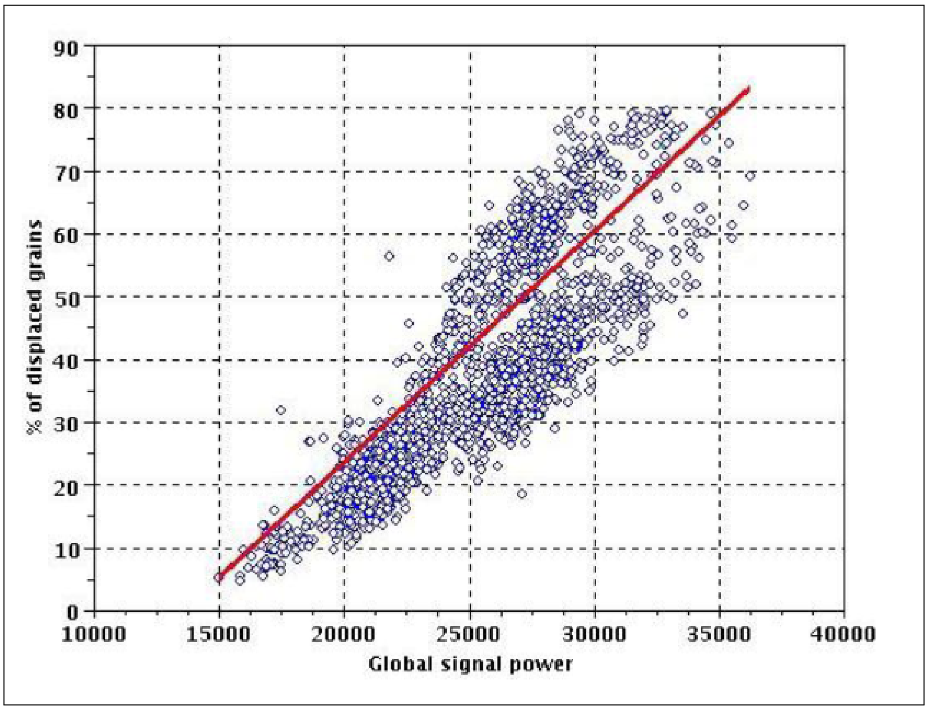

Figure 3.4: Correlation between the percentage of displaced stones and global signal power of 1,600 simulations (Saussine et al., 2009).

Majority of the ballast movement were of grains already on the sleepers. This implies that increasing the train speed would increase the energy output thus increasing the risk of ejecting particles especially those that are resting on the sleeper. Unpublished results in Systra (2013), provided by HS2 indicate the risk factor grew by a factor of 10 if the train speed was between 300 to 320 km/h, which discharged around 15 particles. But for speeds from 310 to 350 km/h, the risk increases by a factor of 100 (for 20 particles being ejected) and up to 1,000 (for 30 to 60 ejections) at speeds between 330 and 370 km/h.

However, results from the East-European high-speed Paris East-Strasburg line, travelling at 360 km/h showed a low number of stones being ejected. The end cars of the TGV Duplex was equipped with accelerometers to monitor the number of impacts made by the ballast stones, and it was noted on Figure 3.5 that double train set (UM) configurations were more likely to cause ballast flight than single-trainset (US) configuration. Therefore, the results are dependent on the aerodynamic stress imposed by the train. As a countermeasure, the East-European high-speed line section had lowered the ballast level.

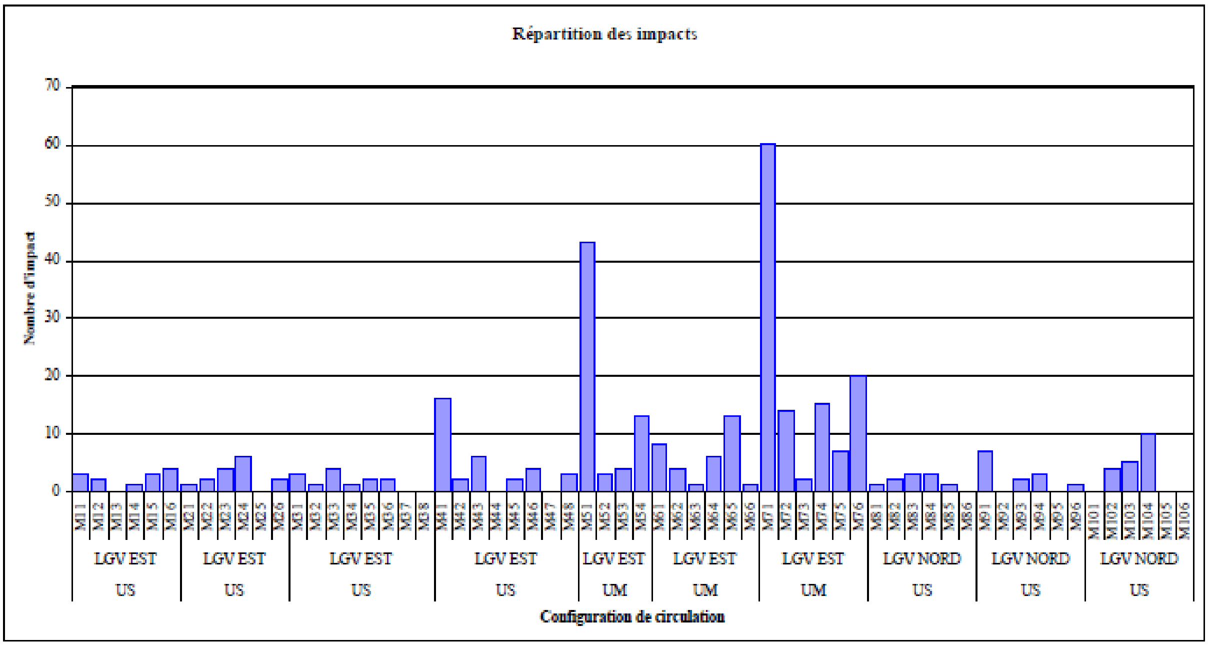

Figure 3.5: Number of ejected ballast particles during the tests on LGV EE line running at 360 km/h (Systra, 2013).

Ballast flight has also been a problem in Spain, which leads to an aerodynamic sleeper being developed and tested on the Madrid to Barcelona high-speed line, which showed a 20 percent reduction of ballast flight occurrence (Adif, 2012).

In recent studies by Milne et al. (2016), for selected track sections, accelerometers (Axivity AX3) were placed inside four ballast stones of similar size and shape and placed on the ballast bed surface. Data acquired includes displacement, velocities and acceleration of the ballast as high-speed trains passed. Ballast acceleration time-histories were obtained for 23 passages of the same train type operating at speeds up to 225 km/h (62.5 ms^{-1}). The data provided a better understanding of the mechanics of ballast behaviour in the context of movement, migration and flight.

3.2.3 Mitigation Strategies

Although the phenomenon of ballast flight is not fully understood, there are currently some mitigation strategies in place to reduce the risk. One solution would be to lower the speed of the train itself or replace the ballast track with slab track. However, reducing the speed would defeat the general purpose of the high-speed lines. A temporary reduction might be acceptable in poor weather conditions. Slab track would not only solve the problem of ballast flight, but it could reduce maintenance costs. Slab track is worth looking into during the planning stages of new high speed lines.

A proposed solution by Jacobini et al. (2013) was to make use of *ballast bagging*; this has been tested in Japan, as shown on Figure 3.6.

Figure 3.6: Ballast bags; the solution proposed in Japan (photo by T.C. Kao) (Jacobini et al., 2013).

This method keeps the ballast in the bag thus no ballast flight can occur while ballast functions including drainage, stress distribution and lateral stability are retained. However, the bags would need to be replaced after track maintenance.

Current mitigation strategies are to lower the ballast level by 40 to 60 mm below the top surface of the sleeper or to use slab track with constrained particles to reduce the particle movement. By lowering the level of the ballast, the aerodynamic loads between the sleepers diminish.

In Jacobini et al. (2013), the ballast profile of the track was lowered by 20 to 30 mm, in France, Italy and Spain. Lowering the profile, generated voids between the bottom of the rail and the ballast, allowing compressed air between the train and track to escape. However, it was reported in France the tampering frequency has increased, which could have been caused by the reduction of lateral resistance (Jacobini et al., 2013). Another countermeasure was to fill the cavities between the ballast particles to prevent ballast flight initiation due to pressure forces. The damaging impact caused by ballast projection can be reduced by reinforcing fragile parts underneath the train structure to break down large high momentum ballast using termination plates.

Best practices would need to be followed by evaluating the risk factors and consequences of ballast flight including:

- Potential risk of the underfloor region being hit by a ballast particle.
- The chances of a particle damaging a critical device in the under-frame that can lead to an immediate stop of the train.
- The momentum of ballast hitting the train.

For ballast flight being triggered by snow and ice falls, one preventative measure was to use ballast screens at sections of the track to prevent the falling ice striking the ballast bed, as introduced by the East Japan Railway Company as shown (Figure 3.7):

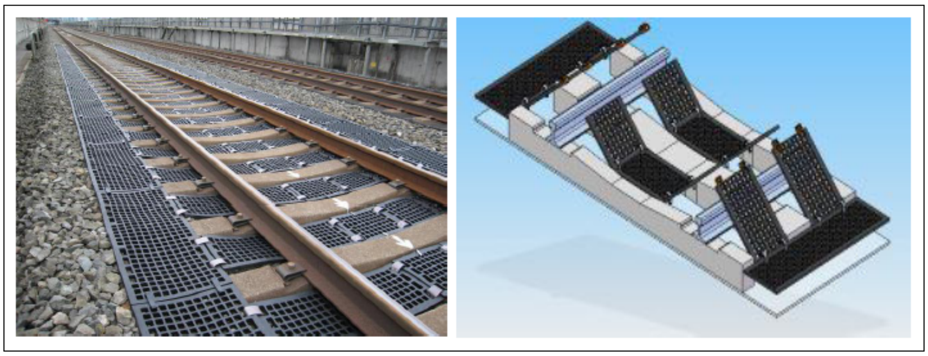

Figure 3.7: Ballast screens used to protect the ballast bed (Systra, 2013).

For the investigative chapters in this report, numerical and experimental studies were conducted on individual ballast stones understand the aerodynamic performance on different stone characteristics. The particles remain static in turbulent flow, but realistically, it is a dynamic system due to the relative movement between the train and the track.

3.3 High-Speed Train aerodynamics

3.3.1 Aerodynamics of High-Speed Trains

Aerodynamic studies have traditionally been applied to air and ground vehicles including trains, aircrafts and racing cars, to improve performance and efficiency. Aerospace technologies comprise structural mechanics, fluid mechanics and automated control. But fluid mechanics is essential when dealing with aerodynamic forces, which influences vehicle design. Aerodynamic studies have taken place for different high-speed trains with various design shapes including the distance between the ground and the train's underbody, the length and diameter ratio.

In full-scale testing, apart from costs and access to facilities, there are issues including the lack of control of ambient wind conditions that would impact on aerodynamic resistance. This was why scaled models in lab facilities are preferred to monitor the flow. Cutting back the physical parameters to match only the Reynolds number (Re) or the Mach number (M) can cause marginal errors when comparing its measurements to its full-scale counterpart. The smallest scaled down ratio of the train model should not be less than 10 percent of the full-scale model (Peters, 1983).

It can be challenging to reproduce the correct flow behaviour when running wind tunnel tests on ground vehicles. In reality, the vehicle is moving while the air is stationary and the ground conditions change; whereas in a wind tunnel facility the field conditions are limited, the vehicle is static and the air is being projected at the vehicle. To reduce the associated error, a moving wind tunnel wall was introduced by using a conveyor belt, with the belt speed matching the wind speed. For automobiles, this is achievable but for high-speed trains it can be difficult since the travel speed can reach at least 120 ms^{-1} ($\approx 430km/h$). The flow around the train is highly three-dimensional, therefore it varies very significant around the vehicle.

When a train passes through a tunnel, series of compression and expansion waves are formed that transmit throughout the tunnel at near the speed of sound. These cause problems when entering/exiting the tunnel for the train, its passengers and residents living nearby. When a pressure wave is applied onto the train structure as a load, the pressure field begins to affect its aerodynamic drag, slowing down the train (Raghunathana et al., 2002).

3.3.2 Flow behaviour between the ground ballast and the under-body of high-speed trains

Investigations of ballast flight have involved studies of velocity and pressure fields beneath high-speed trains. Previous studies conducted in Korea (Kwon & Park, 2006) and in Japan (Quinn et al., 2009) shows measurements of velocity profiles beneath the train at various heights for a given train speed. The average freestream velocity of the flow underneath the train are potentially equivalent to half of the train's velocity in certain regions, at the centre of the track in Figure 3.8.

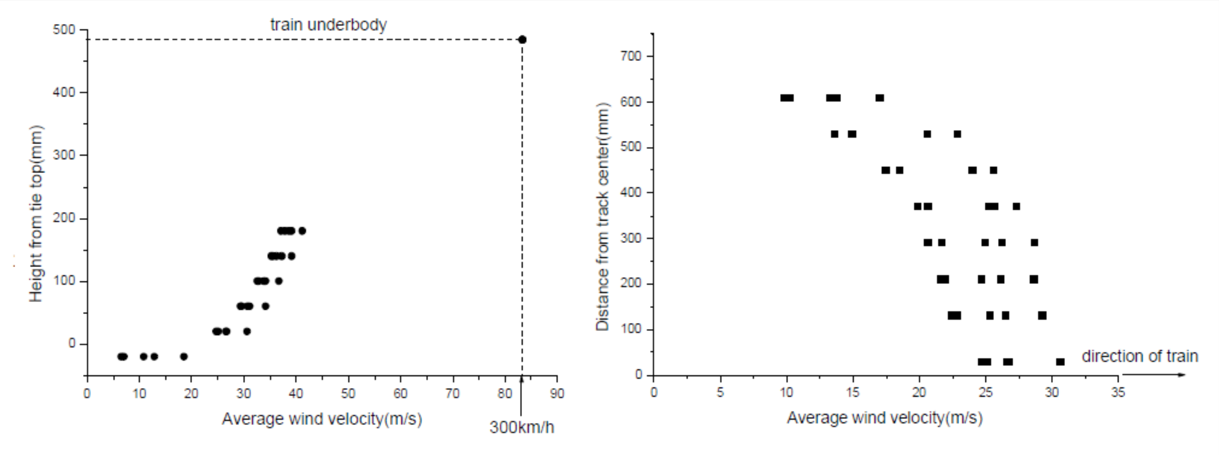

Figure 3.8: Measured time-averaged velocity profiles beneath the passing train running at 83.3 ms^{-1}. Measured streamwise profile at the centre of track (left). Spanwise velocity profile measured horizontally from the track centre (20 mm high from the upper surface of tie) (right). (Kwon & Park, 2006).

According to Baker (2010), the velocities drift towards their peak at the centre line of the track and then dissipate outwards. For the remainder of the train, the velocity profiles fluctuated due to the surface roughness from bogies and inter-car systems underneath the train in Figure 3.9 (Kwon & Park, 2006).

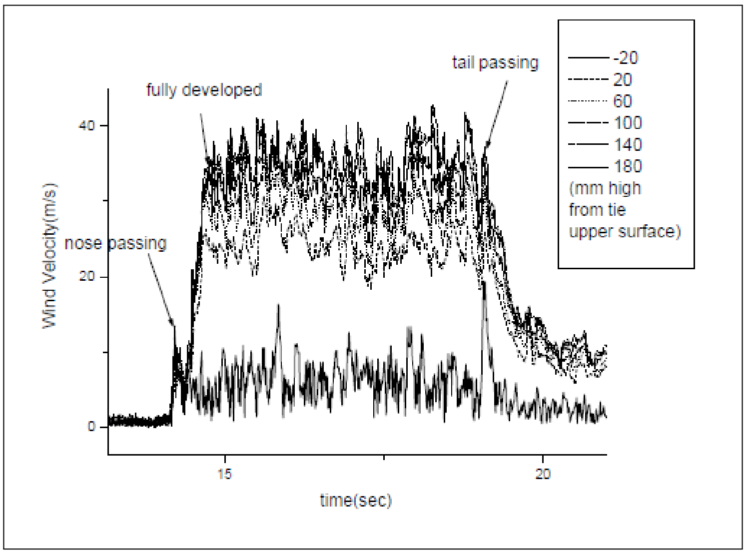

Figure 3.9: Instantaneous velocity profiles during train passage operating at train speed 291 km/h (80.83 ms^{-1}) (Kwon & Park, 2006).

In Figure 3.10 the measured pressure coefficient C_p beneath the train carriage reaches its peak magnitudes at the leading and trailing edge of the train, and lower pressure is found in-between the carriages. The results in Figure 3.10 demonstrate this type of behaviour for the Eurostar train, with the undercarriage geometry including the bogies influencing the flow.

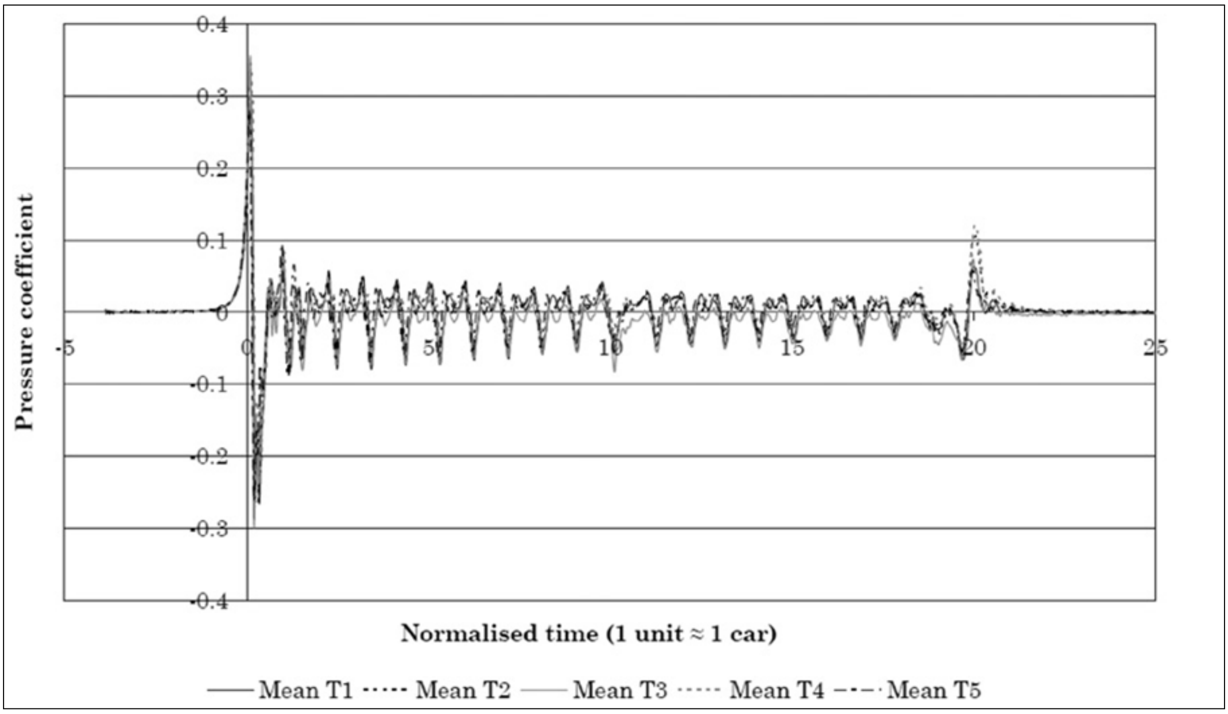

Figure 3.10: Pressure coefficients beneath the Eurostar train carriage (Baker, 2010).

Thus ballast flight has motivated wind tunnel and computational research around the track and bogies. However, this type of problem is challenging, and further work is being conducted at present.

Previous computational studies on high-speed trains carried out using RANS turbulence models showed that helical vortices occur behind the train and extend throughout the wake (Baker, 2001). Unsteady RANS results demonstrated the unsteadiness of the helical structures in the wake region, and implied that particles would subject to unsteady forces (Baker, 2010).

In the paper by Garcia et al. (2011), the flow between the undercarriage and the ballast track was approximated using the turbulent Couette flow and comparisons were made using the analytical solution provided by Wilcox (1998) and wind tunnel results. The purpose was to obtain equivalent roughness of a track comprising sleepers and ballast particles. The energy conservation was taken into account such that the equivalent roughness of the ballast track was achieved by comparing with the analytical solution. The obtained parameters were dependent on the height of the gap between the train and the ballast, the Reynolds number and the roughness of the upper wall. However, only the sleepers were modelled in this study and were assigned a parameter of roughness along the surface. The flow between the high-speed train and the ballast tracks is complicated and unsteady since the roughness varies throughout the ballast positioning and geometries.

The use of extensive tunnels for the high-speed rail is becoming more frequent and was discovered that due to the tunnel effect, unsteady aerodynamic effects are contained and reflected by the walls, which can increase the likelihood of ballast flight (Baron et al., 2001).

Because of these issues, a decrease in operational speed was imposed to ensure safety especially to stabilise lightweight trains. Thus, the unsteady aerodynamic field around the train also influences the tunnel configuration including its cross-sectional size and shape and pressure relief ducts, particularly for long-distance tunnels.

These problems can be addressed for modern trains running mainly in the open-air, but understanding the aerodynamics such as turbulent flow effects is still a developing topic. Areas include understanding the effect of flow through different shapes, size configurations, environmental constraints and rough ground surface effects. It is noted that this investigation is based on conventional wheel-to-rail trains only.

The four different aerodynamic analysis are analytical theory, full-scale/scaled model experimental testing, and CFD analysis. Full-scale testing can be difficult due to scale and cost, and the aerodynamic environment can be difficult to replicate. No modelling assumptions are made and the measurements achieved can be used as a benchmark when comparing results through different techniques. Anemometers are used to measure the unsteady turbulent flow under the train, and velocities and pressures are time-averaged. For repeatability, multiple runs, and need to be carried out.

For scaled modelling, the experiment would be carried out in a controlled environment (i.e. a wind tunnel). For wind tunnel experiments, the model of the track system would need to be mounted onto the wind tunnel platform or the train model placed onto a moving belt. Having a scaled model can resolve some issues relative to full-scale. Similar to full-scale, boundary layer growth around the train is considerable but at the rear of the train, unrealistic conditions occur. Additional flaws in this method include the scaled Reynolds number effect, modelling realistic atmospheric conditions and differences in relative motions between the train, track and air.

An alternative to wind tunnel testing is the moving model approach, where a scaled model of the train is launched across a test track that simulates the ground conditions more accurately. Such tests have been carried out at the University of Birmingham in the UK, Central South University and Beijing

Jiaotong Universities in China with track that ranges between 100 to 200 metres in length at speeds up to around 100 ms^{-1} (Baker, 2014a). Having scaled the model, the sample rate of the measuring equipment would need to be much higher.

With CFD analysis, high-resolution flow information around the train can be obtained compared with experimental data. However, a full-scale model is harder to mesh with high resolution only to hardware constraints and difficulty in convergence. Different models and filters can be used to obtain an approximate description of specific regions of the train. Advantages include ease of model modifications and re-evaluations of turbulent flow. However, difficulty can arise when the boundary layer thickness of the train is too large along the length of the train or in the train wake where large-scale separations occur. Unsteady flow methods including LES and DES are needed to simulate the flow fields accurately (Baker, 2014a), but due to hardware constraints, the Reynolds numbers achieved in simulations are quite small at present.

Baker (2014b), discussed the design and operation of modern trains in relation to the aerodynamic issues mentioned previously, but the main focus of the paper was the flight of ballast and ice particles beneath the trains.

Possible causes of ballast movement include track vibrations by the speeding train that can loosen the ballast stones, suction peaks at the front and rear of the train as shown in Figure 3.10, and the shear velocities underneath the train. The induced flow velocity would increase with height above the bed may be crucial if a ballast grain lies on top of a sleeper. A full-scale track bed with a model of the under-body was tested in the wind tunnel to see whether the ballast would displace due to a sudden gust. The conclusion was for a wind speed less than 180 km/h the ballast would not displace whereas, for wind speeds at 240 km/h, most of the particles have moved, which can be prevented by reducing the level height of the ballast (Baker, 2014a); (Baker, 2014b); (Quinn et al., 2009).

3.4 Flow physics around isolated bluff bodies

3.4.1 Wind flow over a cube

For the computational studies in this report, a comparison was made between calculated results using CFD and experimental data, using similar parameters to Castro & Robins (1977). Castro & Robins (1977) has investigated flows around a surface mounted cube of 60 mm length using uniform and boundary layer profile. Measurements were made around the cube of surface pressures along with the mean and fluctuating velocities within the wake using a pulsed wire anemometer.

The flow separates from the front surface and the velocity increases in proportion to the length of the cube. Small vortices would occur around the isolated particle and would reattach. Figure 3.11 illustrates the flow structure of the vortices around the cube that arise as a result of the flat frontal surface facing the flow.

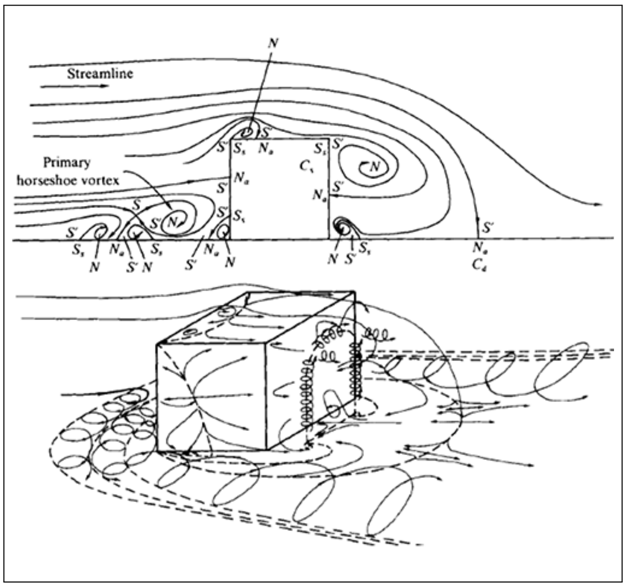

Figure 3.11: Streamline flow around the mounted cube featuring horseshoe vortices (Hunt et al., 1978).

Previous numerical studies of sharp edged bluff bodies including cuboids reported that using steady RANS models is unsuitable in calculating flow separation. It was concluded by Rodi (1997) that the standard k-ε model produces poor results around the cube owing to excessive production of turbulence near the stagnation point. Using the modified version of k-ε has improved the solution but the length of the flow reattachment was greater in the computed model.

3.4.2 Wind flow behaviour across buildings

A similar example was previously conducted using 3D scaled models of buildings by Hur et al. (2008) where wind loading was applied to model buildings. Simulation of incompressible flow was carried out using a RANS k-ε model, validated against wind tunnel results.

In Korea, the shape of the train station was geometrically smooth to reduce the wind loading effect for safety reasons during unusual weather conditions (Hur et al., 2008). The wind loading effects on large obstacles were previously conducted on tall buildings, using LES and RANS modelling techniques mentioned in Versteeg & Malalasekera (2007) and Daniels et al. (2013) that influenced the building design before construction. The model of the object can be scaled down by $\frac{1}{N}$ such that the wind velocity on the model is N times faster than the actual wind speed.

The pressure coefficients are velocity independent via turbulent flow hence the pressure coefficients from experimental, and computational results are compared. The calculated results and the experimental data are in good agreement, showing that CFD is capable of producing computational loads/flow on conflicting obstacles. The procedures and techniques used in Hur et al. (2008) can be adopted and applied to the numerical studies in later chapters.

3.4.3 Wind flow around a wall-mounted hemisphere and smooth shaped geometries

Studies of flow around wall-mounted hemispheres would give further inside on ballast flight aerodynamics since its shape can resemble a ballast grain. The expected flow behaviour should be that of a full sphere shown in Figure 3.12:

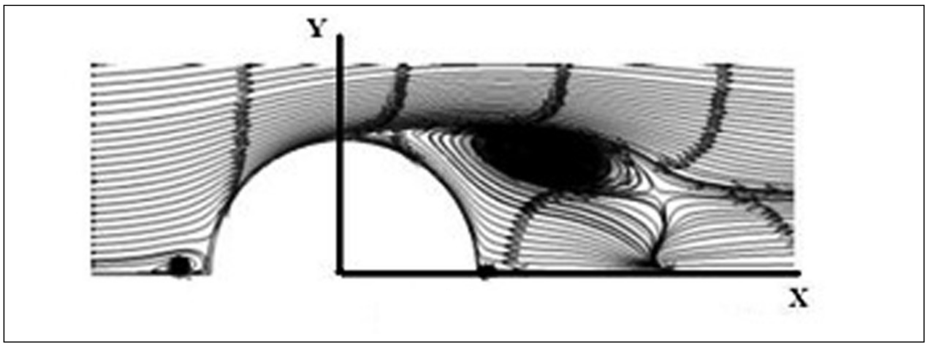

Figure 3.12: Time-averaged streamlines in the x-y plane, z/h = 0.0 and $Re = 36,000$ (Tavakol et al., 2014).

A horseshoe trailing vortex is expected to occur around the hemisphere along with shear layer vorticity, producing a complex flow topology. Tavakol et al. (2014) conducted investigations of flow over a wall-mounted hemisphere numerically and experimentally, using LES and RANS RNG k-ε turbulence models at different Reynolds numbers (36,000 & 64,000). It was proved that the RANS model had some shortcomings whereas LES was more beneficial when it came to modelling external flows from a bluff body. These results can be used as a benchmark comparison to validate numerical in the computational chapter since the results in Tavakol et al. (2014) have been validated using experimental data. Amongst the sub-grid models, the prediction of kinetic energy showed a better correlation with the experimental data.

The LES model was more suitable to model a complex flow field in the wake region of the hemisphere whereas RANS was clearly unable to predict the complex flow field accurately. However, with URANS and DES, the results accuracy should improve by resolving the majority of the turbulence flow but computational time and resources will increase by doing so.

Tavakol et al. (2009) carried out a similar investigation for the wall-mounted hemisphere at a fixed height to compare two turbulent boundary layers (thick and thin). The Reynolds number for this study was $Re = 32,000$ with RNG k-ε turbulence model. The mean surface coefficients and the velocity field were determined by the numerical solution and the turbulence flow field, and intensity was measured for the hemisphere in both streamwise and spanwise directions and presented graphically using flow path lines to determine the separation regions and recirculation area. Using the RNG k-ε model for the hemisphere, the computed results were inaccurate as the model overestimates the streamwise velocity after the separation point.

A similar numerical and experimental study of flow around dome-shaped structures was conducted by Taniguchi et al. (1982) for time-averaged pressure distribution in a fully-developed turbulent boundary layer. The drag coefficient $C_{D\tau}$ of the hemisphere was calculated based on the shear velocity u_τ, which is related to $Re_\tau = {}^{u_\tau D}/_{v}$ in the range of $D/\delta \leq 1$ where δ is the boundary layer thickness and D is the diameter of the hemisphere.

Toy et al. (1983) carried out some experimental investigations on a hemisphere (D = 225 mm), using two thick turbulent boundary layer profiles (δ = 32.26, 64.77 mm) of different turbulence intensities were blended in. Results in Toy et al. (1983) indicated by increasing the turbulence intensity in the boundary layer will lead to a translation of separation and reattachment of flow further downstream. Savory & Toy (1986) performed another experiment with the hemisphere but with three different boundary layers, which concentrated on the near wake regions from separation to reattachment on the ground surfaces. Pressure distributions were measured from the centre line of the hemisphere in three different boundary layers, which revealed the maximum pressure gradient has occurred over the dome in the thin boundary layer whilst the lowest gradient was formed in the rough velocity profile (generated using rough ground effects). Further experiments by the same authors (Savory & Toy, 1986) indicated that by having a rough boundary layer, the recirculation zone of the flow field behind the hemisphere decreased in size compared to a smooth boundary layer flow.

Wind tunnel experiments and numerical simulation by Meroney et al. (2002) studied the wind loads on domes and hemispheres in thick boundary layer flows. Numerical results reported that the mean pressure coefficient distributions became insensitive to Reynolds number as the distributions for Reynolds numbers of 185,000 and 1,440,000 were similar. This was backed up by another experiment implemented by Taylor (1990) to measure pressure distributions around a hemispherical dome immersed in thick boundary layer flow at Reynolds number 110,000 and 310,000 for two different turbulence intensity profiles. Some transient numerical computations were performed in Hadavand et al. (2008) on vaulted roof structured exposed to wind flow and solar radiation. The results revealed that the ratio of pressure difference above the arched roof to the flat roof have increased substantially with the vault rim angle, but was fairly consistent for various flows of Reynolds number between 500,000 to 1,000,000 based on the building height.

Tamura et al. (1990) performed numerical computations involving three-dimensional flow over a hemisphere. The flow Reynolds numbers based on the hemisphere diameter and the freestream velocity were $2,000$ and $20,000$. The boundary layer thickness is 0.5 h where h is the dome height. Tamura et al. (1990) reported separation over the dome at the leeward direction at $x/2h = 0.1$ and the reattachment point was at $x/2h = 1.0$ from the dome centre.

A comparison was made between Unsteady RANS (URANS) and LES by Lubke et al. (2001) to calculate turbulent flow around bluff bodies, which concluded that the conventional Boussinesq Viscosity Models (BVM) and Explicit Algebraic Stress Models (EASM) showed an over-prediction of recirculation length for EASM and excessive damping of transient motion with BVM, which resulted in the prediction of a stretched wake region behind the square cylinder. But with LES, the global prediction was in better agreement with the experimental than URANS.

The problem with predictive modelling for smooth shaped curved bodies is the location of the flow separation cannot be judged purely on its geometry. The flow field is dependent on the Reynolds Number, boundary layer thickness and its free stream turbulence intensity.

The modified version of k-ε had issues when it came to simulating the time-dependent phenomenon in the flow domain. However, LES compensated by producing more realistic vortex shedding results. Tutar & Holdo (2001) claimed that the cause of this overestimation was due to the vortex stretching process being neglected in the 2D turbulence simulation.

A similar report conveyed by Xu et al. (2007) said additional numerical experiments of turbulent flow around a circular cylinder at Re = 3,900. The turbulence models used included LES, DES Spalart-Allamaras (SA) and DES-based Shear Stress Transport (SST) and unsteady forms of SA and SST models. Results included the mean pressure and drag coefficients, velocity profiles, Strouhal Number, flow structures and Reynold Stresses. LES and DES provided sufficient results for the flow field, but significant discrepancy was reported between the calculated results from unsteady RANS and experimental data. Therefore, the above literature indicates the LES model is capable of producing flow around curved bodies accurately, but DES is yet to be determined as it was recently developed.

Tests conducted in Tavakol et al. (2014); Tavakol et al. (2009) used an open-circuit, subsonic wind tunnel located at Shiraz University, of cross section of 460 × 460 mm and test length of 3,260 mm. The airspeed for this wind tunnel was up to 32 ms^{-1}, using a split fibre sensor.

The hemisphere diameter was 120 mm with a blockage ratio of about 3% in the tunnel thus no correction of measured freestream velocity was required. The Reynolds number was approximately 32,000 where the freestream velocity and hemisphere height was 8.5 ms^{-1} and 60 mm respectively. A hot-wire anemometer was used to measure the wind speed, which was attached to a three-dimensional traversing mechanism. The set-up for this wind tunnel experiment is pictured on Figure 3.13:

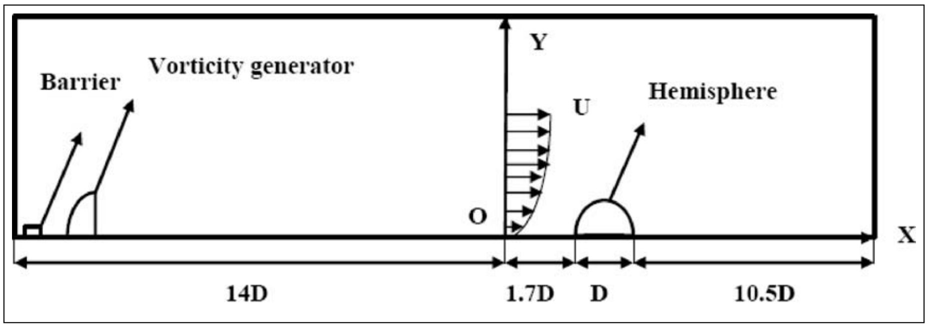

Figure 3.13: Wind tunnel and relative dimension set-up (Tavakol et al., 2009).

A split-fibre sensor (Dantec Co.) was used to determine the freestream velocity and its direction along with a hot-wire sensor (Fara Sanjesh Saba Co.) to measure the freestream velocity in the recirculation zone and freestream regions. A thin boundary layer was achieved through a smooth tunnel floor surface whereas a thick boundary layer profile would require vorticity generators to trip the boundary layer if the length of the wind tunnel is not large enough. The turbulence intensity within the boundary layer is high but declines outside the region.

The hot-wire anemometer was adjusted accordingly for measurements where Δy would be more refined at the near wall region. Its accuracy is dependent on the precision of the equipment and the software program to process the raw data. Experimental errors are expected over time due to change in air temperature that can marginally affect the velocity results. This can be compensated for by correcting the anemometer output during variation of temperature such as altering the bridge voltage to a standard temperature multiplied by a correction factor (Tavakol et al., 2009). The parameters to consider at the plane of symmetry ($z/h = 0.0$) would be the point of separation, angle of separation and the reattachment point in the freestream direction.

New experimental techniques presented by Williamson (1996) included the use of a laser induced fluorescence and particle image velocimetry to analyse vortex dynamics of the cylinder wake visually.

3.5 Ballast grain shape and size properties

Owing to the size and complexity of ballast particles, experiments can be difficult using standard apparatus. However, with 3D scanning and Computer Aided Design, sample particles can be modelled, scaled and simplified to approximate the characteristics of a full-scale ballast stone.

The size of a ballast grain can influence its strength since smaller particles are stronger owing to the lower probability of containing flaws, whereas larger particles are more prone to fracture when sufficient stress is applied. This means that, under load, the individual ballast can break, changing the condition of the system, and generating smaller particles more prone to ballast flight due to lower mass.

When characterising ballast, there are at least three variables including:

- The roundness and describing roughness surface the shape formation.
- The material stiffness, especially at contact points and its density.
- Its strength, quantified as toughness and abradability.

Le Pen et al. (2013) suggested that ballast particles could be characterised by its shape and aspect ratios of the shape that is termed *ellipseness*. These aspect ratios illustrated in Figure 3.14 are defined for each orthogonal dimension to categorise ballast shapes. For larger particles, the aspect ratio (maximum to minimum dimensions) tends to be greater with sharper corners at greater angularity. The form of the ballast particle(s) is dependent on the largest scale property where the orthogonal dimensions are longest (**L**), shortest (**S**) and intermediate (**I**).

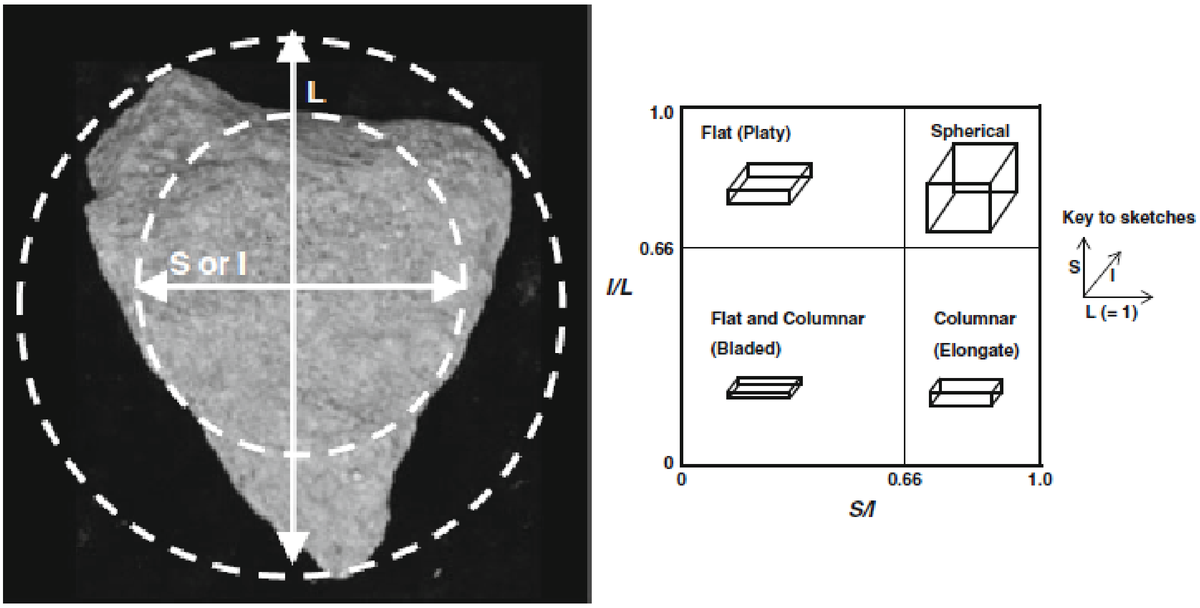

Figure 3.14: Zingg plot of ballast classifications using the aspect ratios (Le Pen et al., 2013).

The *ellipseness* (**E**) of a ballast particle is defined by a ratio of the particle's perimeter P_o to that of the ellipse of equivalent area P_e. This method is similar to the *equivalent disc method*, which uses a circle of the same area (Le Pen et al., 2013). However, using a circle would imply the intermediate dimension

I is greater than physically possible, which is why the ellipseness approach is a better representation of the ballast shape. An estimate of the shape's smoothness can be found by using an ellipse with the same major dimension and area (Wadell, 1932).

The form parameters of the shape can be determined using the dimensions **S**, **I** and **L** by capturing the dimensions through two orthogonal images of the particle or by measuring **L** and **I** from the first image, which can derive **S** via the Scalene Ellipsoid Equivalent Sphericity (SEES) approach (Abbireddy et al., 2009):

$$S = \left(\frac{m_p}{\rho_w G_p}\right)\left(\frac{6}{\pi L I}\right) \tag{3.3}$$

where G_p is the specific gravity of the particle (typically 2.65 for granite), ρ_w is the water density ($\approx$ 1,000 kg/m^3 at 4 °C) and m_p is the mass of the ballast particle.

For the roundness, the area (A_0) and perimeter can be measured from the digital images that are used to determine the ellipse value **E**. The perimeter of equivalent area ellipse $\mathbf{P_e}$ is defined on Equation 3.4:

$$a = \frac{L}{2} \qquad b = \frac{A_0}{\pi a} \qquad P_e \approx \pi(a+b)\left(1 + \frac{3(\frac{a-b}{a+b})^2}{10 + \sqrt{4 - 3(\frac{a-b}{a+b})^2}}\right) \tag{3.4}$$

where a and b are the major and minor radius of the area ellipse respectively. The particle formation is a dimensionless ratio of a combination of **L**, **I** and **S**. It is found that most particles do have similar ratios.

These methods found in Le Pen et al. (2013) can be used to classify ballast shapes prior to experimentation to observe which types are more prone to ballast movement. Another approach would be to determine the roundness of the particle, which links the perimeter of the measured particle to the perimeter of the elliptical shape of the same area using imaging analysis software.

In later stages of this report, ballast grain of different masses and shapes are categorised and its aerodynamic behaviours were assessed through four different angles of attack around the particle to determine whether there is a link between risk of ballast movement and the grain shape classification.

3.6 Summary of literature review

The information and results provided in the the literature can be used to benchmark computational results before moving onto more complex studies. However, the literature review did not have many articles that combined the use of experimental and computational studies of cubes and hemispheres for different turbulent boundary layer flows. It also showed that there had been no experimental or numerical studies on elevated cubes or irregular shapes at various orientations.

Chapter 4

Aerodynamic Analysis of Flow over Isolated Particles

4.1 Introduction

For the computational part of this research, AnSys Workbench and Pointwise were used to model and mesh the geometries and imported into AnSys Fluent to perform the numerical analysis. The general procedure of CFD analysis follows a similar principle to the waterfall model (Figure 4.1).

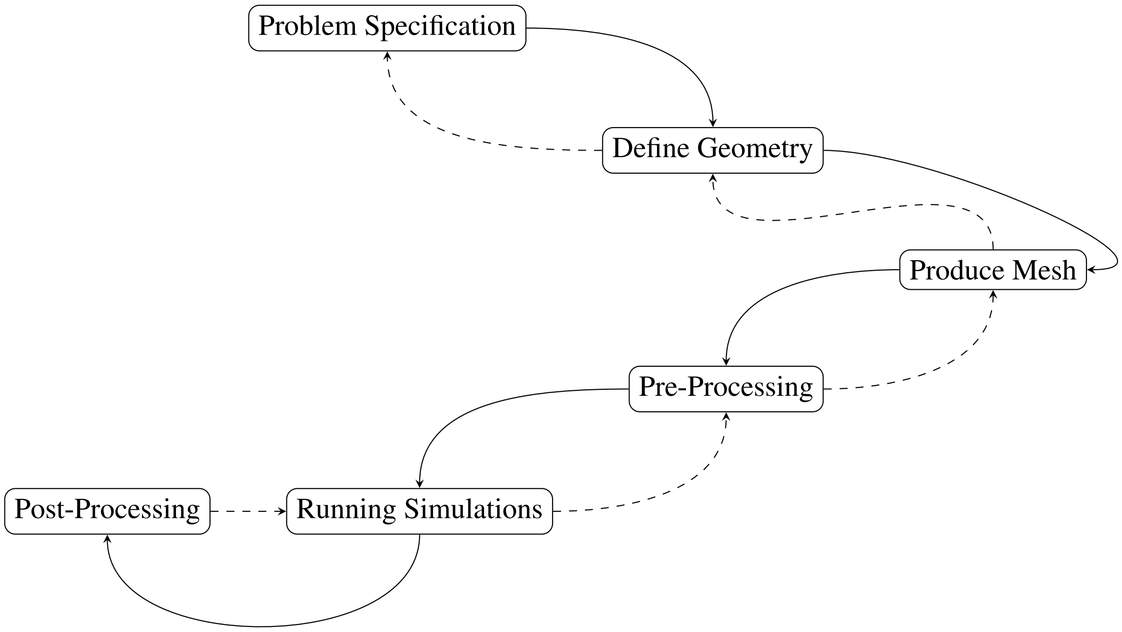

Figure 4.1: Procedure diagram for CFD modelling and analysis.

Steady RANS and unsteady turbulence models (URANS and DES) have been used with different geometries representing different ballast shapes. RANS models including SST k-ω and Realisable k-ε have been used throughout this report.

Grid-independent studies, the effects of Reynolds number, particle elevation and moving wall conditions have been reported. Initial studies of the cube have been benchmarked against Castro & Robins

(1977). Castro & Robins (1977) did a wall-mounted cube measurement, which uses uniform flow as the inlet flow profile. Furthermore, a boundary layer profile will be generated using a moving wall above the cube to see the changes in aerodynamics. The flow speed used is low enough to make the flow incompressible. The hemisphere numerical study was benchmarked using Tavakol et al. (2014). Further studies on the cube involved different orientations and elevation levels in observing the changes in forces and flow behaviour.

A structured mesh was used for better efficiency and orthogonal quality by refining the mesh around the body and critical regions. Fourteen realistic ballast shapes at four different orientations were also studied. Owing to their complex shape, the mesh was unstructured, with a structured inflation boundary near the solid objects.

Unsteady flow analysis was also studied, requiring additional time and resources. Recent advances in High-Performance Computing (HPC) have made it more feasible to carry out transient simulations where velocity and pressure fields change over time.

4.2 Applying Steady and Unsteady RANS solver for flow over cubic particle

4.2.1 Performing steady analysis of a wall-mounted cube at 90 degrees

Domain and Boundary Conditions

The cube was mounted onto a smooth platform surface adjacent to the flow at a specified distance (Figure 4.2):

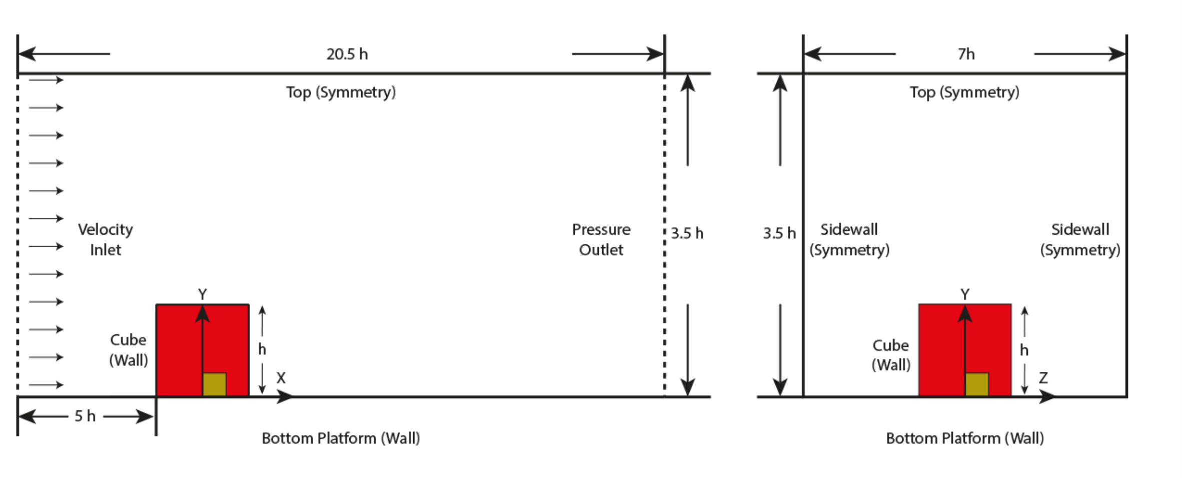

Figure 4.2: Computational domain of the cubic particle case (not to scale).

The domain size was large enough to provide sufficient data and flow visualisation as the flow passes the cube. The freestream velocity U_∞ was set to 83.3 ms^{-1} (300 km/h) similar to the high-speed trains' operational speed. The cube height h is 0.06 m, which gives the Reynolds number Re of 330,000.

The domain was modelled and meshed using Pointwise, as the grid can be exported into many CFD packages including AnSys Fluent, Star-CCM+ and OpenFOAM. The first layer height y_1^+ was also designed to achieve the non-dimensional target y^+:

Table 4.1: Pre-defined variables used to calculate the dimensionless wall height y_1^+ and the Reynolds Number Re.

Variable	**Value**	**Units**
Freestream Velocity U_∞	83.3	ms^{-1}
Density ρ	1.2047	kgm^{-3}
Dynamic Viscosity μ	0.000018191	$kgm^{-1}s^{-1}$
Kinematic Viscosity ν	0.0000151	m^2s^1
Reference Length	0.06	m
Reynolds Number Re	$\approx$ 330,000	

The standard case was run at an air temperature of 20 °C, which would imply the air density ($\rho = 1.2047$ kgm^{-3}) and the dynamic viscosity (μ = 1.8191 × 10^{-5} $kgm^{-1}s^{-1}$).

The flow is turbulent with a Reynolds number approximately 330,000. For steady-state analysis, both Realisable k-ε and SST k-ω turbulence models are used for comparison, so two meshes were generated with different y-plus values to accommodate these models. Thus two different first layer heights are calculated in Table 4.2:

Table 4.2: Calculated first layer heights for two different turbulence models.

	Realisable k-ε	**SST k-ω**
Desired y plus y^+	30	5
First layer height y_1^+	0.000118 m	1.97062 × 10^{-5} m
Cell Count	6.4 Million	9.0 Million

The y-plus y^+ values differ since the Realisable k-ε model uses an Enhanced Wall Function whereby the first cell can be within the log layer. A typical y^+ value should be between 30 $\leq y^+ \leq$ 300 to use a wall function. However, with SST k-ω, the viscous sub-layer needs to resolved meaning the y^+ should be less than 5 but ideally around 1 with a growth layer height no greater than 1.2. The first layer height (y_1^+) was calculated by substituting the target y^+, $U_\infty = 83.3$ ms^{-1}, $x = 0.06$ m and $\nu = 1.51 * 10^{-5}$ kg/ms into a y-plus equation that was used for a thin airfoil or flat plate.

The mesh on the cubic faces were sub-divided to reduce the aspect ratio near the wall, with the highest element quality and resolution around the cubic surfaces and the wake region. The aspect ratio of the cells should not exceed 200, particularly near the critical regions. For $y^+ \leq 5$, the cell count had to be greater to obtain higher resolution at the boundary layer. The grid type structure for the cube was non-uniformly structured (Figure 4.3). The grid was refined near the ground and around the cube, where vortical flow is expected to occur.

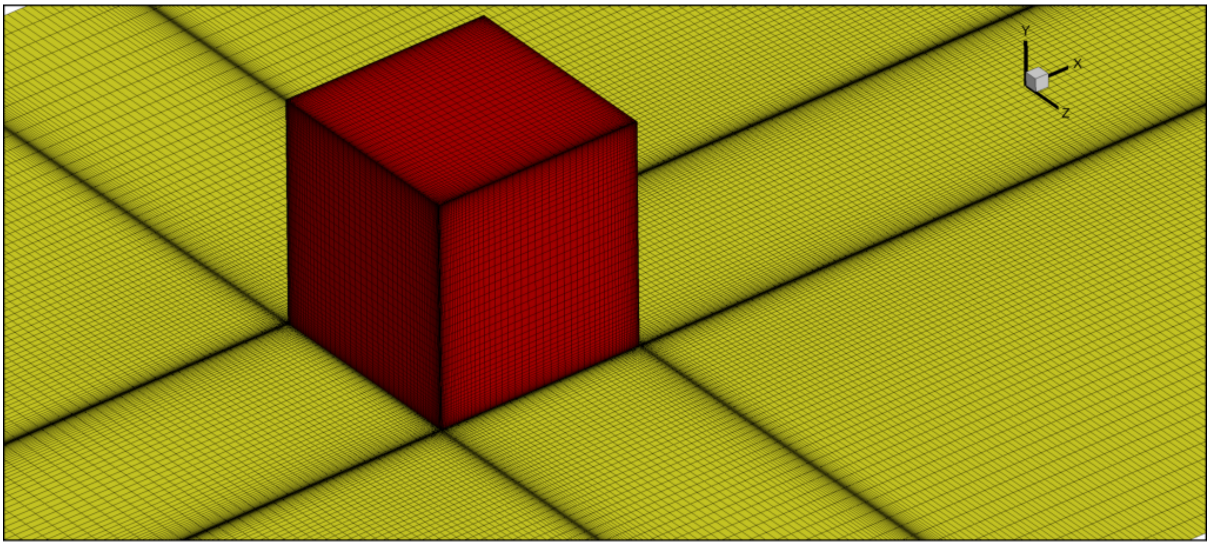

Figure 4.3: Cubic mesh using a structured grid configuration.

A steady pressure-based solver was used initially as the simulation undergoes incompressible flow.

For the inlet flow properties, a uniform flow was applied with a streamwise component of U_x = 83.3 ms^{-1}, a gauge pressure of zero. The turbulent intensity I is the ratio between the root mean square of turbulent velocity fluctuations and the Reynolds averaged velocity $\bar{U}$. The viscosity ratio (${}^{\mu_T}/_{\mu}$) is the ratio of turbulence μ_T and the dynamic molecular viscosity μ.

$$I = \frac{u_{rms}}{\bar{U}} \tag{4.1}$$

The turbulence intensity and viscosity ratio were set to 0.5% and 0.1 respectively, on the basis of wind tunnel data from Castro & Robins (1977). Although the viscosity ratio was set to laminar, it was adjusted in later stages to match conditions in the experiments (between 5 to 10).

The wall-mounted particle and the platform are the only solid boundaries with a no-slip condition; The other boundaries are shear-stress free. The ambient pressure was set to 101,325 Pa.

SIMPLEC was used for the Pressure-Velocity coupling scheme as it provides better convergence than SIMPLE as explained in Chapter 2. The Least Squares Cell-Based method was used for the gradient and the Second Order Upwind Scheme was chosen for pressure, momentum, turbulent kinetic energy and specific dissipation rate for better accuracy after establishing convergence. The absolute convergence criterion for each residual was set to 10^{-5}, which will resolve majority of the flow features and reduce iteration errors. The number of iterations was set to 50,000 steps, which should be enough for the residuals to converge towards reasonable values (AnSys, 2009).

Aerodynamic properties of the cube have been monitored including lift, drag and side forces on Equation 4.2 where A is the projection area of the cube facing the inlet flow.

$$C_D = \frac{D}{\frac{1}{2}\rho U_\infty^2 A} \qquad C_L = \frac{L}{\frac{1}{2}\rho U_\infty^2 A} \qquad C_S = \frac{S}{\frac{1}{2}\rho U_\infty^2 A} \tag{4.2}$$

A grid dependence study using the RANS model, (Table 4.3) showed the force coefficients converging as the cell count increases. Additional cells were focused around the cube and critical regions where a larger cell count is better suited for unsteady analysis and to get better detail of the flow structure.

Table 4.3: Grid dependence study of the 90-degree cube.

	Realisable k-ε			SST k-ω		
Subject	**Cell Count (Hex)**	$\bar{C}_D$	$\bar{C}_L$	**Cell Count (Hex)**	$\bar{C}_D$	$\bar{C}_L$
Cube 90°	6.4 million	1.272	0.569	9.0 million	1.264	0.618
Cube 90°	5.1 million	1.270	0.570	7.9 million	1.268	0.618
Cube 90°	3.8 million	1.270	0.570	5.8 million	1.270	0.570
Cube 90°	2.5 million	1.263	0.583	3.9 million	1.270	0.570

Comparing the force coefficients between the two methods show small differences. In further analyse, the Realisable k-ε model was used rather than the SST k-ω model as it gives similar results with a smaller cell count. Additional cases have been assessed with different freestream velocities of the inlet flow (10 ms^{-1}, 40 ms^{-1}, 83.3 ms^{-1}, 100 ms^{-1} and 120 ms^{-1}), and used to compare lift and drag forces and its coefficients (Table 4.4). Five different meshes were generated to keep the first layer height within the logarithmic layer ($y^+ \geq 30$) for these velocities. Results from RANS will be compared with URANS and DES results in Section 4.2.2.

Table 4.4: Force comparison of the 90-degree cube undergoing different freestream velocity.

Velocity (ms^{-1})	y_1^+ (m)	C_D	**Drag (N)**	C_L	**Lift (N)**
10.0	0.00099	1.244	0.270	0.594	0.129
40.0	0.00027	1.266	4.393	0.574	1.992
83.3	0.00014	1.272	19.134	0.569	8.564
100.0	0.00012	1.272	27.590	0.570	12.360
120.0	0.00010	1.272	39.729	0.570	17.799

Table 4.4 shows that the lift and drag coefficients are fairly insensitive to the freestream velocity. The lift (L) and drag (D) forces are proportional to U_∞^2. The streamwise velocities plotted in Figure 4.4 reveal similarities of flow separation and reattachment at U_∞ = 10 and 120 ms^{-1}.

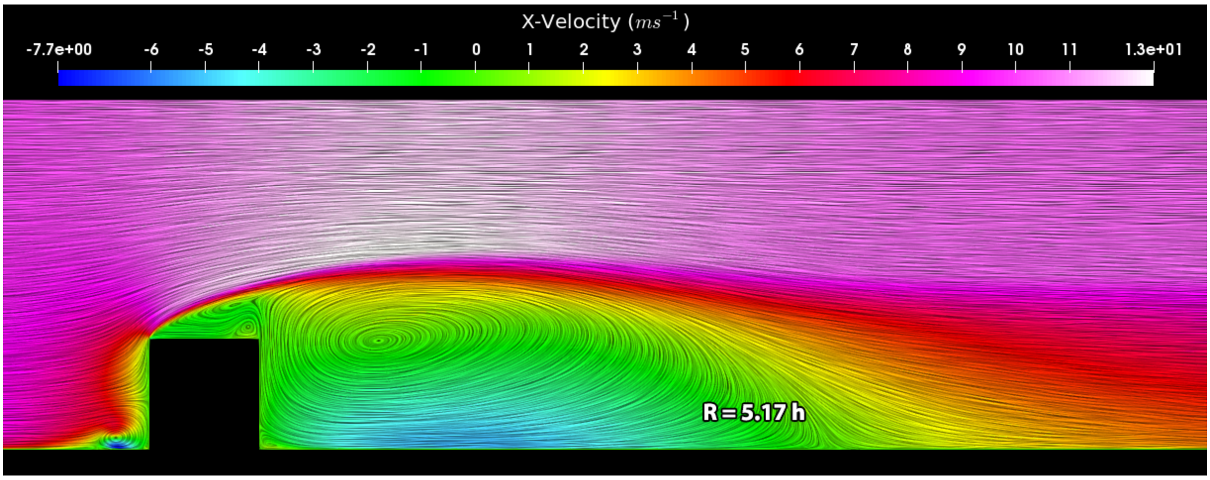

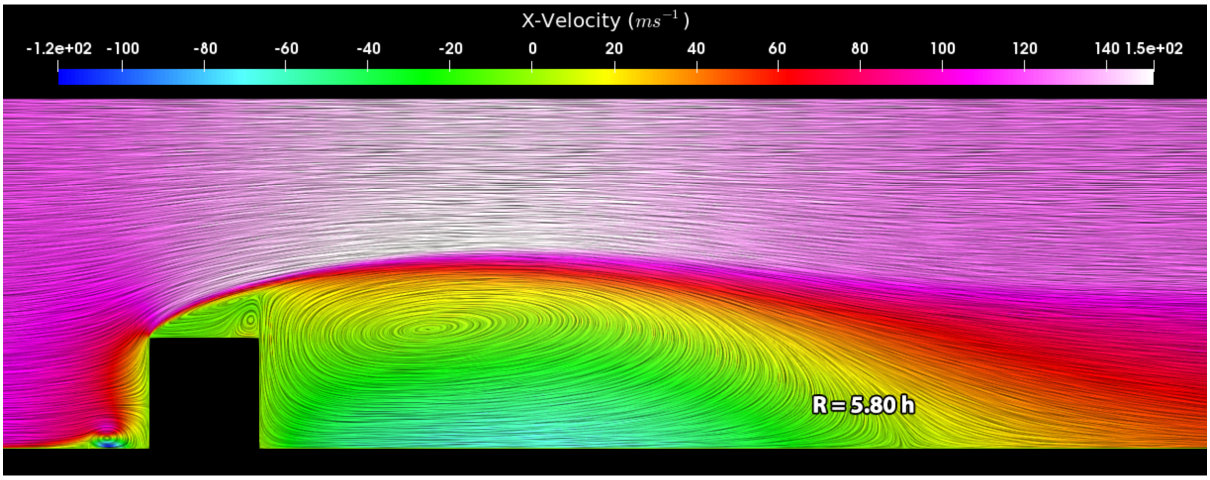

Figure 4.4: Contours of streamwise velocity at two different freestream velocities. U_∞ = 10 ms^{-1} (top), U_∞ = 120 ms^{-1} (bottom).

The re-attachment length has increased as the Re increases. However, the flow separation and re-attachment is over-estimated due to the turbulence model (RANS Realistic k-ε) used. Therefore, replacing the RANS model with DES can provide more realistic results where the flow separation length is reduced (Figure 4.11) and changes depending on the Reynolds number (Figure 4.4). The normalised velocity profile are similar as shown in Figure 4.5, which has not changed much even by increasing the Reynolds Number from Re = 40,000 to 330,000.

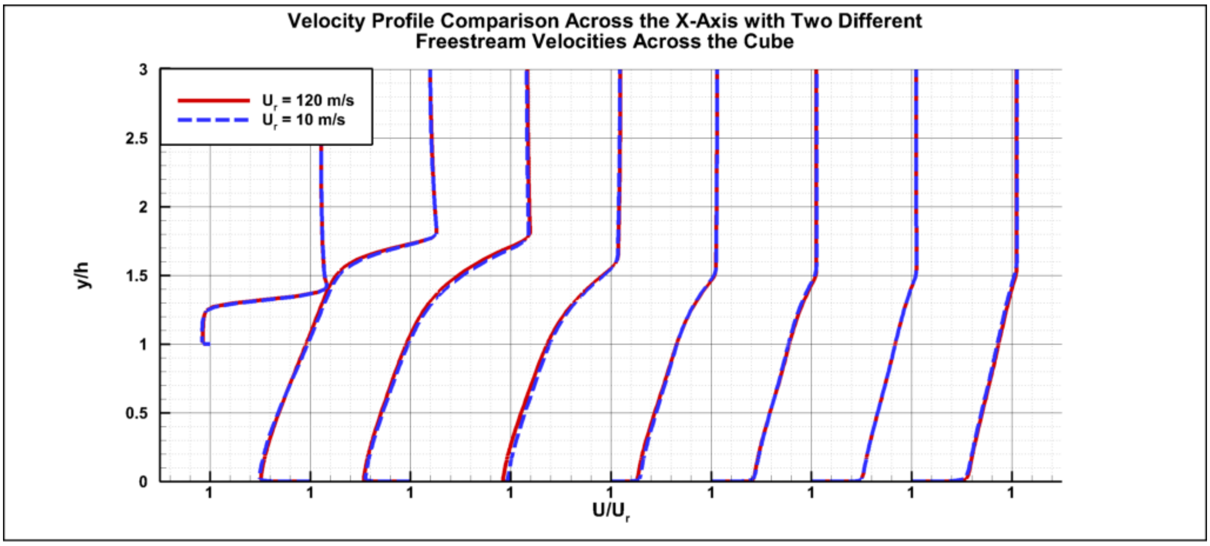

Figure 4.5: Comparison of normalised velocity profiles along the x-axis. Each step represents x/h = 0.06 from the centre of cube.

4.2.2 Unsteady analysis of the cube (URANS vs DES) 90 degrees

For an unsteady flow, an instantaneous flow field is calculated. For Unsteady RANS, ‘Realisable k-ε’ and SST k-ω were used as the RANS component of the turbulence model. The high-resolution structured mesh has sufficient resolution to handle both steady and unsteady models. Results from RANS are interpolated to speed up convergence.

The time step Δt was carefully chosen to prevent the solution from diverging (numerical instability), on the basis of the Courant number (Equation 4.3).

$$CFL = \frac{u\Delta t}{\Delta x} \leq CFL_{max} \tag{4.3}$$

An explicit time-marching solver was used in AnSys Fluent, which by default uses a four stage Runge-Kutta Scheme, thus $CFL_{max} = 1$ meaning a small time-step was expected. The smallest cell size in the streamwise direction is Δx. AnSys is robust and can use adaptive time stepping to reduce calculation time by finding the appropriate time-scale. For simplicity however, the time step was fixed throughout the simulations. Sufficient flow time was required to acquire a representative set of results. At 0.20 seconds, sufficient flow passes have already been made when U_∞ = 83.3 ms^{-1}.

The Transient Formulation was set to Second Order Implicit for improved stability, and the grid was refined. URANS was used initially, then a repeat study was performed using the DES turbulence model for further comparison with RANS.

The force coefficients calculated in each case are summarised in Table 4.5, where URANS and DES results are time-averaged from 0.2 to 0.3 seconds:

Table 4.5: Calculated force coefficients for wall-mounted 90-degree cube.

	$\bar{C_D}$	C_{Drms}	$\bar{C_L}$	C_{Lrms}
RANS Realisable k-ε	1.272	N/A	0.569	N/A
RANS SST k-ω	1.264	N/A	0.618	N/A
URANS Realisable k-ε	1.304	1.303	0.628	0.628
URANS SST k-ω	1.300	1.300	0.655	0.656
DES Realisable k-ε	1.413	1.414	0.760	0.762
DES SST k-ω	1.426	1.423	0.748	0.746

The time range provided enough convergence for the Mean and Root Mean Square (RMS) values of these force coefficients at approximately 0.3 seconds, where sufficient flow passes have been made. Compared with the URANS results, the lift and drag forces on DES have increased due to additionally resolved turbulence. However, although no force measurements were made by Castro & Robins (1977), the surface pressure distribution in Figure 4.9 would suggest that C_D would be close to the URANS and DES results.

For fully developed boundary layer flow, the expected drag coefficient of a cube would be $C_D \approx$ 1.05 as shown in many Aerodynamics textbooks. However, in this case the flow is more uniform and the boundary layer thickness δ is much smaller, which would result the drag force increasing. This is backed up by experimental studies by Sakamoto et al. (1982) and Sakamoto et al. (1984) mentioned in Diaz-Daniel et al. (2017) where C_D is dependent on the h/δ ratio. Therefore, the force coefficients are affected by the flow profile.

For each time-step, instantaneous force coefficients and other residuals fluctuate over time owing to turbulence, as demonstrated for C_D on Figure 4.6:

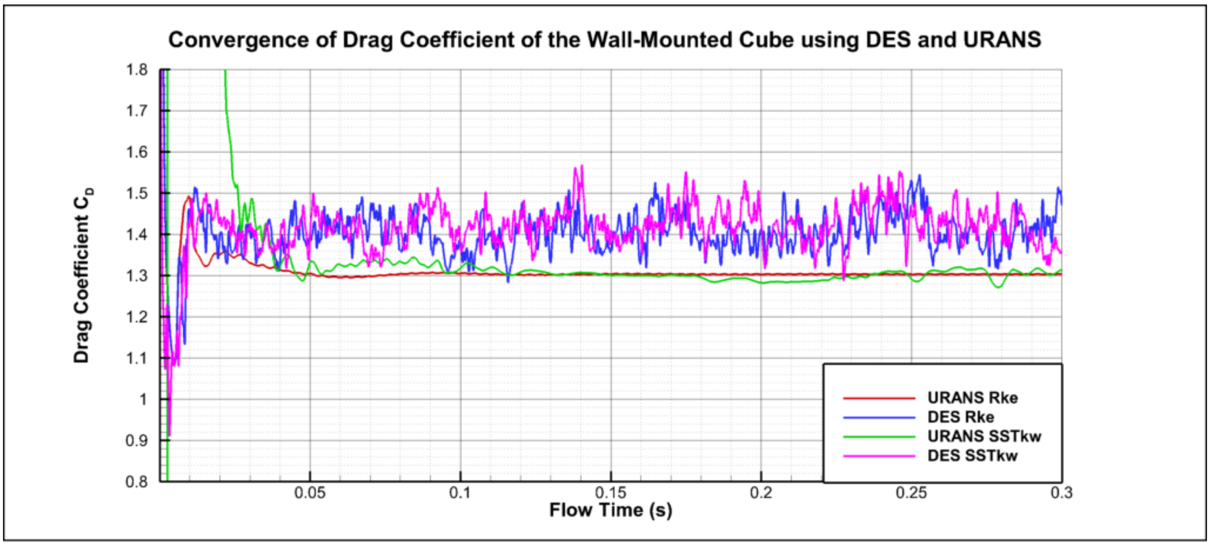

Figure 4.6: Convergence of C_D against flow time for URANS model and DES model.

Figure 4.6 shows that the calculated C_D using URANS becomes more steady whereas C_D from DES results remains unsteady over time. This is due to additional smaller eddies being resolved, which would impact on the overall turbulent structure representing turbulent behaviour in comparison when using URANS. DES results tends to reach a steady state at a range of values for each force coefficient.

The static pressure field of the flow can be used to calculate the forces on the object by integrating the pressure over the cubic surfaces. The flow structure is visualised quantitatively using streamlines and contours of the mean velocity field. Other variables such as shear stresses and vorticity can be derived, describing the deformation of fluid elements and fluid rotation respectively. For turbulence, the kinetic energy and dissipation rate would be relevant in boundary layers for processes in heat and mass transfer.

Figure 4.7 illustrates the static pressure field development between 0.0125 and 0.3 seconds. Results from URANS and DES turbulence models were compared. This revealed that additional detail of turbulence in DES compared with URANS. URANS results also dissipate rapidly, resulting in the URANS model neglecting certain details that would represent the aerodynamics accurately. The URANS results reaches to a steady state after 0.125 seconds, whereas DES continuously sheds vortices, providing more realistic results.

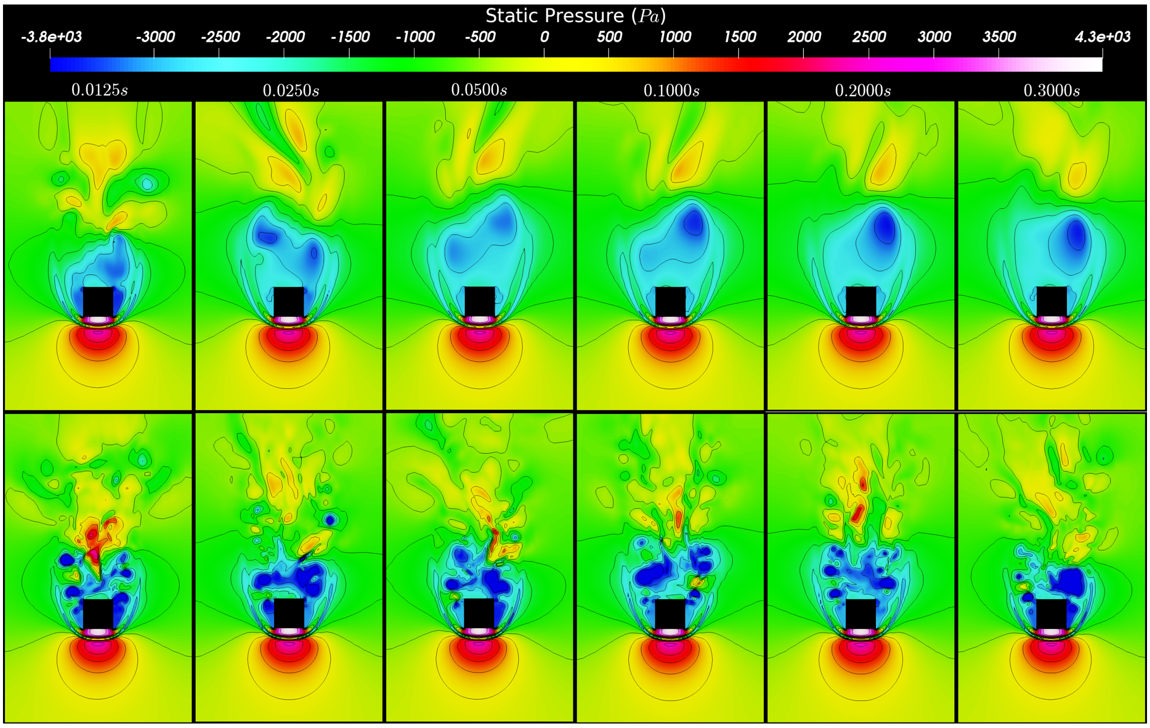

Figure 4.7: Static pressure field development around the cube from 0.0125 to 0.3 seconds flow time. Using URANS k-ε (top) and DES k-ε (bottom). Y-plane located at y/h = 0.0.

The quality of the results was then explained by evaluating the wall distance y^+ of each side of the cube where the grid resolution for Realisable k-ε should not exceed $y^+ \leq 40$ for the wall function to work correctly. Figure 4.8 presents the y^+ contour around the cube during simulation; the largest is around the frontal surface, where separation occurs. The largest static pressure was located near the cube's frontal surface, where most of the lift and drag forces occur. The lowest values are around the other surfaces due to flow separation.

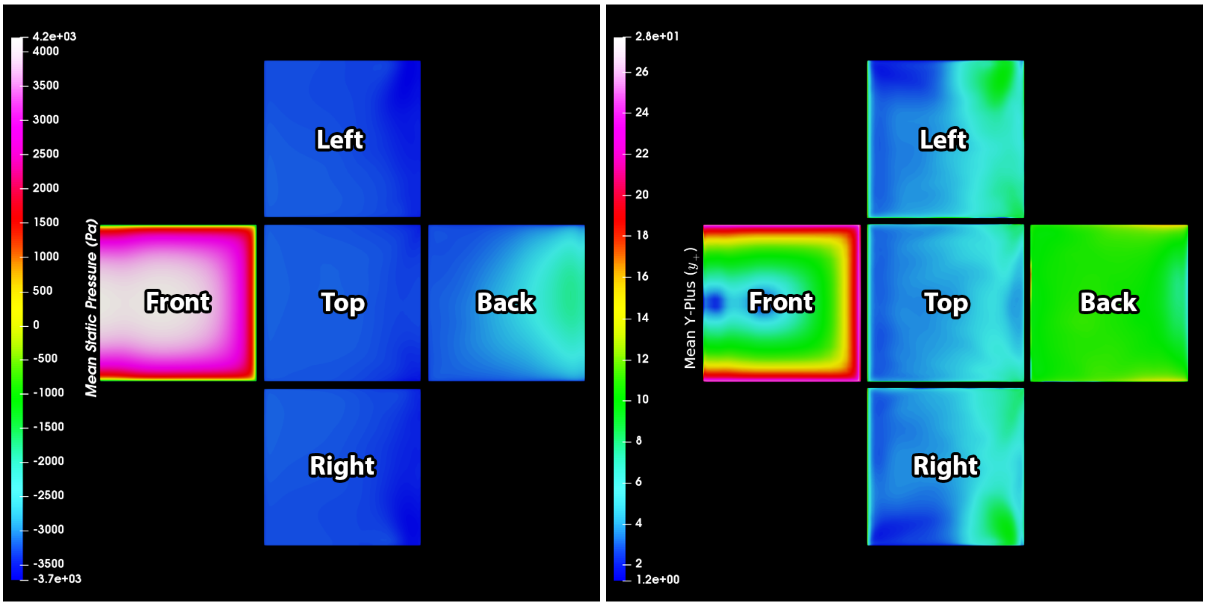

Figure 4.8: The mean static pressure contour along the cubic surfaces (left). Mean y^+ contour along the cubic surfaces (right). Cube rotated at 90 degrees.

Quantitative analysis (Re = 330,000) of the pressure coefficients C_p around the cubic surfaces is compared with Castro & Robins (1977) experimental data (Re ≈ 30,000) in Figure 4.9 where C_p is defined by:

$$C_p = \frac{(p_s - p_\infty)}{\frac{1}{2}\rho U_\infty^2} \tag{4.4}$$

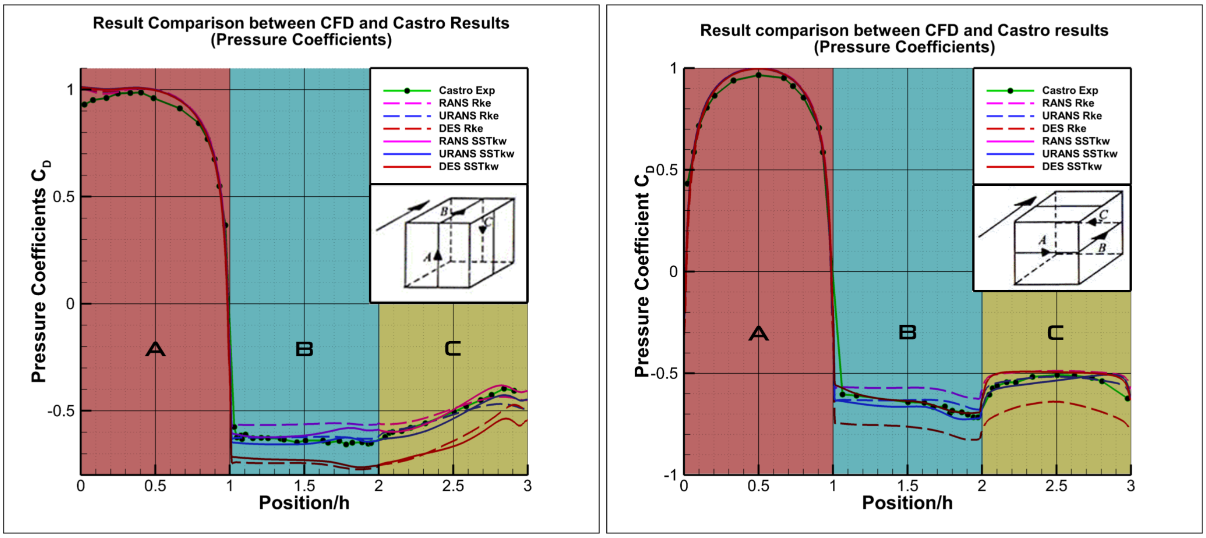

Figure 4.9: Surface pressure coefficient C_p comparison between CFD and Castro's experimental results.

Although the Reynolds number is much higher than Castro & Robins (1977), the flow is not too sensitive to geometries with sharp edges meaning the normalised surface pressure and velocity profiles should be similar to Castro & Robins (1977). For the pressure distribution, Figure 4.9 it was expected that DES is in better agreement with the experimental results than RANS and URANS. However, particularly after separation URANS is in better agreement than DES. This was likely due to the physical conditions do not fully represent the ones used in the experiment as the mesh resolution was high, particularly around the cubic surfaces. Therefore, the force coefficients in the DES results are overestimated.

The flow structure and its evolution are illustrated in greater detail by streamline plots of the mean streamline velocity (Figure 4.10):

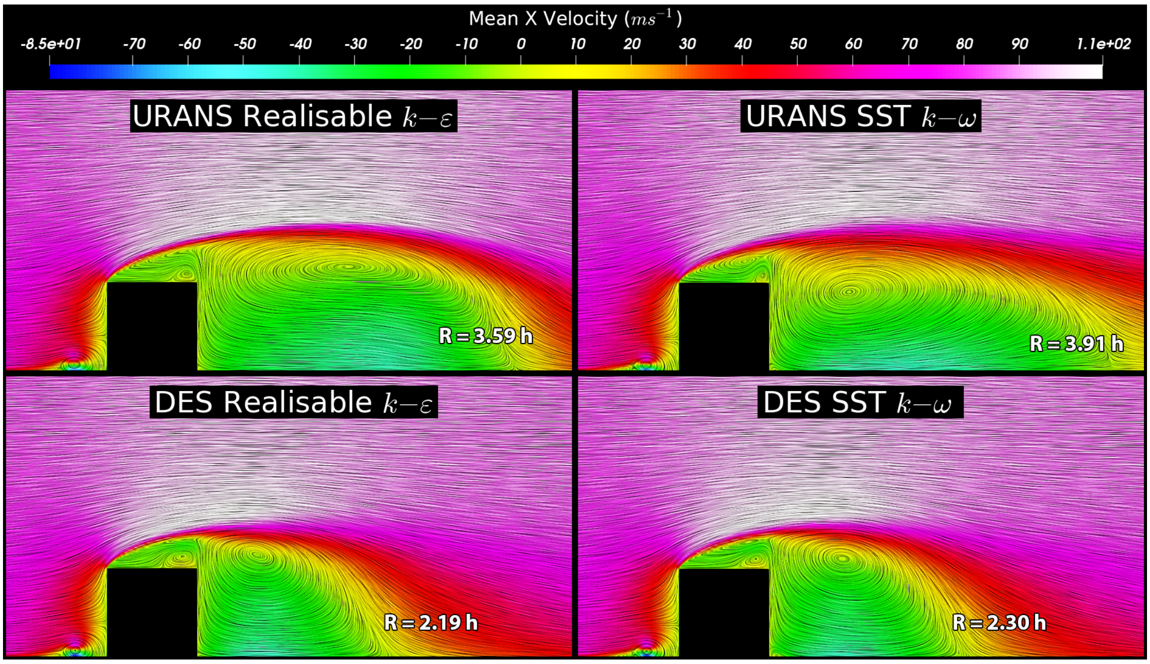

Figure 4.10: Streamline plot of the mean streamwise velocity around the cube (t = 0.3 s) using URANS (top) and DES (bottom). Z-plane located at z/h = 0.0.

Streamlines (Figure 4.10) indicate a substantial recirculation in the wake region, with a horseshoe vortex formed at the front and went through sides of the cube as illustrated in Figure 3.11. Using the DES model instead of URANS (or RANS) significantly improves wake recovery after separation.

Published CFD results by Diaz-Daniel et al. (2017) (Re = 3,000) and experimental results by Hearst et al. (2016) (Re = 180,000), stated the cube re-attachment length was approximately 1.50 h and 1.90 h respectively. This would imply that the DES results in Figure 4.10 are more representative than URANS and RANS regardless of turbulence model used.

The instantaneous velocities are time averaged between 0.2 to 0.3 seconds and plotted on Figure 4.11, which demonstrates URANS and DES are in better correlation than RANS with the experimental results, including the wake region (at x/h = 2.0).

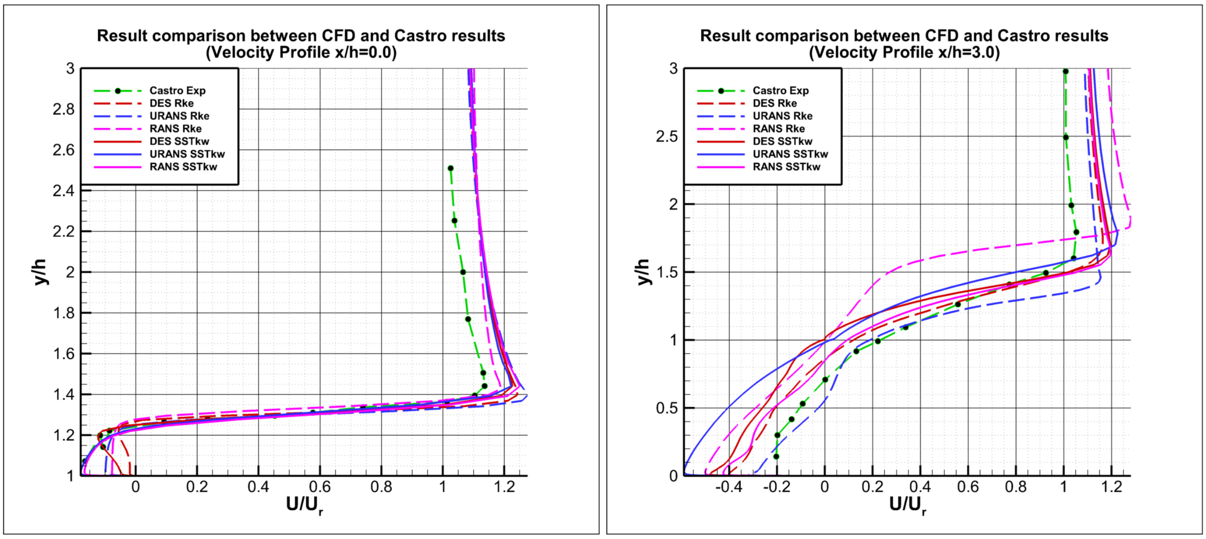

Figure 4.11: Streamwise quantitative comparison of velocity profiles at x/h = 0.0 (left) and x/h = 2.0 (right).

It was noted that there were some uncertainties with the velocity profiles in Figure 4.11 as it does not reach its freestream velocity until approximately 10.0 h after separation. Steady RANS in particular does not agree with the experimental data of Castro & Robins (1977). This can be due to limitations in the turbulence model or the large change in Reynolds number since Castro & Robins (1977) was much lower. The cross flow velocities for each turbulence model and are compared with the Castro & Robins (1977) data in Figure 4.12:

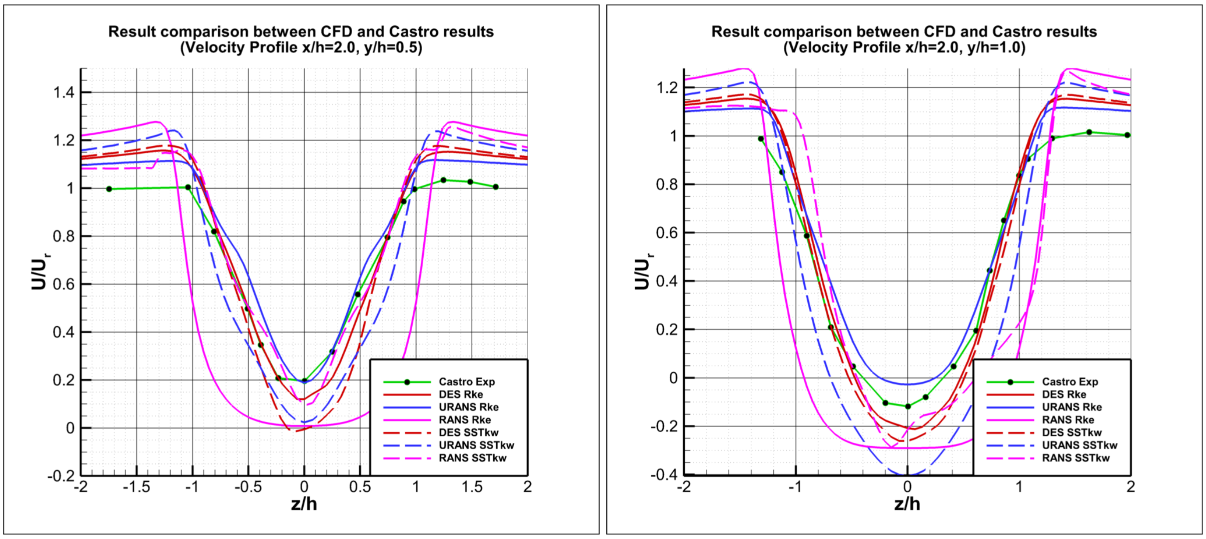

Figure 4.12: Comparison of the cross flow velocity profiles at x/h = 2.0.

Overall, DES gives a better match to the experimental data than URANS and RANS. Figure 4.11 illustrates recirculation activity in the wake where the streamwise velocity becomes negative. The mean velocity of the profile decreases within the wake region but outside the vortex zone, the velocity profile returns to freestream flow.

The turbulent flow can be described and visualised in greater detail by using an iso-surface plot of the Q-Criterion. The Q-Criterion (Q) defines a vortex as connected fluid regions with a positive second invariant of the Velocity Gradient tensor ∇U. The following expression represents Q:

$$Q = \frac{1}{2}(\mathbf{\Omega_{ij}\Omega_{ij}} - \mathbf{S_{ij}S_{ij}}) \tag{4.5}$$

where $\mathbf{\Omega_{ij}}$ represents the vorticity magnitude (scalar) and $\mathbf{S_{ij}}$ is the mean rate of strain (scalar):

$$\mathbf{\Omega_{ij}} = \frac{1}{2}\left(\frac{\partial u_i}{\partial x_j} - \frac{\partial u_j}{\partial x_i}\right) \qquad \mathbf{S_{ij}} = \frac{1}{2}\left(\frac{\partial u_i}{\partial x_j} + \frac{\partial u_j}{\partial x_i}\right) \tag{4.6}$$

When Q is positive, implies local pressure in flow is smaller than the surrounding pressure. For URANS, only the mean flow structure was visualised as no turbulent eddies was resolved. The selected Q-Criterion magnitude is similar to the Reynolds number to provide sufficient detail of vortices on Figure 4.13.

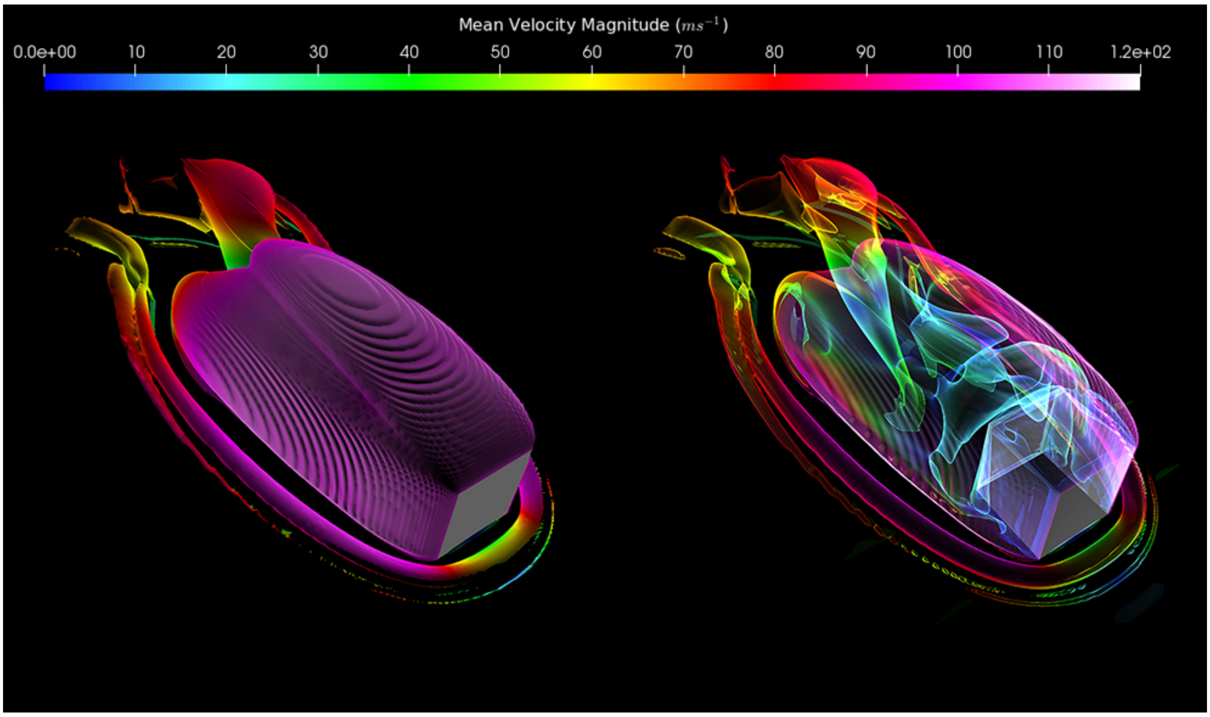

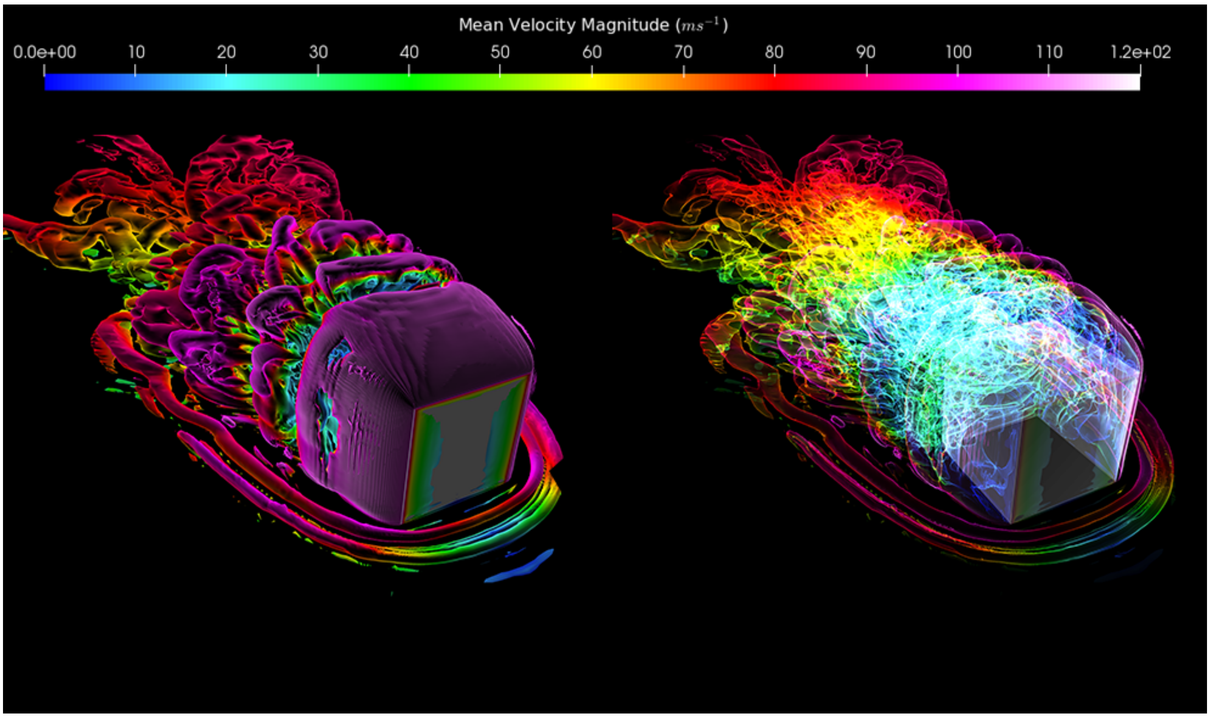

Figure 4.13: Iso-surfaces of the Q-Criterion at 330,000 coloured by the mean velocity magnitude. URANS turbulence model (top) and DES turbulence model (bottom). Solid isosurface view (left), translucent view (right).

The iso-surface plot of the Q-Criterion in Figure 4.13 shows greater detail in turbulence flow when using DES models than those using URANS, because smaller eddies have been resolved in DES.

The flow structure can differentiate the potential for the occurrence of ballast flight by revealing smaller eddies. The contour plot of Turbulent Kinetic Energy shown in Figure 4.14 shows the flow transition from laminar to turbulent flow particularly near the wall within the vortex regions.

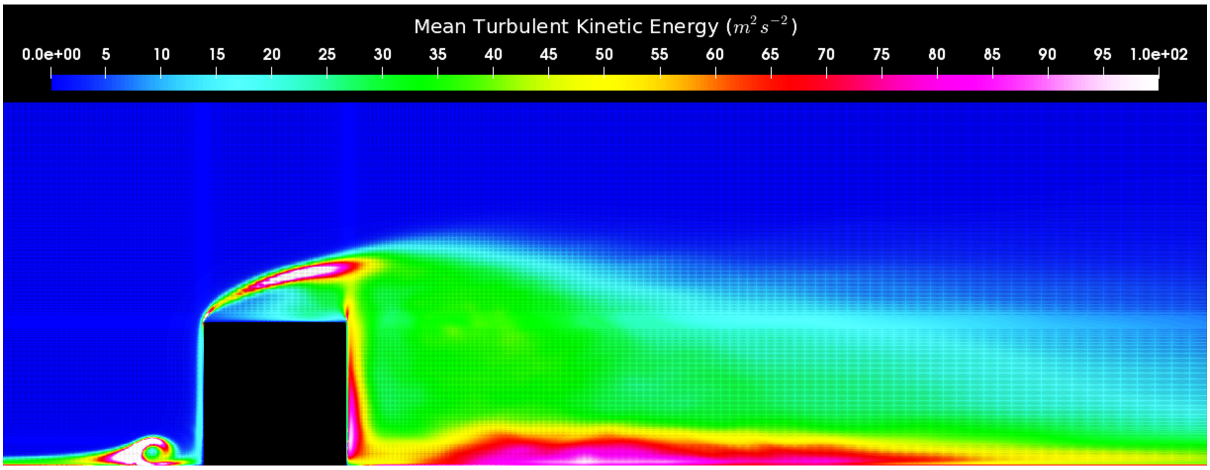

Figure 4.14: Instantaneous turbulent kinetic energy (k_T) contour ranged from 0 to 1,100 m^2s^{-1} using DES. Z-plane located at z/h = 0.0.

The largest turbulent kinetic energies are found at the point of separation, the horse-shoe vortex region and the bottom of the wake where vortex shedding occurs. This would imply that any over objects that are placed within its regions are likely to be influenced by its vortices.

Further studies investigated the effect of changing the orientation of the cube, and of the elevation level above ground.

4.2.3 Unsteady analysis of the cube (DES) 45 degrees

The numerical study was repeated for the cube rotated 45 degrees by the y-axis as shown in Figure 4.15. The boundary conditions including inlet settings remain consistent as the 90 degree study.

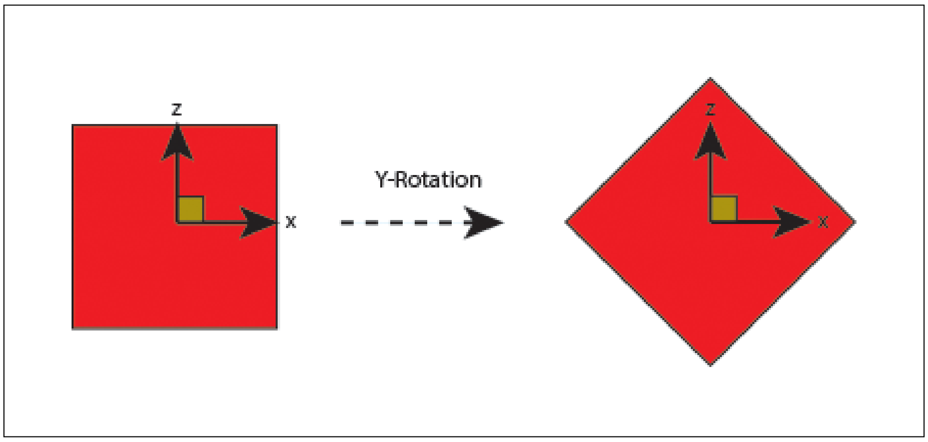

Figure 4.15: Cube case study undergoing 45-degree rotation via the y-axis.

The aerodynamic forces for each case were evaluated. In this case, the projected area A has changed from 0.0036 m^2 to $0.06 \times \sqrt{2} \times 0.06 \approx 0.0050911$ m^2. The wall-mounted cube was rotated about the y-axis and can be validated using the Castro & Robins (1977) results. The structured mesh generated for this study has high resolution near the solid boundaries as illustrated in Figure 4.16:

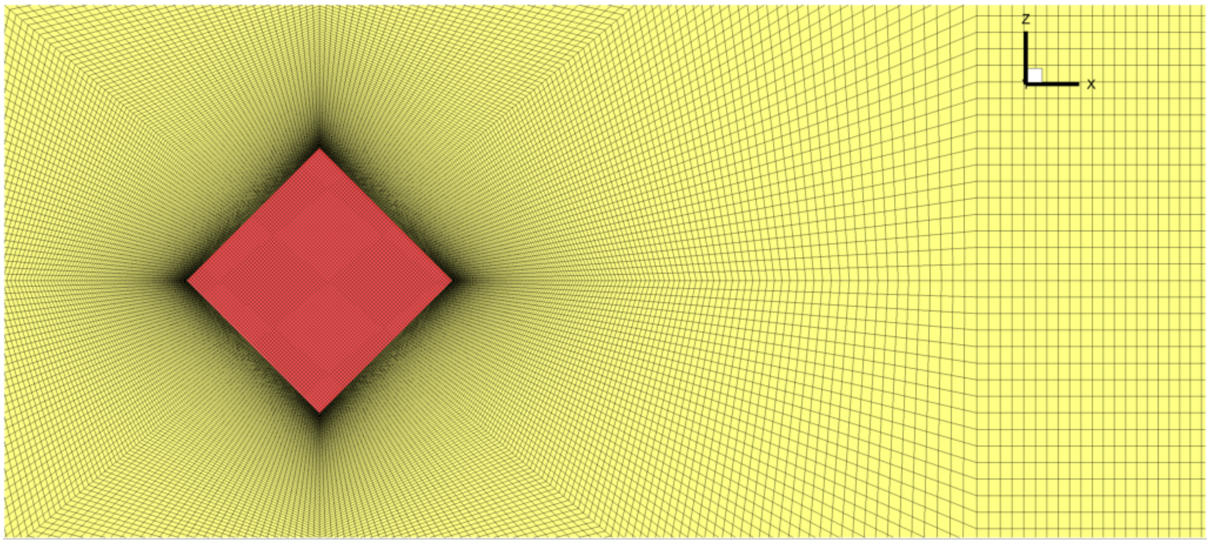

Figure 4.16: Spanwise view of the mesh grid for 45° cube (via y-axis). Y-plane located at y/h = 0.0.

The y_1^+ is similar as the 90-degree cubic studies. However, the number of cells has been increased to reduce the skewness and aspect ratio. The mesh would need to be sufficiently refined in the crucial areas to produce reasonable results. Again, the flow field was simulated for up to 0.3 seconds in time, which is giving the force coefficients in Table 4.6:

Table 4.6: Mean and RMS force coefficients received for the 45-degree cube (y-axis rotation). DES and URANS compared with RANS.

	$\bar{C}_D$	C_{Drms}	$\bar{C}_L$	C_{Lrms}
RANS Realisable k-ε	1.011	N/A	0.533	N/A
RANS SST k-ω	1.043	N/A	0.588	N/A
URANS Realisable k-ε	1.006	1.006	0.529	0.529
URANS SST k-ω	1.056	1.057	0.545	0.546
DES Realisable k-ε	1.048	1.048	0.592	0.592
DES SST k-ω	1.023	1.023	0.548	0.548

The force coefficient C_D decreases despite the greater projection area compared with the cube at 90° probably owing to the sharp leading edge dividing the flow more smoothly.

Figure 4.17 shows that the front sides of the cube experience larger pressure forces, while a small separation region occurs at the top front corner generating vortices along the top surface.

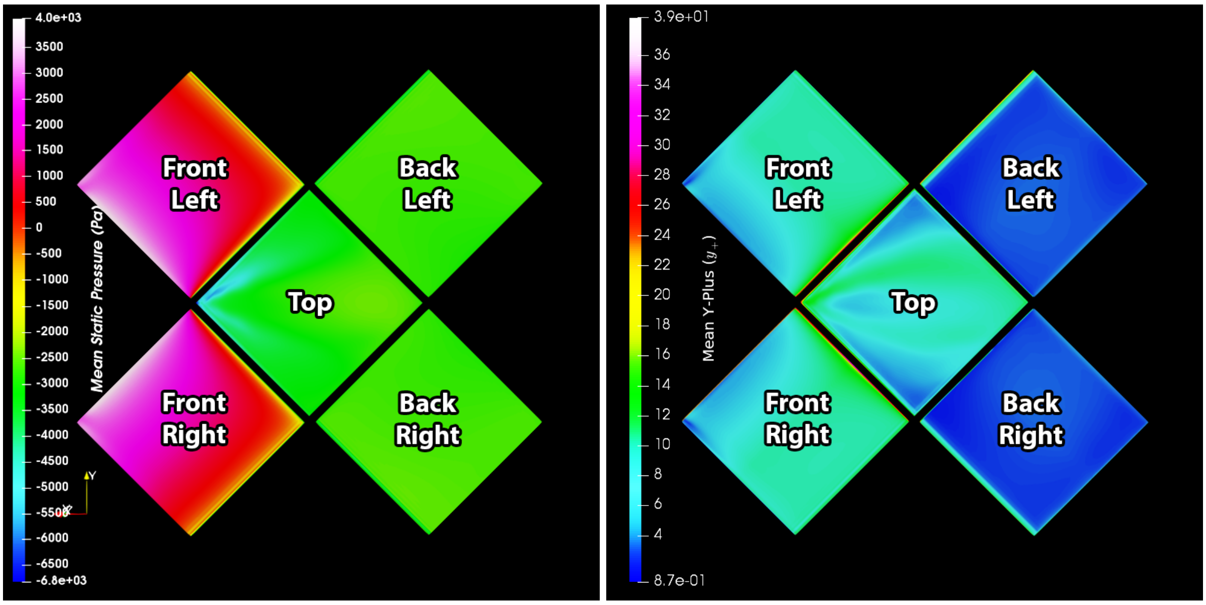

Figure 4.17: Mean static pressure contour across the cubic surfaces (left). The mean y-plus distribution across the cubic surfaces (right). Cube at 45 degree rotation.

Quantitative analysis in Figure 4.18 shows reasonable agreement between the CFD and experimental results, where two sets of probes were placed starting from the left side of the right side of the cube as illustrated.

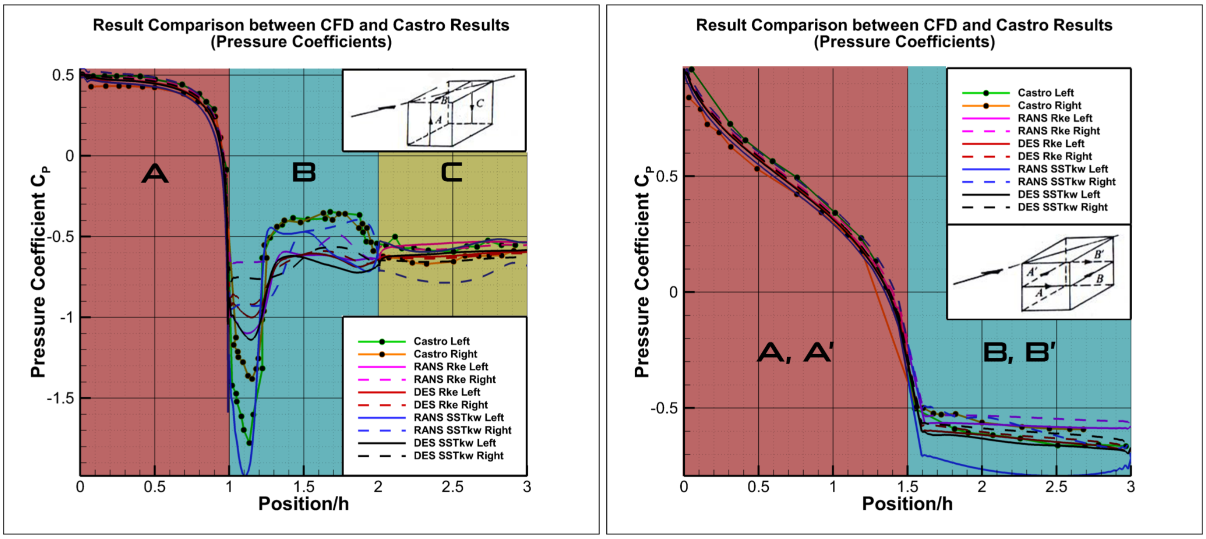

Figure 4.18: Comparison of surface pressure coefficient C_p between CFD and experimental results Castro & Robins (1977).

Streamline plots of the mean streamwise velocity in Figure 4.19 identify a larger vortex region behind the cube (Re-attachment length ≈ 2.62), owing to the spanwise separation into several recirculating lower speed flows.

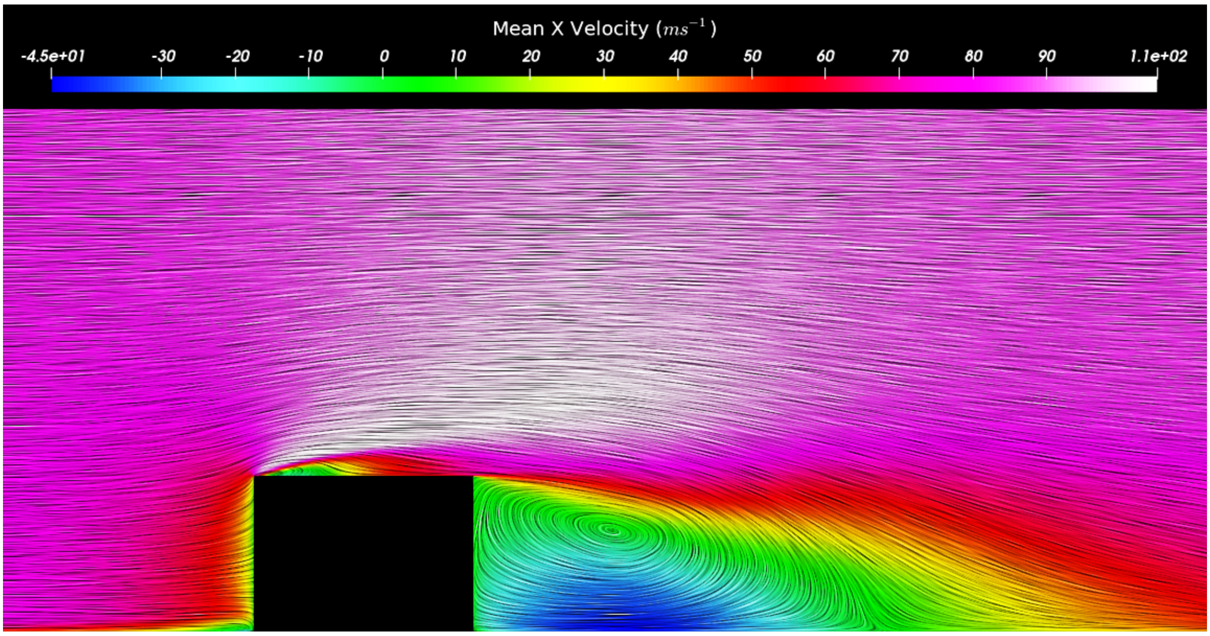

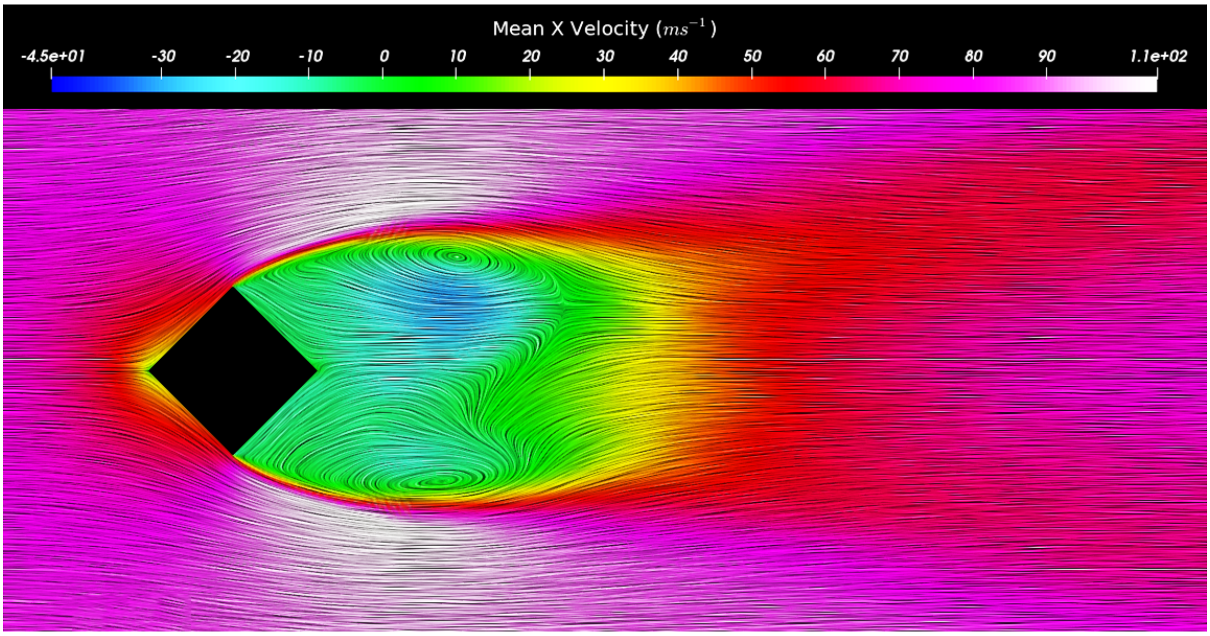

Figure 4.19: Streamline plots of the mean streamwise velocity around the cube calculated (t = 0.3 s) using DES k-ε. Streamline plot at z/h = 0.0 (top), at y/h = 0.5 (bottom).

Qualitative analysis indicates a larger wake region in the spanwise direction than in the streamwise direction, owing to the orientation of the cube (Figure 4.19). Flow separation over the cube was minimal, since the flow was divided rather than blocked as with to the 90-degree cube. A similar horseshoe vortex was developed around the cube. Quantitative analysis (Figure 4.20) suggests that the calculated flow separation is marginally greater than expected at x/h = 0.0:

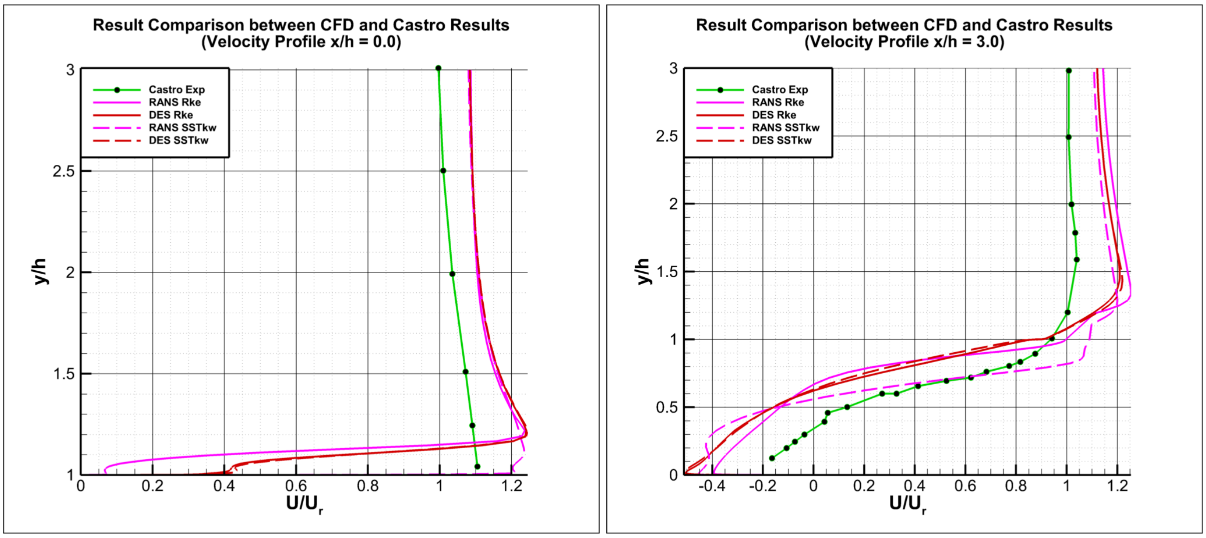

Figure 4.20: Quantitative comparison of velocity profiles at x/h = 0.0 (left) and x/h = 2.0 (right) between CFD and Castro & Robins (1977) experiment. Cube rotated 45 degrees via y-axis.

As previously mentioned, the Reynolds number in the CFD study was much greater (Re = 330,000) than Castro & Robins (1977) (Re = 30,000), which could be the cause of uncertainty as the mesh density was high. The normalised velocity U/U_r = 1.0 at around $y/h \approx$ 10.0. However, the velocity profile at

$x/h = 2.0$ is in good agreement. The velocity profiles in the spanwise direction are similar in magnitude to the experimental results in Figure 4.21. The profiles should be symmetrical since the system is also symmetrical but it is also very turbulent making it difficult to resolve accurately. Nevertheless, DES models resolves the flow after separation better than RANS models.

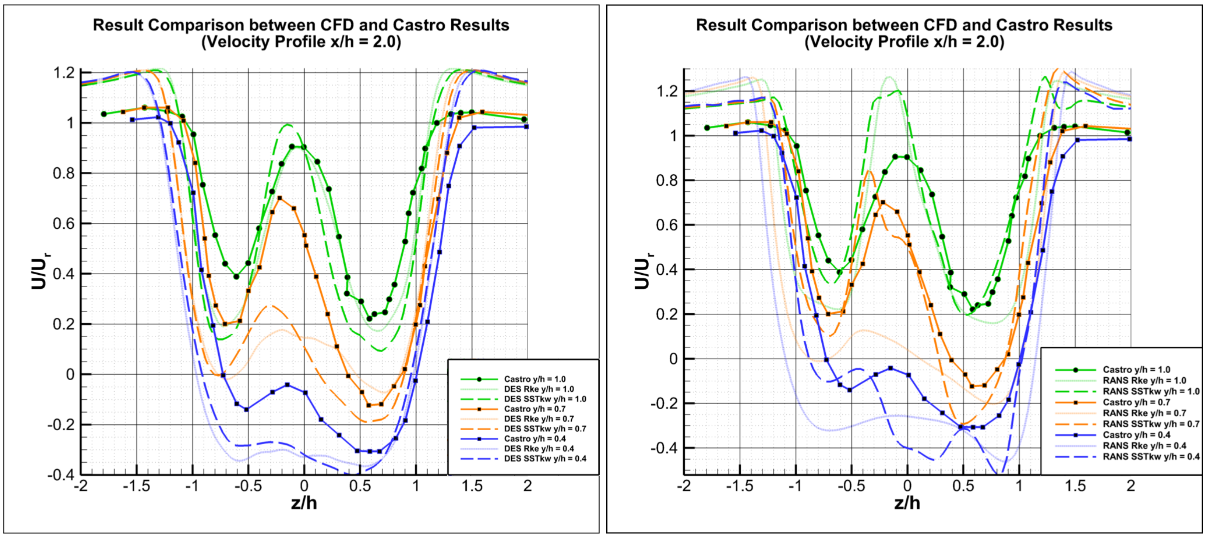

Figure 4.21: Spanwise quantitative comparison of velocity profiles at x/h = 2.0. Cube rotated 45 degrees via y-axis. Using unsteady Detached Eddy Simulation models (left), using Steady RANS models (right).

The Q-Criterion was visualised using iso-surfaces, coloured according to the velocity magnitude in Figure 4.22:

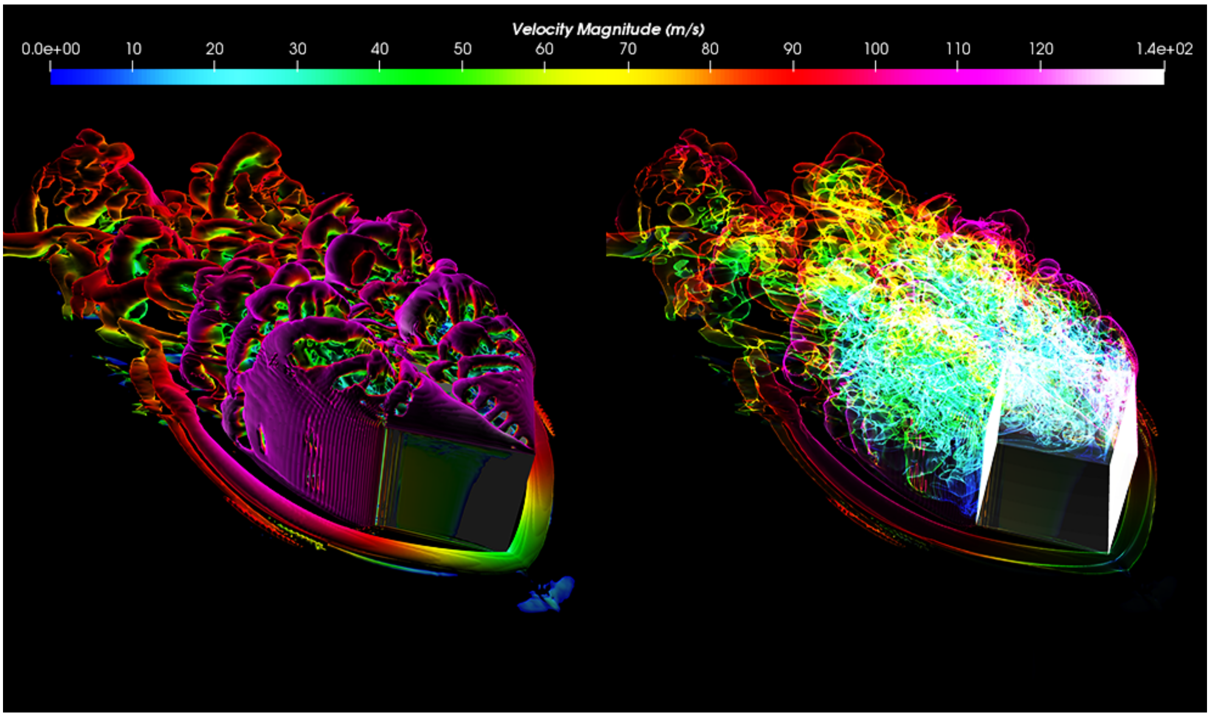

Figure 4.22: Iso-surface of the Q-Criterion at 330,000 coloured by the mean streamwise velocity. Turbulent flow passing wall-mounted cube at 45 degrees.

The vortices spread horizontally across the domain, with horseshoe vortices formed around the cube and hairpin structures at the wake. Contours of the turbulent kinetic energy (Figure 4.23) demonstrate the flow transition from laminar to turbulent after encountering the cube.

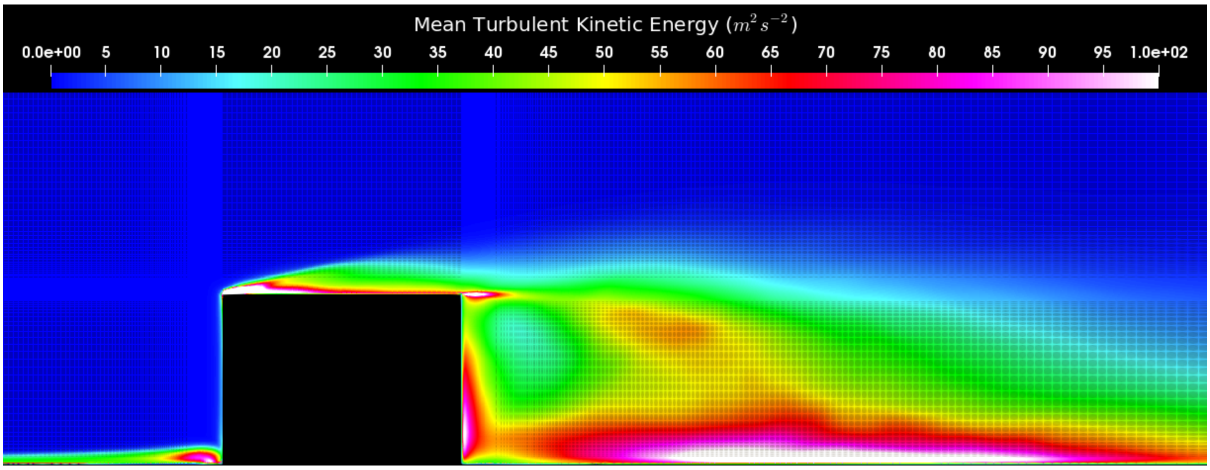

Figure 4.23: Mean turbulent kinetic energy (k_T) contour for 45-degree cube. Z-plane located at z/h = 0.0. Range constrained to 100 $m^2 s^{-2}$.

As before, the largest regions of turbulent kinetic energy are at the centre of vortices. The contour range was from 0 to 100 $m^2 s^{-2}$ or J, with a maximum kinetic energy at the centre of up to 3,000 $m^2 s^{-2}$. For the remaining cases, there are no experimental data available for comparison. The remaining cubic studies involve the elevation of the cube, and using a moving wall above the cube instead of an inlet flow.

4.2.4 Unsteady analysis of a cube above ground (DES)

The aim of these studies was to assess the changes in the aerodynamics when the particle was elevated above ground by different amounts (Figure 4.24). This might happen when external forces lift the particle or when the particle is standing on two particles with a gap in-between. Distances between the cube bottom surface and the platform between $0.50\ h$ and $0.03125\ h$ were investigated.

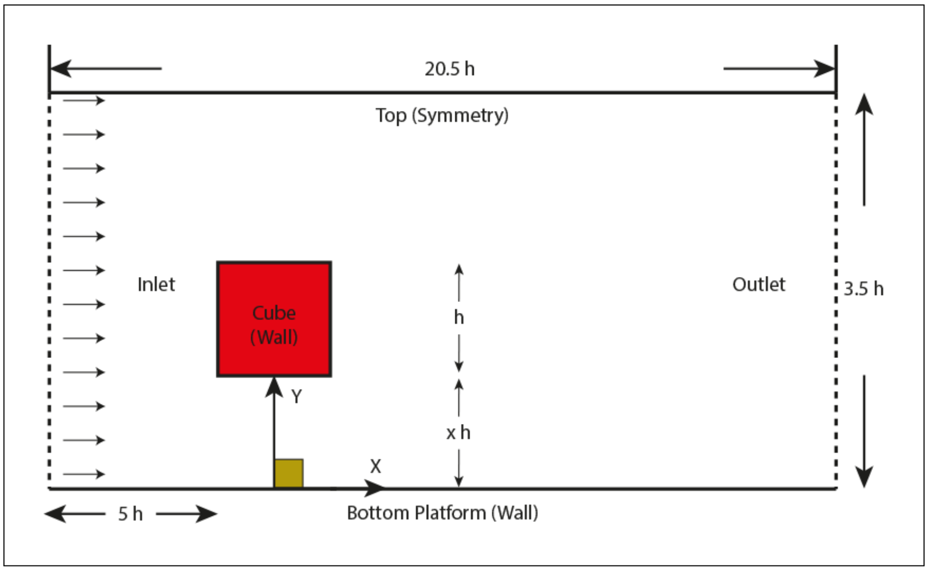

Figure 4.24: Domain system design of an elevated cube above ground.

For these cases, the domain needed to be re-meshed with the cube above ground so that the flow underneath the cube could be clearly resolved to investigate changes in force coefficients and flow reaction. Table 4.7 outlines the converged force coefficients established; the lift force decreases as the cube is raised, until the cube is no longer being affected by the ground.

Table 4.7: Force coefficient achieved for cubes at different heights above ground using DES (Realisable k-ε) model.

90 Degrees	$\bar{C_D}$	$\bar{C_L}$	$\bar{C_S}$	**45 Degrees**	$\bar{C_D}$	$\bar{C_L}$	$\bar{C_S}$
y/h = 0.00000	1.413	0.760	-0.003	y/h = 0.00000	1.048	0.592	-0.116
y/h = 0.03125	1.381	-0.139	-0.002	y/h = 0.03125	1.072	0.168	-0.005
y/h = 0.06250	1.360	-0.147	-0.005	y/h = 0.06250	1.059	0.098	-0.008
y/h = 0.12500	1.335	-0.137	-0.004	y/h = 0.12500	1.081	0.087	-0.011
y/h = 0.25000	1.360	-0.030	-0.002	y/h = 0.25000	1.057	0.061	0.016
y/h = 0.50000	1.365	-0.033	0.002	y/h = 0.50000	1.023	0.017	0.001

When the cube is close to the ground, the lift force increases. With the cube above ground, the downforce dominates the lift, particularly for the 90-degree cube. However, flow is purely in the streamwise direction from the inlet, which is not representative of the passing train as in reality there will be gusts and different velocity profiles.

The surface contour plot in Figure 4.25 shows similar pressure levels when the cube was wall-mounted except that the flow also separates underneath the cube. As the cube approaches the ground, the bottom surface pressure increases, which would increase lift in doing so.

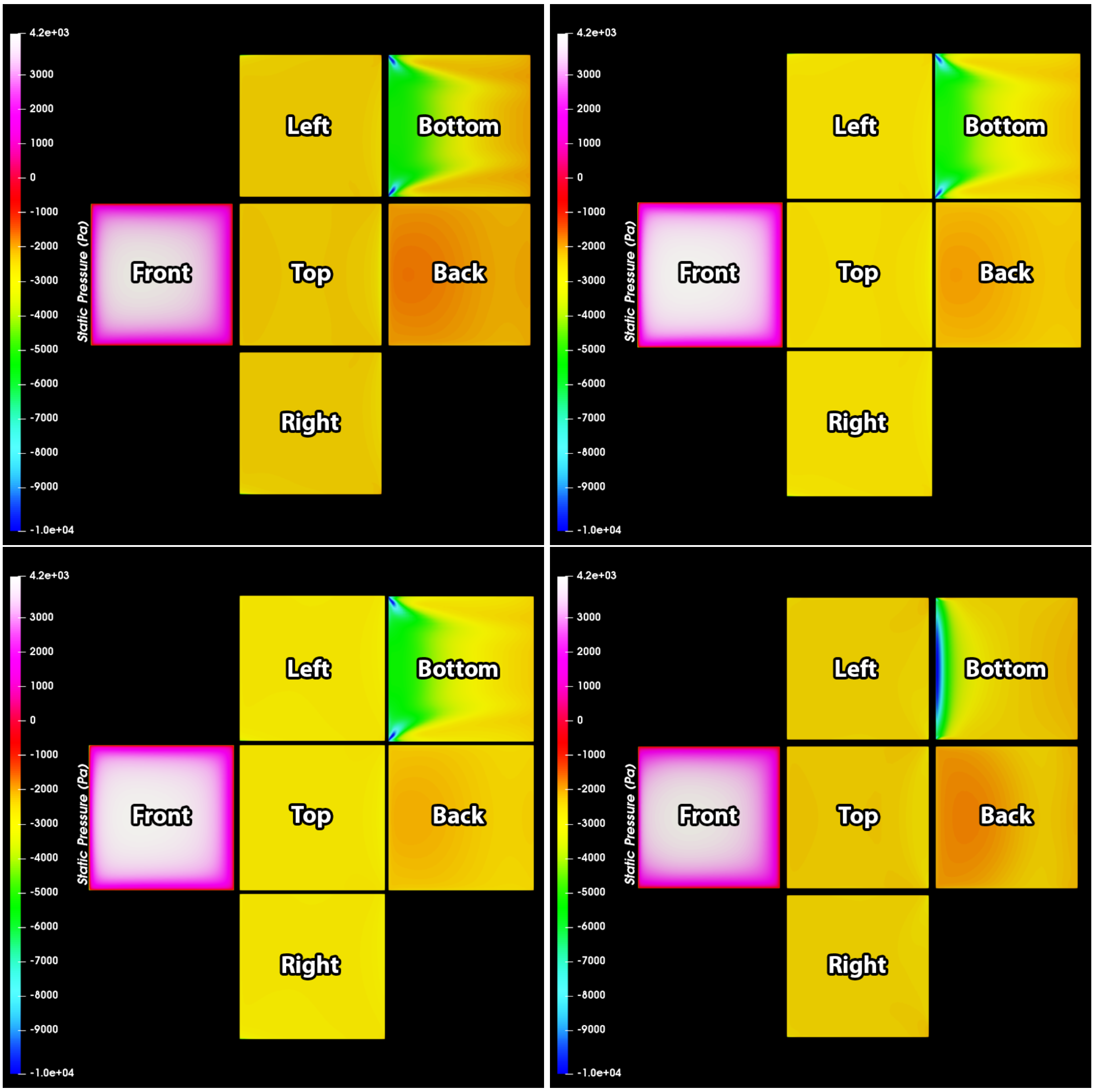

Figure 4.25: The Mean static pressure around the cubic surfaces at 90 degrees (Realisable k-ε). Cube above ground 0.50 h (top left), 0.025 h (top right), 0.0125 h (bottom left) and 0.03125 h (bottom right).

Quantitative values around the cubic surface (Figure 4.26) suggests that the largest pressure magnitudes are at the front of the cube, followed by the recirculation underneath it. The lowest pressure magnitudes are around the sides and top surfaces, due to flow separation.

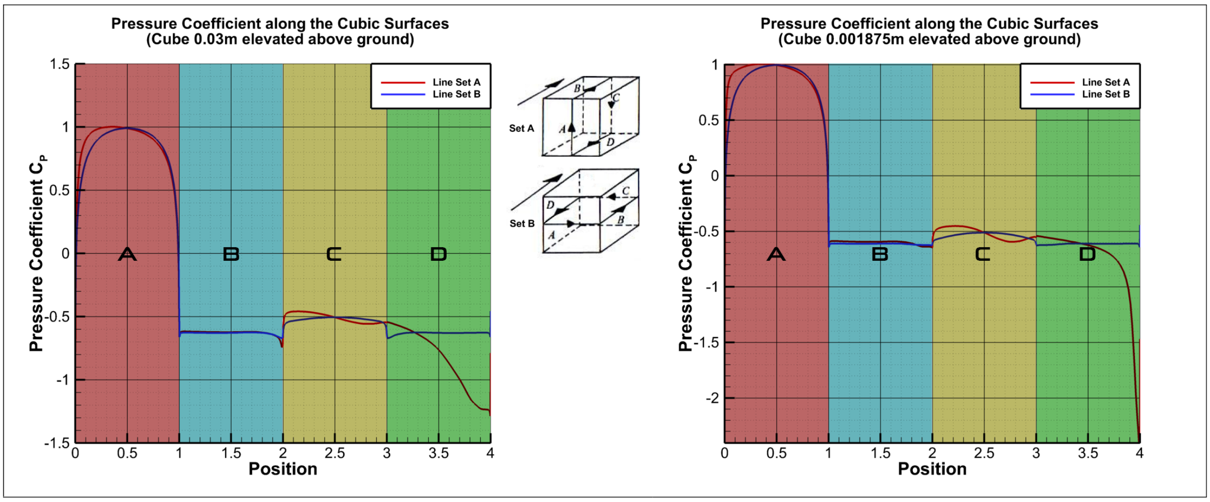

Figure 4.26: Surface pressure coefficient C_p across the elevated cube. Cube above ground 0.50 h (left), 0.03125 h (right).

As the cube approaches the ground, the static pressure on the bottom surface of the cube rapidly drops near the front surface. Streamline plots in Figures 4.27 feature multiple vortices around the cube when there is ground interaction. A horseshoe vortex is only developed when the cube is close enough to the ground.

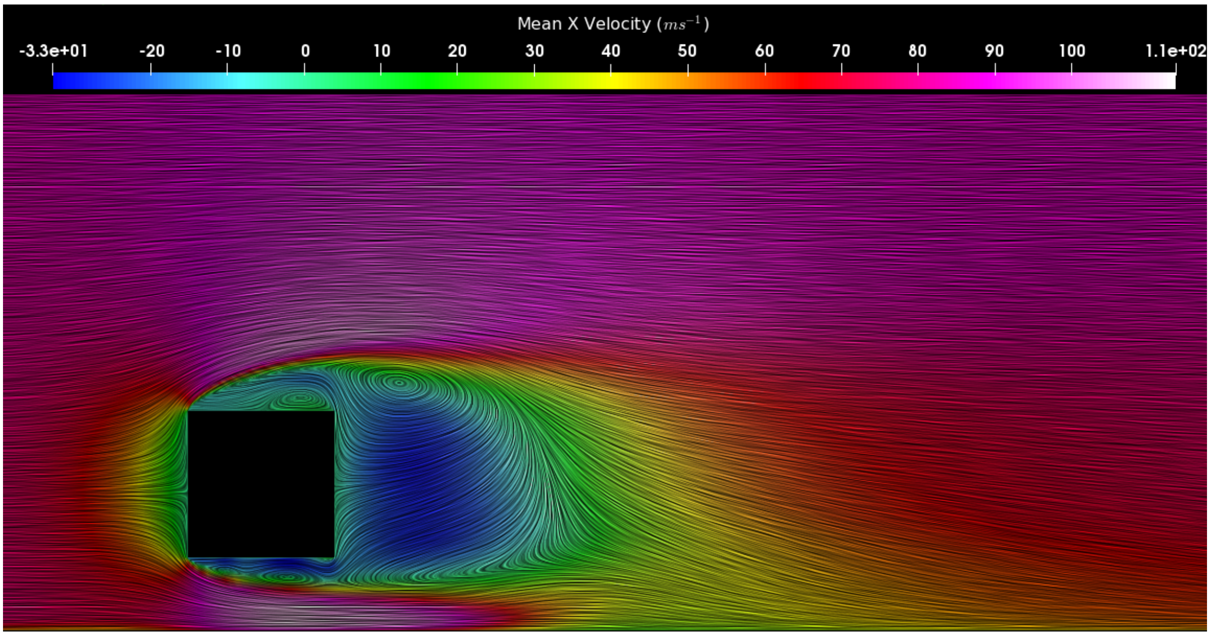

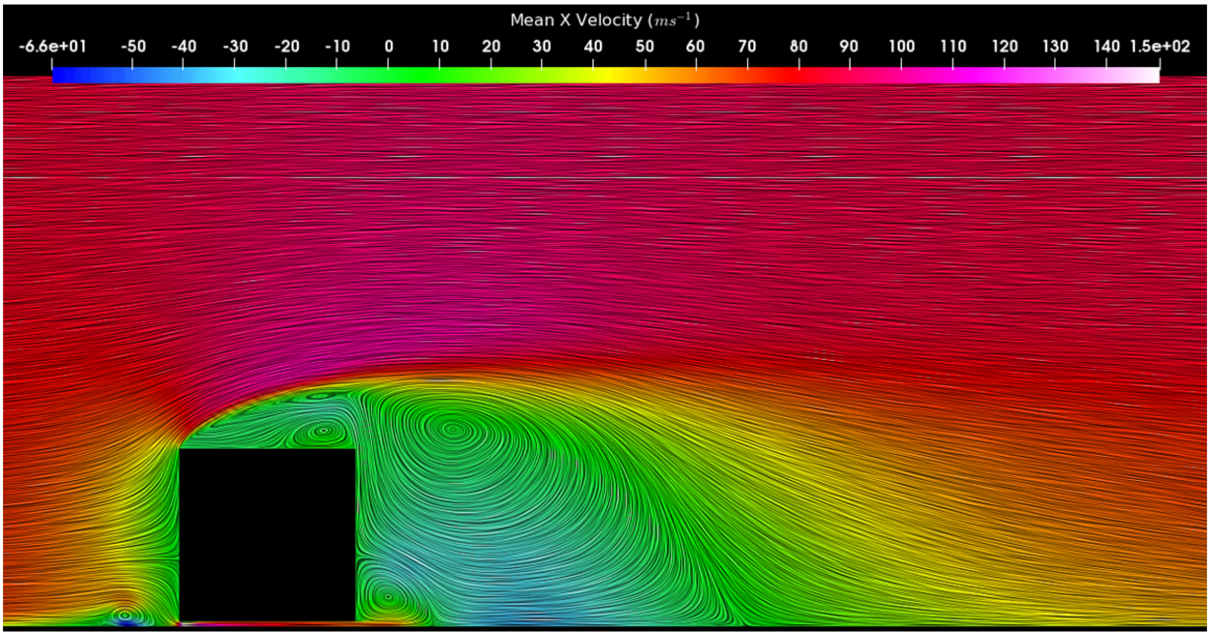

Figure 4.27: Streamline plot of the streamwise velocity around the elevated cube. Z-plane located at z/h = 0.0. Cube elevated 0.50 h above ground (top) and 0.03125 h above ground (bottom).

Velocity profiles across the domain (Figure 4.28) show how the flow separation changes, particularly underneath the cube when close to the ground.

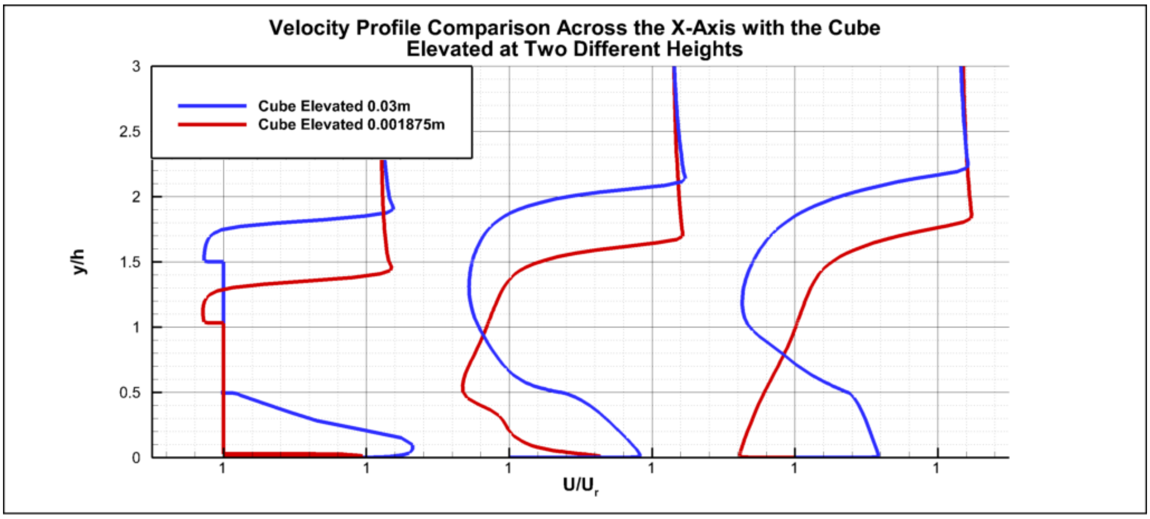

Figure 4.28: Normalised velocity profile comparison across the x-axis for elevated cubes.

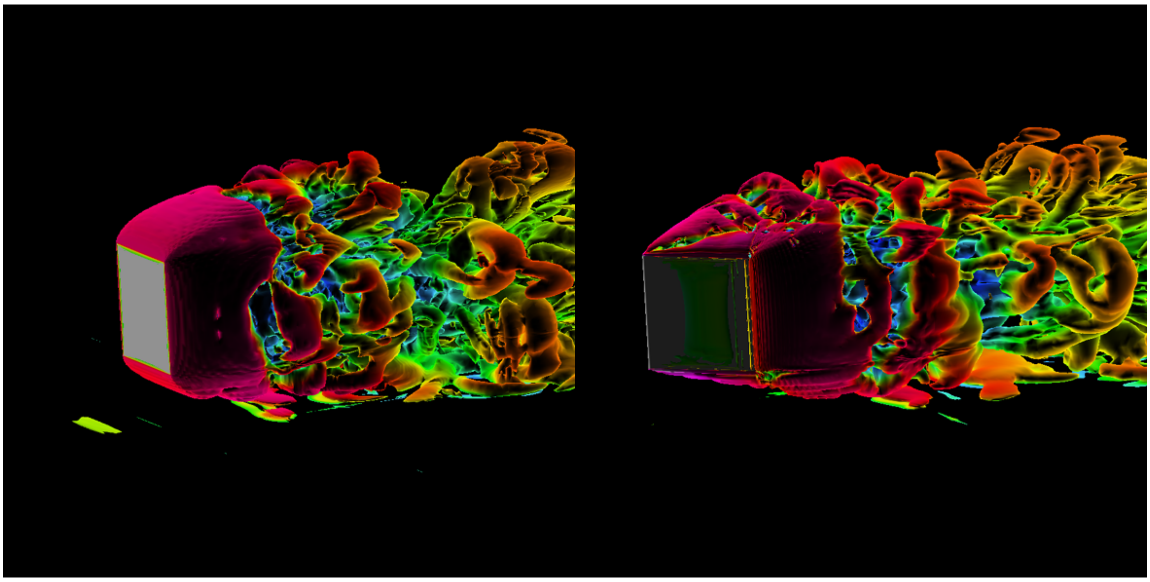

Figure 4.29: Iso-surface of the Q-Criterion at 330,000 coloured by the mean streamwise velocity. Turbulent flow passing elevated cubes 0.03 m above ground.

Further parametric studies include a moving wall study, in which the top of the domain was a solid boundary movings in the freestream direction without any free-stream airflow from the inlet.

4.2.5 Unsteady analysis of the cube with a moving wall boundary condition

In this study, a moving wall running at a speed of 83.3 ms^{-1} along the x-axis was applied above the cube (Figure 4.30). The inlet and outlet conditions were periodic it with no assigned mass flow rate. This means that the flow was fully developed by the moving wall itself. Results can be compared with the cube subjected to uniform inlet flow. Periodic boundary conditions are useful to model geometries of a repeating nature or to fully develop flow when using a moving wall condition.

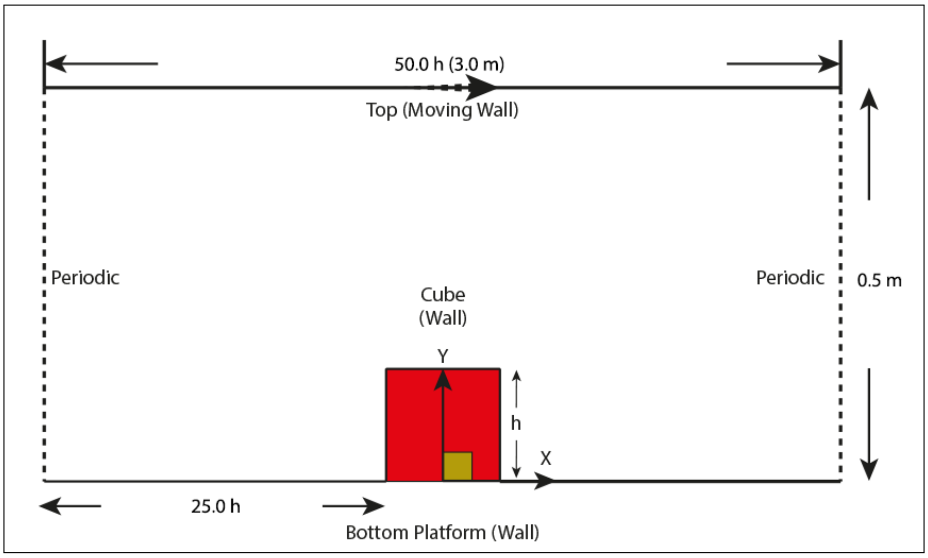

Figure 4.30: Domain system design of the cube with a moving wall above the cube and periodic conditions with no mass flow rate (not to scale).

This feature will also be used in the next chapter, to represent the moving train passing the track with the air being stationary. The moving wall develops a velocity profile and a boundary layer near the ground. Computational analysis was carried out using RANS for 300,000 iterations and DES for 0.5 seconds flow time (Figure 4.31). The flow passing the cube separates similarly compared to using inlet flow but the lift and drag forces have been reduced due to the larger boundary layer (Table 4.8):

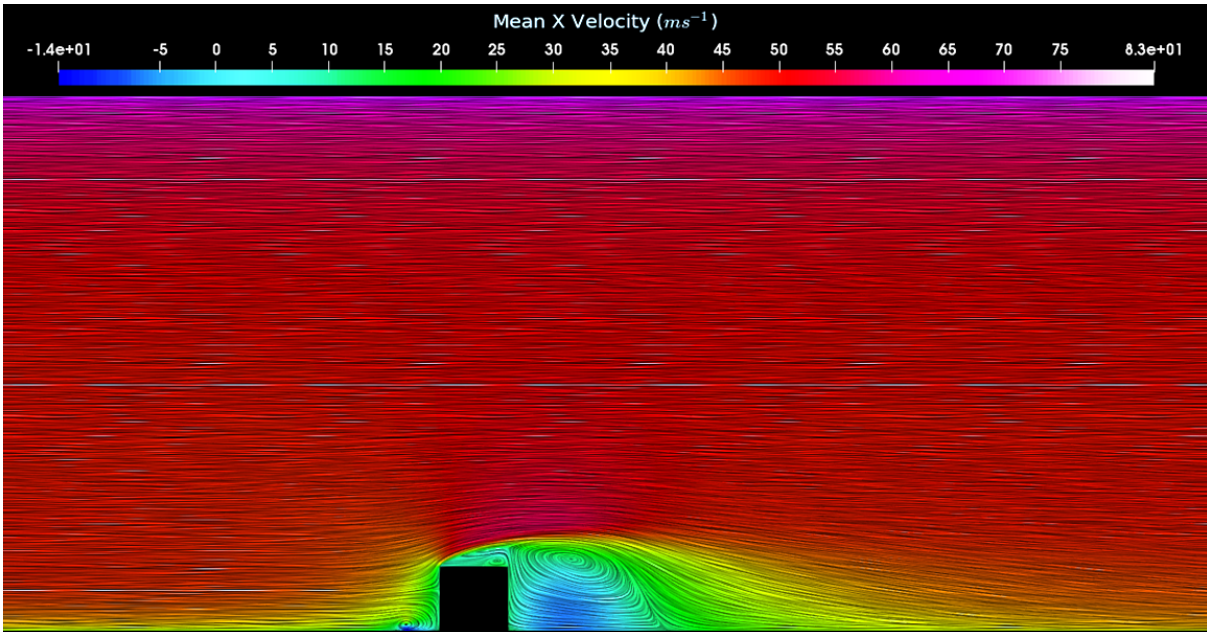

Figure 4.31: Streamwise velocity contour development around a wall mounted cube and moving wall condition.

It was noted that the inlet and outlet distance from the cube would need to be significant to allow the flow to fully reattach after separation from the cube. Otherwise, flow separation would affect the results. Force coefficients summarise in Table 4.8 shows significant changes in force coefficients due to change in velocity profiles. When using a moving wall, a boundary layer profile is generated whereas with uniform flow, the boundary layer is thin such that there's greater lift and drag forces on the cube.

Table 4.8: Calculated force coefficients of the cube underneath a moving wall.

Subject	$\bar{C}_D$	$\bar{C}_L$	$\bar{C}_S$
RANS Realisable k-ε Moving Wall	0.692	0.341	-0.000
DES Realisable k-ε Moving Wall	1.078	0.536	-0.006
RANS Realisable k-ε Inlet Flow	1.272	0.569	-0.000
DES Realisable k-ε Inlet Flow	1.413	0.760	-0.003

This was confirmed by plotting a velocity profile at x/h = -3.0 (Figure 4.32), which shows that the separated flow has fully reattached by the end of the domain.

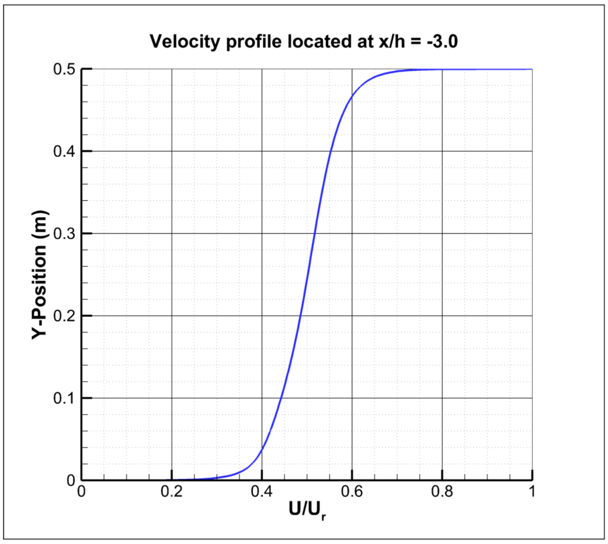

Figure 4.32: Measured velocity profile to confirm full reattachment of separated flow.

Therefore, this technique will be further applied in the track section chapter as it provides a realistic profile of the flow. However, the number of iterations required to fully develop the flow profile is far greater than using an inlet flow. There are alternatives such as using a user-defined function to map the profile, which is ideal for isolated particles but not for the track section study since the track study has many solid objects in the domain.

4.2.6 Summary of flow around cubic case studies

The results are summarised in Table 4.9.

Table 4.9: Summarised force coefficients received for all cubic case studies using steady and unsteady turbulence models.

Case Study	$\bar{C}_D$	C_{Drms}	$\bar{C}_L$	C_{Lrms}	$\bar{C}_S$	C_{Srms}
90° Cube Turbulence Model Studies						
90° y/h = 0.0 RANS Realisable k-ε	1.272	N/A	0.569	N/A	-0.000	N/A
90° y/h = 0.0 RANS SST k-ω	1.264	N/A	0.618	N/A	-0.001	N/A
90° y/h = 0.0 URANS Realisable k-ε	1.304	1.304	0.628	0.628	-0.000	0.000
90° y/h = 0.0 URANS SST k-ω	1.300	1.300	0.655	0.656	-0.006	0.006
90° y/h = 0.0 DES Realisable k-ε	1.413	1.414	0.760	0.761	-0.003	0.003
90° y/h = 0.0 DES SST k-ω	1.426	1.423	0.748	0.746	-0.017	0.017
45° Cube Turbulence Model Studies						
45° y/h = 0.0 RANS Realisable k-ε	1.011	N/A	0.533	N/A	-0.031	N/A
45° y/h = 0.0 RANS SST k-ω	1.043	N/A	0.588	N/A	0.052	N/A
45° y/h = 0.0 URANS Realisable k-ε	1.006	1.006	0.529	0.529	-0.051	0.511
45° y/h = 0.0 URANS SST k-ω	1.056	1.057	0.545	0.546	0.049	0.046
45° y/h = 0.0 DES Realisable k-ε	1.048	1.048	0.592	0.592	-0.116	0.116
45° y/h = 0.0 DES SST k-ω	1.023	1.023	0.548	0.549	-0.064	0.064

90° Cube Elevated Studies						
90° y/h = 0.000 DES Rke	1.413	1.414	0.760	0.762	-0.003	0.003
90° y/h = 0.03125 DES Rke	1.381	1.381	-0.139	0.144	-0.002	0.113
90° y/h = 0.06250 DES Rke	1.360	1.360	-0.147	0.154	-0.005	0.128
90° y/h = 0.12500 DES Rke	1.335	1.335	-0.137	0.144	-0.004	0.077
90° y/h = 0.25000 DES Rke	1.360	1.361	-0.030	0.073	-0.002	0.087
90° y/h = 0.50000 DES Rke	1.365	1.365	-0.033	0.095	0.002	0.117
45° Cube Elevated Studies						
45° y/h = 0.00000 DES Rke	1.048	1.048	0.592	0.592	-0.116	0.116
45° y/h = 0.03125 DES Rke	1.072	1.072	0.168	0.170	-0.005	0.027
45° y/h = 0.06250 DES Rke	1.059	1.059	0.098	0.101	-0.008	0.038
45° y/h = 0.12500 DES Rke	1.081	1.081	0.087	0.089	-0.011	0.033
45° y/h = 0.25000 DES Rke	1.057	1.057	0.061	0.065	0.016	0.039
45° y/h = 0.50000 DES Rke	1.023	1.024	0.017	0.028	0.001	0.043
90° Moving Wall Study						
90° y/h = 0.0 RANS Rke Moving Wall	0.692	N/A	0.341	N/A	-0.000	N/A
90° y/h = 0.0 DES Rke Moving Wall	1.078	1.078	0.536	0.537	0.006	0.117

In general, the aerodynamic coefficients (particularly drag and lift) are influenced by the orientation of the cube and its elevation above the ground. If a ballast stone becomes airborne, the lift and drag effects decrease.

The results also demonstrate that a larger projection area can potentially increase the lift and drag forces but only if the projected faces are normal to the incoming flow. If the faces are at an angle like the 45-degree cube, the static pressure around the cube decreases hence the forces are lower.

To assess the expected forces, experimental measurements using a force transducer inside a wind tunnel. Velocity profiles were also measured using a pitot-tube inside the wind tunnel.

4.3 Experimental Force Measurements of Isolated Shapes

4.3.1 Introduction

Sufficient validated cases in Chapters 4 have proven AnSys Fluent is capable of producing useful results by determining turbulent flow around objects accurately with the correct settings and a decent mesh. However, new studies were introduced, which required validation through experimental results.

Certain variables can be measured in a wind tunnel experiment including:

- Forces using a mechanical balance, load cell or a force transducer.
- Pressure distribution around an object by using pressure taps or pressure sensitive paint.
- Measuring the flow velocity at different points by using hot wire anemometers or manometer.
- Obtain flow information across a plane using Particle Image Velocimetry (PIV).

Experimental techniques allowed engineering researchers to perform practical tests by replicating similar conditions in a controlled environment compared to field studies and collect data using specialised equipment. The data is initially captured as raw data (i.e. volts, images, displacements, etc.), which is then converted into useful data (i.e. velocity, force, pressure, etc.).

In some cases, the raw data would need to be calibrated by using known variables to achieve decent results by establishing a relationship between the input and output variables. But there is a risk of calibration error as well as other biased uncertainties including bias drift (e.g. time) and background noise such as electrical interference.

The equipment availability and specification affect the technique and precision of the acquired experimental data due to bias and precision uncertainties. The University of Southampton has a range of experimental facilities including wind tunnels with the following specifications on Table 4.10:

Table 4.10: Wind Tunnel specifications at University of Southampton.

	R.J. Mitchell	**7' x 5' High**	**7' x 5' Low**	**3' x 5' (Boldrewood)**
Working Section	3.5 m × 2.4 m	2.1 m × 1.5 m × 4.4 m	4.6 m × 3.7 m × 3.7 m	0.9 m × 0.6 m × 4.5 m
Maximum Wind Speed	40 ms^{-1}	45 ms^{-1}	11 ms^{-1}	35 ms^{-1}
Moving Ground	Yes	No	No	No
Balance	Nutem overhead 6-component balance	3-component weigh beam balance in tunnel roof. 4-component strut mounted Aerotech balance for vehicle tests.	3-component weigh beam balance in tunnel roof. 4-component strut mounted Aerotech balance for vehicle tests.	6-component strain gauged balance in tunnel floor on a controllable turntable. 2D Traverse gear for moving instrumentation across the working section.

The Bolderwood wind tunnel lab (Figure 4.33) was used for aerodynamic studies on isolated shapes. Data including force measurements, velocity and pressure, can be collected from the Bolderwood wind tunnel. But for PIV experiments, a different wind tunnel would be required since it required smoke, lasers and a closed circuit wind tunnel to visualise the flow movement. The R.J. Mitchell and 7' x 5' wind tunnel can accommodate PIV for more complex case studies, but it would induce a daily cost of approximately £2,000 and £1,500 respectively.

Figure 4.33: Boldrewood wind tunnel lab facility.

The wind tunnel test section at Boldrewood campus is 0.45 × 0.6 m^2 with a maximum operational flow speed of 35 ms^{-1}. For health and safety reasons, the maximum operational flow was restricted to 30 ms^{-1}. The remainder of this chapter contains results achieved for a wall mounted cube and ballast grains placed in the wind tunnel.

4.3.2 Force Measurements for Isolated Particles

The aim of this study was to measure the aerodynamic forces on isolated particles to compare with the calculated results using CFD. The critical velocities of individual ballast movement was also measured from its starting position.

To measure the aerodynamic forces on the cube, a 6-axis force transducer was used which influenced the experiment design. The load cell used was an ATI Force Transducer (Mini 40) manufactured by National Instruments (Figure 4.34), which was available at the University of Southampton. The experiment design involved having the force transducer pocketed inside the isolated shape, which can measure forces up to 40 N at high resolution.

Figure 4.34: Setup for the ATI Mini-40 Force Transducer, using National Instrument Chassis and configured laptop.

Therefore, the fixtures and the bottom surface of the wind tunnel would need to be designed to accommodate this method.

4.3.3 Instrumentation and Methodology Design

The aerodynamic (lift, drag and side) forces of different isolated shapes would need to be measured at different angles and elevation levels meaning the rig would need to allow rotation and height adjustments before fixing the object in place.

Adapter plates were used to attach the force transducer into the particle and other fixtures (Figure 4.35), which allowed the transducer cable to be threaded through to be connected into the laptop and chassis to collect data:

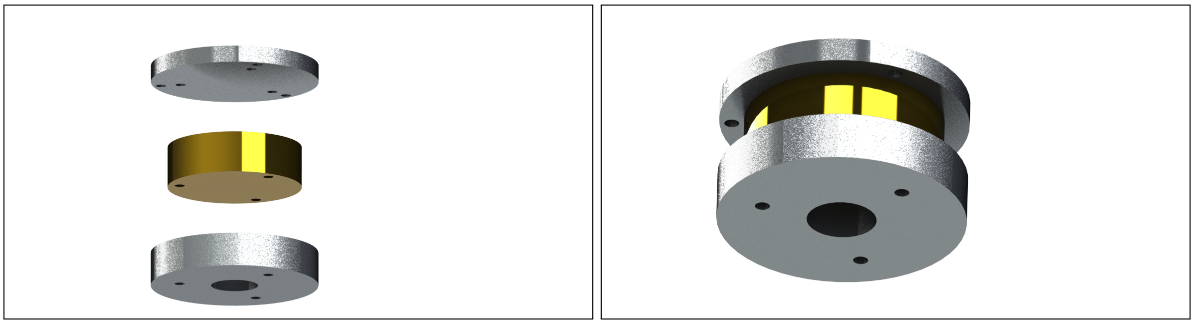

Figure 4.35: Render of designed adapter plates assembly attached to the Mini40 transducer.

To allow the force transducer to be pocketed inside the measured shape, the material density would need to be strong enough to allow screw threading to secure the adapter plates in place. The material needed to be light and durable, therefore a cube was 3D printed using ABS Plastic alongside with a larger cube made of Sikablock M700.

A hollow aluminium tube was threaded and attached to the lower adapter plate, allowing passage of the transducer cable and to leave the test section without disrupting the flow.

If the cube was to be elevated, the tube would be exposed in the passing flow causing vortices, which can affect the results. This was prevented by 3D printing an aerofoil (NACA0020) with a chord length of 175 mm length to pocket the tube. The metal tube and airfoil were held in place using bolts as shown in Figure 4.36 where the detailed CAD drawings can be found on Appendix A.

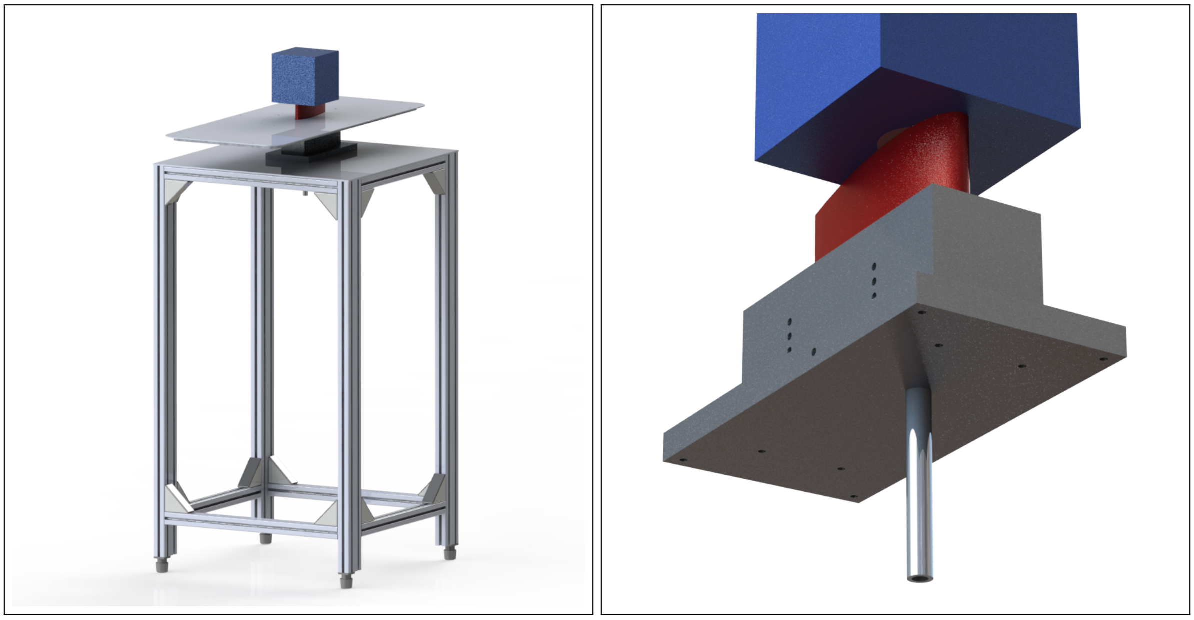

Figure 4.36: Full assembly supported by the fixtures underneath the Boldrewood wind tunnel (left). Sub-assembly for the force measurements (right).

Prior to testing and measurements, the force transducer was tested by placing known masses onto the cube with the transducer attached at different axes to test its reliability. The sampling rate of 10,000 Hz was used for the transducer with a fixed mass and time sampling. For the y-axis, the mass was placed on top of the cube whereas for the other axes a pulley system was used to pull the cube horizontally.

Sample data of the results can be found in Figure 4.37 where 0.5 kg was placed on top of the cube for five seconds, which showed a small range in results over time.

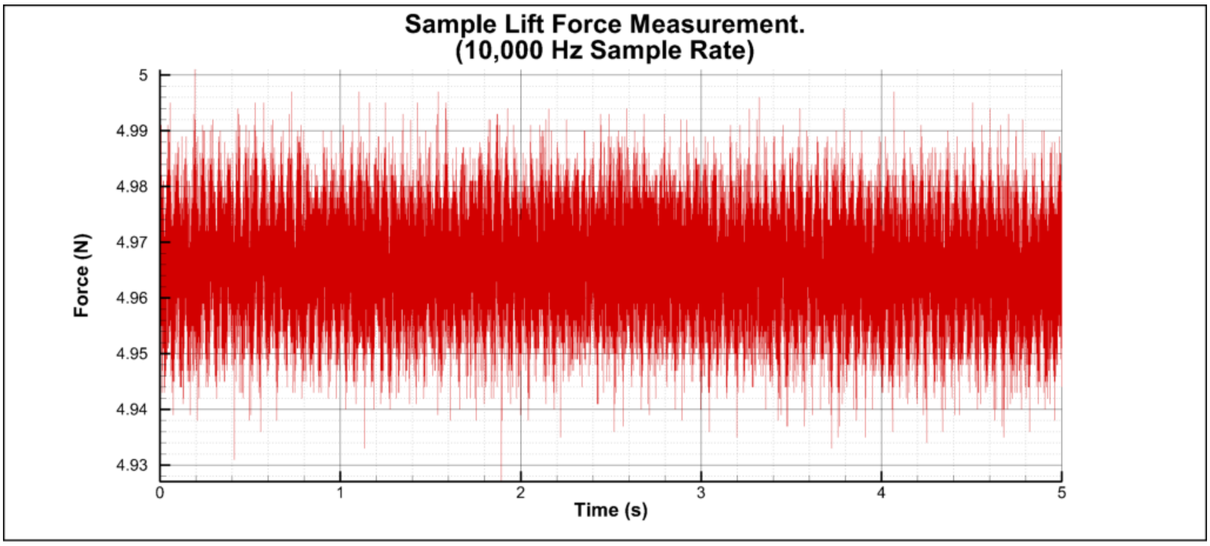

Figure 4.37: Boldrewood Wind Tunnel lift force measurements using ATI Mini40 Force Transducer.

Time-averaged results was summarised in Table 4.11, which has confirmed the error in results is negligible, which made the force transducer suitable for force measurements. This test was repeated for consistency.

Table 4.11: Mass calibration results for the ATI Mini40 Force Transducer.

Mass	$\bar{D}$	**Error %**	$\bar{L}$	**Error %**	$\bar{S}$	**Error %**
0.1 kg	0.99719	1.01651	0.98808	1.00722	1.01927	1.03901
0.2 kg	1.98909	1.01381	1.98384	1.01113	2.00344	1.02112
0.3 kg	2.97801	1.01189	2.97910	1.01226	3.00054	1.01955
0.4 kg	3.96686	1.01092	3.97090	1.01195	3.99057	1.01697
0.5 kg	4.95787	1.01078	4.96563	1.01236	4.97937	1.01516

The next piece of equipment tested was the FCO520 Air Pro Micro-manometer Pitot Tube manufactured by Furness Controls, which was previously calibrated and certified (*UKAS Certificate No. 1705190*) by Furness Control. The Boldrewood Wind Tunnel speed controls are linked to the turbine rotation displayed in RPM (revolutions per minute) units. In order to test its reliability, the Pitot tube was placed in the 7 × 5 wind tunnel, which runs towards the targeted speed.

Table 4.12: Velocity calibration results for the pitot tube, compared with the 7 × 5 wind tunnel measurements.

7 × 5 Wind Tunnel Velocity (ms^{-1})	6.00	10.00	14.00	18.00	22.00	26.00
FCO520 Pitot Tube Velocity (ms^{-1})	6.00	10.00	14.01	18.00	22.00	26.01

The results in Table 4.12 showed good agreement between the FCO520 pitot tube and wind tunnel readings. Therefore, the pitot tube was used in this experiment.

Furthermore, the FCO520 pitot tube was attached to the upper surface of the test section, measuring the freestream velocity 750 mm away from the inlet. The next phase was to find the relation between the wind tunnels turbine speed and the freestream velocity produced.

Table 4.13: Relationship between the wind tunnel turbine speed against the measured freestream velocity. Boldrewood wind tunnel lab.

RPM (Hz)	5	7	9	11	13	15	17	19
Velocity (ms^{-1})	0.0	3.8	5.9	7.6	9.4	11.3	12.9	14.6
RPM (Hz)	21	23	25	27	29	31	33	35
Velocity (ms^{-1})	16.3	17.9	19.6	21.3	22.8	24.5	26.1	27.8

Table 4.13 and Figure 4.38 revealed that the measured flow speed at operational speed above 5 RPM is linear as expected. However, the error resided in the beginning at lower operational speeds where the freestream flow was hardly detected despite the flow being uniform.

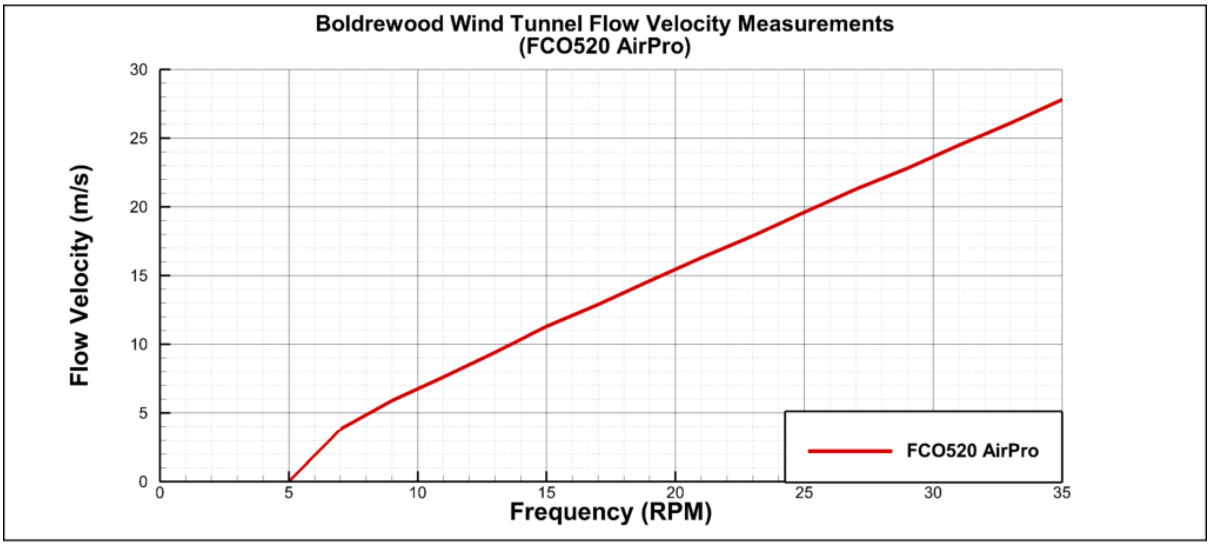

Figure 4.38: Plot of freestream velocity measurements using the FCO520 pitot tube. Boldrewood wind tunnel facility.

The cubic particle with the pocketed slot was designed and 3D printed using the UpBox printer. The UpBox printer can print up to 255 × 205 × 205 mm^3 at high resolution (UpBox, 2016). ABS plastic or biodegradable PLA plastic can be used for this printer. The cubic length is 100 mm, which makes the Reynolds number approximately 200,000 when the flow speed is at 30 ms^{-1}.

The particle size was constrained due to the blockage ratio of the wind tunnel. The maximum recommended blockage ratio is $\leq 5\%$ to establish accurate flow data across the domain. Therefore, the largest cubic length should not exceed $\approx 0.1162\ m$.

$$\frac{\text{Projection Area of Subject}}{\text{Test Section Area}} = \text{Blockage Ratio}$$

Therefore, the cube of length 100 mm was chosen and its Reynolds Number would be approximately:

$$Re = \frac{\rho U_\infty h}{\mu} = \frac{1.2047 \times 30 \times 0.10}{1.81 \times 10^{-5}} \approx 200,000 \tag{4.7}$$

The advantage of using 3D printing is the possibility of printing complex shapes using CAD files. Therefore, the ballast shapes can be scaled to a fixed volume scaled up to have a similar Reynolds number as the computational cases (Figure 4.39).

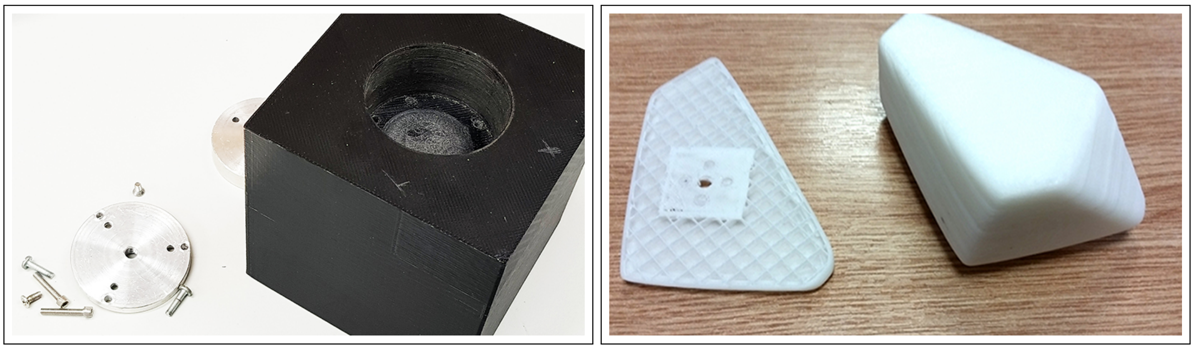

Figure 4.39: Cubic shape being 3D printed using the UpBox 3D printer (left). 3D printed example of a simplified ballast shape (right).

The CAD files from Figure 4.65 were used to compare with the simulations to see how different aspect ratios could affect the likelihood of ballast movement outcome.

The final piece designed and manufactured at the EDMC workshops in the University of Southampton is the Acrylic test section platform (Figure 4.40), which contains a subsection (400×200 mm ellipse), which can be replaced with different laser cut slots providing flexibility in design for many projects, reducing costs.

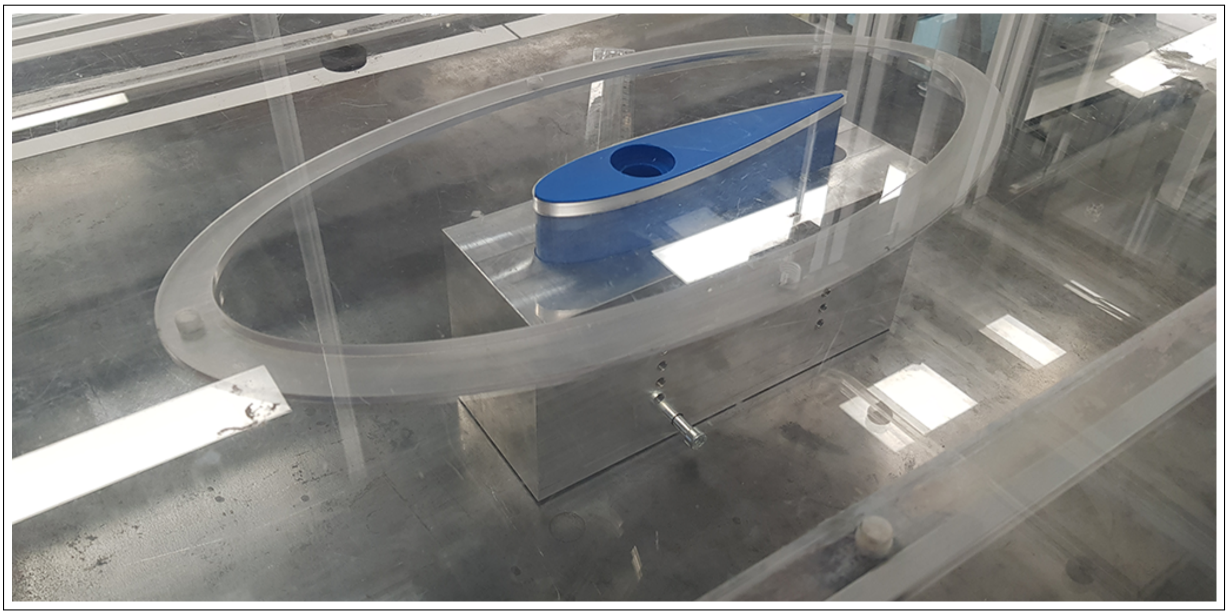

Figure 4.40: Manufactured wind tunnel platform by the EDMC workshop (Southampton University). Platform includes subsection, allowing flexibility in platform design.

The final variable considered is the air density in the lab based on the air properties measured using the weather station sensor by Imagintronix. The sensor measured the atmospheric pressure P_{atm} and the room temperature T, which was substituted in Equation 4.8 to calculate the air density:

$$\rho = \frac{P_{atm}}{RT} = \frac{100800}{287.058 \times (22.3 + 273.15)} = 1.1885\ kgm^{-3} \tag{4.8}$$

Hence, the maximum Reynolds number would be:

$$Re = \frac{\rho U_{\infty} h}{\mu} = \frac{1.1885 \times 30 \times 0.10}{1.824 \times 10^{-5}} \tag{4.9}$$

Therefore, the experiment set up pictured on Figure 4.41 was ready to measure forces on the wall mounted cube:

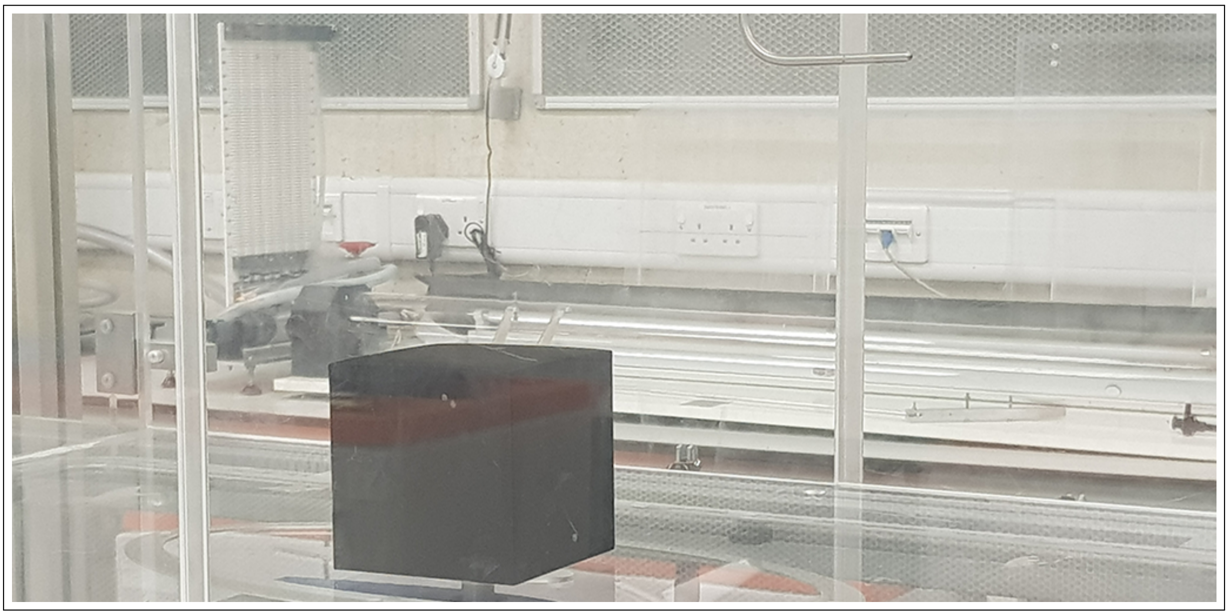

Figure 4.41: Wind tunnel setup to measure forces of a cube placed onto the wind tunnel floor. Bolderwood wind tunnel facility.

Three trials of lift, drag and side forces were measured by obtaining sufficient samples over time and time-average the results once the wind tunnel flow stabilises. Furthermore, the cube would be rotated by 45 degrees and the procedures were repeated.

The measured laminar boundary layer thickness was very thin as the flow speed reaches freestream velocity a few millimetres away from the wind tunnel platform. Therefore, the flow is mostly uniform. To thicken the boundary layer profile, the wind tunnel would need to be modified by increasing the test section length or by applying ground roughness to the wind tunnel platform.

4.3.4 Raw Data Collection and Post Processing

Each force was measured using the transducer and was time-averaged for 10 seconds at wind tunnel turbine speeds from 10 to 30 Hz. The first set of measurements were carried out on the wall-mounted cube at 90 degrees, placed 750 mm away from the inlet where the flow is uniform. To reduce the error further, a Pro 350 Digital Protractor was used to measure the angle the cube is held in place. The cube slope was positioned such that the incline would not exceed more than 0.5 degrees. Figure 4.42 shows sample data for the aerodynamic forces on a wall-mounted cube in Newtons.

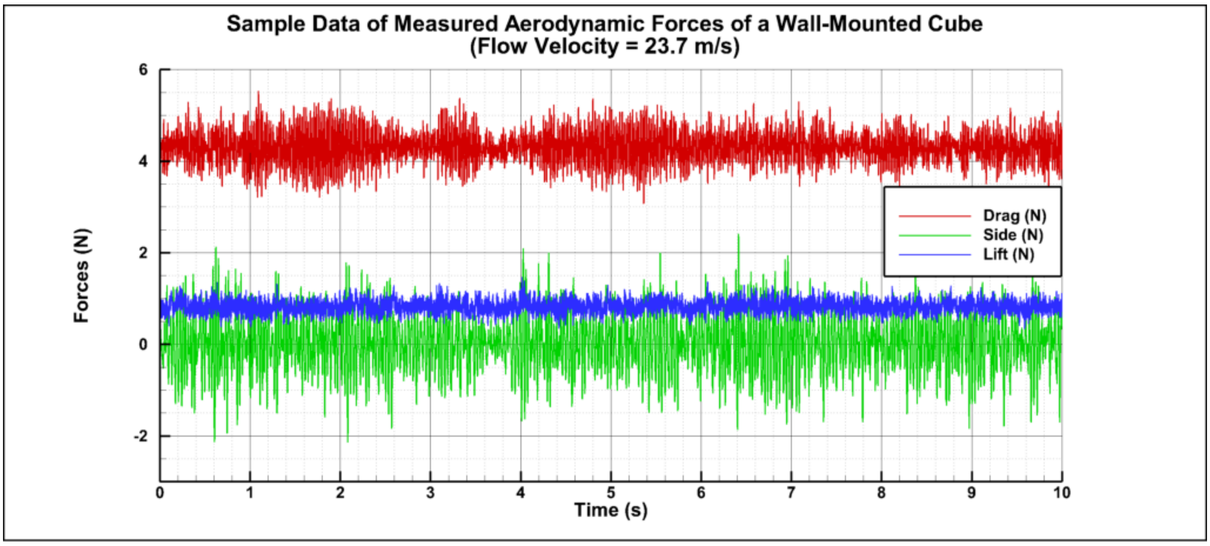

Figure 4.42: Sample data measured using a force transducer on the wall mounted cube.

The side forces has the largest fluctuations due to the vortices on both sides of the cube. These raw data values are then time averaged and converted into force coefficients on Table 4.14, which revealed that the measured lift forces on the third trial contained errors so the third trial was ignored.

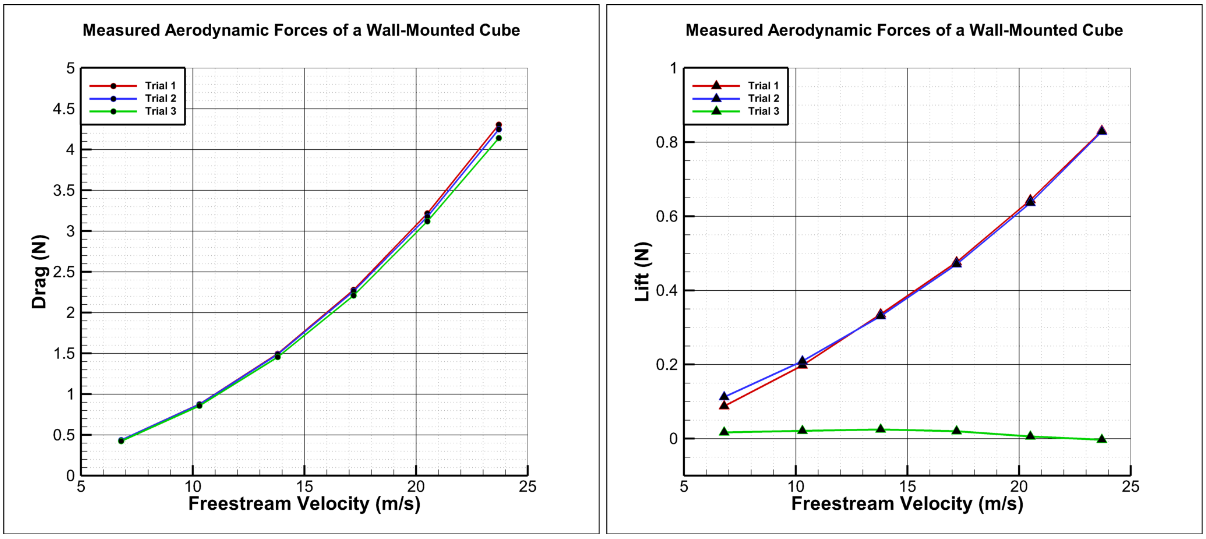

Figure 4.43: Measured forces against freestream velocity for 90 degree cube. Drag forces (left) and lift forces (right).

The trend in the valid results in Figure 4.43 suggests that the measured forces are proportional to the freestream velocity squared, which the curve represents. The measured force coefficients in Table 4.14 are in some agreement with the computed forces in Table 4.9.

Table 4.14: Time-averaged force measurements for wall-mounted cube at 90-degree angle at different wind tunnel speeds.

	Wind Tunnel Turbine RPM (Hz)	10	14	18	22	26	30
	Freestream Velocity (ms^{-1})	6.8	10.3	13.8	17.2	20.5	23.7
Trial 1	Drag (N)	0.437	0.876	1.495	2.279	3.216	4.306
	C_D	1.589	1.389	1.321	1.296	1.288	1.290
	Lift (N)	0.087	0.198	0.336	0.476	0.644	0.831
	C_L	0.318	0.313	0.297	0.271	0.258	0.249
	Side (N)	0.006	0.011	0.014	0.020	0.015	0.018
	C_S	0.022	0.018	0.013	0.011	0.006	0.005
Trial 2	Drag (N)	0.435	0.874	1.488	2.262	3.178	4.249
	C_D	1.583	1.387	1.315	1.287	1.272	1.273
	Lift (N)	0.112	0.209	0.330	0.470	0.636	0.828
	C_L	0.409	0.332	0.292	0.268	0.255	0.248
	Side (N)	0.002	0.005	0.009	0.010	0.018	0.013
	C_S	0.008	0.007	0.008	0.006	0.007	0.004
Trial 3	Drag (N)	0.423	0.858	1.455	2.209	3.119	4.141
	C_D	1.541	1.361	1.286	1.256	1.249	1.241
	Lift (N)	0.017	0.021	0.025	0.020	0.006	-0.003
	C_L	0.061	0.033	0.022	0.011	0.002	-0.001
	Side (N)	0.011	0.018	0.030	0.048	0.064	0.089
	C_S	0.041	0.028	0.027	0.027	0.026	0.027

The cube was then rotated 45 degrees along the y-axis and fixed into place where the procedure was repeated. The only changes from the 90 degree cube force measurement would be the projection area facing the flow as the air conditions in the lab were consistent and the operational speed settings of the wind tunnel remain the same.

Again, the results in Figure 4.44 and Table 4.15 showed that again, there was a set of results where the lift force on the third trial was not consistent with other trial results.

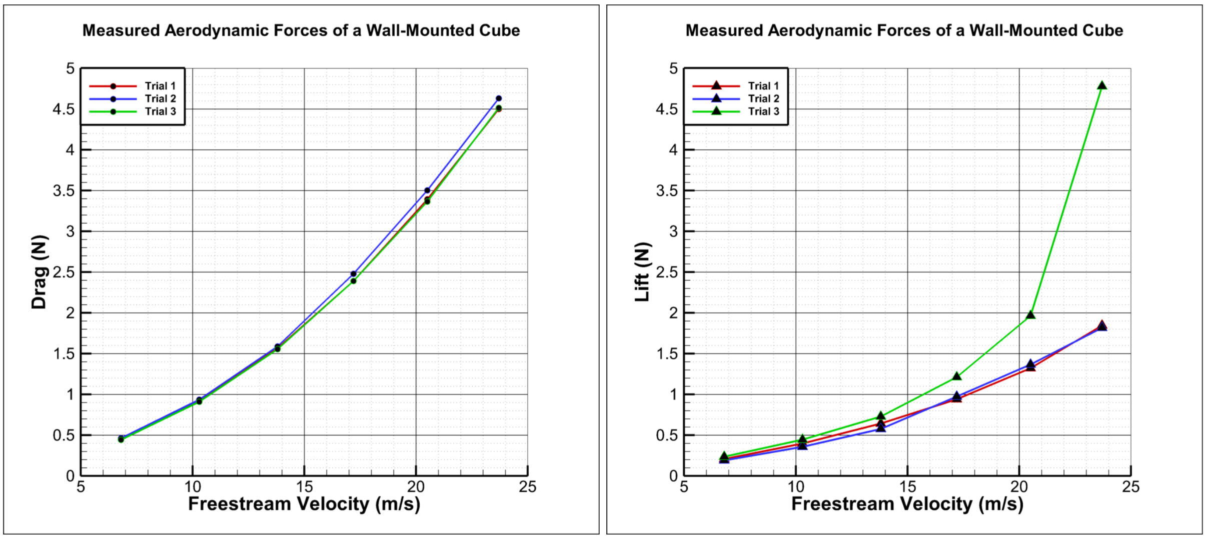

Figure 4.44: Measured forces against freestream velocity for 45 degree cube. Drag forces (left) and lift forces (right).

Table 4.15: Time-averaged force measurements for wall-mounted cube at 45-degree angle at different wind tunnel speeds.

	Wind Tunnel Turbine RPM (Hz)	10	14	18	22	26	30
	Freestream Velocity (ms^{-1})	6.8	10.3	13.8	17.2	20.5	23.7
Trial 1	Drag (N)	0.449	0.916	1.568	2.391	3.394	4.501
	C_D	1.146	1.020	0.973	0.955	0.954	0.947
	Lift (N)	0.206	0.399	0.642	0.941	1.323	1.845
	C_L	0.527	0.444	0.399	0.376	0.372	0.388
	Side (N)	0.094	0.187	0.321	0.486	0.697	0.850
	C_S	0.241	0.209	0.199	0.194	0.196	0.179
Trial 2	Drag (N)	0.462	0.935	1.589	2.478	3.502	4.631
	C_D	1.182	1.041	0.986	0.990	0.985	0.974
	Lift (N)	0.190	0.356	0.575	0.974	1.366	1.818
	C_L	0.484	0.397	0.357	0.389	0.384	0.382
	Side (N)	0.027	0.065	0.114	0.197	0.263	0.358
	C_S	0.069	0.072	0.071	0.079	0.074	0.075
Trial 3	Drag (N)	0.442	0.909	1.555	2.392	3.365	4.514
	C_D	1.130	1.012	0.965	0.955	0.946	0.950
	Lift (N)	0.236	0.446	0.728	1.211	1.964	4.779
	C_L	0.602	0.496	0.452	0.484	0.552	1.005
	Side (N)	0.004	0.027	0.025	0.118	0.042	0.236
	C_S	0.010	0.030	0.015	0.047	0.012	0.050

The likely cause of error in lift force measurements was due to the force transducer and adapter plates pocketed inside the cube rather than being attached to the cube's bottom surface, which could have affected its sensitivity in the vertical axis. Another source of error is having a small gap between the cube bottom surface and the wind tunnel platform as the cube is not wall mounted but fixed onto a hollow tube with adjustable heights.

In further comparison, the force measurements from the experiment in Tables 4.14 and 4.15 (Re = 200,000) were compared with the computational results in Table 4.9 (Re = 330,000). These cases both have a high Reynolds Number, which would imply the force coefficient should be similar. There are some agreement between these computational and experimental results, particularly side and drag coefficients.

For future reference the experiment should be repeated with the force transducer attached to the bottom surface of the cube instead of pocketed. If clarified, the experiment can be repeated at elevated cube and onto different shapes including hemisphere and ballast at a fixed volume.

In the next section, CFD analysis was applied to a hemisphere in similar conditions to the cube. Results are compared with experimental and computational results of Tavakol et al. (2014).

4.4 Applying Steady and Unsteady RANS for Flow over a Hemisphere

Hemispheres were studied alongside cubes since ballast shapes are more spherical than cubic. Both steady and unsteady simulations were performed with a structured mesh. The domain set-up was similar to the cubic study, as is shown in Figure 4.45:

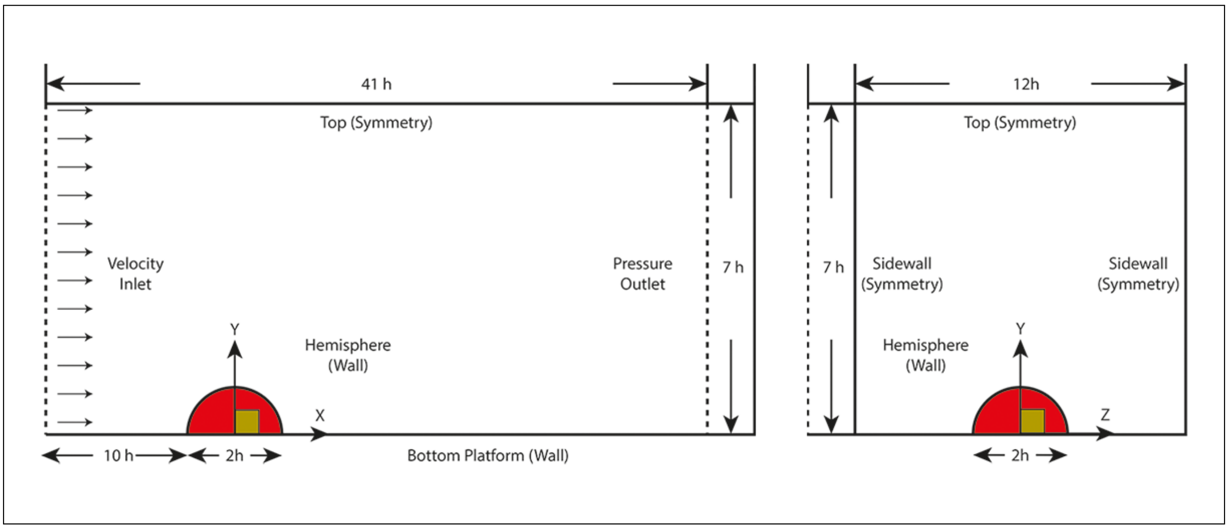

Figure 4.45: Domain system design of a wall-mounted hemisphere (not to scale).

The hemisphere has a radius $h = 0.03\ m$. Pointwise meshing software was used to design the structured grid, with the domain split into multiple grid blocks. The mesh was generated around the hemisphere by using multiple blocks expanding outwards towards the domain. The lowest quality cells are located on the ground due to large aspect ratio related to the y-plus to resolve the boundary layer especially for the k-ω model. The mesh cell count for all simulations was 9.0 million, and refined around solid boundaries and turbulence regions as illustrated in Figure 4.46.

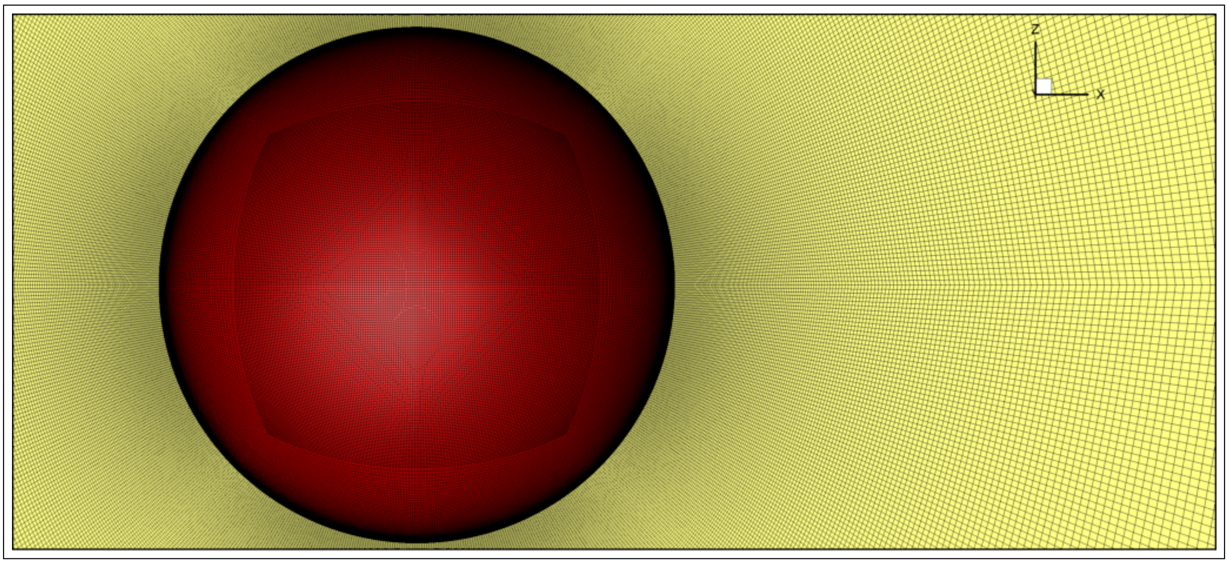

Figure 4.46: Mesh layout of the hemisphere using a structured grid configuration.

The projection area of the hemisphere was approximately 0.00141372 m^2. The wall-mounted hemisphere was analysed using both unsteady and steady models of Realisable k-ε and SST k-ω. To validate the case, initially the freestream velocity was set to 10 ms^{-1}, making the Reynolds number approximately 40,000 since Tavakol et al. (2014) experiment used Reynolds numbers of 36,000 and 64,000. The resulting forces of the hemisphere are the following given in Table 4.16:

Table 4.16: Time-averaged force coefficients for the hemisphere between 0.2 to 0.3 seconds flow time.

Subject	$\bar{C}_D$	$\bar{C}_L$	$\bar{C}_S$
RANS Realisable k-ε	0.278	1.063	0.000
RANS SST k-ω	0.393	0.086	-0.022

Looking at the pressure coefficient distribution across the hemisphere surface (Figure 4.47) the pressure distribution is very sensitive to the Reynolds number and smooth hemisphere, which would affect the forces.

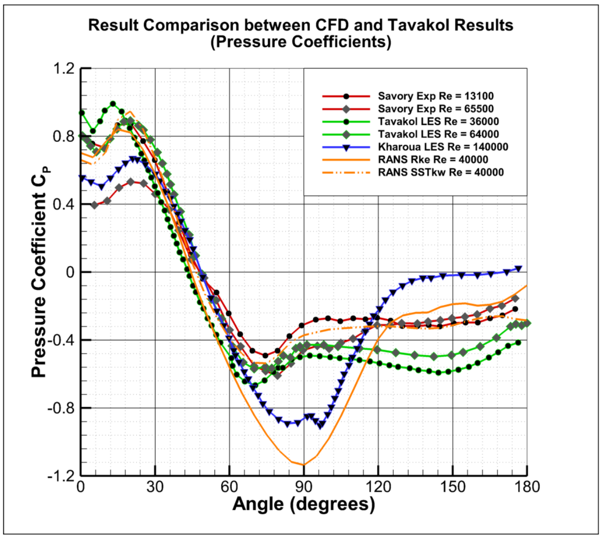

Figure 4.47: Mean Pressure Coefficient distribution across the hemisphere surface at Re = 40,000.

The static pressure contours is shown in Figure 4.48. The two flow separation bubbles, are smaller than for the cube, demonstrating that the length of the flow reattachment depends on the geometry and the Reynolds number.

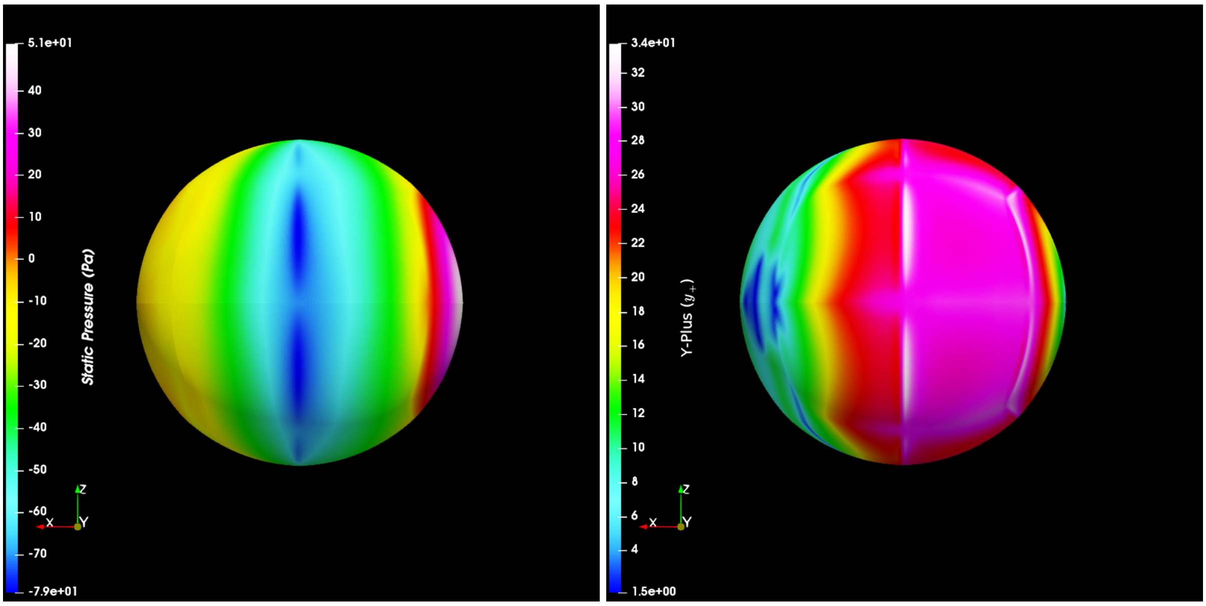

Figure 4.48: Plan view of the Static Pressure Field around the hemisphere at Re = 40,000 (left) and the Y-Plus (right). SST k-ω turbulence model.

Both RANS models were compared with Tavakol et al. (2014) results using LES model in Figure 4.50. Clearly at a similar Reynolds number, the main cause of error is the turbulence model used to calculate the separated flow where SST k-ω is in better agreement than Realisable k-ε.

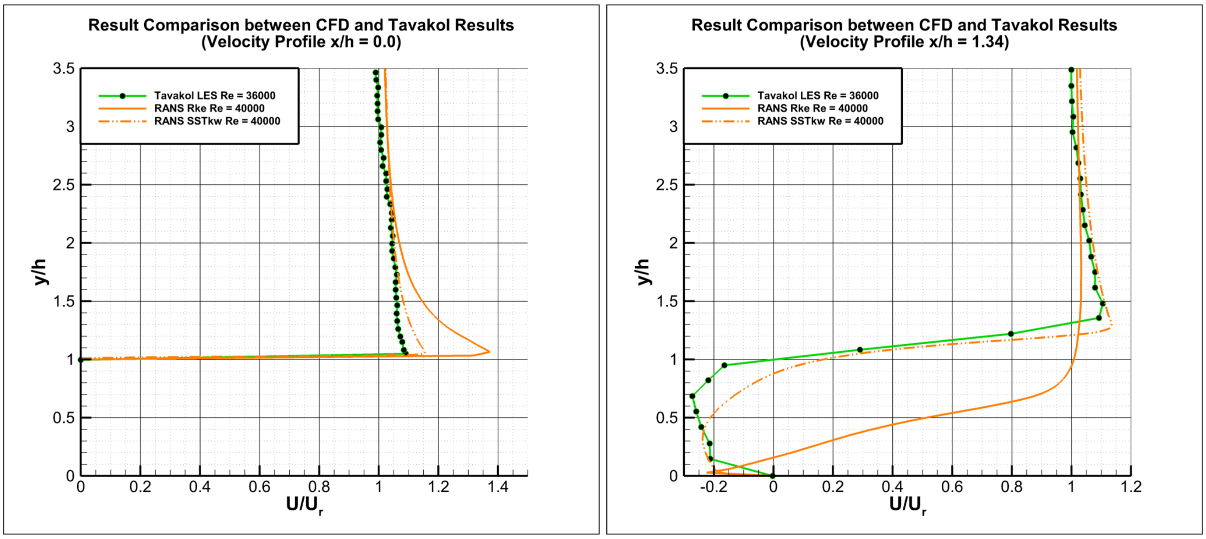

Figure 4.49: Velocity profiles over the hemisphere at x/h = 0.0 (left), x/h = 1.34 (right). Reduced Reynolds number 40,000.

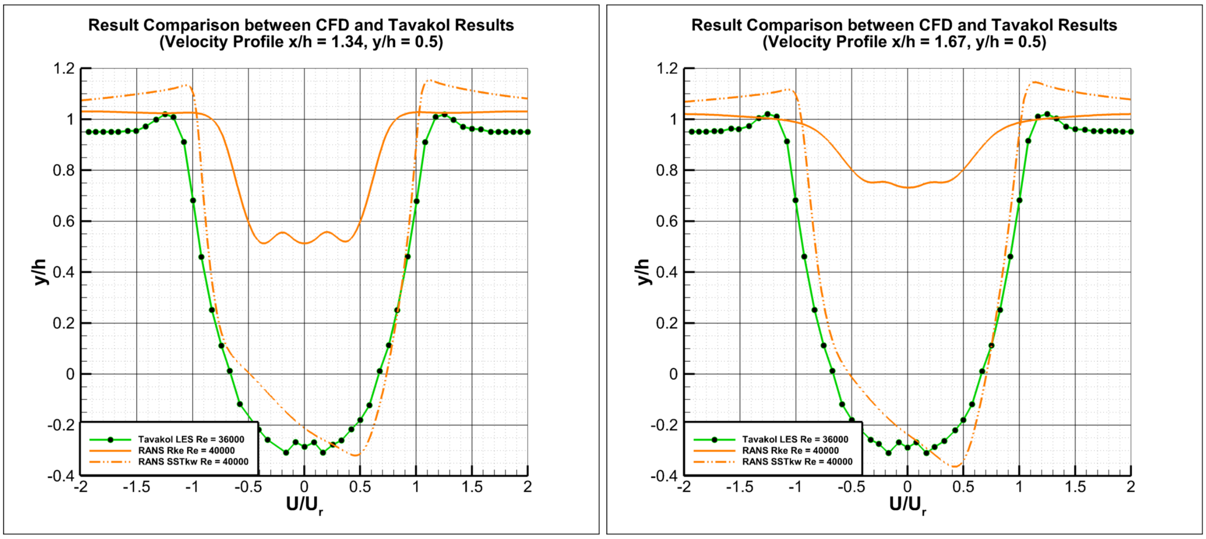

Figure 4.50: Spanwise velocity profiles at x/h = 1.34, y/h = 0.5 (left). Spanwise velocity profiles at x/h = 1.67, y/h = 0.5 (right). Reduced Reynolds number 40,000.

The computational studies was then repeated with a refined mesh with the freestream velocity set to 83.3 ms^{-1}. Both steady RANS and Unsteady DES has been used from 0.0 to 0.3 seconds where from 0.2 to 0.3 seconds, variables are time averaged for further analysis. The mean force coefficients are summarised and compared in Table 4.17:

Table 4.17: Time-averaged force coefficients for the hemisphere between 0.2 to 0.3 seconds flow time.

Subject	$\bar{C}_D$	C_{Drms}	$\bar{C}_L$	C_{Lrms}	$\bar{C}_S$	C_{Srms}
RANS Realisable k-ε	0.159	N/A	0.071	N/A	-0.048	N/A
RANS SST k-ω	0.264	N/A	0.199	N/A	0.111	N/A
DES Realisable k-ε	0.140	0.140	0.007	0.010	-0.001	0.003
DES SST k-ω	0.270	0.270	0.317	0.328	0.009	0.088

The forces given by the two turbulence models are quite different from each other, as is the static pressure distribution in Figure 4.52. Tavakol et al. (2014) do not give data on forces or pressure distribution on the hemisphere surface at a high Reynolds number.

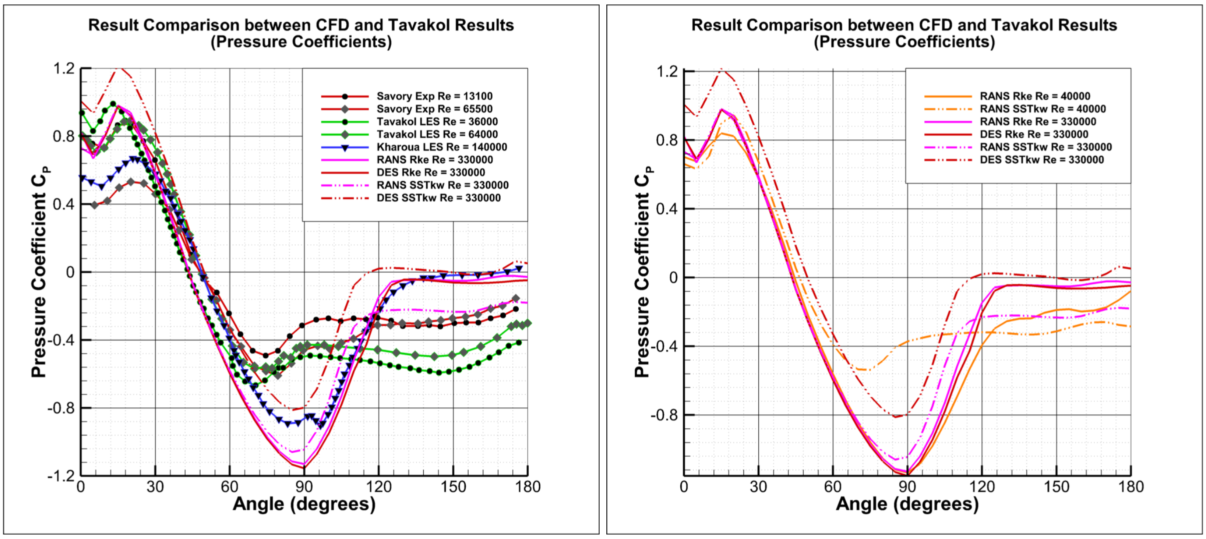

Figure 4.51: Mean Pressure Coefficient distribution across the hemisphere surface at different Reynold numbers.

However, the lift and drag coefficients of the hemisphere are smaller than the cubic studies due to its shape. Even the cube at 45 degrees experiences more drag than the hemisphere, although in some cases the lift force is similar.

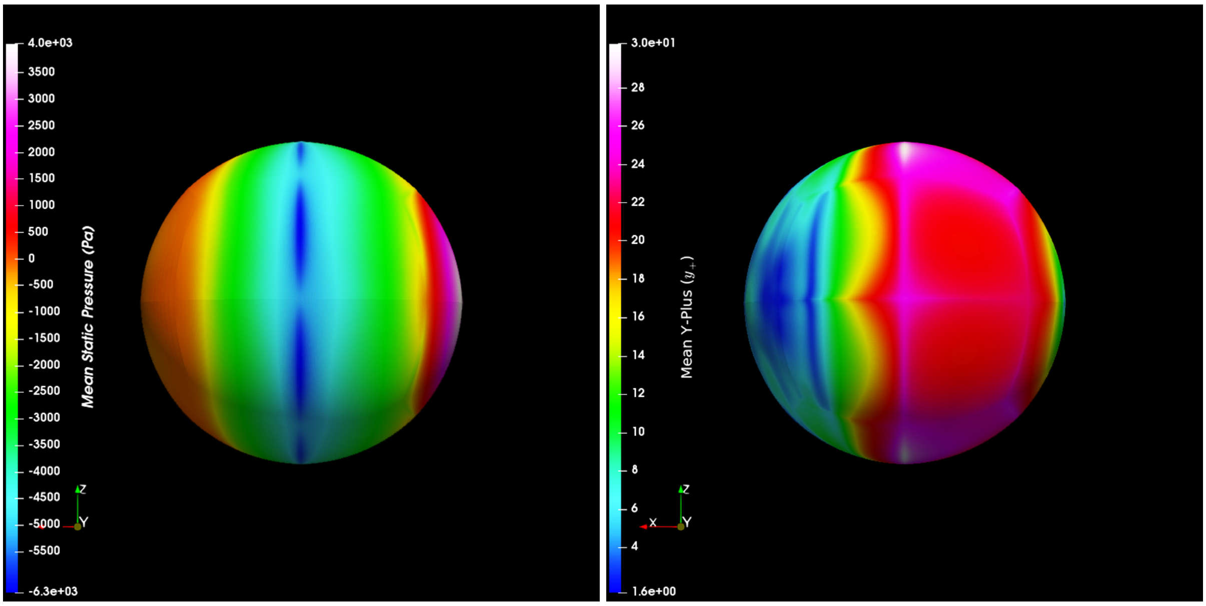

Figure 4.52: Mean static pressure field around the hemisphere at Re = 330,000 (DES) at 0.3 seconds at plan view (left) and the y-plus contour for SST k-ω (right).

Velocity profiles from the CFD studies are compared with the computational results produced by Tavakol et al. (2014) in Figures 4.53 and 4.54; DES is in better agreement than RANS. However, both models over-predicted the velocity output during separation, owing to the Reynolds number ($Re \approx$ 330,000) being much higher than Tavakol et al. (2014) ($Re \approx$ 36,000).

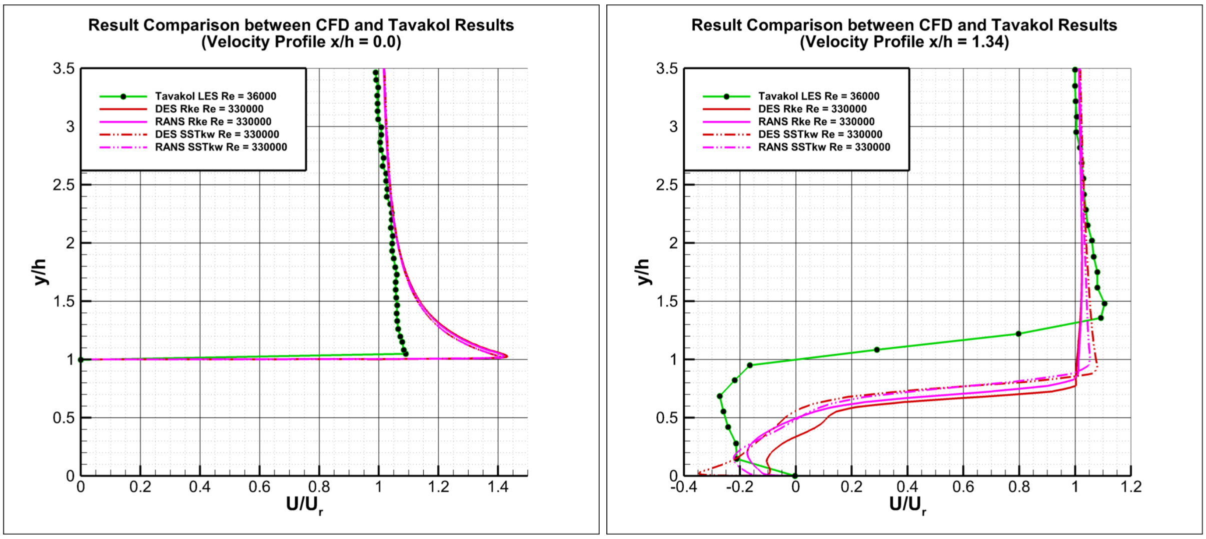

Figure 4.53: Quantitative comparison of velocity profiles over the hemisphere at x/h = 0.0 (left), x/h = 1.34 (right).

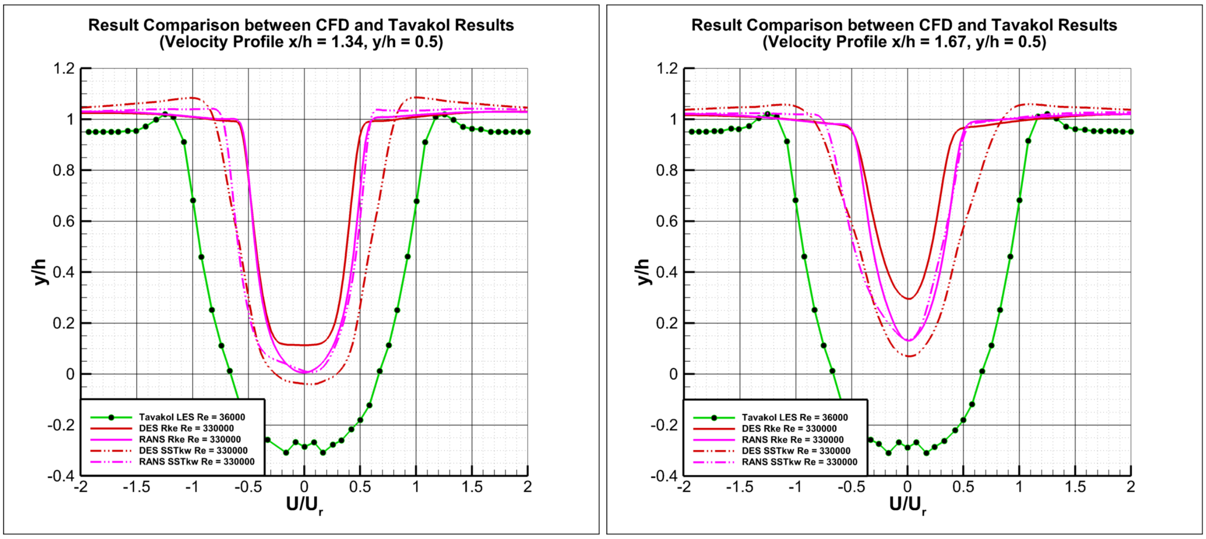

Figure 4.54: Spanwise velocity profiles at x/h = 1.34, y/h = 0.5 (left). Spanwise velocity profiles at x/h = 1.67, y/h = 0.5 (right).

Therefore for the hemisphere study, increasing the Reynolds number would influence the size of flow separation. Streamline plots (Figure 4.55) show a horseshoe vortex around the hemisphere similar to that for the cube, and two large vortices behind the hemisphere. The biggest velocity magnitude was located at the apex of the hemisphere.

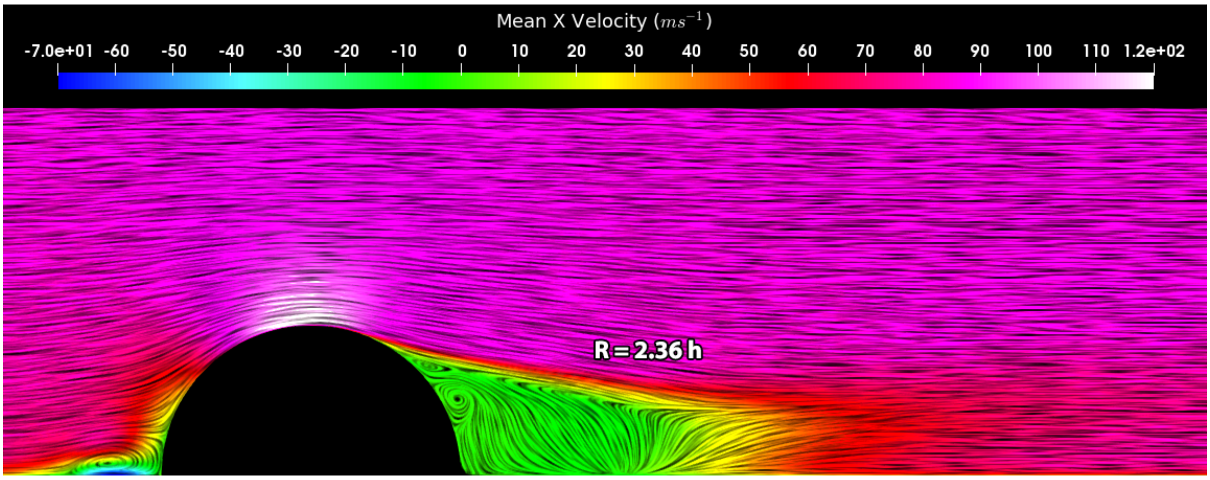

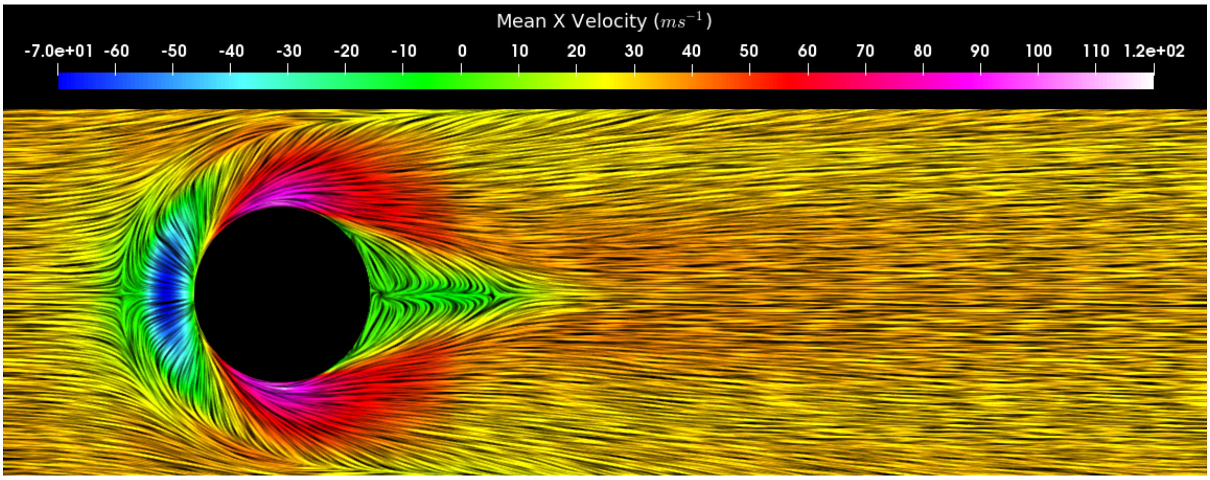

Figure 4.55: Streamline path of the mean velocity over the hemisphere from 0.2 to 0.3 seconds. (a) Side view at symmetry plane z/h = 0.0. (b) Top view of streamlines y/h = 0.0.

The point of separation of flow begins at x/h = 0.0 and its size of the recirculation for Re = 330,000 is approximately 2.36 h from the separation point. Iso-surfaces of the Q-Criterion and turbulence kinetic energy contour in Figure 4.56 shows a reduction in vortices in comparison to the cube.

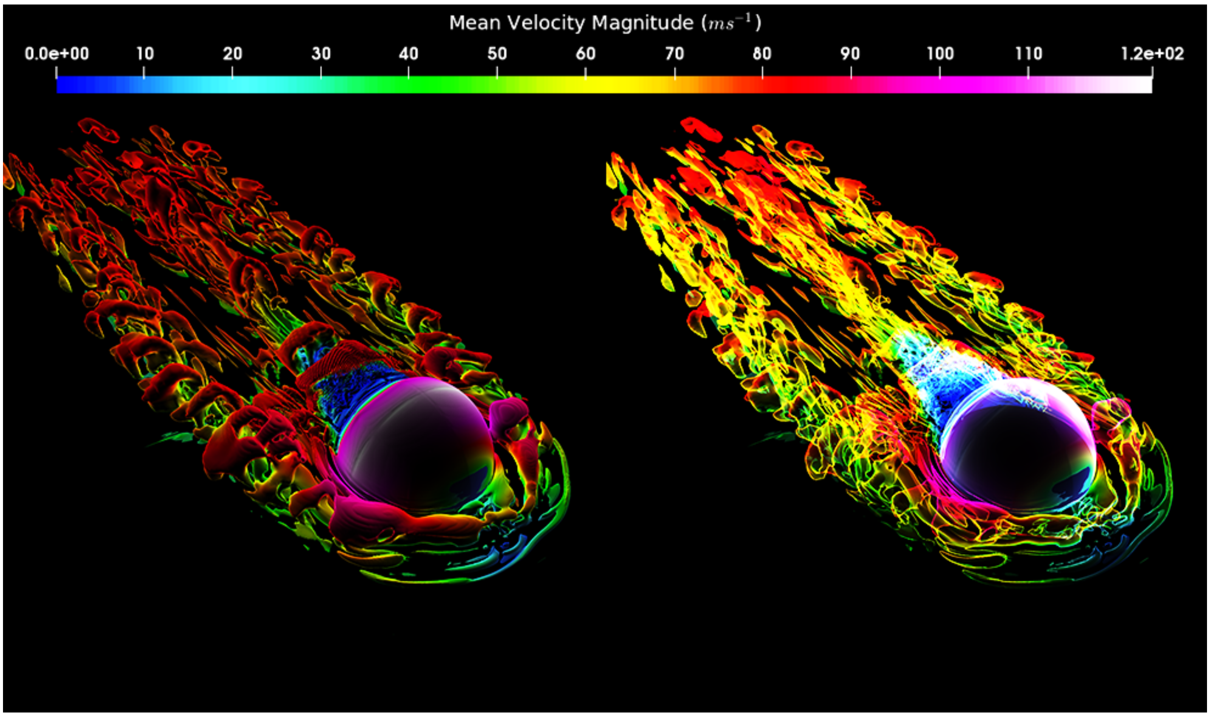

Figure 4.56: Iso-surface of the Q-Criterion at 330,000 coloured by the mean velocity magnitude. Wall-mounted hemisphere. Solid iso-surfaces (left) and transparent vision (right).

Like the cubic studies, the front and side surfaces is surrounded by a horseshoe vortex with trailing vortices in the streamwise direction. Shear layer vorticity is found directly behind the hemisphere where its length is much smaller than the vortices around the cube.

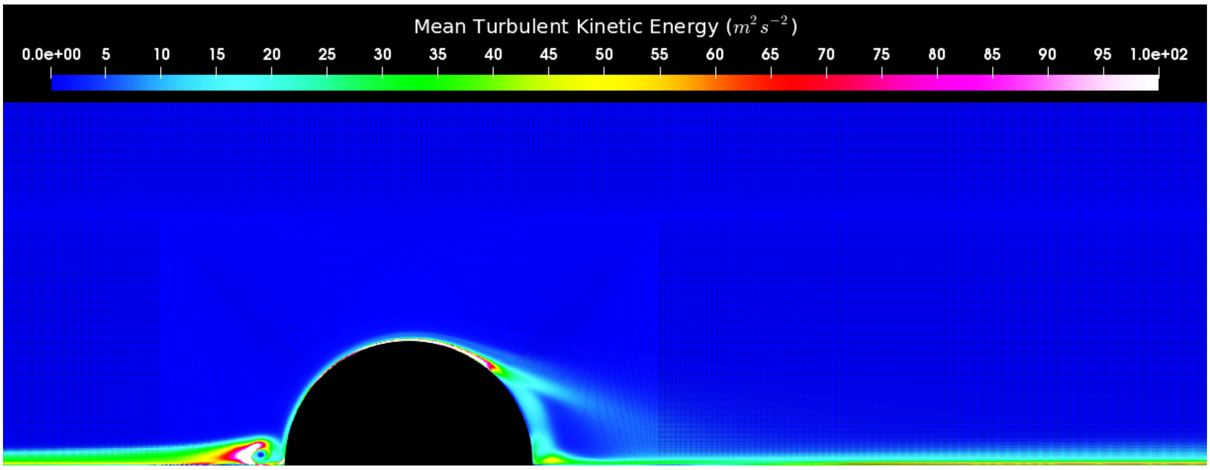

Figure 4.57: Streamwise view of the turbulent kinetic energy contour at z/h = 0.0. Wall-mounted hemisphere particle in contact with the ground.

The following conclusions may be drawn by comparing results for the hemisphere and the cube;

- Rounder shapes are less affected by drag than flat surfaced objects.
- The object experiences more lift and drag if it has a flat surface directly facing the flow.
- When a particle is elevated, aerodynamic effects are reduced.
- Particle orientation and shape can influence whether the ballast would be displaced by aerodynamic loads.

Having validated these cases and CFD techniques, the next objective was to evaluate the aerodynamic forces on fourteen different ballast shapes at four different orientations where the projected area varies due to its irregular shape.

4.5 Unsteady RANS simulations for typical ballast particles

The final part of this study involves the CFD analysis of fourteen realistic ballast shapes to determine the aerodynamic forces for each particle at four different orientations. Sizes of ballast grains vary, with large ballast generally on the top and smaller ballast underneath. The average sizes of large and small ballast are approximately 50 mm and 30 mm length respectively since the sieve sizes used for rail ballast are between 15 mm to 65 mm.

For the CFD analysis, fourteen different ballast shapes will be scaled to a fixed volume representative of small and large ballast, which was determined by measuring the average volume of twenty small and large ballast stones using a Eureka Can.

4.5.1 Volume measurement of ballast particles

The mean density and volume of granite ballast stones was determined by measuring the mass and volume of displaced water using a Eureka Can, pictured in Figure 4.58:

Figure 4.58: Eureka Can Experiment to measure volume of twenty large and twenty small granite particles.

Twenty granite stones of two different sizes were acquired, cleaned, labelled and weighed using an electronic balance (Oxford Balance F12102) when dry. The Eureka Can was filled to the point where water displacement would be caused by placing the ballast grain from inside the Eureka Can, and the volume of water displaced would represent the volume of the ballast. Once all twenty ballast grains had been placed in the can, the volume of water was recorded along with the summarised weight of ballast and then dried for the next day to repeat the experiment. The equation used was Equation 4.10:

$$\rho_p = \frac{m_p}{V_p} \tag{4.10}$$

where the ballast particle density ρ_p is the ratio of particle mass m_p and its volume V_p. Three trials were completed and summarised in Appendix B on Tables B.1 to B.3 and the average on Table B.4. A correction factor from BS 1377-5 (1990) was applied to the measured water density based on the waters temperature.

The mean bulk ballast density of granite was found to be 2,650 kg/m^3, which is within the expected range of granite ballast for both sizes. The average volume of large and small ballast grains was rounded off to 0.00006 m^3 and 0.000013 m^3 respectively. Therefore, the ballast models will be scaled to these volumes after simplification.

4.5.2 CFD Modelling Design and Setup

Having established the mean volume of large and small ballast, the computational domain was set up with the ballast particle wall-mounted at the centre of the domain pictured in Figure 4.59:

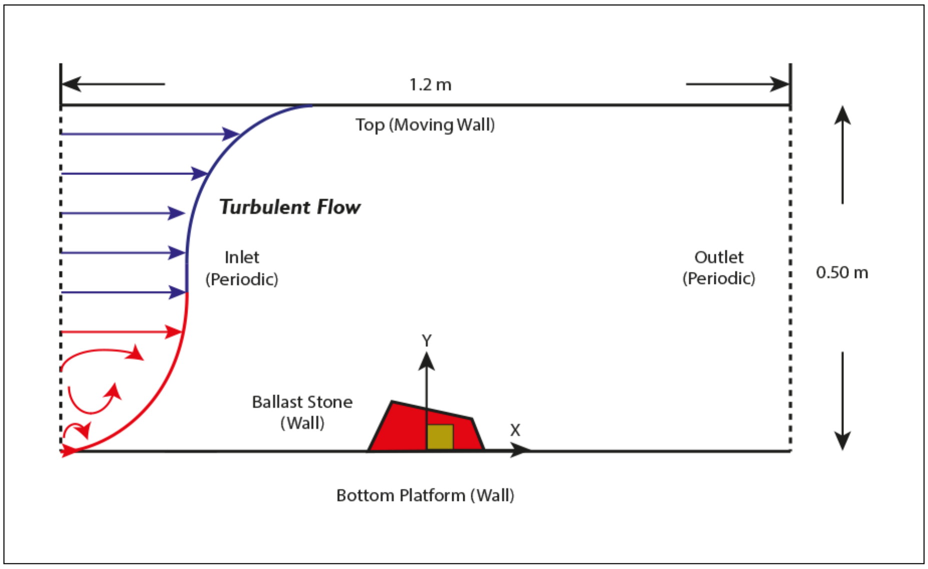

Figure 4.59: Domain design for the ballast particle case studies (not to scale).

The height of the domain was 0.5 m, which represents a typical distance from the ballast surface to the underbody of the train. The lengths along the x and z-axes are sufficient to allow flow reattachment. For each grain orientation, the inlet and outlet boundary conditions were rotated around the stone shape (Figure 4.60), which changes the projected area of the stone.

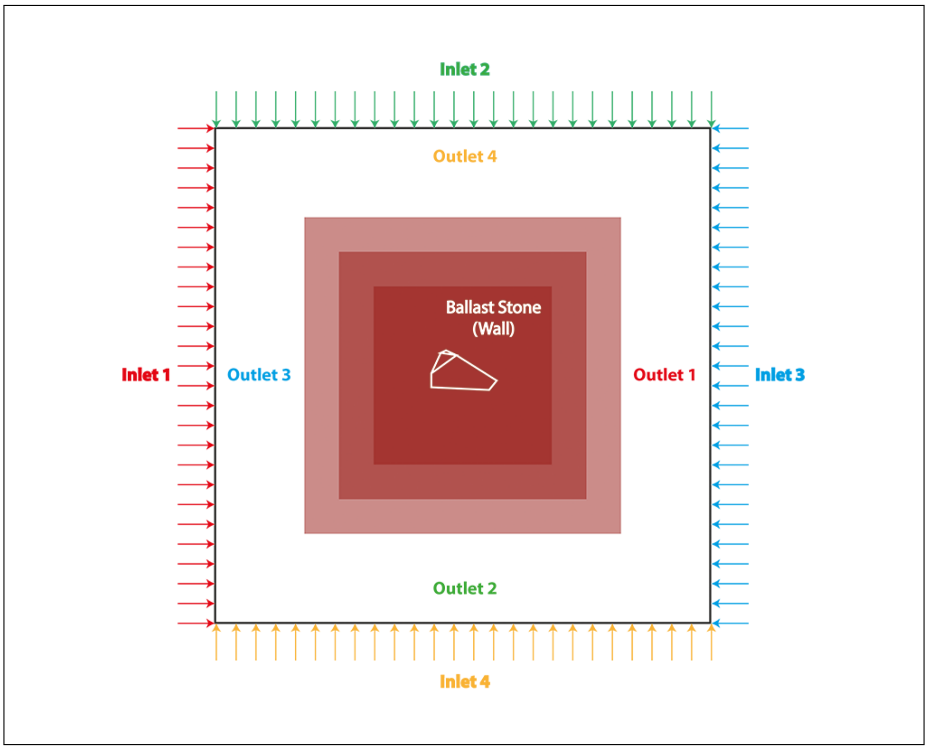

Figure 4.60: Rotation of boundary rotations for four different angles of attack.

The top part of the domain becomes a moving wall at speeds representative of the train to generate an S-shaped boundary layer profile as shown in the channel flow study in Section 5.2.

The inlet and outlet boundary conditions where periodic to allow flow development with a fixed mass flow rate to speed up the flow development. For moving wall speed of 120 ms^{-1}, $U_x = 0$ at $y = 0$ m, $U_x \approx 60$ at $y = 0.25$ m and $U_x = 120$ at $y = 0.5$ m.

4.5.3 Original modelling and meshing procedure

The ballast shapes were used for a study of the mechanical behaviour (Ahmed et al., 2015), and were generated numerically by slicing around a sphere and creating curved edges and faces to obtain similar shapes to the real ballast stones shown in Figure 4.61:

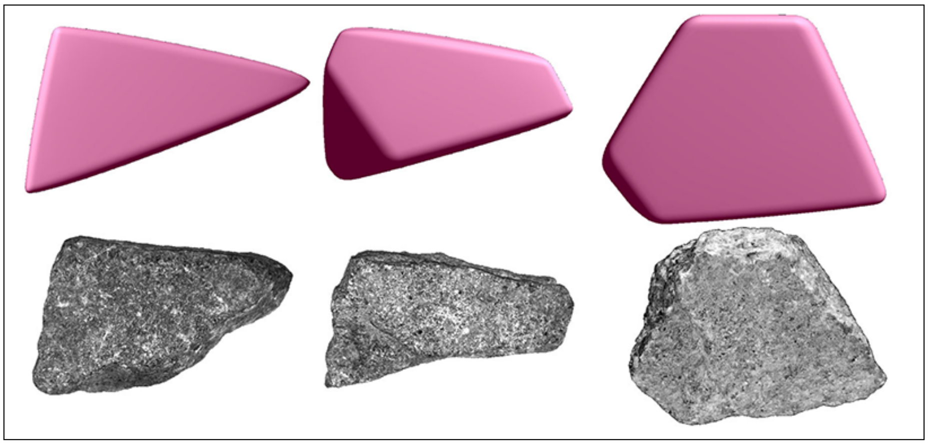

Figure 4.61: Example numerical ballast particle with its real counterpart (Ahmed et al., 2015).

A selection of shapes was used for this study (Figure 4.62), having different length parameters, changing the geometry.

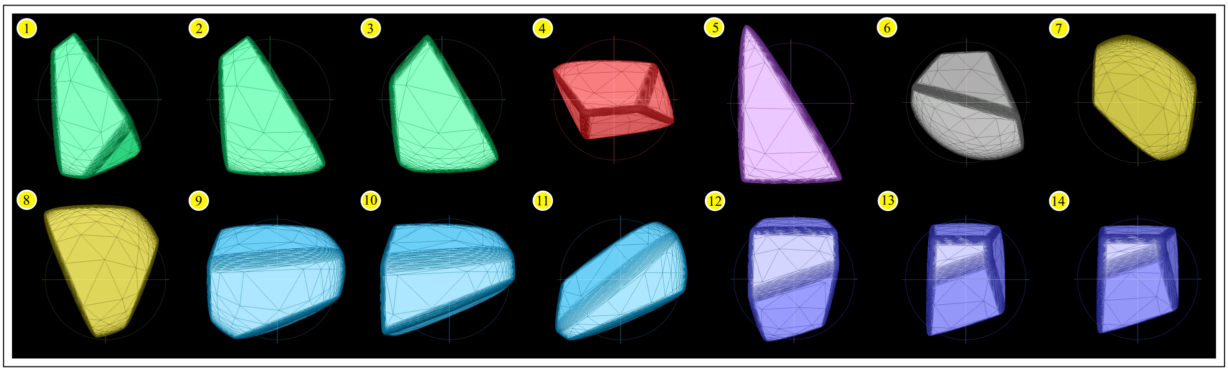

Figure 4.62: Original object (.obj) files of the fourteen particles before modifications. Created by John Harkness (Ahmed et al., 2015).

The original mesh files are in .obj format with more than 20,000 faces. For easier meshing, the particle shapes needed to be simplified. The number of faces was reduced and the faces and edges smoothed out using features in Solidworks. The geometry was then converted into the .stl format for compatibility with AnSys. In this way, the mesh was transformed into a solid object. Figure 4.63 shows the reduction of the particle caused by reducing the number of faces while retaining the geometry as much as possible.

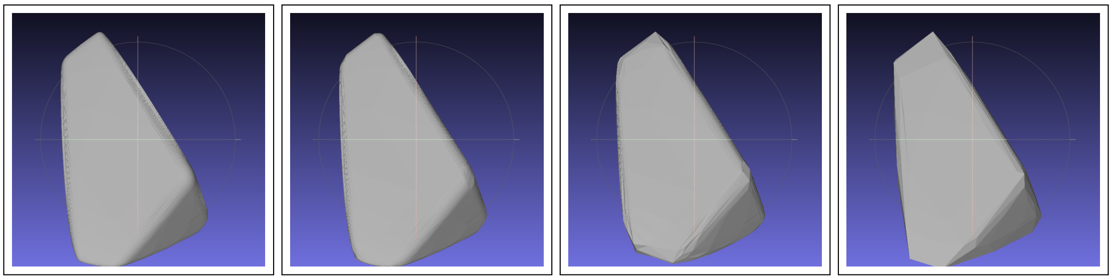

Figure 4.63: Quality comparison of particle model with 20,380 → 5,120 → 1,280 → 320 faces (left to right).

The particle was reduced to 320 faces and exported into Solidworks. The faces were flattened using a slicing tool and the edges were rounded using a fillet tool. The conversion process in Figure 4.64 shows the particle transformation before meshing.

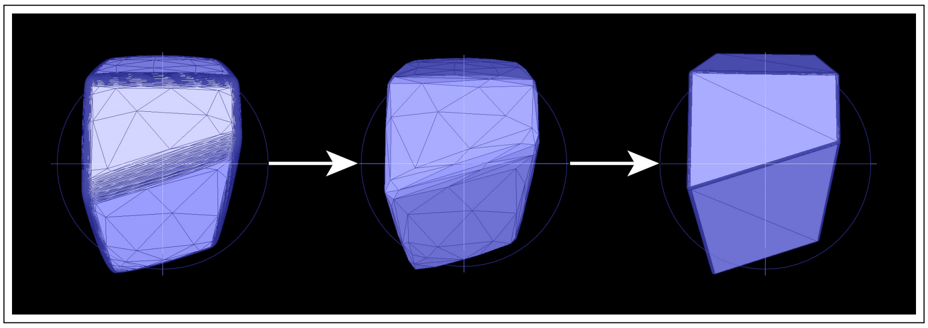

Figure 4.64: Conversion process of a single particle to increase succession in meshing (Particle No.12).

These changes would affect the original shape marginally. The process was repeated for all fourteen particles as shown in Figure 4.65. The volumes were then scaled to two different sizes and saved in .stl format for meshing.

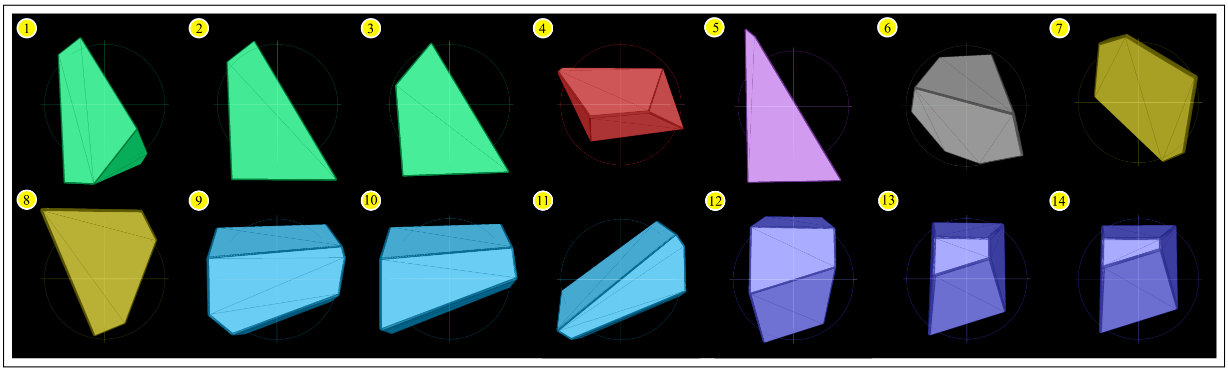

Figure 4.65: Modified version of the fourteen particles before exporting into AnSys meshing software.

The characteristics of the ballast shapes were measured before and after modifications and were compared prior to computational analysis. This involves finding the best fit ellipsoid and measuring the dimensions of the model to calculate the aspect ratios as described in Section 3.5. This was implemented by using a script used in Ahmed et al. (2015) research, which evaluates every combination of points in the model and calculates the radii of the ellipsoid.

This approach was applied to both the original and the modified models (Figure 4.66) producing different outcomes since the number of points are different and the surfaces were flattened.

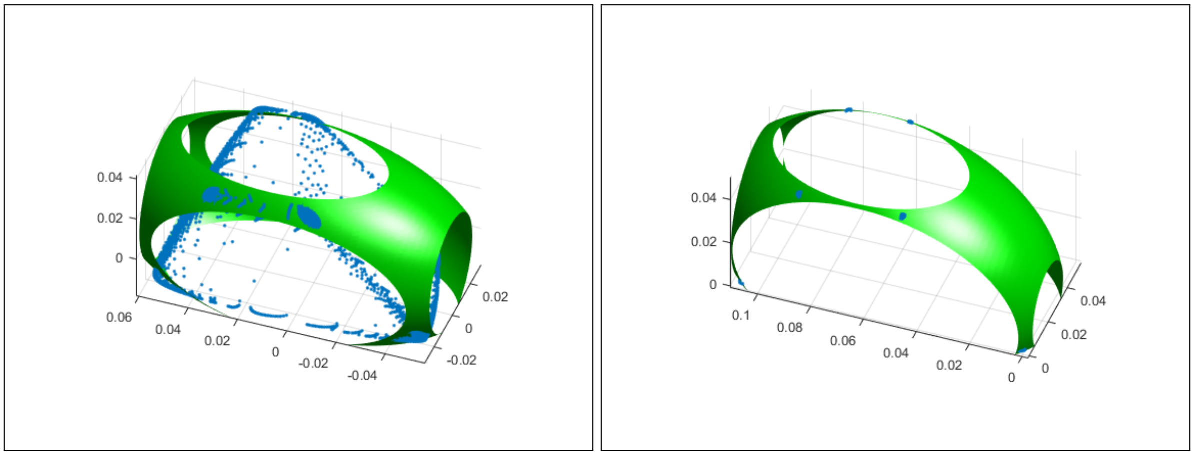

Figure 4.66: The ellipsoid fitting for Particle11. Using original models (left) and the modified version (right).

The dimensions (S, I and L) were quantified and the aspect ratios I/L, S/I and S/L was calculated to determine the classifications of each ballast shape on Table 4.18.

Table 4.18: Classification of the modified ballast stones determined by dimensional ratios.

	Modified Version				**Original Version**			
Name	**I/L**	**S/I**	**S/L**	**Classification**	**I/L**	**S/I**	**S/L**	**Classification**
Particle01	0.65924	0.52795	0.34805	Flat-Columner	0.61926	0.54209	0.33570	Flat-Columner
Particle02	0.70337	0.61006	0.42910	Flat	0.55943	0.36085	0.20187	Flat-Columner
Particle03	0.72385	0.62053	0.44917	Flat	0.79017	0.32699	0.25838	Flat
Particle04	0.83907	0.80187	0.67283	Spherical	0.87570	0.53335	0.46705	Flat
Particle05	0.32128	0.87649	0.28160	Columner	0.44064	0.69862	0.30784	Columner
Particle06	0.78487	0.55322	0.43421	Flat	0.88456	0.58637	0.51869	Flat
Particle07	0.86095	0.50572	0.43540	Flat	0.83303	0.52116	0.43414	Flat
Particle08	0.91994	0.59922	0.55125	Flat	0.73641	0.43555	0.32074	Flat
Particle09	0.86752	0.31557	0.27376	Flat	0.90622	0.26727	0.24221	Flat
Particle10	0.87481	0.45289	0.39620	Flat	0.80393	0.24241	0.19488	Flat
Particle11	0.83534	0.25979	0.21701	Flat	0.78348	0.23874	0.18704	Flat
Particle12	0.67950	0.95518	0.64905	Spherical	0.54039	0.99391	0.53710	Columner
Particle13	0.74712	0.87946	0.65706	Spherical	0.72180	0.86686	0.62569	Spherical
Particle14	0.56599	0.83537	0.47281	Columner	0.71249	0.80055	0.57039	Spherical

which was plotted onto a Zingg diagram (Figure 4.67), which reveals a majority of particles are either Spherical or Flat in both versions.

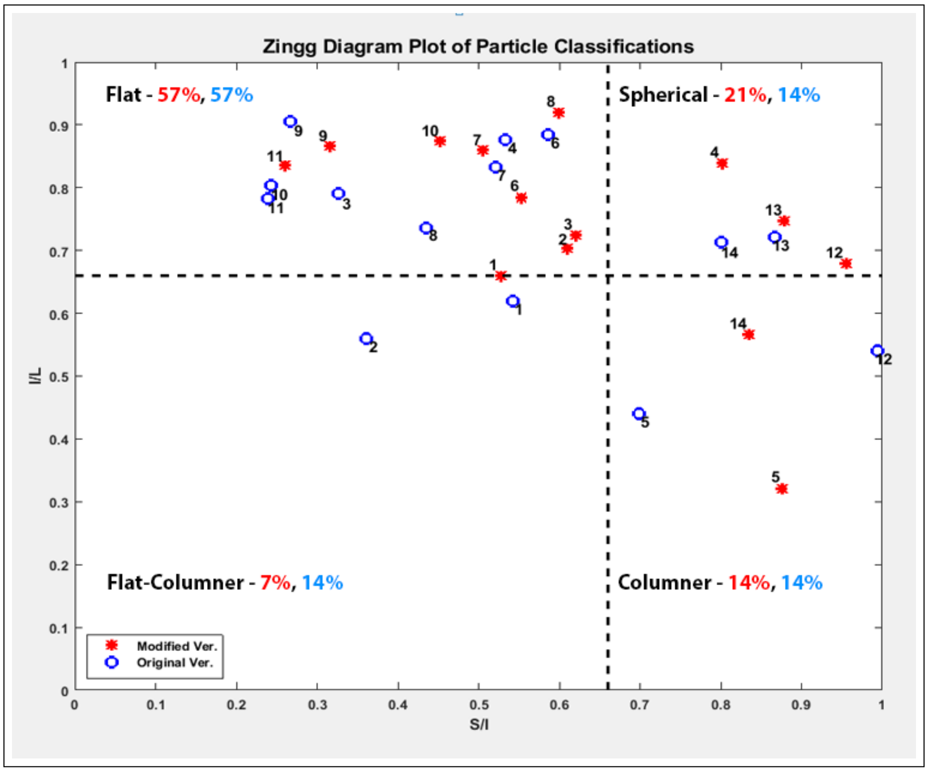

Figure 4.67: A zingg diagram of the ballast stones classifications. Comparing original models to the modified versions.

Due to the modifications applied to the original ballast, the aspect ratios have changed where some of which have caused the classifications to change in doing so. Looking at the overall outcome, there is at least one particle in each classification which is sufficient enough to see if there is a link between ballast shape and its aerodynamic performance. The projection area of each ballast grain at different angles are summarised on Table 4.19.

Table 4.19: Calculated projection areas of ballast stones at different angles (m^2).

	Particle01	**Particle02**	**Particle03**	**Particle04**	**Particle05**	**Particle06**	**Particle07**
0°, 180°	0.00149	0.00170	0.00151	0.00110	0.00142	0.00180	0.00200
90°, 270°	0.00187	0.00138	0.00159	0.00240	0.00227	0.00159	0.00226
	Particle08	**Particle09**	**Particle10**	**Particle11**	**Particle12**	**Particle13**	**Particle14**
0°, 180°	0.00190	0.00125	0.00108	0.00135	0.00131	0.00148	0.00160
90°, 270°	0.00159	0.00101	0.00136	0.00152	0.00184	0.00176	0.00172

The projection area alongside with the shape classification will be compared with the aerodynamic results to discover any links between them.

For these shapes, an unstructured grid was used with an inflation layer around the particle. Refinement boxes were placed around the particle for better cell size transition. The cell count was approximately 6 million polyhedra cells, which provided good orthogonal mesh quality (Figure 4.68).

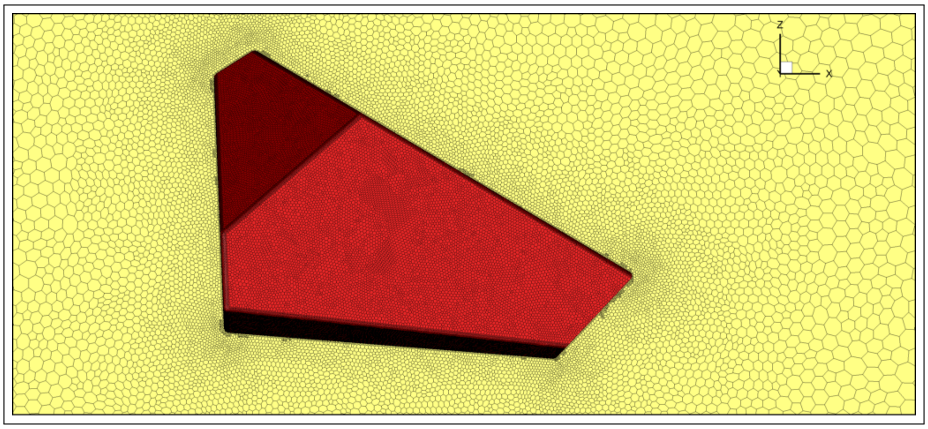

Figure 4.68: Mesh cell conversion from triangular to polyhedra, reducing cell count and improving skewness and orthogonality. Viewpoint facing underneath bottom surface of mesh.

The problem set-up and boundary conditions were similar to the previous studies, and SST k-ω was used throughout. No wall roughness was applied to the ground and the solution algorithm used was SIMPLEC. For the reference values, the area values were calculated using the report feature in AnSys Fluent to find the projection area, used to determine the force coefficients.

4.5.4 Summary of flow around ballast case studies

A grid depending study was carried out on one of the ballast shapes to find an ideal cell count for application to the other shapes (Table 4.20).

Table 4.20: Grid independent study of a ballast shape.

Subject	**Cell Count (Poly)**	**Face Cell Size** (m)	$\bar{D}$	$\bar{L}$	$\bar{S}$
Particle 01	5.6 million	0.00500	1.395	1.731	-0.106
Particle 01	4.0 million	0.00550	1.328	1.722	-0.104
Particle 01	1.9 million	0.00600	1.221	1.580	-0.103

From 2.0 to 6.0 million cells, the calculated forces changed slightly. To guarantee a detailed mesh, the targeted cell count was between 17 to 18 million triangular cells for each shape. The aerodynamic force coefficients were determined for each particle and direction (56 cases) using URANS. The study was repeated using DES for up to six cases with the largest lift and drag forces. Furthermore, the selected ballast shapes will be scaled down to smaller volume and repeated to observe its change in forces.

Unsteady RANS (SST $k-\omega$) Results

The mean drag ($\bar{D}$) and lift ($\bar{L}$) forces for each particle are summarised on Tables 4.21 and 4.23 respectively.

Table 4.21: Mean drag force comparison between individual ballast shapes at different angles. Turbulence model Unsteady RANS SST k-ω utilised. Time-averaged from 0.4 to 0.5 seconds.

$\bar{D}$							
	Particle01	**Particle02**	**Particle03**	**Particle04**	**Particle05**	**Particle06**	**Particle07**
0°	1.395	1.643	1.259	0.523	1.637	1.902	1.899
90°	1.434	0.828	1.495	2.909	2.408	1.123	2.137
180°	1.106	1.274	1.087	1.047	1.617	1.653	3.020
270°	2.000	1.248	1.573	2.527	3.305	1.872	3.357
$\bar{D}$							
	Particle08	**Particle09**	**Particle10**	**Particle11**	**Particle12**	**Particle13**	**Particle14**
0°	1.795	0.605	0.645	0.884	1.261	1.724	1.976
90°	1.630	0.526	0.885	1.143	1.885	1.588	1.461
180°	3.483	0.399	0.687	0.855	1.048	1.601	1.926
270°	0.979	0.446	0.400	1.251	1.879	1.458	1.612

Highlighted in red in Table 4.21 are the top five cases, which experiences the most drag force. These three shapes are amongst the flat or columnar classification with the largest projection areas. For better comparison, the force coefficients were also summarised in Table 4.22

Table 4.22: Mean drag force coefficients between individual ballast shapes at different angles. Turbulence model Unsteady RANS SST k-ω utilised. Time-averaged from 0.4 to 0.5 seconds.

C_D							
	Particle01	**Particle02**	**Particle03**	**Particle04**	**Particle05**	**Particle06**	**Particle07**
0°	0.432	0.446	0.384	0.219	0.532	0.487	0.438
90°	0.354	0.277	0.434	0.559	0.489	0.326	0.436
180°	0.342	0.346	0.332	0.439	0.525	0.423	0.696
270°	0.493	0.417	0.414	0.486	0.672	0.543	0.685
C_D							
	Particle08	**Particle09**	**Particle10**	**Particle11**	**Particle12**	**Particle13**	**Particle14**
0°	0.436	0.223	0.275	0.302	0.443	0.537	0.569
90°	0.473	0.240	0.300	0.347	0.472	0.416	0.392
180°	0.845	0.147	0.293	0.292	0.369	0.499	0.555
270°	0.284	0.204	0.136	0.379	0.471	0.382	0.432

The mean drag ($\bar{D}$) was plotted in Figure 4.69, which has revealed 'Particle05', 'Particle07' and 'Particle08' experience the largest drag force of up to $\approx 3.5N$.

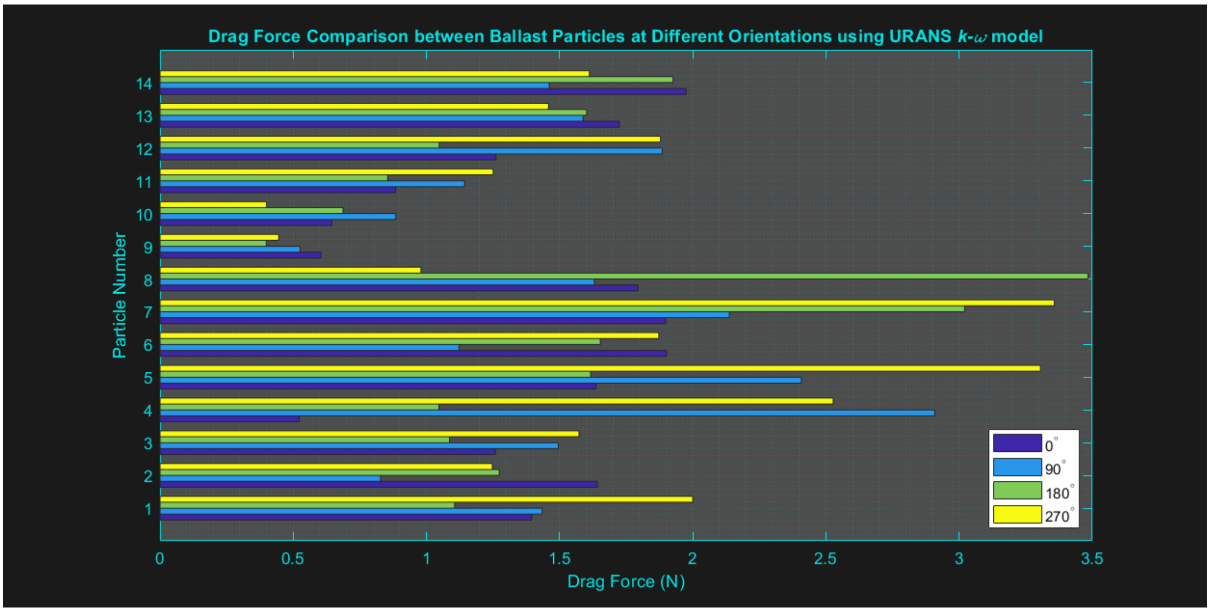

Figure 4.69: Horizontal bar plot of $\bar{D}$ between ballast particles at different orientations using Unsteady RANS SST $k - \omega$ model.

Similar analysis was repeated for the mean lift force ($\bar{L}$) in Table 4.23 and plotted in Figure 4.70.

Table 4.23: Mean lift force comparison between individual ballast shapes at different angles. Turbulence model Unsteady RANS SST k-ω utilised. Time-averaged from 0.4 to 0.5 seconds.

$\bar{L}$							
	Particle01	**Particle02**	**Particle03**	**Particle04**	**Particle05**	**Particle06**	**Particle07**
0°	1.731	1.731	1.443	1.023	1.287	1.037	-0.748
90°	1.113	1.515	2.097	1.150	1.494	1.022	-0.326
180°	0.856	0.408	1.129	1.708	1.640	0.491	3.358
270°	2.051	2.256	2.322	0.440	2.199	2.015	3.694
$\bar{L}$							
	Particle08	**Particle09**	**Particle10**	**Particle11**	**Particle12**	**Particle13**	**Particle14**
0°	-0.479	2.011	1.410	2.830	0.331	0.730	0.548
90°	2.354	1.915	2.403	3.829	1.565	1.237	1.163
180°	3.501	1.374	2.049	2.112	0.663	1.137	1.155
270°	0.786	1.235	1.112	2.219	1.998	1.192	1.289

Table 4.24: Mean lift force coefficients between individual ballast shapes at different angles. Turbulence model Unsteady RANS SST k-ω utilised. Time-averaged from 0.4 to 0.5 seconds.

C_L							
	Particle01	**Particle02**	**Particle03**	**Particle04**	**Particle05**	**Particle06**	**Particle07**
0°	0.536	0.470	0.441	0.429	0.418	0.266	-0.173
90°	0.274	0.506	0.608	0.221	0.304	0.297	-0.066
180°	0.265	0.111	0.345	0.716	0.533	0.126	0.774
270°	0.506	0.754	0.620	0.085	0.447	0.585	0.754
C_L							
	Particle08	**Particle09**	**Particle10**	**Particle11**	**Particle12**	**Particle13**	**Particle14**
0°	-0.116	0.742	0.602	0.967	0.116	0.227	0.158
90°	0.683	0.874	0.815	1.162	0.392	0.324	0.312
180°	0.850	0.507	0.875	0.721	0.234	0.354	0.333
270°	0.228	0.564	0.377	0.673	0.501	0.312	0.346

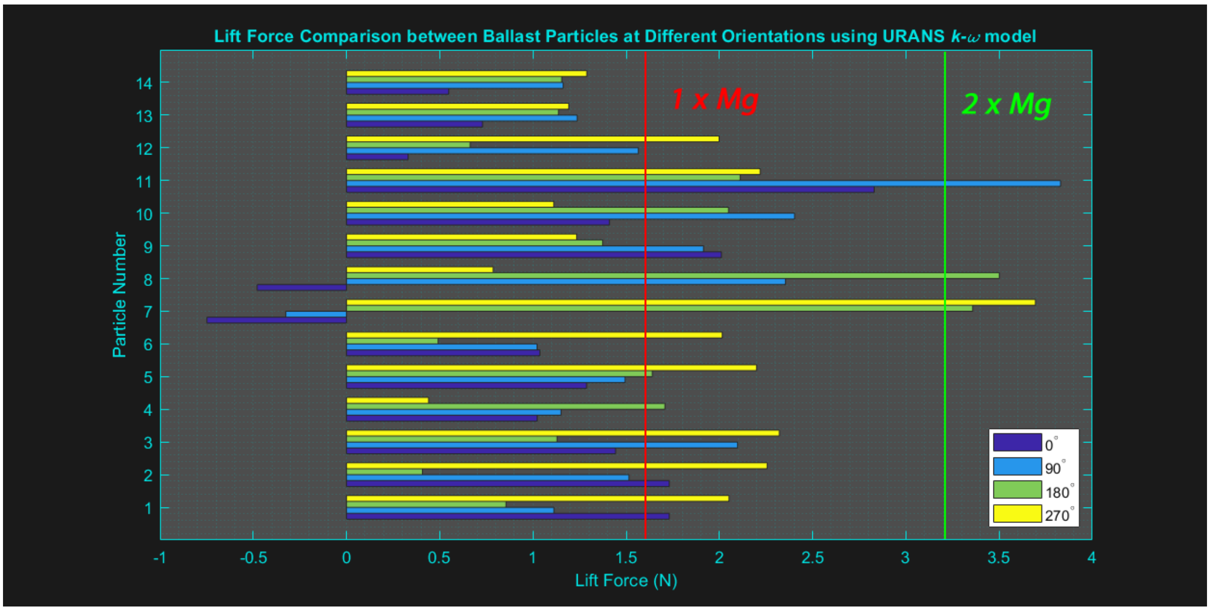

Figure 4.70: Horizontal bar plot of $\bar{L}$ between ballast particles at different orientations using Unsteady RANS SST $k - \omega$ model.

For this analysis, ‘Particle07’, ‘Particle08’ and ‘Particle11’ experience the largest lift forces up to approximately 4.5 N, which is almost three times of its weight. But the projection area of ‘Particle11’ is not the amongst the largest. The weight of each stone was calculated by using the density of granite material (2,650 kgm^{-1}) and the shape’s volume. An assumption was made that there are no void gaps inside the ballast or any impurities.

The aerodynamic lift for at least half of these cases exceeds the weight of the particle when placed by itself with a moving wall placed 0.5 m above the sample speeding at 120 ms^{-1}. By replacing the granite ballast material with a different material of larger density can reduce the impact. But take into account that the ballast stones are normally embedded in the track, meaning the aerodynamic loads would be lower due to the sleeper blocks and the interlocking of particles keeping the ballast stones in place. Another point worth mentioning is that if the ballast begins to move as a result of aerodynamic forces, the projection area and contact force of the ballast stone changes, which can cause the ballast to resist additional movement or roll continuously depending on its shape.

However, it is also worth noting that mechanical loads have not been applied to this study, which its vertical movement can influence the entire system. A large number of samples have exceeded 2 N lift force and 'Particle07' and 'Particle08' experienced downforce instead of lift due to the geometry shape, which is beneficial in keeping it in its place.

The surface pressure in Figure 4.71 reveal largest pressure regions facing the flow and negative pressure zones around the other surfaces due to flow separation that can reduce the impact of aerodynamic forces.

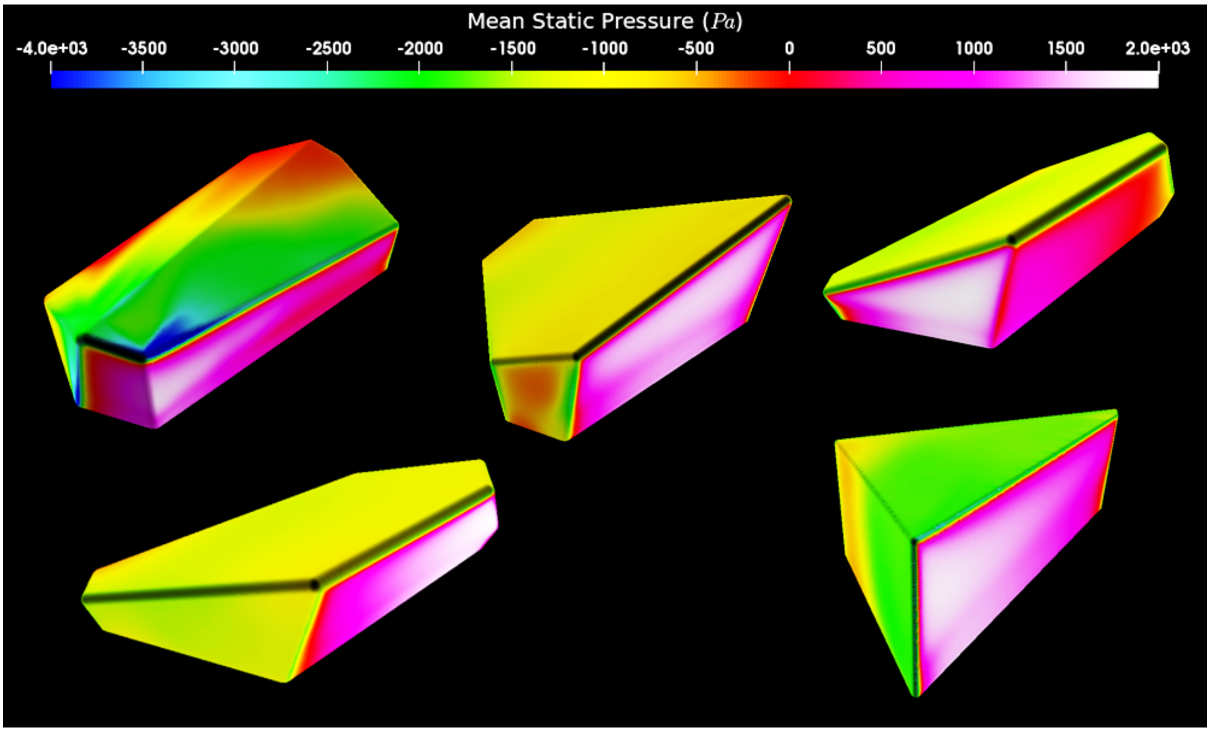

Figure 4.71: Surface static pressure across different ballast shapes.

To understand the instantaneous turbulence flow field better, an iso-surface of the Q-criterion was plotted on Figure 4.72, which revealed the basic changes of vortex structures when the ballast grain is rotated. By rotating the ballast particle by 180 degrees, the horseshoe vortex dissipation changes and the vortex distributions.

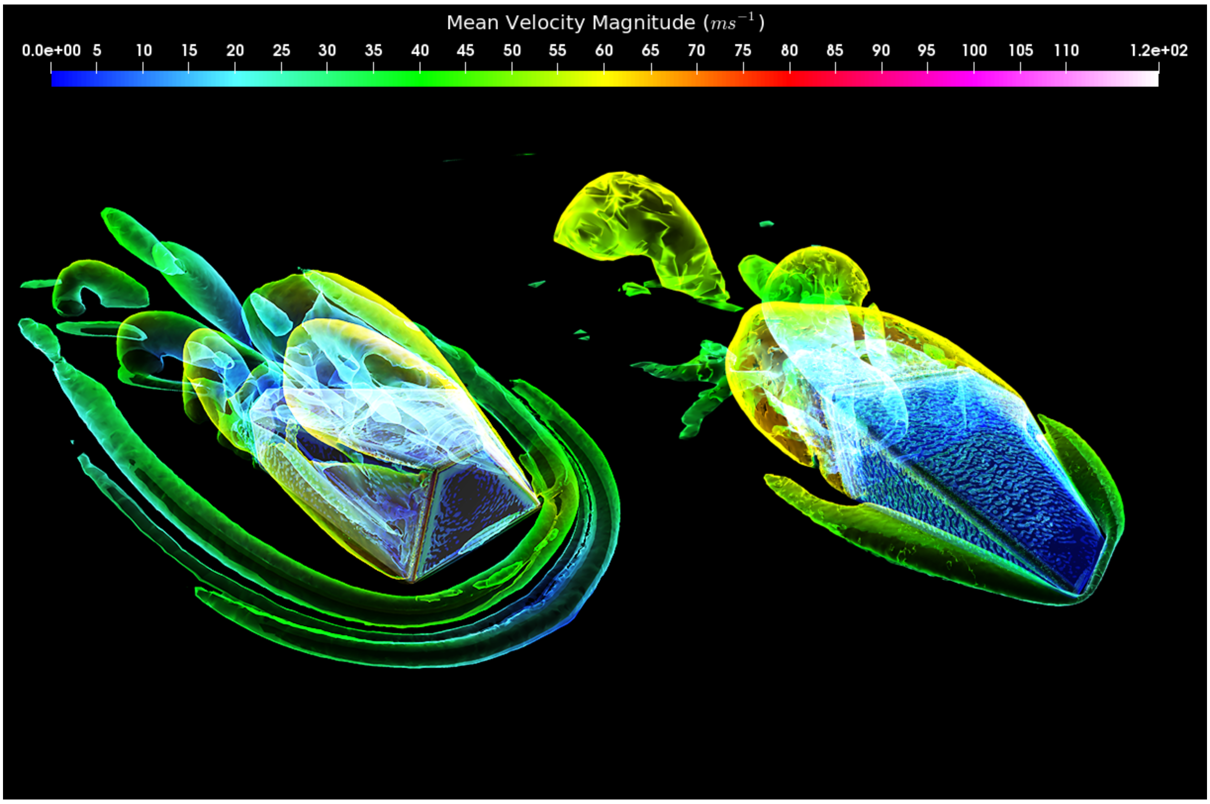

Figure 4.72: Transparent iso-surface of the Q-Criterion coloured by mean velocity magnitude around the ballast particle at using URANS. Changes in vortex structure by rotating the ballast shape.

Altogether, five ballast cases were selected for further analysis, most of which are in the flat category. This would include repeating the studying using DES to see the changes in results and scale down the volume to represent smaller ballast.

Unsteady DES ($k-\omega$) Results

Unsteady turbulence model was swapped from URANS to DES by resolving additional turbulence to observe changes in results. The difference of calculated forces for these cases are summarised in Table 4.25.

Table 4.25: Mean calculated lift and drag forces/coefficients for selected ballast shapes. URANS against DES results.

	DES SST k-ω				**URANS SST k-ω**			
	$\bar{D}$	D_{rms}	$\bar{L}$	L_{rms}	$\bar{D}$	D_{rms}	$\bar{L}$	L_{rms}
Particle 05 270°	4.405	4.415	3.093	3.106	3.305	3.306	2.199	2.200
Particle 07 180°	3.549	3.555	3.943	3.950	3.020	3.021	3.358	3.359
Particle 07 270°	4.121	4.125	4.751	4.756	3.357	3.357	3.694	3.694
Particle 08 180°	3.513	3.524	3.580	3.598	3.483	3.484	3.501	3.510
Particle 11 90°	1.372	1.373	4.794	4.796	1.143	1.144	3.829	3.830
	DES SST k-ω				**URANS SST k-ω**			
	$\bar{C_D}$	C_{Drms}	$\bar{C_L}$	C_{Lrms}	$\bar{C_D}$	C_{Drms}	$\bar{C_L}$	C_{Lrms}
Particle 05 270°	0.895	0.897	0.628	0.631	0.672	0.672	0.447	0.447
Particle 07 180°	0.818	0.820	0.909	0.911	0.696	0.697	0.774	0.775
Particle 07 270°	0.841	0.842	0.969	0.971	0.685	0.685	0.754	0.754
Particle 08 180°	0.853	0.855	0.869	0.873	0.845	0.846	0.850	0.852
Particle 11 90°	0.416	0.417	1.455	1.455	0.347	0.347	1.162	1.162

By resolving additional turbulence, the calculated lift and drag have increased/decreased by up to 1 N, which can influence the outcome whether the ballast would move or not. The time-history of the lift and drag forces are shown in Figure 4.73.

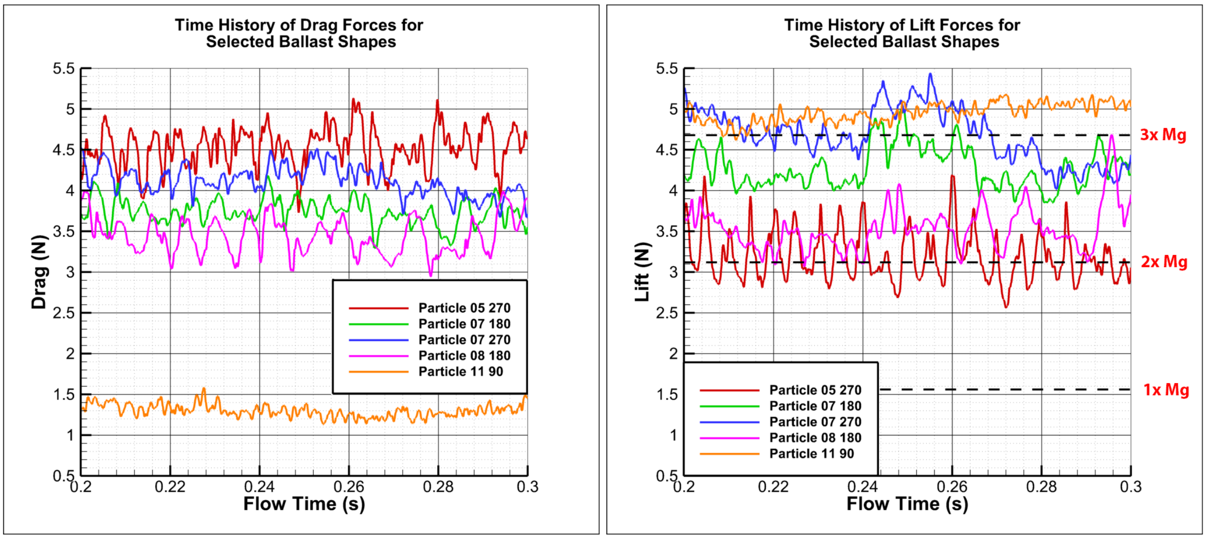

Figure 4.73: Time-history of lift and drag (N) for the five selected ballast cases.

Results revealed that for three ballast shapes, the lift force on the ballast exceeds three times of its weight whereas on URANS the calculated lift force was less than 3 × Mg. The variation of these fluctuations are quite large, which exceeds the calculated weight of granite ballast. Particle11 has an interesting outcome, which has the lowest mean drag but the largest average lift force. This is likely due to being the flattest shape out of the entire set with the smallest height and reasonable projection area. The range of fluctuating lift and drag coefficients are summarised on Table 4.26:

Table 4.26: Force statistics of selected ballast cases using DES.

	$\bar{D}$	D_{p10}	D_{p90}	D_{range}	$\bar{L}$	L_{p10}	L_{p90}	L_{range}
Particle 05 270°	4.405	4.032	4.755	1.746	3.093	2.764	3.484	1.674
Particle 07 180°	3.549	3.309	3.769	1.191	3.943	3.642	4.221	1.336
Particle 07 270°	4.121	3.905	4.345	0.977	4.751	4.468	5.055	1.384
Particle 08 180°	3.513	3.108	3.901	1.371	3.580	3.194	4.093	2.051
Particle 11 90°	1.372	1.288	1.447	0.497	4.794	4.599	4.951	0.671

	$\bar{C_D}$	C_{Dp10}	C_{Dp90}	C_{Drange}	$\bar{C_L}$	C_{Lp10}	C_{Lp90}	C_{Lrange}
Particle 05 270°	0.895	0.819	0.966	0.355	0.628	0.561	0.708	0.340
Particle 07 180°	0.818	0.763	0.869	0.275	0.909	0.840	0.973	0.308
Particle 07 270°	0.841	0.797	0.887	0.199	0.969	0.912	1.031	0.282
Particle 08 180°	0.853	0.754	0.947	0.333	0.869	0.775	0.993	0.498
Particle 11 90°	0.416	0.391	0.439	0.151	1.455	1.395	1.502	0.204

Again, out of the five shapes, Particle11 seemed to stand out due to smallest range and fluctuation in results owing to the short flat shape, which would suggest there is less vortex break up along the shape. A Power Spectral Density analysis was performed for each force in Figure 4.74, which demonstrates large transient variations. The sampling frequency $f = 10\ kHz$ determined from $f = \frac{1}{2\Delta t}$ where $\Delta t = 0.00005\ s$ is the flow time step.

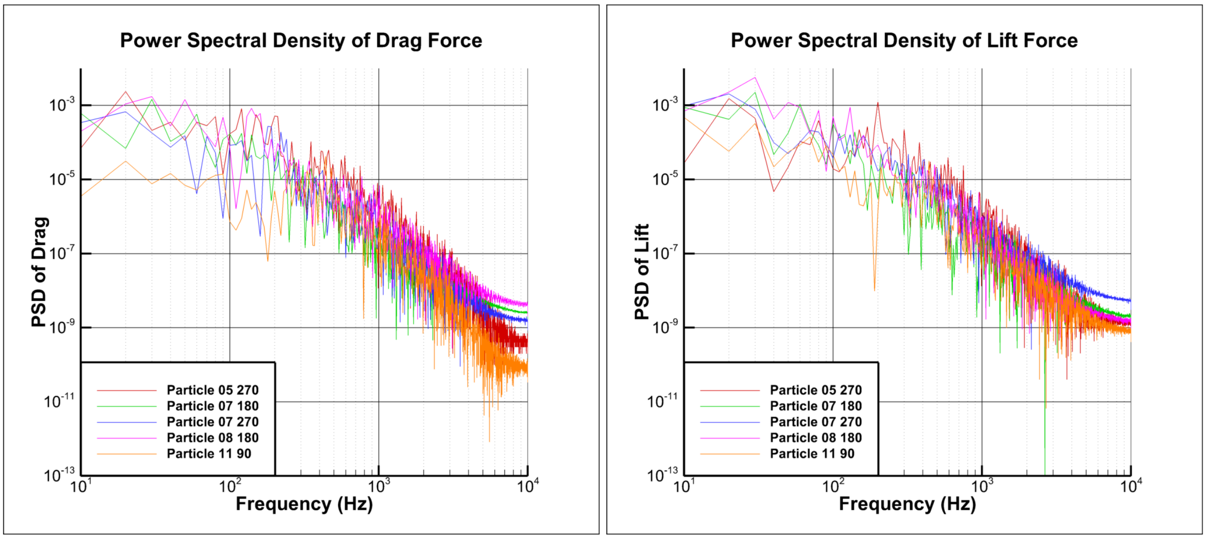

Figure 4.74: Power spectral density of lift (right) and drag (left) forces for the selected ballast shapes.

The spectrum values of lift and drag forces reveal that are at its peak values at the lowest frequency, which can be used to find the vortex shedding frequencies. A clearer indication can be found by applying a window filter onto the PSD results to remove noise fluctuations.

The Q-Criterion in Figure 4.75 revealed rotating vortex structures behind around the particle in greater detail, showing the vortex sheet and strength of the wake characteristics. Like most particle shapes, a horseshoe vortex is generated near the front surface but its distribution of vortices and its dissipation changes depending on the ballast shape.

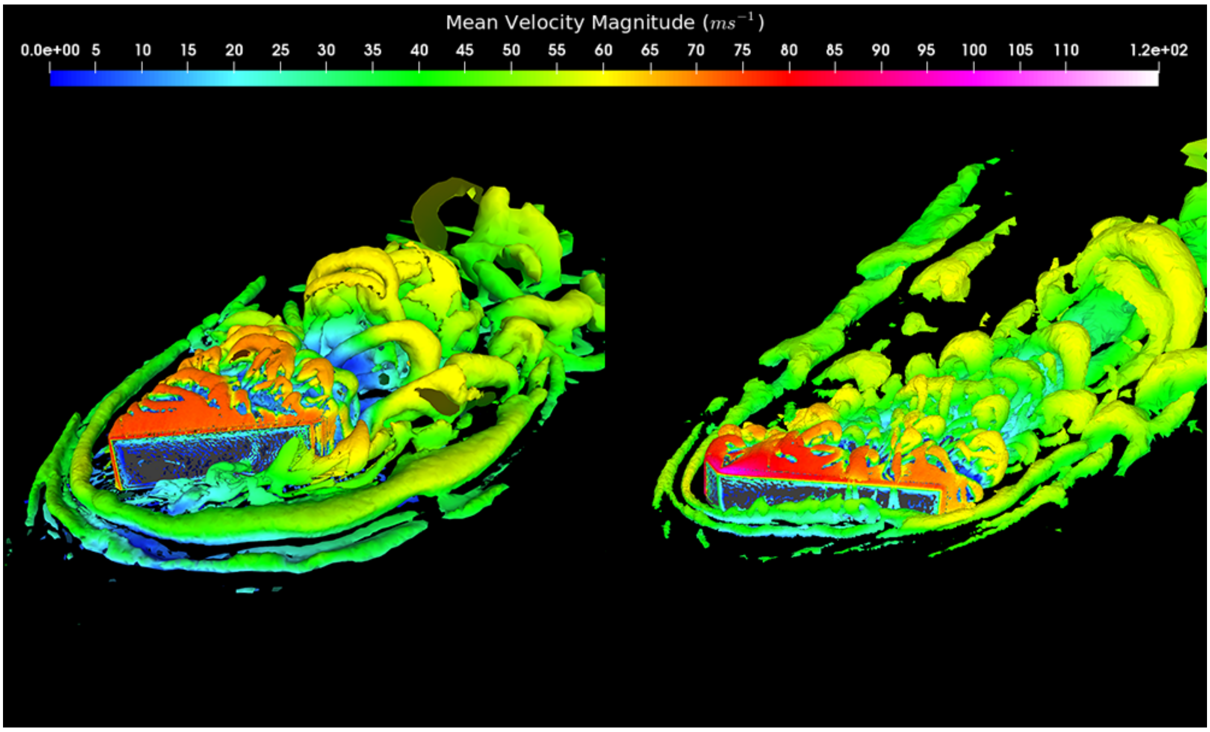

Figure 4.75: Iso-surface of the Q-Criterion (Q = 330,000) coloured by mean velocity magnitude around the ballast particle at using DES.

For final analysis, the same ballast shapes in these cases was scaled down to 0.000013 m^3 volume and CFD analysis was repeated using DES model.

Unsteady DES ($k - \omega$) Analysis on Smaller Ballast

To observe changes in aerodynamic forces for these particles, the geometries was scaled down and re-meshed, following similar procedures used on the larger particles. It was expected that the smaller particles are more prone to movement than the larger version of the same geometries. Even though the projection area and pressure force decreases from the boundary layer effect so does its weight and contact force to the ground. Its shape remains the same meaning the classifications is consistent. Table 4.27 has time-averaged aerodynamic forces for the selected ballast and compared with the larger version both using DES.

Table 4.27: Force statistics of selected small ballast cases using DES.

	$\bar{D}$	D_{p10}	D_{p90}	D_{range}	$\bar{L}$	L_{p10}	L_{p90}	L_{range}
Particle 05 270°	3.203	3.058	3.350	0.514	1.814	1.733	1.900	0.350
Particle 07 180°	2.851	2.704	2.986	0.656	3.239	2.983	3.496	0.987
Particle 07 270°	2.543	2.386	2.673	0.639	3.008	2.790	3.200	0.820
Particle 08 180°	3.499	3.216	3.768	1.133	3.433	3.115	3.772	1.589
Particle 11 90°	0.692	0.661	0.729	0.135	1.708	1.677	1.734	0.143
	$\bar{C}_D$	C_{Dp10}	C_{Dp90}	C_{Drange}	$\bar{C}_L$	C_{Lp10}	C_{Lp90}	C_{Lrange}
Particle 05 270°	0.615	0.588	0.644	0.099	0.349	0.333	0.365	0.067
Particle 07 180°	0.730	0.693	0.765	0.168	0.830	0.764	0.896	0.253
Particle 07 270°	0.738	0.692	0.775	0.185	0.872	0.809	0.928	0.238
Particle 08 180°	0.807	0.742	0.869	0.261	0.791	0.718	0.870	0.366
Particle 11 90°	0.235	0.224	0.247	0.046	0.579	0.569	0.588	0.049

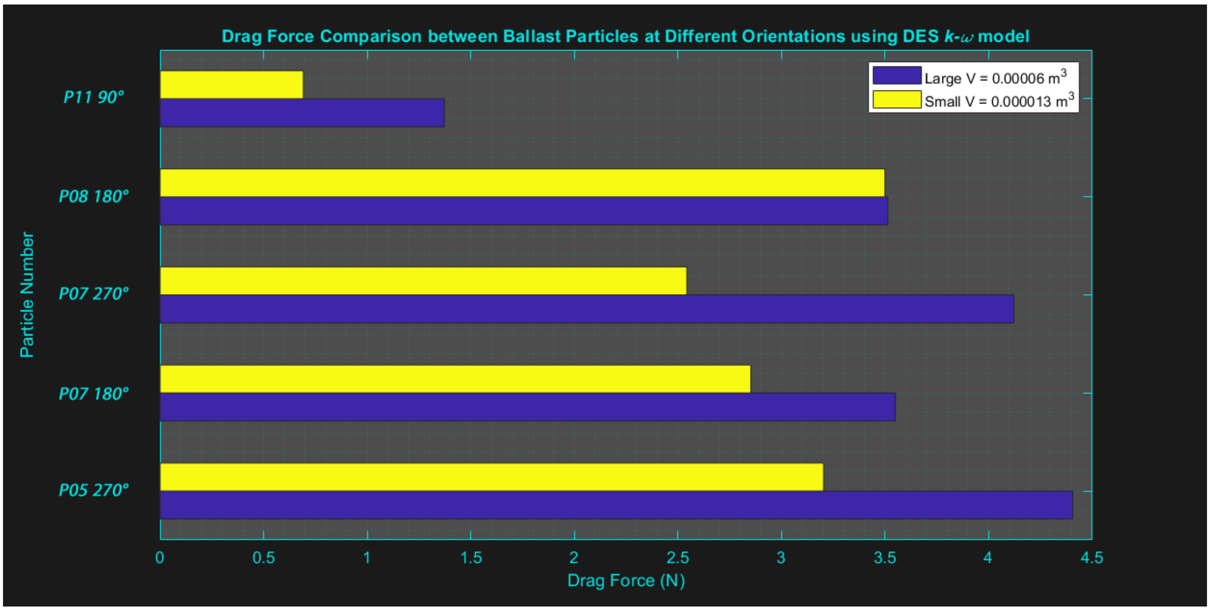

Figure 4.76: Horizontal bar plot of $\bar{D}$ between selected different sized particles using DES.

In Figure 4.76, even though the ballast is 4.5 times smaller, the drag force is still quite similar to the larger ballast. The main reasons for lower drag force would be the boundary layer effect and the smaller projection area.

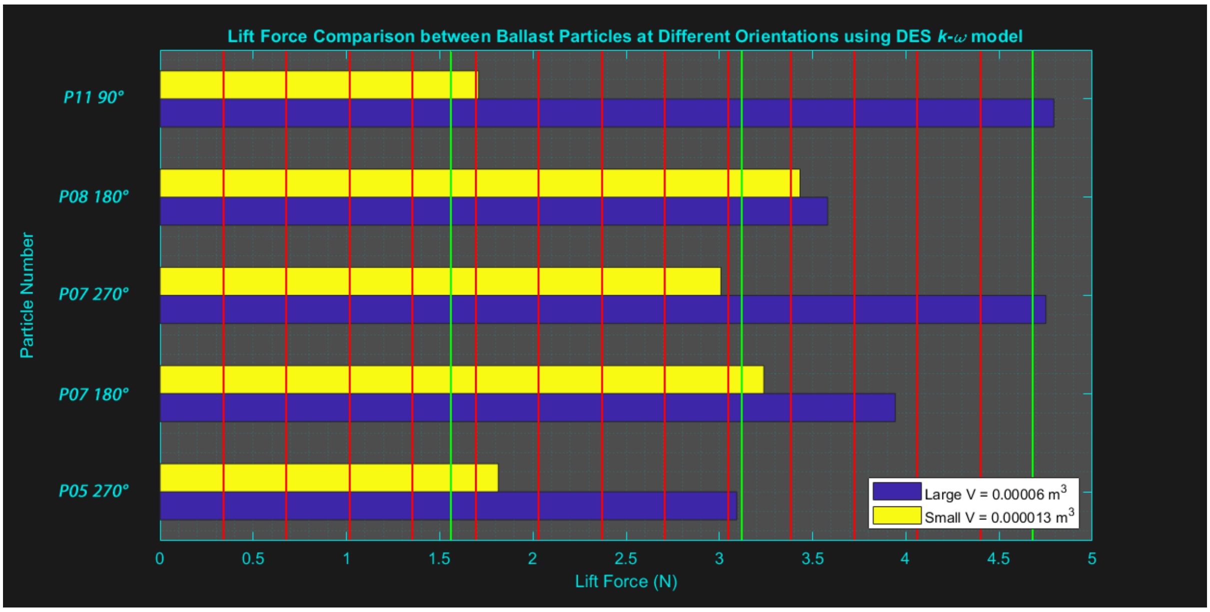

Figure 4.77: Horizontal bar plot of $\bar{L}$ between selected different sized particles using DES.

In Figure 4.77 for smaller ballast, the lift force exceeds its weight (marked red) more times than the larger ballast (marked green). This supports the idea that smaller ballast shapes are more prone to movement due to lower resisting forces. By having smaller ballast on the upper surface of the ballast bed or on the sleeper can increase the risk of ballast flight.

Looking at the results from both DES and URANS cases, it seems that most ballast shapes that are classified as 'Flat' at shorter heights are more prone to lift whereas ballast with larger projection areas are more influenced by drag forces. Spherical ballast on the other hand experience lower lift forces with average drag forces.

Iso-surfaces of the Q-Criterion was compared when using different volumes of the same ballast shape, which showed minor changes in the flow structure.

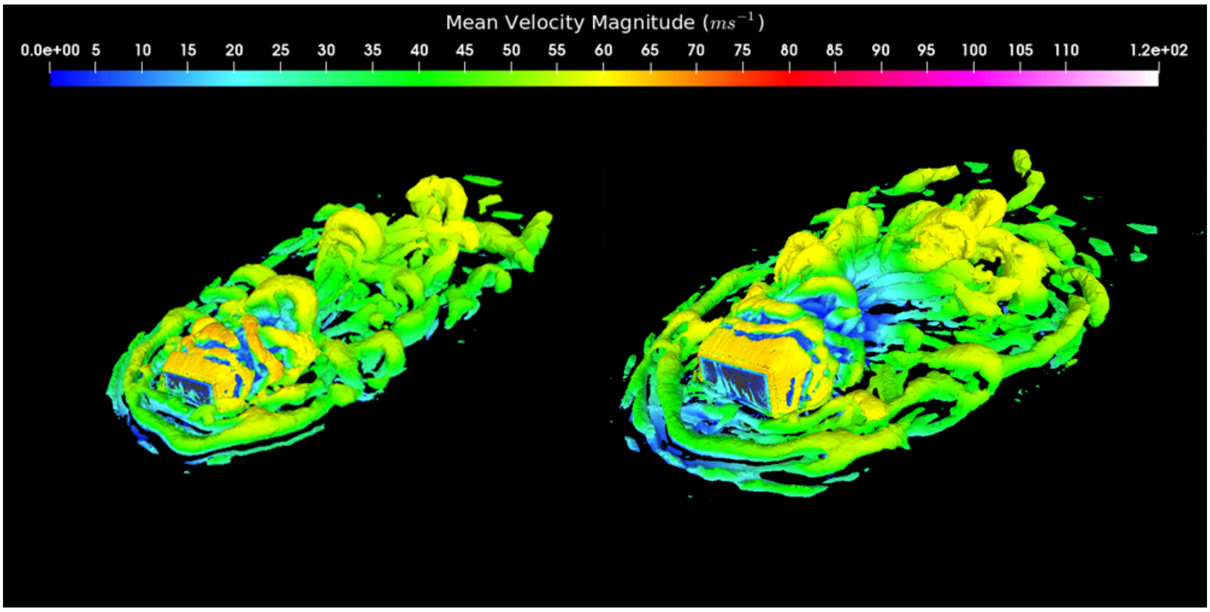

Figure 4.78: Iso-surface of the Q-Criterion around a ballast grain at different volumes. V = 0.000013 m^3 (left), V = 0.00006 m^3 (right)

Having completed the necessary computational analysis, the next step would be to perform simple wind tunnel experiments by using regular granite ballast and 3D printed ballast shapes made of aluminium due to similar material density to measure the critical velocity in which ballast begins to move.

4.6 Critical Velocity Measurements of Ballast Grain

There was two set of experiments carried out in the wind tunnel facility in Southampton University. The first experiment involves granite ballast of different shapes and masses that was placed adjacent to each other where the critical velocity would be determined when the ballast grain moves more than 100 mm from its starting point.

The other experiment would be to replace the granite ballast with the simplified ballast shapes, with a fixed volume of V = 0.00006 m^3 and 3D print the shapes using aluminium alloy powder developed by Concept Laser. This aluminium alloy was used as the density was similar to the granite material used in railway ballast.

4.6.1 Wind Tunnel Analysis on Realistic Granite Ballast

For this wind tunnel analysis, a wooden platform was placed throughout the bottom surface of the wind tunnel and fifteen different ballast stones of different shapes and masses was selected to be placed onto the wind tunnel platform 1,300 mm away from the inlet. The stone samples used are the same ones that were used for the Eureka can experiment to measure water displacement for large ballast (labelled Stone01 to Stone15). Up to three ballast stones was placed at a time with space in between. The freestream flow velocity and ballast mass would be measured. Due to the surface roughness of the ballast shape, the contact area to the ground would need to be measured with use of an ink pad where the number of pixels was measured and converted into surface area. Other variable(s) to consider would be the ballast shape classification and its projection area. Each ballast grain was labelled and placed in the wind tunnel at the same orientation for each trial.

Figure 4.79: Wind tunnel setup to measure critical velocity to trigger ballast movement.

The general procedure was to start the wind tunnel at a starting velocity and increment the wind tunnel turbine speed by 1 RPM until each ballast moved more than 100 mm where its critical velocity was noted. The flow profile used in the wind tunnel was uniform rather than a boundary layer due to lack of vortex generator and other roughness elements to develop the flow. Three trials was performed and the critical velocities was noted in Table 4.28.

Table 4.28: Measurements of critical velocity on different granite ballast grain.

			Critical Velocity (ms^{-1})					
	M (g)	M_{mod} (g)	**Trial 1**	**Trial 2**	**Trial 3**	**Proj. Area**	**Con. Area**	**Classification**
Stone01	143.49	126.29	21.4	23.1	22.2	0.001856	0.000005	Columnar
Stone02	167.40	170.08	21.4	20.6	21.4	0.002084	0.000011	Spherical
Stone03	116.90	115.29	28	28.8	28	0.001159	0.000018	Flat
Stone04	266.73	280.87	26.3	26.3	27	0.002576	0.000046	Spherical
Stone05	180.32	190.23	32	–	–	0.001791	0.000025	Spherical
Stone06	261.70	249.68	21.4	25.6	22.1	0.003007	0.000015	Columnar
Stone07	174.56	189.21	25.5	26.2	24.5	0.002225	0.000019	Flat-Columnar
Stone08	155.13	143.19	23.9	27.9	28.7	0.001687	0.000037	Spherical
Stone09	125.36	106.12	27.2	25.4	25.4	0.001367	0.000032	Flat
Stone10	167.86	159.25	18.1	17.1	17.1	0.002535	0.000029	Columnar
Stone11	131.61	131.95	26.4	23.8	23.8	0.001499	0.000012	Flat
Stone12	170.91	174.57	23.1	23.8	21.3	0.002382	0.000012	Columnar
Stone13	140.56	142.48	24.7	22.2	24.7	0.001848	0.000017	Columnar
Stone14	125.20	121.34	21.4	23	22.1	0.001328	0.000027	Spherical
Stone15	145.10	146.43	23	21.3	26.2	0.001907	0.000013	Spherical

Results in Table 4.28 show small changes in critical velocities between each trial for the sampled particles at a similar orientation. However, mass alone does not influence the critical velocity but also the projection area of the shape and how many faces are normal to the incoming flow. Thus, the critical velocity is related to the lift and drag forces applied to the individual grain.

Generally, as the freestream velocity increases, the surface pressure on the ballast begins to increase and vortices occur around the ballast. As the aerodynamic forces begin to overcome the ballast resisting forces, the ballast begins to shake. Once the critical velocity has been reached, the ballast begins to slide, rotate and roll across the wind tunnel. By doing so, the ballast orientation changes rapidly meaning the ballast projection area and contact to the ground also changes rapidly. As the ballast moves, it can either accelerate or decelerate depending on its orientation. The computational results support that by having different forces at different orientations even with the same projection area.

The projection area of each ballast shape was measured with the use of a 3D scanner developed by Apple called iSense. The device and its application produced a decent mesh for each ballast shape with a spacial and depth resolution of approximately 1 mm. This produced the general shape of the ballast, which did not include the surface roughness. Each mesh was processed using CAD tools before importing it onto AnSys Fluent to determine the models volume, mass and projection area. Some sample meshes can be found in Figure 4.80:

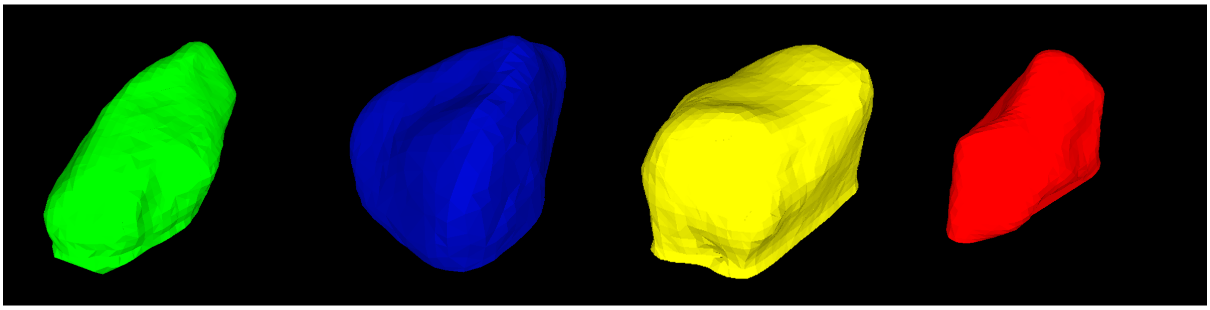

Figure 4.80: Ballast samples scanned and modelled using Apple iSense.

To improve the resolution and output, a better 3D scanner would be required to produce a better mesh detailing the surface roughness and geometry. By doing so would take longer to modify and more difficult to import onto AnSys Fluent due to complications.

To measure the surface contact to the ground, the bottom surface of the ballast was marked with black ink and stamped onto white paper. The paper was then scanned and image processing was used to detect the number of pixels of a fixed area that was black. The number of pixels was then converted into a surface area in which the ballast stone was touching the ground.

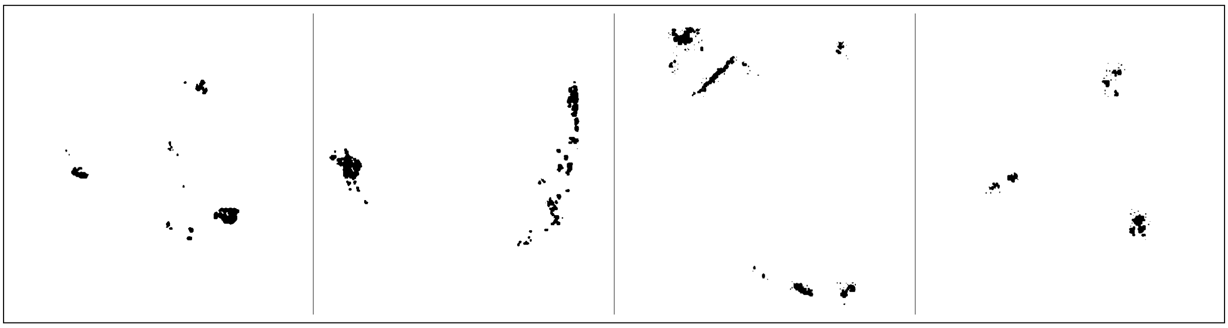

Figure 4.81: Samples of measuring contact surface area to ground using ink pad and image processing.

There are better methods in measuring the contact surface area and projection area by using laser mapping equipment but for the time being this method was utilised. By contacting the ground, the ballast would have frictional force to counteract the drag force. However, the projection area and the ballast mass would most likely influence the outcome of ballast movement. The wind tunnel experiment was repeated by replacing the granite ballast with aluminium ballast shapes that was used earlier for numerical analysis.

4.6.2 Wind Tunnel Analysis on Aluminium Ballast Shapes

For this wind tunnel analysis, the general procedure remains the same except the granite ballast was replaced with modelled aluminium ballast that was placed in four different orientations at the same station point. The CAD models used are the same as those used in the large ballast study using CFD in Figure 4.65. The shapes was printed at a fixed volume (V = 0.00006 m^3) and the bottom surface was then polished to remove any residual as shown in Figure 4.82.

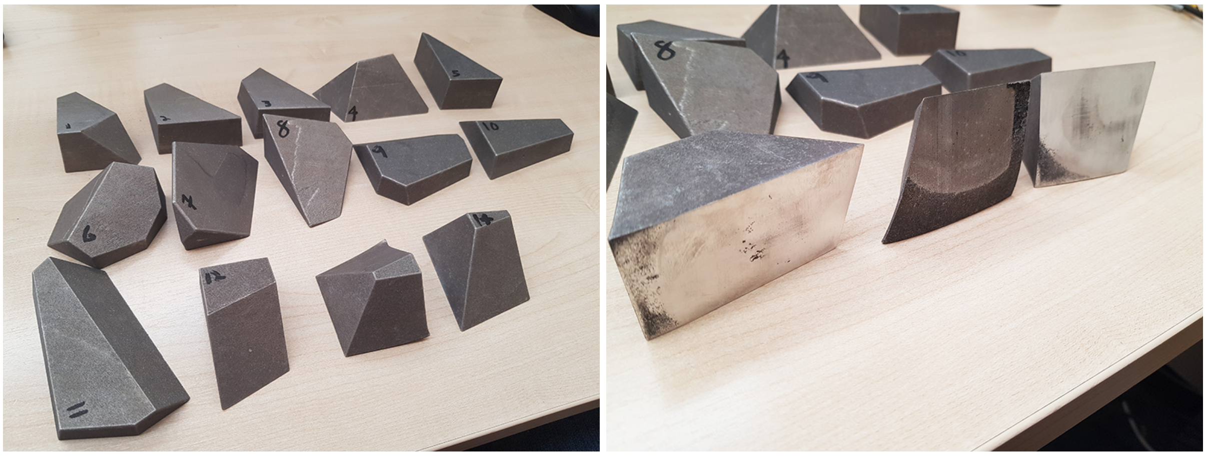

Figure 4.82: Fourteen simplified ballast grains (V = 0.00006 m^3) 3D printed using CL 30AL aluminium alloy (left). Shape deformity due to thermal warping during production (right).

However, due to the thermal warping in production, the last three shapes had some deformity near the bottom surface. Particle13 deformation was too great, which meant Particle13 was removed from experiment due to time and cost of production.

The purpose of this experiment was to determine which shape is more prone to movement where the bottom surface is flat which would maximise the contact force to the ground, the volume was consistent which meant the mass should be similar. This suggests the only resisting forces would be the frictional force between the ballast and platform surfaces and the weight of the ballast itself.

The printed ballast was weighed and summarised in Table 4.29, which revealed some discrepancy due to printing errors where the expected mass would be approximately 0.159 kg.

Table 4.29: Measured mass of each ballast grain 3D printed using aluminium alloy.

	Particle01	**Particle02**	**Particle03**	**Particle04**	**Particle05**	**Particle06**	**Particle07**
Mass (g)	157.92	157.73	160.90	150.84	155.18	154.63	156.65
	Particle08	**Particle09**	**Particle10**	**Particle11**	**Particle12**	**Particle13**	**Particle14**
Mass (g)	150.63	153.71	151.96	151.54	160.02	157.47	162.20

The surfaces of the printed ballast was rough except the bottom surface. To improve the roughness, sandpaper of similar roughness (P600) was attached to the bottom surface. The outline of the bottom surface was printed to help position the particle correctly in the wind tunnel for each angle. The particle was placed inside the Boldrewood Wind Tunnel as previously mentioned where the flow profile is uniform and is placed 1300 mm away from the inlet.

However after initial testing, it was found that due to the larger surface contact area and frictional resistance that many shapes did not move even at maximum operating speed of 35 ms^{-1}. This would make it difficult to obtain reasonable samples of data for comparison. By removing the surface roughness off the ballast shapes, due to the smoothness of aluminium coating, the shapes easily rotated and slid across the wind tunnel during operation. By removing the rough surface from the aluminium shapes would poorly represent the ballast frictional properties, which makes the experiment unrealistic. Thus the only solution would be to place these shapes in a larger wind tunnel at higher operational speeds.

It was noted that by applying small amount of vertical force onto the platform during operation, the shapes have moved with ease as the ballast lost contact with the ground momentarily. These vertical forces can occur as trains pass the track section.

An alternate experiment would be to measure the aerodynamic forces for each shape by using the force transducer similar to the one used on the cube. To do so, the force transducer should be wall mounted and a new adapter plate can be made to connect the force transducer onto the ballast shape. The measurements then can be used to compare with the numerical results in the computational chapter. Some discrepancy would be expected due to different flow profiles.

4.7 Summary of aerodynamic flow over isolated particles

A comprehensive study was carried out using CFD and experimental techniques on a variety of shapes including cubes, hemispheres and realistic ballast. The first set of simulations and experimental analysis was conducted on a cube due to its simplicity and validation data available including Castro & Robins (1977). It was concluded that DES turbulence models are more suitable in determining the flow behaviour and separation accurately whereas RANS models overestimated its separation. However, by doing so required additional computational resources and had taken longer to calculate sufficient flow time to collect meaningful data. URANS was able to describe the main structure of the unsteady flow but its energy dissipates over time making the simulation less representative of real-time turbulent flow. It was also established that by increasing the Reynolds number, the force coefficients began to converge and the velocity profiles remained the same. Also by elevating cube would substantially reduce the lift force, allowing downforce and gravitational force to be dominant. Finally, by replacing the inlet uniform flow condition with a moving wall condition from above would represent the flow conditions better of a passing train. By doing so, the streamwise velocity near the ground would be significantly less, which would mean the lift and drag forces on the cube was less compared to uniform flow. A wind tunnel study was carried out on both orientations, which provided similar aerodynamic forces as the computational analysis as the flow profile was close to uniform. However, pocketing the force transducer inside the cube had caused some difficulty in measuring lift forces accurately. Therefore, no further force measurements would take place until the experiment was re-designed and manufactured to resolve this error.

Further computational studies have then been implemented on a hemisphere, using Tavakol et al. (2014) results for comparison. It was identified that increasing the Reynolds number can drastically change the velocity profile and pressure distribution. At Re = 40,000, similar to Tavakol et al. (2014), the flow behaviour behind the hemisphere was poorly represented when using Realisable k-ϵ whereas SST k-ω was in good agreement. However, at Re = 330,000, both RANS and DES had established similar profiles but DES SST k-ω was most accurate. This would suggest that Unsteady models of SST k-ω was better suited for complex analysis. Due to its round shape, the hemisphere would have less lift and drag force than the cube since most of its faces is not facing the flow direction. This would imply that ballast of a large projection area facing the flow is more likely to move than spherical ballast.

For the studies of ballast, the Eureka experiment approach provided two reasonable measurements of volume, which represents small and large ballast grains. By doing so, two sets of simplified ballast shapes have been modelled, which has no surface roughness. The design and layout was set-up to represent a train moving at 120 ms^{-1} passing over a single ballast grain at four different directions. Due to a large amount of CFD analysis, URANS SST k-ω was used instead of DES as the main variable of interest was the calculated aerodynamic forces. The results revealed that certain flat/columnar shaped ballast with a large projection area would experience more drag than any other shapes, particularly those of a larger height with faces normal to the flow. This was identified by comparing the outcome of a ballast grain with the same projection area but flow in the opposite direction as the shape is irregular. Shapes with the largest lift and drag forces were selected and the study was repeated using DES. The results revealed that the time-averaged lift and drag forces have changed by up to 20% that can change the outcome of ballast movement. Although the calculated lift exceeds the ballast weight, the simulations do not consider factors including interlocking forces of other ballast, vertical forces exerted by the train bogies, other solid boundaries surrounding the ballast reducing the aerodynamic loads. For the calculated drag forces, the frictional resistance has not been determined for the granite and concrete interaction to determine whether the ballast would move in the streamwise direction but realistically there would be surface roughness obstructing the ballast from moving. Furthermore, reducing the selected ballast volume in the DES studies from 0.00006 to 0.000013 m^3 had resulted in up to 40% reduction in drag force and the lift force exceeds up to ten times its weight, which suggests smaller ballast is more prone to ballast flight than larger ballast.

Further wind tunnel experiments had taken place by measuring the critical velocity when the ballast began to move more than 100 mm from the starting point. The projection area and the ballast classification was determined using a basic 3D scanned that provided a 3D model of reasonable quality. It was found that most columnar ballast with a large projection area and lower mass are prone to movement. Flat ballast shapes are more resistant to drag force due to the boundary layer effect and spherical ballast currently has no clear link towards ballast movement. Therefore, further samples and experiments should be carried out in an attempt to find a clearer indication. The granite ballast was then replaced with simplified aluminium ballast. Due to the frictional force between the ballast flat bottom surface and the wooden test section, most samples were unable to move from its starting position, making the experiment unsuccessful. The experiment would need to be repeated in a different wind tunnel with a larger freestream velocity to measure the critical velocity or be re-designed to attach each grain onto a force transducer at four orientations.

Having completed this area of study, the next part of this research would be to model the track section and place isolated particles in specified regions of the track. For simplicity, a cube shall represent the isolated ballast as the cube is more prone to ballast movement than most isolated shapes.

Chapter 5

Computational Analysis of Flow across a Channel

This chapter presents the results of computational studies of a track section model as the under-body of a train passes. A typical track section is illustrated in Figure 5.1, which defines the components of the track.

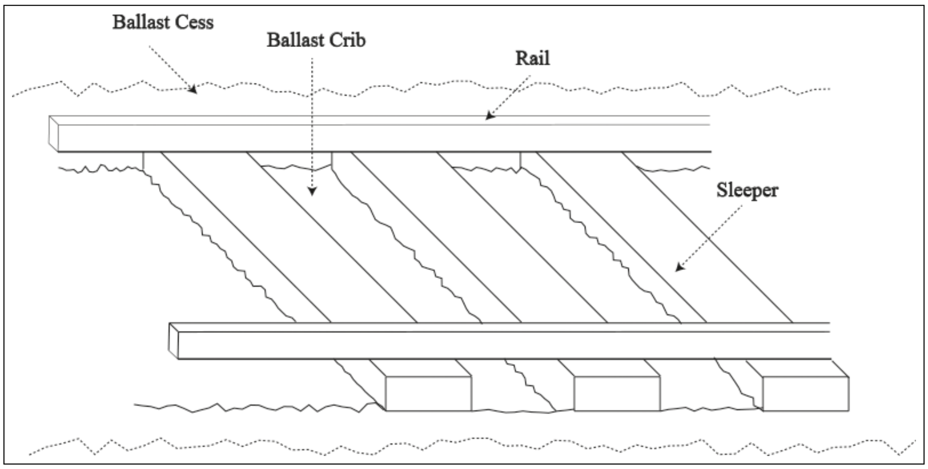

Figure 5.1: Sketch of a typical ballasted track, illustrating its main components.

This study was undertaken to evaluate the aerodynamic loads on isolated particles in different regions of the track to assess in which scenarios the ballast is most likely to move. Different track configurations were studied by changing the sleeper blocks shape or type and the ballast bed height.

Modelling a length of the track with several sleeper blocks can be computationally expensive. As an alternative, periodic boundary conditions may be used for the inlet and outlet for one sleeper block with the ballast crib in between. This type of boundary condition is used to simulate processes in a small part of an extensive system, where the flow in the outlet is mirrored in the inlet as in a closed circuit wind tunnel.

Two validation cases were studied; first, using a two-dimensional wavy channel to verify the effectiveness of the periodic condition and secondly, a moving wall study on a channel flow, before applying these techniques to a track section.

5.1 Steady analysis of wavy channels

For the wavy channel analysis, steady RANS was used to assess the difference between k-ε and k-ω methods. Experimental data from Kuzan (1986) were used to benchmark the results for 7,200 cells, which was sufficient for a 2D problem to provide meaningful results (Figure 5.2).

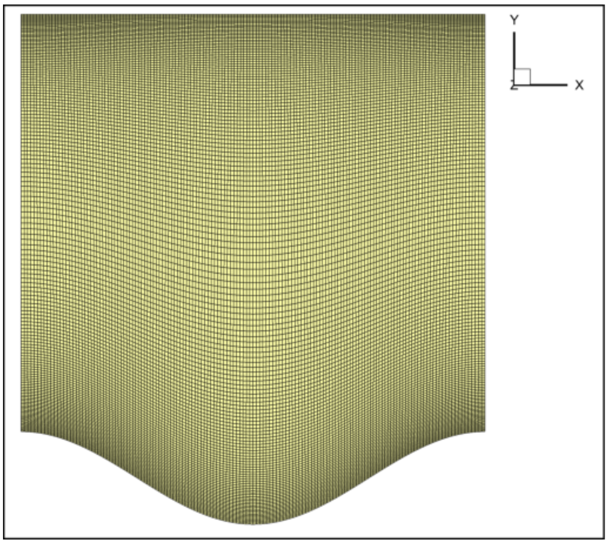

Figure 5.2: Mesh of the wavy channel using a structured grid configuration.

Three variants of k-ε were used (Standard, Realisable and RNG) and SST k-ω. The velocity contour plots in Figure 5.3 shows that the vortex region is smaller for k-ε than for k-ω, in which the flow fully reattaches within the full wave period.

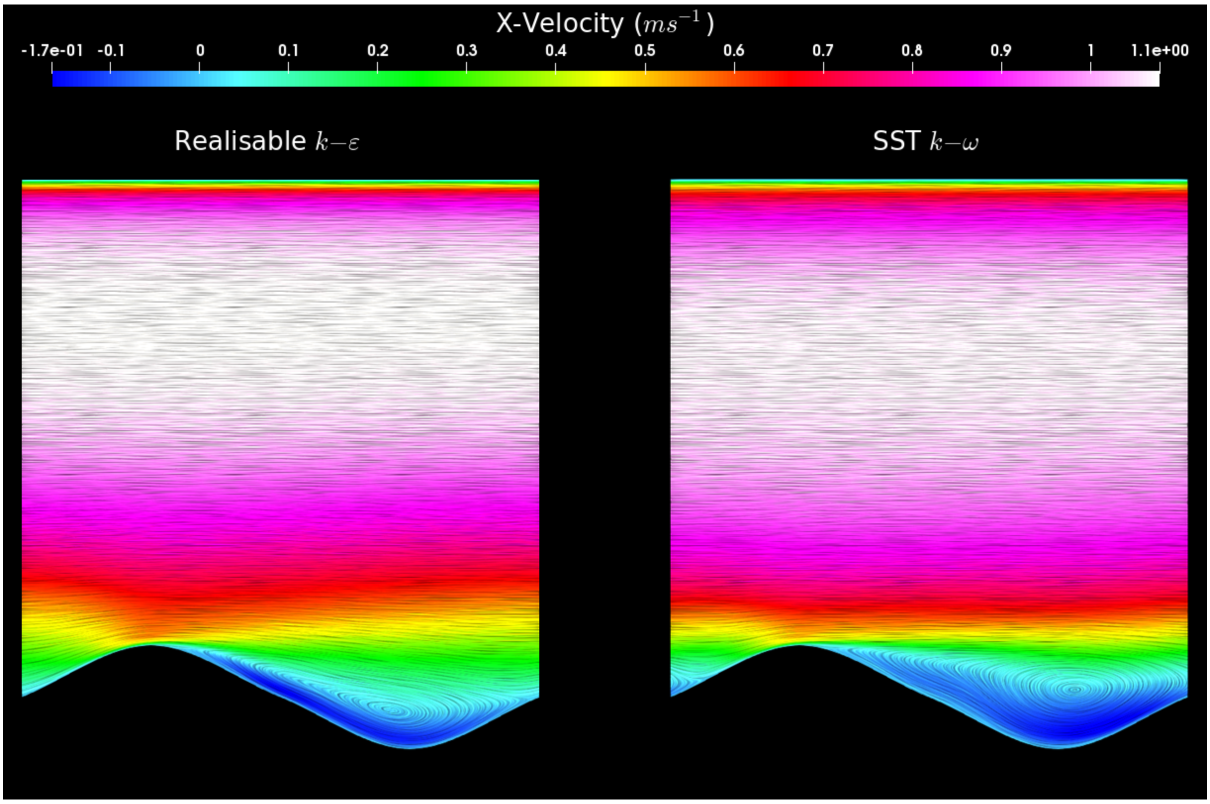

Figure 5.3: Streamline path of the mean velocity across the wavy channel where z/h = 0.0. Realisable k-ε (left) and SST k-ω.

However, the comparisons in Figure 5.4 show that all variants of k-ε are in better agreement with the experimental data than SST k-ω, particularly away from the wall for the 2D wavy channel. The velocity profile for SST k-ω slightly overestimates the flow separation in the wavy channel. Even by refining the mesh further, the highest achieved residuals was at order 1^{-8}, which is good for a 2D case. This may suggest the source of error is related to the turbulence model used for this problem or in rare circumstances its coding error within the commercial software.

For more complicated 3D problems containing flows undergoing additional strains such as curved boundary layers and swirling flows, SST k-ω would be better suited since Realisable k-ε performs poorly in these situations Versteeg & Malalasekera (2007). The SST k-ω model also provides a wall roughness feature which would be useful to represent the ballast bed surface around the sleeper blocks.

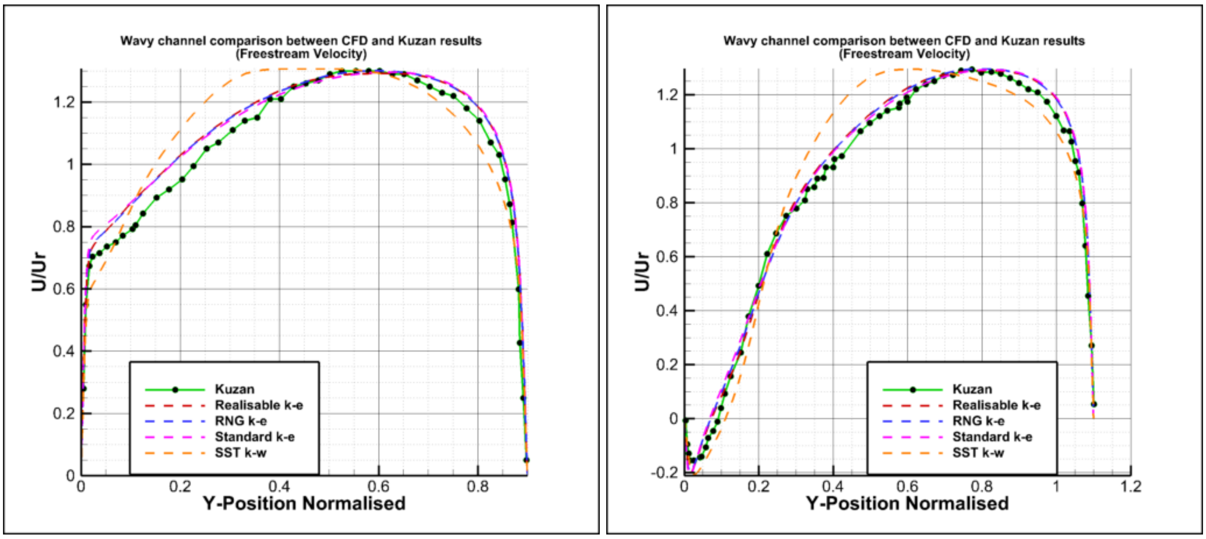

Figure 5.4: Quantitative comparison of velocity profiles flow at the crest (left) and the trough (right) of the wavy channel.

However, convergence using SST k-ω can be challenging and expensive as it requires a larger mesh density near the solid region. Thus for simple cross-sectional studies, steady RANS Realisable k-ε was used throughout. For the whole track section, SST k-ω was used to provide more realistic results.

5.2 Steady analysis of channel flow using moving wall and ground roughness

The second validation case was to model a channel with a moving upper wall, to represent the moving train carriage underbody. Since the bottom wall is static but the top wall is moving, the velocity between them should be approximately half the moving wall speed when fully developed.

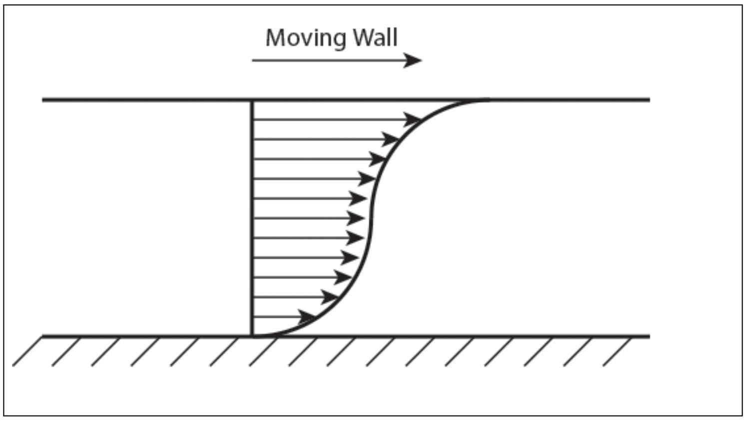

Figure 5.5: Developed velocity profile for a moving wall case.

The channel wall study had a height of 0.5 m, which is representative of the distance between the ballast surface and the under-body of a train. The mesh shown in Figure 5.6 has a domain length of 0.5 m in the streamwise direction, where the inlet and outlet are periodic boundaries.

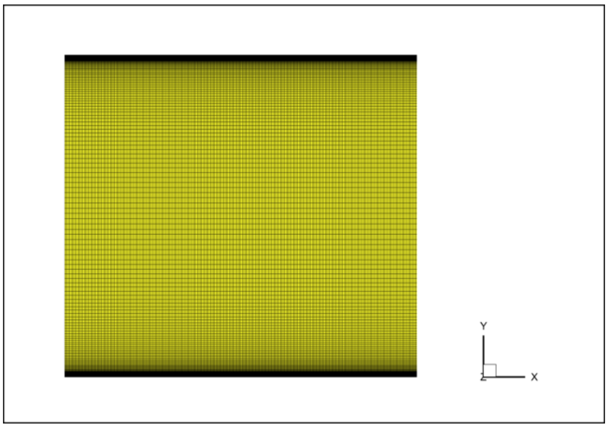

Figure 5.6: Mesh for the standard channel using a structured grid configuration.

A simple comparison of turbulence models was made, followed by an assessment of the effects of ground roughness using the SST k-ω wall roughness parameter. In reality there are many sources of roughness that can make the air flow more turbulent, as shown in Figure 5.7.

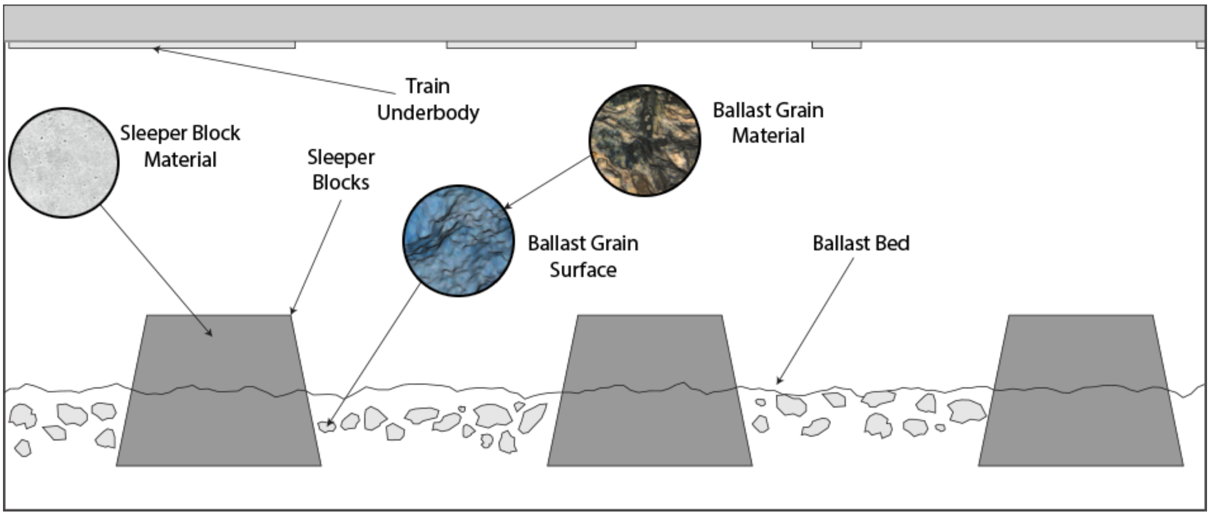

Figure 5.7: Sources of roughness across a track. Scanned images provided by Madhu Bangalore.

There are various layers of roughness at different heights that can trigger turbulent flow development (Figure 5.8). For example, if the ballast bed was tamped, the ballast bed surface may be higher than the sleeper, resulting in ballast bed roughness contributing more to turbulent flow. On the other hand, if the ballast bed surface is below the sleeper block, the sleeper blocks would be the bigger contributing factor to turbulent flow owing to the greater roughness heights.

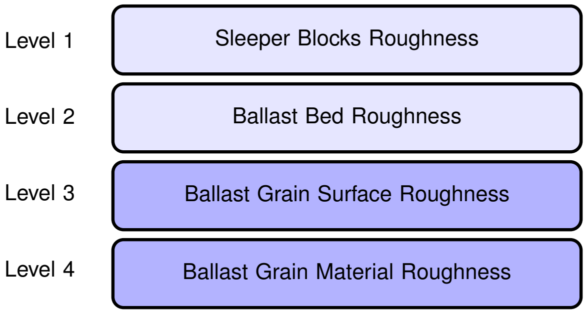

Figure 5.8: Four levels of roughness from sleeper block to material roughness of a ballast grain.

To model ground roughness, the surface can be physically or parametrically modelled using the ground roughness height R_H. This was used to represent the mean changes in height of the surface, where 0.0 m represents a smooth wall. For this case, the expected value would be up to half the mean diameter of a large ballast grain (around 0.02 m); but in some cases, the ballast grain might be sitting on top of the ballast bed. The other variable to consider is the roughness constant R_C, which determines the uniformity of the surface; R_C = 0 is smooth, R_C = 0.5 is towards sand-grain roughness and R_C = 1.0 is wire-mesh roughness. Therefore the idealised parameter settings for a ballast bed would be R_H = 0.02 m to 0.04 m with two roughness constants $R_C = 0.25, 0.5$. The roughness will be applied to the ground, while the moving wall would remain smooth. The mass flow rate and pressure gradient were both set to zero so that the flow was developed entirely by the moving wall. Figures 5.9 and 5.10 show that for all turbulence models the velocity profile remained the same for a given mass flow rate.

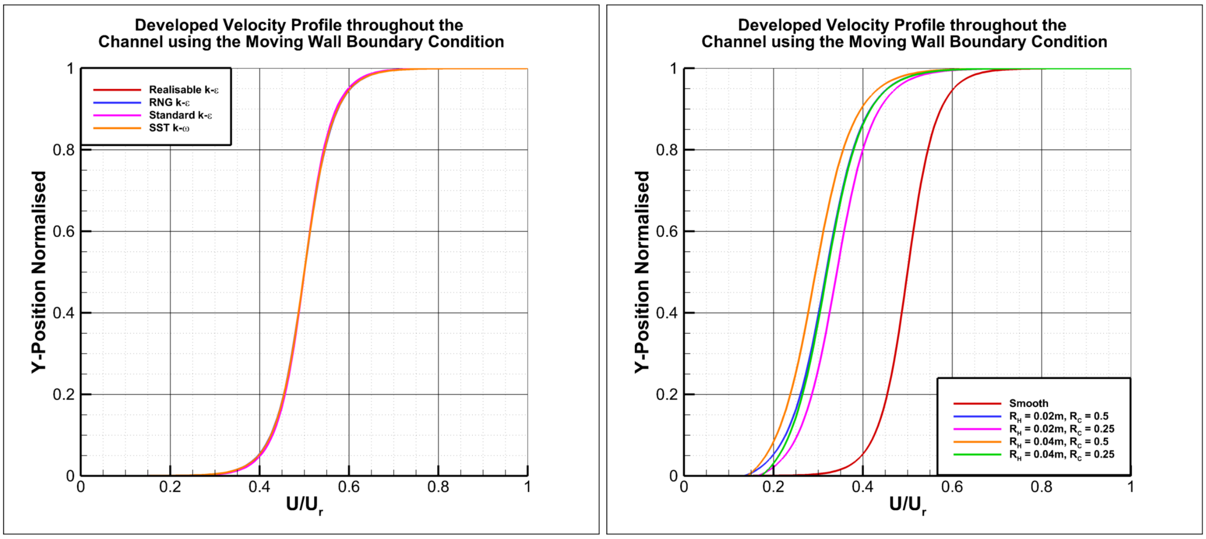

Figure 5.9: Velocity profile comparison between turbulence models (left). Changes in velocity profile with ground roughness applied using SST k-ω.

	Mass Flow Rate ($\dot{m}$)
Smooth	25.088
R_H **= 0.02 m,** R_C **= 0.50**	16.130
R_H **= 0.02 m,** R_C **= 0.25**	17.318
R_H **= 0.04 m,** R_C **= 0.50**	15.050
R_H **= 0.04 m,** R_C **= 0.25**	16.320

Table 5.1: Resulting mass flow rate of the channel flow at different ground roughness parameters.

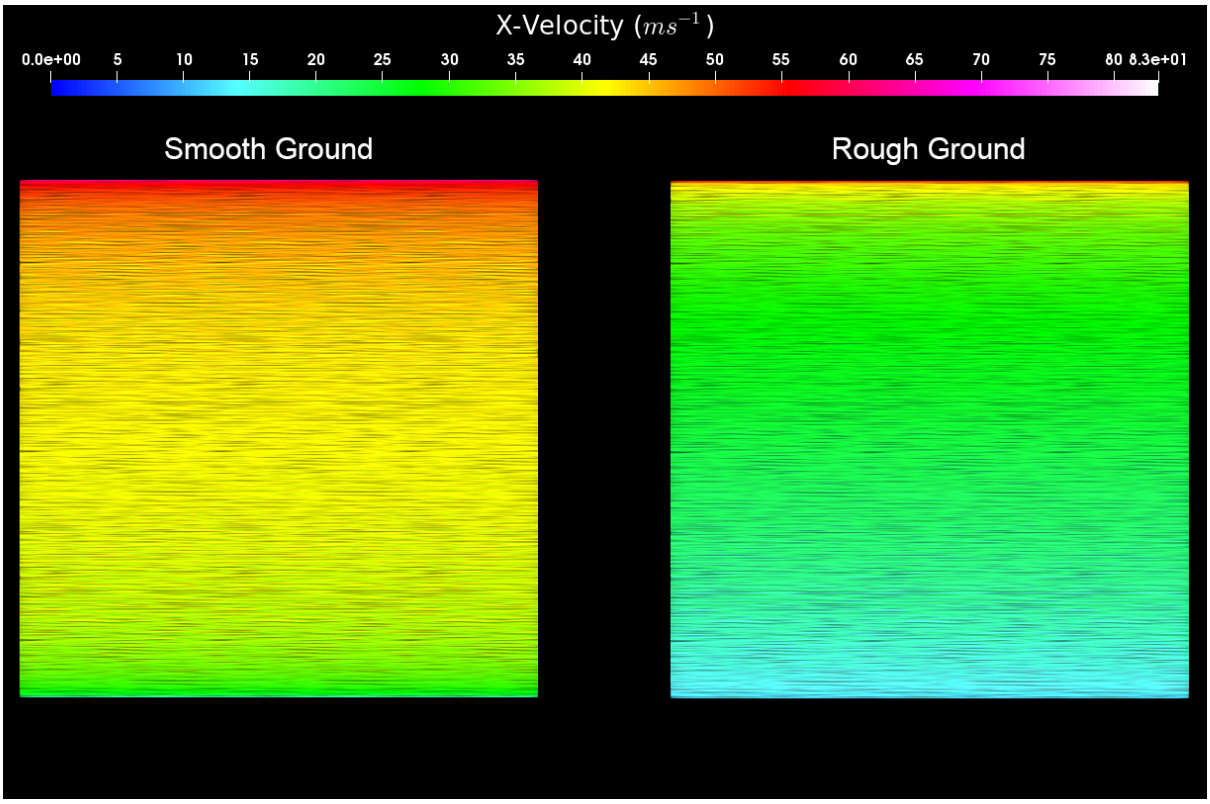

Figure 5.10: Streamwise velocity contour throughout the channel. With smooth ground (left) and with ground roughness (R_H = 0.04 m, R_C = 0.5) (right).

On changing the ground roughness, the flow became more turbulent, decreasing the mass flow rate and the streamwise velocity closer to the ground. The greater the roughness height and roughness constant, the lower the mass flow rate, which would imply that a greater ballast surface roughness would make the flow more turbulent thus decreasing the drag force.

The next step was to perform 2D and 3D analysis on track sections using different sleeper blocks and depths. The cross-section was analysed first, followed by modelling the whole sleeper block with shoulder ballast. Isolated particles were included to determine the conditions in which the ballast might move. Ground roughness was included in later stages of the work.

5.3 Steady Analysis of Simple Track Cross-Sections

The second part of this research involved aerodynamic studies underneath the train along the track bed using CFD tools. The depths of the ballast bed and the sleeper blocks were changed to observe the impact on the passing flow. The approach was to use a moving wall representing a passing train to develop the velocity profile with a periodic boundary condition.

A periodic condition was introduced to represent a continuous track structure, so that the air movement between each sleeper is assumed to be similar. Several sleeper shapes were considered including mono-block and aerodynamic sleepers. To ensure continuous flow between each sleeper, three cases were assessed for each sleeper block; a single sleeper block, two sleeper blocks and four sleeper blocks using periodic conditions across each group. A 2D analysis of the track section was carried out to determine differences in the mass flow rate between each case for different sleeper blocks, which were then applied to the 3D cases to reduce computational time.

For each sleeper block, the velocity profiles and mass flow rate were compared initially using steady RANS (Realisable k-ε). For each sleeper block, the cross-section of the sleeper was modelled with different ballast depths; 20 mm above the top surface of the sleeper representing recent packing maintenance, and 40 mm below. The ballast level is generally 200 mm below the rail top surface based on site measurements. The reference used for the under-body distance is the Eurostar Train, and the distance between sleeper blocks was 600 mm (Soper et al., 2017).

These results provide a better understanding of how the flow reacts across the track to changing physical parameters and how the aerodynamic load would interact with the ballast surface, to assess the likelihood of individual ballast movement.

5.3.1 2D Analysis using Periodic and Moving Wall Conditions

Mono-block

The dimensions of a standard G44 Mono-block sleeper manufactured by Tarmac were measured at the Civil Engineering Laboratory, University of Southampton and then modelled using CAD. In this study, only the middle cross section was modelled as shown in Figure 5.11. The speed of the moving wall was set to 120 ms^{-1} to generate turbulent flow towards the track section.

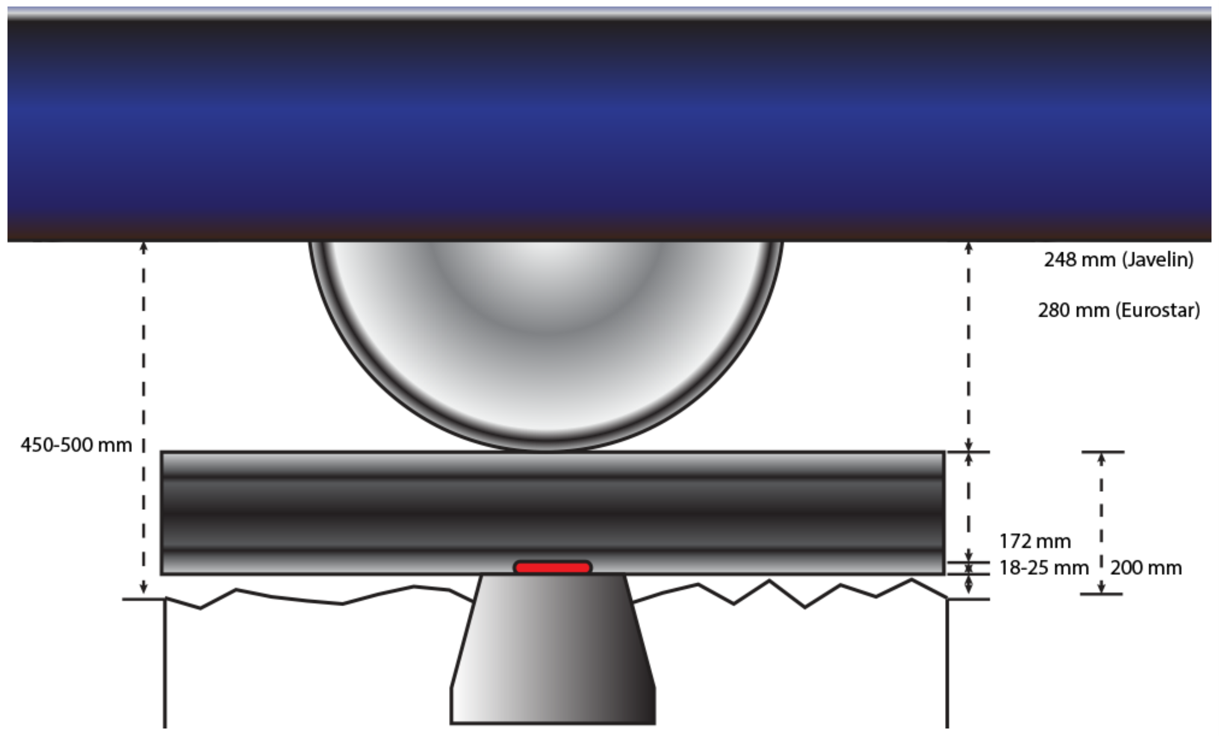

Figure 5.11: Problem specification for CFD analysis of the mono-block sleeper (Not to scale).

Once the flow was fully developed, the mass flow rate was noted and applied to the 3D cases where the cross section was extruded, producing similar results to a moving wall at lower computational cost. Velocity profiles were determined between the sleeper blocks and at the centre of the sleeper top surface. The mesh layout in Figure 5.12 shows two mono-block cases, in which the ballast surface is raised by 20 mm above and lowered by 40 mm below the standard.

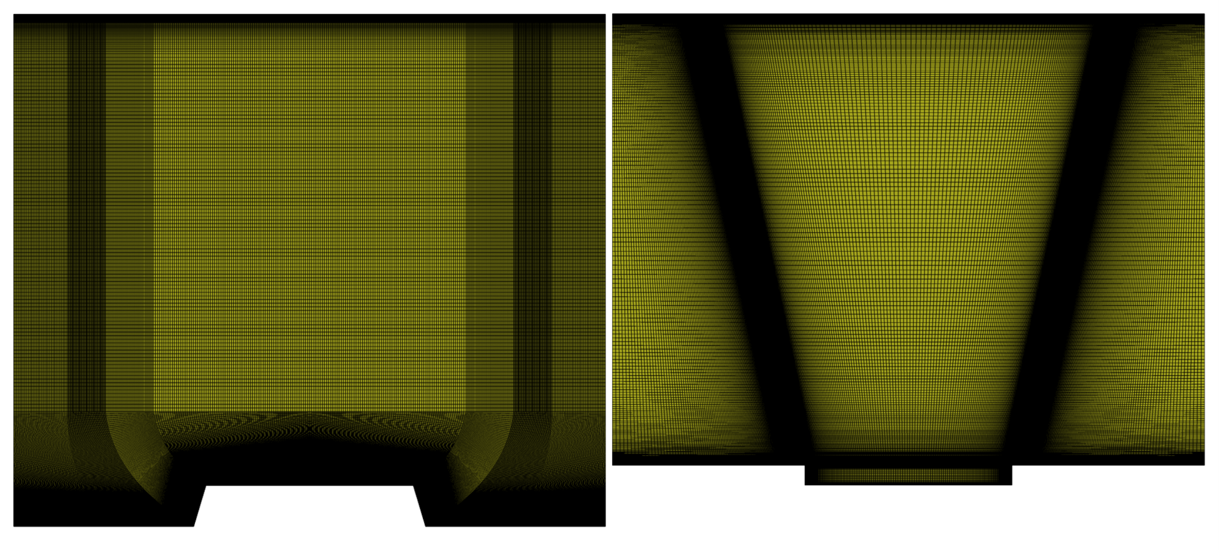

Figure 5.12: Mesh of the fluid domain over the mono-block sleeper. Ballast depth 40 mm below the sleeper top (left) ballast depth 20 mm above the sleeper top (right).

Velocity profile data was collected at every inlet, track centre and interface as illustrated in Figure 5.13.

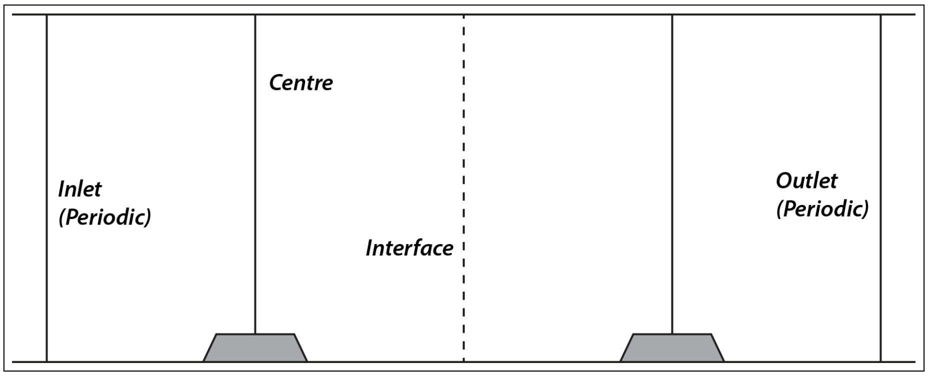

Figure 5.13: Plot line locations across the track section.

Results for the two ballast depths are shown in Figure 5.14, which confirms that induced mass flow rate around in periodic 3D system gives the same velocity profiles as the moving wall in the 2D system. However, additional computational resources would be required for 3D cases to achieve the same velocity profiles when using a moving wall instead of a fixed mass flow rate. These 3D cases were determined by extruding the 2D case 1.0 m in the spanwise direction where the track still remains homogenous.

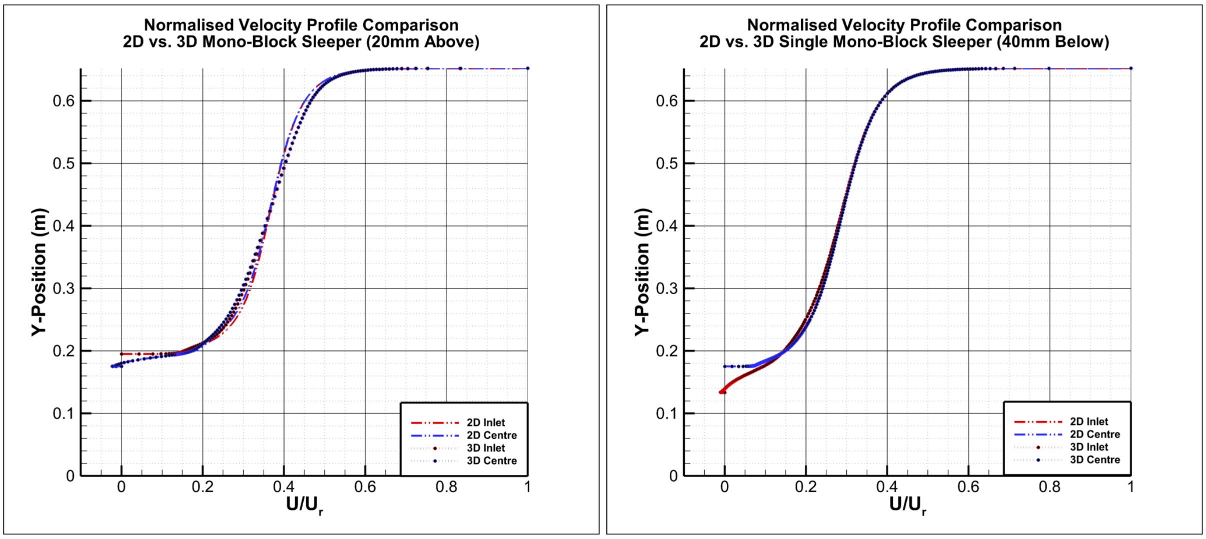

Figure 5.14: Normalised velocity comparison between the 2D moving wall case against the 3D mass flow rate case using a mono-block sleeper. Moving wall velocity at 120.0 ms^{-1}. Ballast bed 20 mm above sleeper (left), ballast bed 40 mm below sleeper (right).

The next analysis was to investigate whether modelling multiple sleeper blocks would influence the velocity profiles between sleeper blocks by comparing three cases; single sleeper block, two sleeper blocks and four sleeper blocks. Both 2D and 3D models were assessed using the techniques described previously. Figure 5.15 show that the results for each case are similar regardless the number of sleeper blocks for each ballast depth. Its also noted that on lowering the ballast depth, the average streamwise velocity profile decreases.

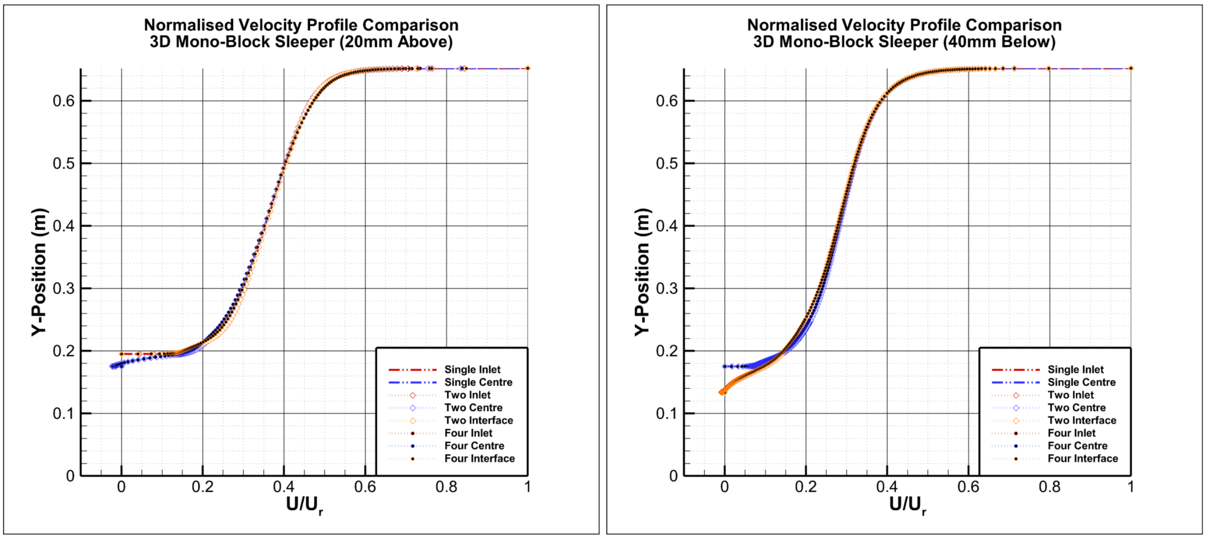

Figure 5.15: Normalised velocity comparison between one, two and four mono-block sleepers at a periodic condition. Ballast bed 20 mm above sleeper top (left), ballast bed 40 mm below sleeper top (right).

Contours on Figure 5.16 reveal similar flow behaviour when passing a cubic structure where vortices occur at the wake regions at lower speeds. The aerodynamic loads on the ballast bed surface are lower when the ballast bed is below the upper surface of the sleeper due to greater roughness heights from the sleeper blocks, increasing flow separation. However, the ballast bed experiences additional aerodynamic loads when the ballast bed is above the sleeper.

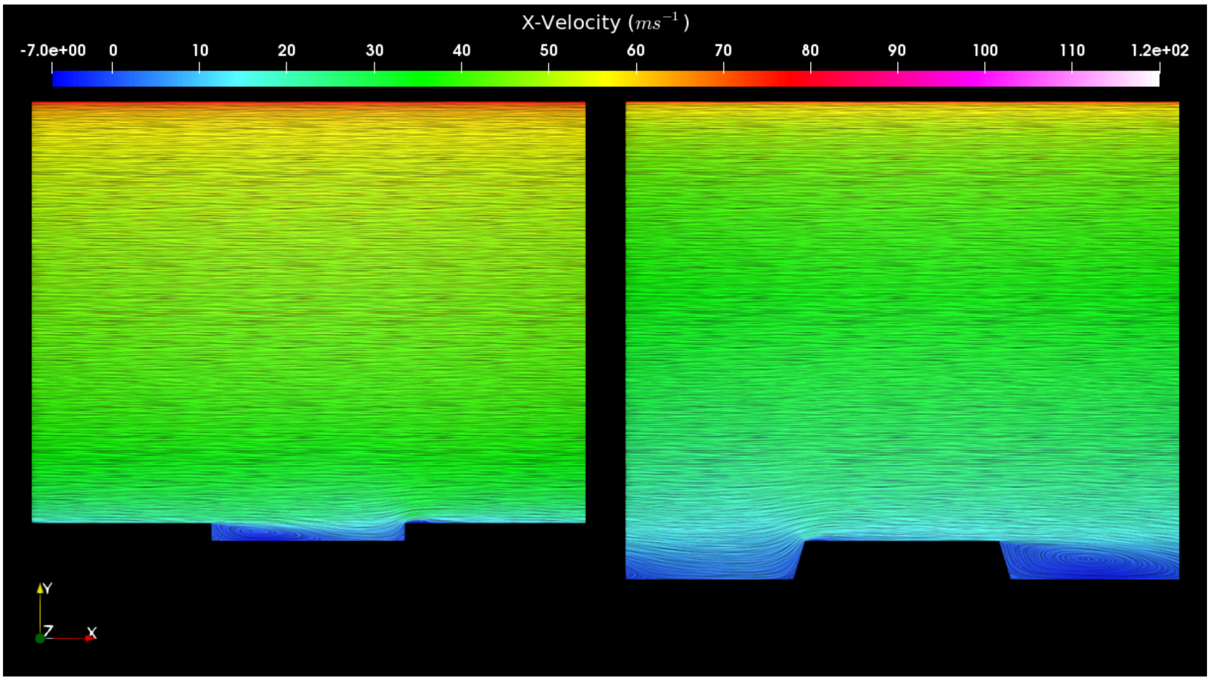

Figure 5.16: Streamwise velocity comparison across mono-block sleepers. Ballast bed 20 mm above sleeper top (left), ballast bed 40 mm below sleeper top (right).

In Figure 5.16, when the ballast bed is lowered, the velocity magnitude between the sleeper blocks is up to 10 ms^{-1}. This suggests the pressure forces on the individual ballast stones will be reduced, making ballast movement unlikely. But if the ballast level is 20 mm above the design the ballast bed is fully exposed to the flow and the top surface of the sleeper is either buried or shielded from the flow.

The mass flow rate ($\dot{m}$) in Table 5.2 supports this argument as the mass flow rate is decreased by lowering the ballast. The mass flow rate remains consistent regardless of the number of sleepers modelled, which shows that modelling one sleeper block provides sufficient information.

	Single Block $\dot{m}$	**Two Blocks $\dot{m}$**	**Four Blocks $\dot{m}$**
Mono 20mm Above	24.114	24.115	24.112
Mono 40mm Below	19.788	19.788	19.788

Table 5.2: Resulting mass flow rate of the mono-block track section from the inlet.

If the cross-section of the sleeper block is constant in the spanwise direction, the mass flow rate would provide quicker and realistic results if the mass flow rate from the 2D case is reasonably accurate. However, for sleepers including the G44 sleeper, the shape of the sleeper block changes in the spanwise direction. This would mean when modelling the entire sleeper block; the mass flow rate would change. Therefore when modelling whole sleeper blocks, the moving wall boundary condition would need to be applied, particularly for unsteady analysis; this would take considerable time. This for unsteady analysis, it would be better to model two sleeper blocks with periodic conditions.

The analysis procedure was repeated on different shaped sleepers before moving on to more complex studies including isolated particles, wall roughness and whole track sections. The next sleeper considered was a simplified version of the aerodynamic sleeper, with the curved upper surface of the sleeper defined using measurements provided by Bazen (2012).

Aerodynamic Sleeper

The main feature of the aerodynamic sleeper is its curved upper-surface, which is designed to prevent ballast from settling on top of the sleeper where ballast is more prone to ballast flight. However, by having a curved upper surface would likely reduce the re-attachment length of the flow, which will cause additional aerodynamic loading on the ballast bed before the flow separates from the next sleeper block. The dimensions used to model the sleeper was found on Bazen (2012). The curved surfaces on Figure 5.17 would need to be exposed to fulfil their purpose when surrounded with ballast.

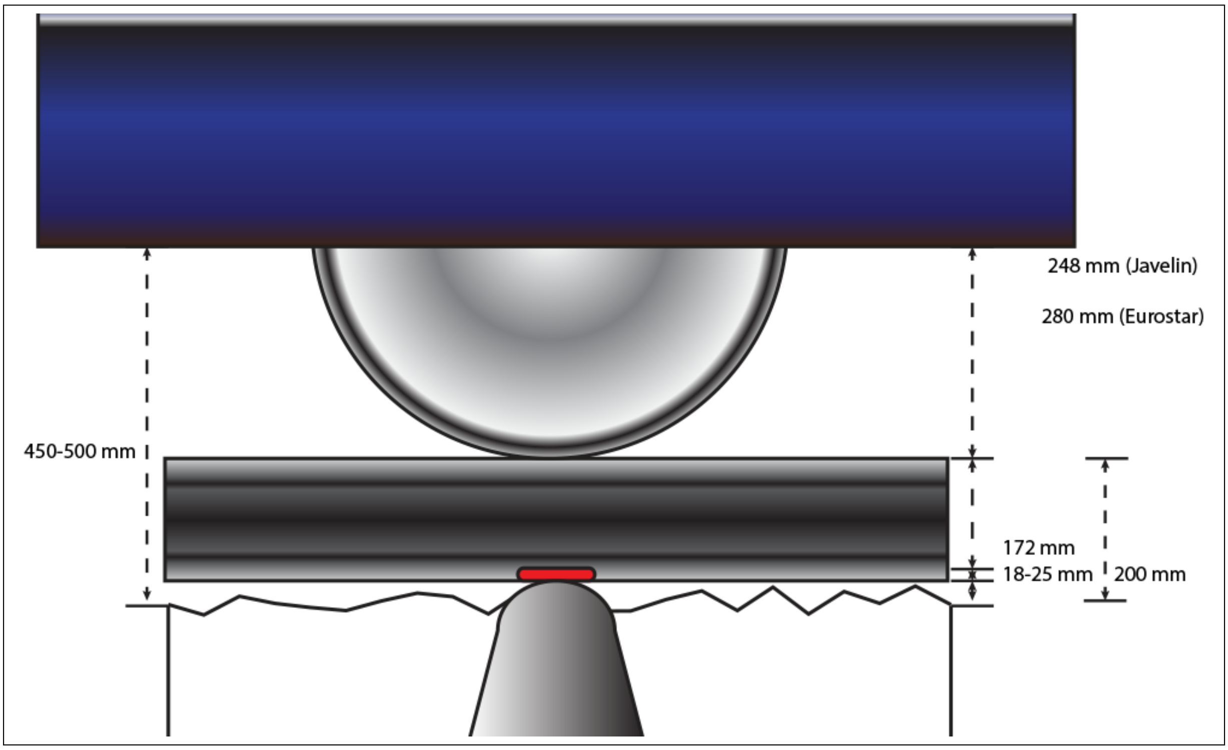

Figure 5.17: Problem specification for the cross-section CFD analysis of aerodynamic sleeper blocks (Not to scale).

Three meshes were produced for this case, with the ballast level at 40 mm below to 20 mm above (Figure 5.18), the design ballast level.

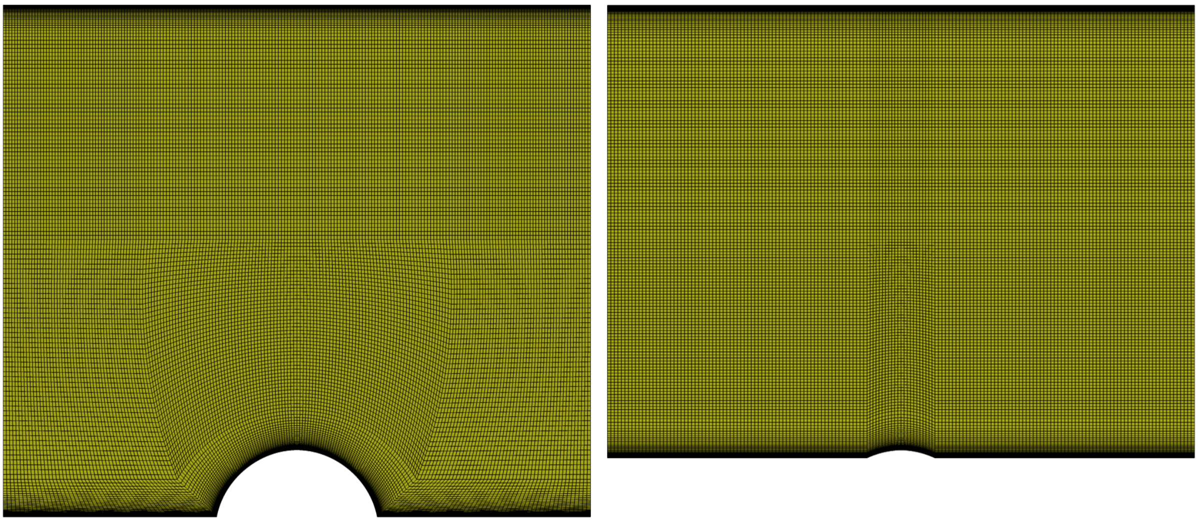

Figure 5.18: Aerodynamic sleeper cross-section with ballast depth 40 mm depth (left), ballast depth 20 mm above (right).

For the ballast level 20 mm above design, the small exposure of the sleeper block would provide a similar outcome to the channel flow study since the velocity profiles are similar in Figure 5.19. The velocity profiles in Figure 5.19 confirms that due to lower sleeper roughness. Again, the results on Figure 5.19 show similarity for each case where the number of sleeper blocks modelled had little influence in the results.

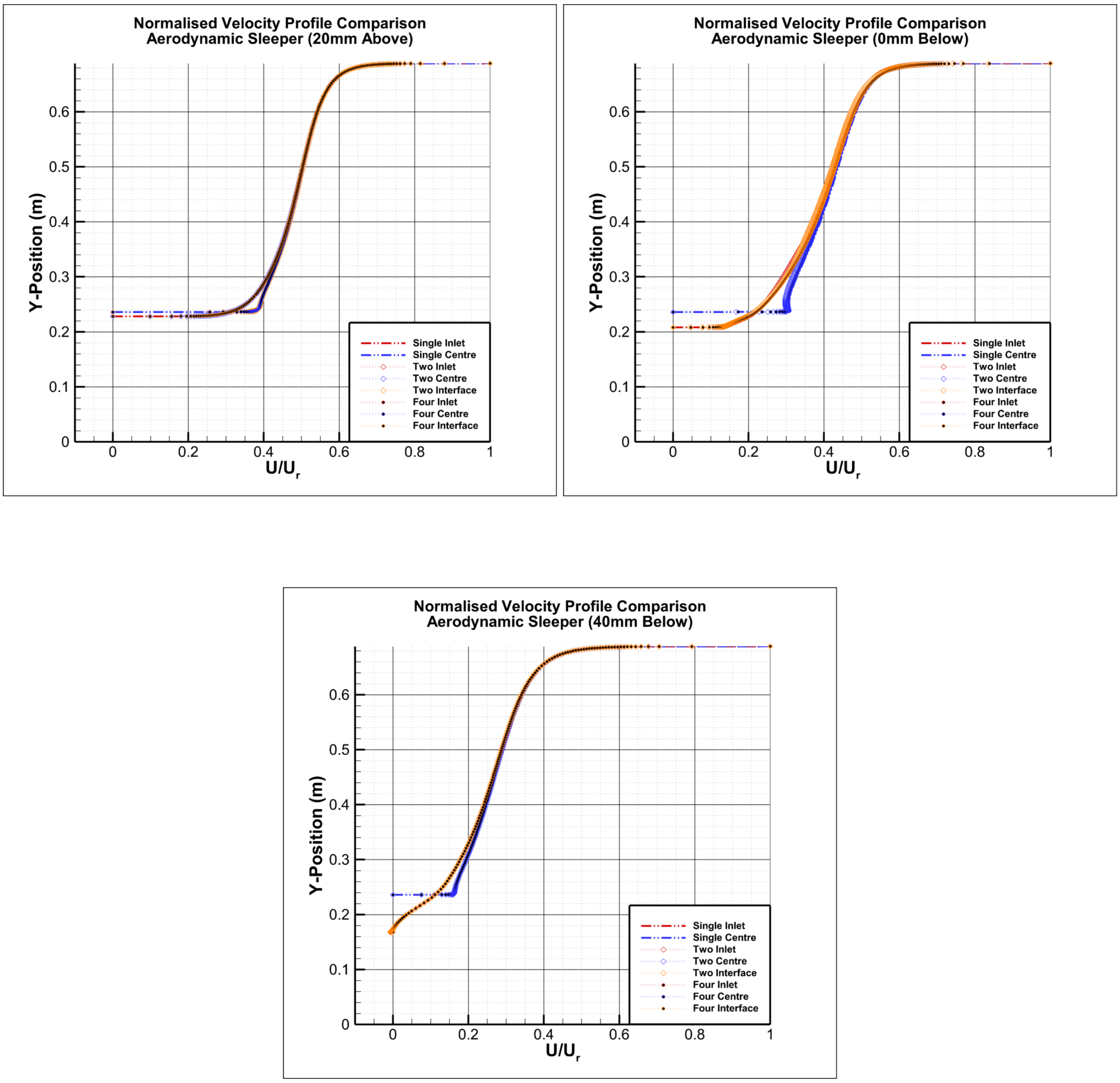

Figure 5.19: Normalised velocity comparison between one, two and four aerodynamic sleepers at a periodic condition. Ballast bed 20 mm above (left), at (right) and 40 mm below design level (bottom).

The streamwise velocity contours reveal smaller reattachment lengths owing to the curved surfaces of the sleeper. This can be problematic if the spacing between the two sleeper blocks are too big. As stated in the mono-block case, lowering the ballast depth increases the wake length and gives smaller velocities in-between sleepers due to roughness effects.

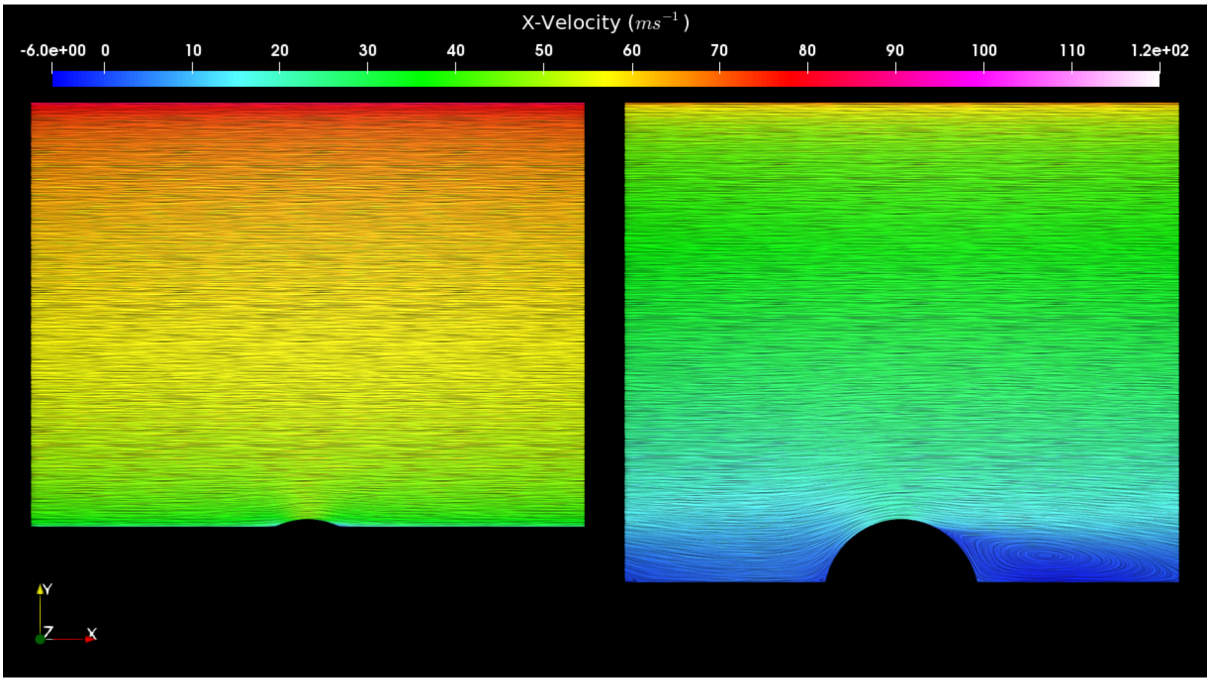

Figure 5.20: Streamwise velocity comparison across aerodynamic sleepers. Ballast bed 20 mm above (left) and 40 mm below design level (right).

The main beneficial effect of the aerodynamic sleeper is to prevent ballast from settling on top of the sleeper, where it is at greater risk of becoming airborne. However, the shape of the sleeper also reduces flow separation and reattachment length, which means that the ballast bed will experience additional aerodynamic loads especially if the ballast level is above the design level. Therefore, the aerodynamic sleeper is only effective if the ballast level is low enough. This is backed up by comparing the calculated mass flow rates from Tables 5.2 and 5.3, which show that the mass flow rate is higher than for the mono-block sleeper when the ballast level is not low enough.

	Single Block $\dot{m}$	**Two Blocks $\dot{m}$**	**Four Blocks $\dot{m}$**
Aero 20mm Above	32.137	32.137	32.137
Aero 0mm Below	27.563	26.778	26.791
Aero 40mm Below	18.294	18.306	18.306

Table 5.3: Resulting mass flow rate of the aerodynamic track section from the inlet.

The mass flow rate between each sleeper block is greater due to the lack of the flow separation from the sleeper. The results so far reveal that:

- Flow separation is the key to reducing aerodynamic loading on the ballast bed.
- Preventing individual ballast from settling onto the sleeper block is crucial as flow separates at greater velocity magnitudes across the sleeper top surface.
- The ballast bed would need to be deep enough to reduce the flow speed on the ballast surface, since the sleeper blocks do play a role as a result of these surface roughness.

Triangular Sleeper

Changing the curved cross-section of the aerodynamic sleeper to a large enough slope can prevent ballast from settling and prevent the separated flow from reattaching before the next sleeper. Therefore, a triangular upper surface was investigated. The triangular sleeper cross-section has the same height and width as the curved surface of the aerodynamic sleeper, which makes the slope around 40 degrees (Figure 5.21). The mesh has a similar cell count as the other sleeper blocks, and is refined near the solid regions.

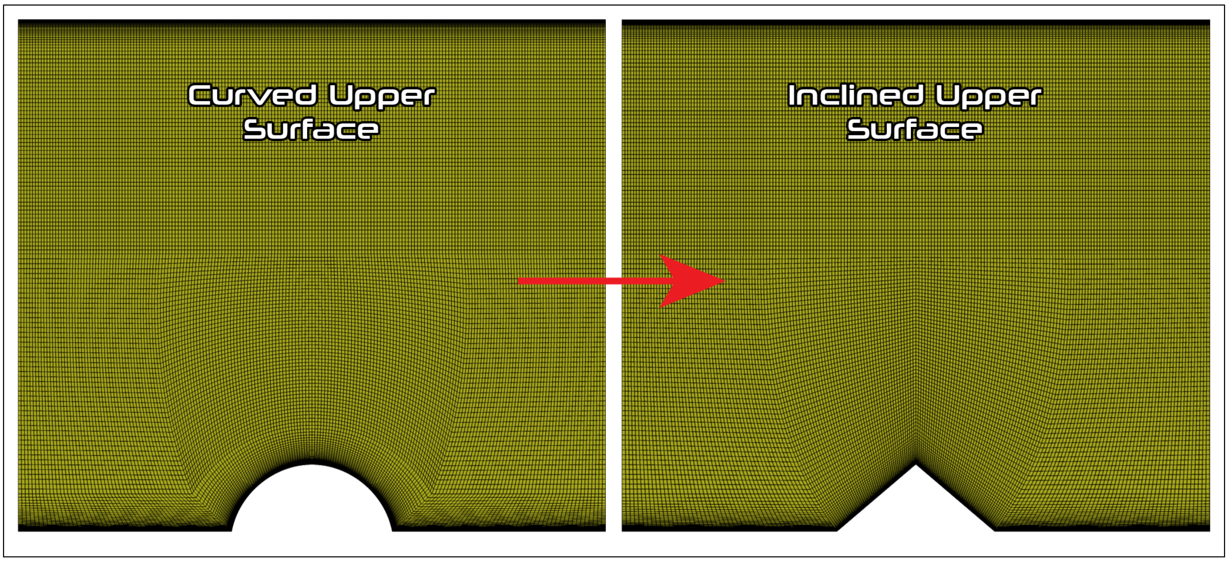

Figure 5.21: Mesh of the original aerodynamic sleeper cross-section (left), aerodynamic sleeper with sloped cross section (right).

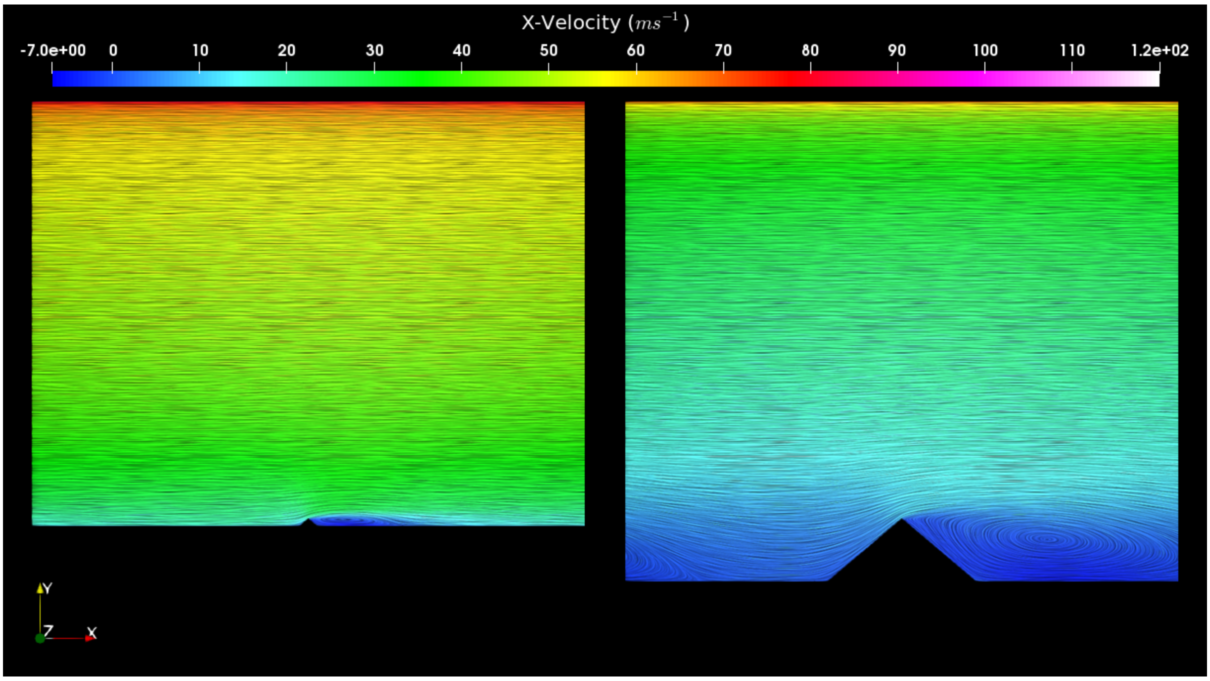

Figure 5.22: Streamwise velocity comparison across triangular block sleepers. Ballast bed 20 mm above sleeper (left), ballast bed 40 mm below sleeper (right).

Table 5.4 and Figure 5.22 shows that the triangular cross-section reduces the mass flow rate and the aerodynamic load across the ballast bed compared with the aerodynamic sleeper. It shares the same flaw as the aerodynamic sleeper when the ballast level rises but the impact has been reduced.

	20 mm Above	**0 mm Below**	**40 mm Below**
Mono Blocks $\dot{m}$	24.115	–	19.788
Aero Blocks $\dot{m}$	32.137	26.778	18.306
Tri Blocks $\dot{m}$	25.600	18.963	14.214

Table 5.4: Mass flow rate comparison of track sections.

However, for this study, only a moving wall profile has been analysed and there are no gusts or different flow angles introduced which may have an effect. If this slope is steep enough to prevent ballast settlement, then it may serve as a better alternative than the aerodynamic sleeper with further modifications such as a curved tip, different slope or a rough mesh surface on the cross-section.

In the next section, the whole track section is modelled including the sleeper blocks surrounded by ballast with isolated cubic particles placed in specified positions on the track, to confirm where ballast is likely to move and what track configurations can potentially prevent ballast movement.

5.4 Unsteady Analysis of Railtrack Sleepers with Isolated Particles

This expanded study was carried out to analyse the flow behaviour across the ballasted track by modelling a whole track section, with isolated cubes placed at certain locations to determine where ballast movement is likely to occur. The distance between the sleeper blocks and to the train underbody was similar to those in the previous section. The sleeper blocks were not of uniform cross-section and it was necessary to model the two sleeper blocks entirely to represent the track study better. The ballast shoulders were also modelled as flat rather than heaped, with a shoulder length of 525 mm measured from the end of the sleeper block (Figure 5.23).

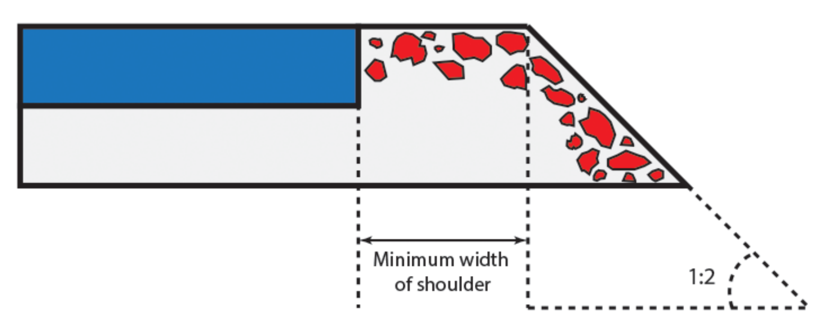

Figure 5.23: Sketch of flat shoulder ballast.

5.4.1 Unsteady analysis using Mono-block sleepers

As mentioned previously, the mono-block sleeper used was the G44 sleeper, which was measured from the Civil Engineering lab in Figure 5.24 to model the shape using CAD software.

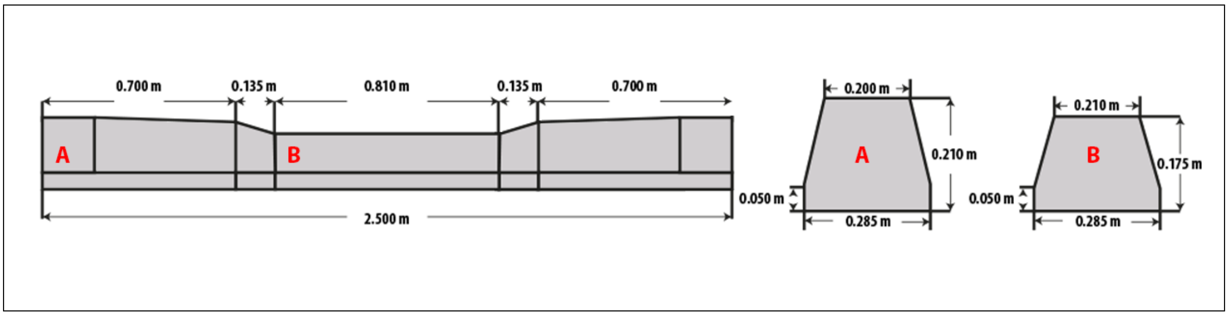

Figure 5.24: Measured dimensions of the G44 sleeper. Front view (left) and the cross-sectional view (right).

There are several variables to consider including the positions of cubes, ballast level, changes in shoulder ballast and the shape of sleeper blocks. This study involves changes in ballast depth and sleeper block geometry where the ballast shoulder remains consistent. In Figure 5.25, one cube was placed on top of the sleeper block and another two placed in between the sleeper blocks.

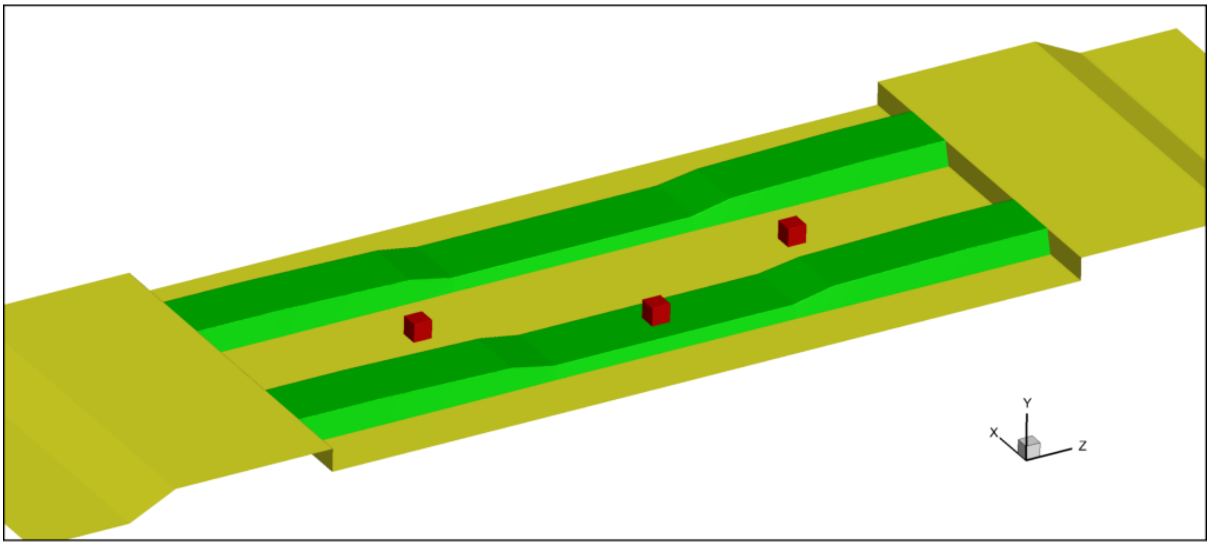

Figure 5.25: Geometry layout of the mono-block sleeper study with three cubes placed between the sleeper blocks.

The cell count for the domain was significantly higher due to the size differences between the cubes and sleeper blocks. The unstructured mesh cell count was approximately 11.1 million polyhedra cells per case, which was refined near the solid boundaries (Figure 5.26):

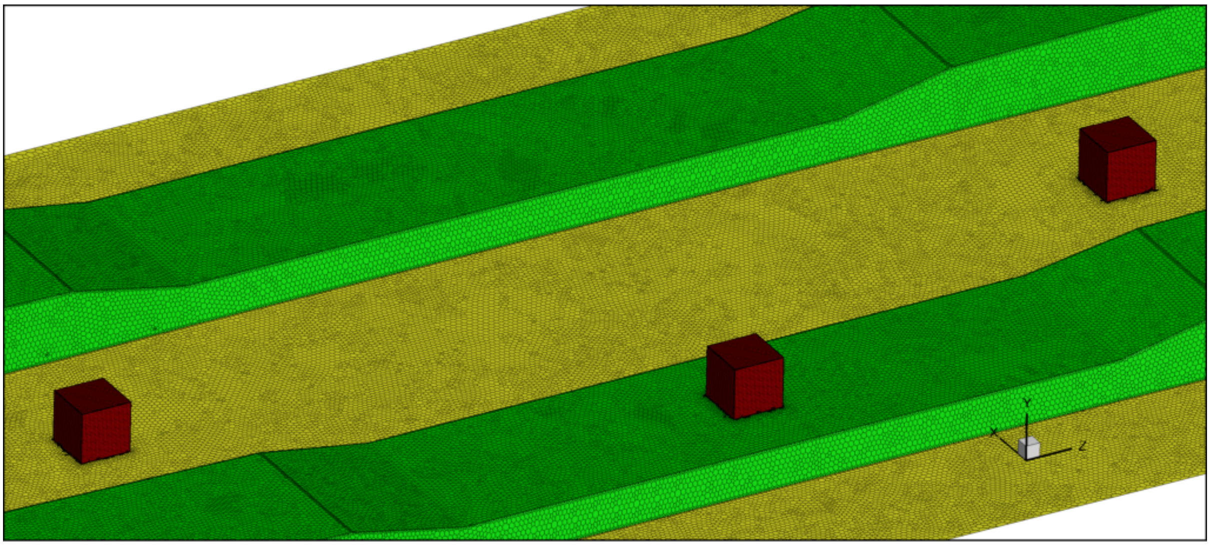

Figure 5.26: Mesh layout for the mono-block sleeper study using polyhedra cells.

The boundary conditions and physical properties of the system were similar to the previous section, where a moving wall (U_x = 120 ms^{-1}) was applied above the track with no mass flow rate or pressure gradient applied to the periodic condition. This problem is unsteady, which meant only DES was with using the SST k-ω model, allowing wall roughness to be modelled parametrically. Two ballast levels were evaluated, starting at the lowest ballast design level (40 mm below the sleeper top) to the level 20 mm above the design. The mass flow rate for the track section was monitored alongside the aerodynamic forces for each cube. It was expected that the cube(s) on top of the sleeper blocks or near the centre will encounter more aerodynamic forces than the cube(s) on the ballast bed, especially when the ballast level is below the design level. Ground roughness was applied on the ballast bed for both ballast depths to better represent the track surface.

The ballast bed could be modelled physically but doing so would be difficult to mesh. An example of modelled roughness can be a structured uniform pattern, which models a shape at a particular height (R_h), distributed uniformly similar to Lego blocks. On the other hand, the ballast bed is non-uniform with varying surface roughness affecting the boundary layer. As a result, the drag and mass transfer on the walls are affected. However, producing such a mesh would be challenging and time-consuming. Therefore, a parametric approach was applied to the ballast bed. Fluent has a feature that considers the wall roughness effects through the law-of-the-wall approach.

For each moving wall study, 2.0 seconds of flow time was calculated, enough for the flow to fully develop. The variables are time-averaged after 1.5 second of flow time, including the aerodynamic forces of each cube. The drag force development of the cube on top of a sleeper is shown in Figure 5.27, which shows a small presence initially because the flow wasn't fully developed.

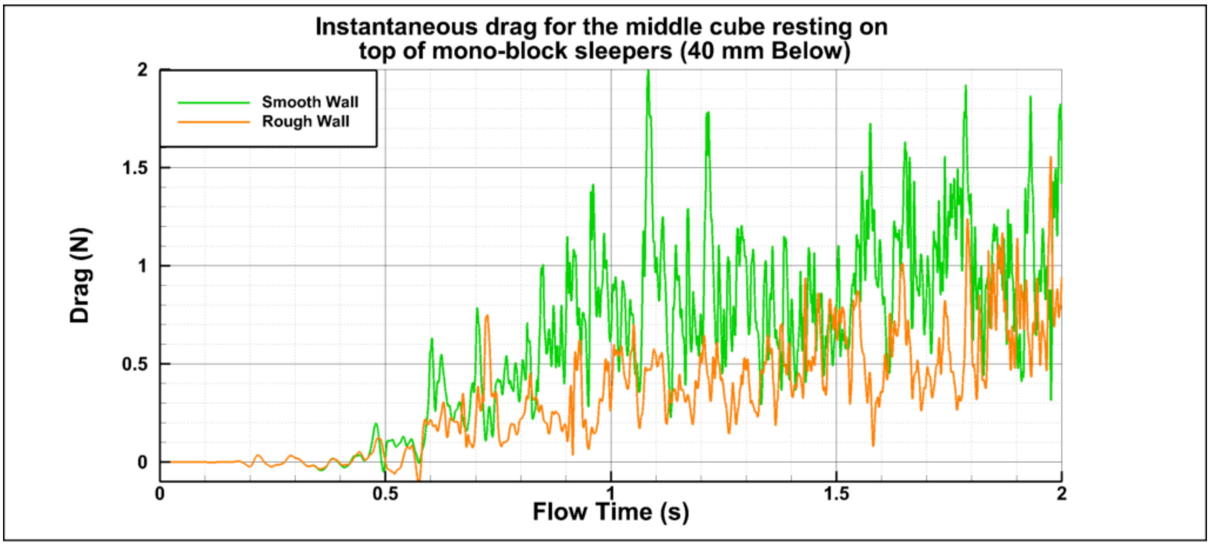

Figure 5.27: Instantaneous drag force for the centre cube resting on the sleeper block (Mono-Block 40 mm below design level).

As the mass flow rate increases, the aerodynamic forces increase unsteadily whereas, with the roughness effect applied to the ground, the drag force range increases marginally. The roughness has no effect until 0.4 seconds of flow time has passed. The mean aerodynamic forces are summarised in Table 5.5, which in both cases the cube placed on top of the sleeper has the largest lift and drag forces.

Table 5.5: Calculated aerodynamic force statistics for each cube between the Mono-block sleepers (40 mm below design).

		40 mm Below Smooth Wall				**40 mm Below Rough Wall**			
		Mean	**RMS**	**p10**	**p90**	**Mean**	**RMS**	**p10**	**p90**
Left Cube	**Drag (N)**	-0.021	0.126	-0.195	0.121	-0.014	0.143	-0.187	0.176
	Lift (N)	-0.021	0.099	-0.147	0.097	-0.039	0.117	-0.179	0.090
	Side (N)	-0.021	0.103	-0.161	0.106	-0.003	0.148	-0.175	0.156
Middle Cube	**Drag (N)**	0.921	0.977	0.540	1.346	0.538	0.581	0.301	0.832
	Lift (N)	0.776	0.802	0.531	1.050	0.449	0.473	0.287	0.664
	Side (N)	-0.135	0.336	-0.536	0.237	-0.084	0.199	-0.299	0.139
Right Cube	**Drag (N)**	0.057	0.217	-0.200	0.335	0.014	0.200	-0.207	0.259
	Lift (N)	-0.047	0.140	-0.214	0.120	-0.042	0.159	-0.214	0.129
	Side (N)	0.038	0.157	-0.143	0.241	0.011	0.180	-0.191	0.228

Table 5.6: Calculated statistics of aerodynamic force coefficients for each cube between the Mono-block sleepers (40 mm below design).

		40 mm Below Smooth Wall				**40 mm Below Rough Wall**			
		Mean	**RMS**	**p10**	**p90**	**Mean**	**RMS**	**p10**	**p90**
Left Cube	C_D	-0.003	0.016	-0.025	0.016	-0.002	0.018	-0.024	0.022
	C_L	-0.003	0.013	-0.019	0.012	-0.005	0.015	-0.023	0.011
	C_S	-0.003	0.013	-0.021	0.014	0.000	0.019	-0.022	0.020
Middle Cube	C_D	0.118	0.125	0.069	0.172	0.069	0.074	0.039	0.107
	C_L	0.099	0.103	0.068	0.134	0.058	0.061	0.037	0.085
	C_S	-0.017	0.043	-0.069	0.030	-0.011	0.025	-0.038	0.018
Right Cube	C_D	0.007	0.028	-0.026	0.043	0.002	0.026	-0.026	0.033
	C_L	-0.006	0.018	-0.027	0.015	-0.005	0.020	-0.027	0.017
	C_S	0.005	0.020	-0.018	0.031	0.001	0.023	-0.024	0.029

Therefore, if the 60 mm cubes are made of granite material, the lift force on these cube(s) will not exceed its weight (5.615 N). However for drag force, if it exceeds $m \times g \times C_k$ where C_k is the frictional coefficient of the ballast material in contact with the material of the sleeper block, the cube should roll off the sleeper block. The frictional properties may vary depending on surface roughness and whether the material is wet or dry. For the ballast between the sleeper blocks, there are additional forces including interlocking forces due to surface roughness between each ballast grain.

However, if the ballast bed was packed and raised to 20 mm above the design level the aerodynamic forces on the cubes will increase if they are placed on the ballast bed as the sleeper blocks are no longer shielding the cubes from the turbulent flow.

Table 5.7: Statistics of aerodynamic forces for each cube between the Mono-block sleepers (20 mm above the design).

		20 mm Above Rough Wall					**20 mm Above Rough Wall**			
		Mean	**RMS**	**p10**	**p90**		**Mean**	**RMS**	**p10**	**p90**
Left Cube	**Drag (N)**	0.758	0.839	0.397	1.204	C_D	0.097	0.107	0.051	0.154
	Lift (N)	0.554	0.607	0.296	0.908	C_L	0.071	0.078	0.038	0.116
	Side (N)	0.002	0.239	-0.251	0.285	C_S	0.000	0.031	-0.032	0.037
Middle Cube	**Drag (N)**	0.642	0.692	0.330	1.003	C_D	0.082	0.089	0.042	0.128
	Lift (N)	0.497	0.531	0.263	0.735	C_L	0.064	0.068	0.034	0.094
	Side (N)	0.016	0.204	-0.245	0.262	C_S	0.002	0.026	-0.031	0.034
Right Cube	**Drag (N)**	1.200	1.274	0.658	1.795	C_D	0.154	0.163	0.084	0.230
	Lift (N)	0.834	0.886	0.431	1.231	C_L	0.107	0.114	0.055	0.158
	Side (N)	0.007	0.314	-0.419	0.424	C_S	0.001	0.040	-0.054	0.054

The mean static pressure distributions in Figure 5.28 show minimal pressure forces across the ballast shoulders. Between the sleeper blocks, the largest forces are on the front surface of the sleeper block, normal to the flow. Applying surface roughness to the ballast bed reduces the range of mean static pressures, and hence reducing the aerodynamic forces on the three cubes. In both cases, only the centre cube encounters substantial pressure magnitudes that can influence its movement. The cubes between the sleepers experience less surface pressure at the front surfaces owing to flow separation between the sleeper blocks.

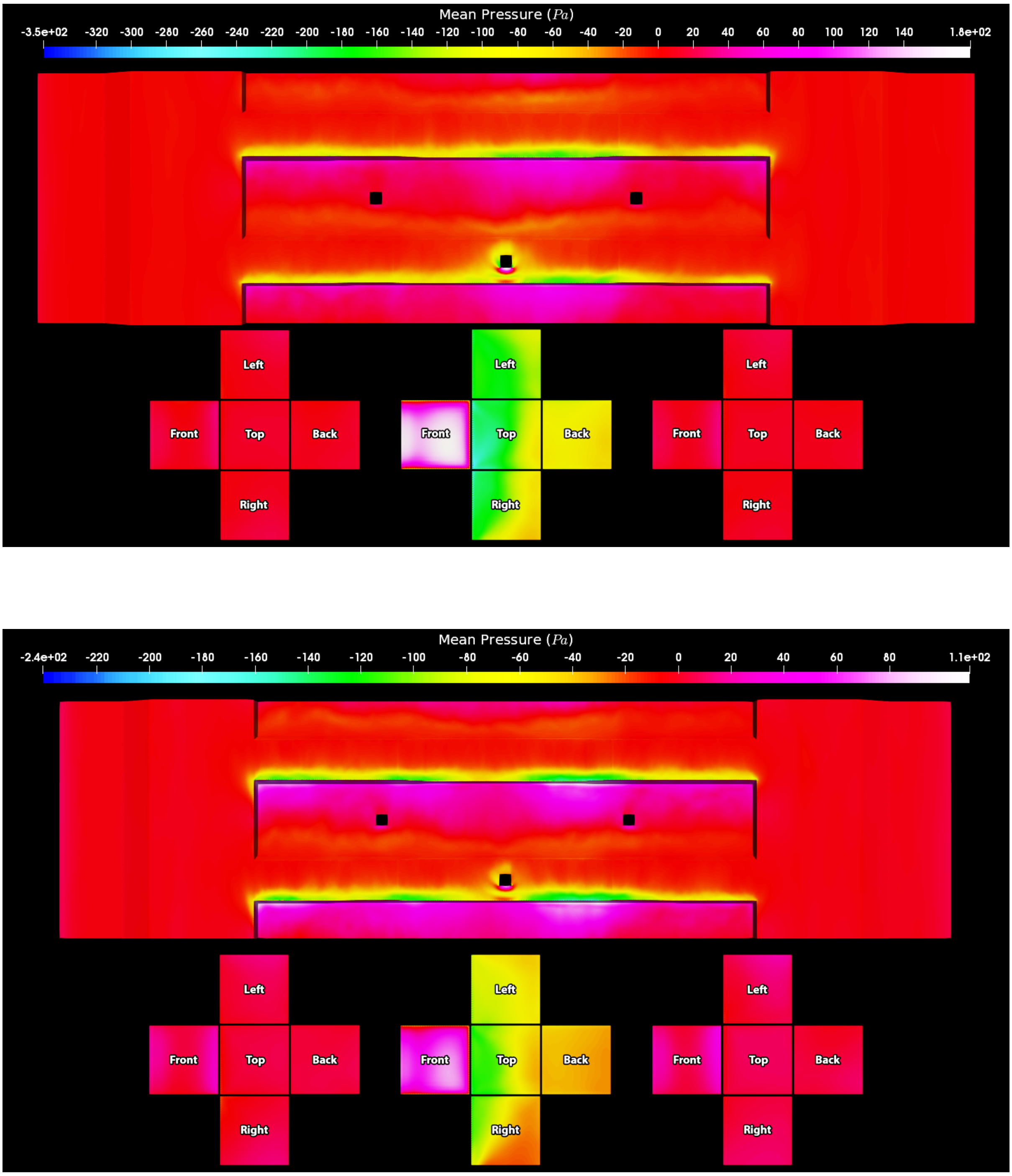

Figure 5.28: The mean static pressure across the track section using mono-block sleepers. Ballast level: 40 mm below design. With smooth ground (top), with wall roughness on ballast bed (bottom).

If the ballast bed is raised, the pressure distribution changes, making the individual ballast on top of the ballast bed more prone to displacement/flight than on top of the sleeper since the raised ballast surface is above the upper surface of the sleeper. In Figure 5.29, the ballast surface is 20 mm above design level with wall roughness applied to the ground surface.

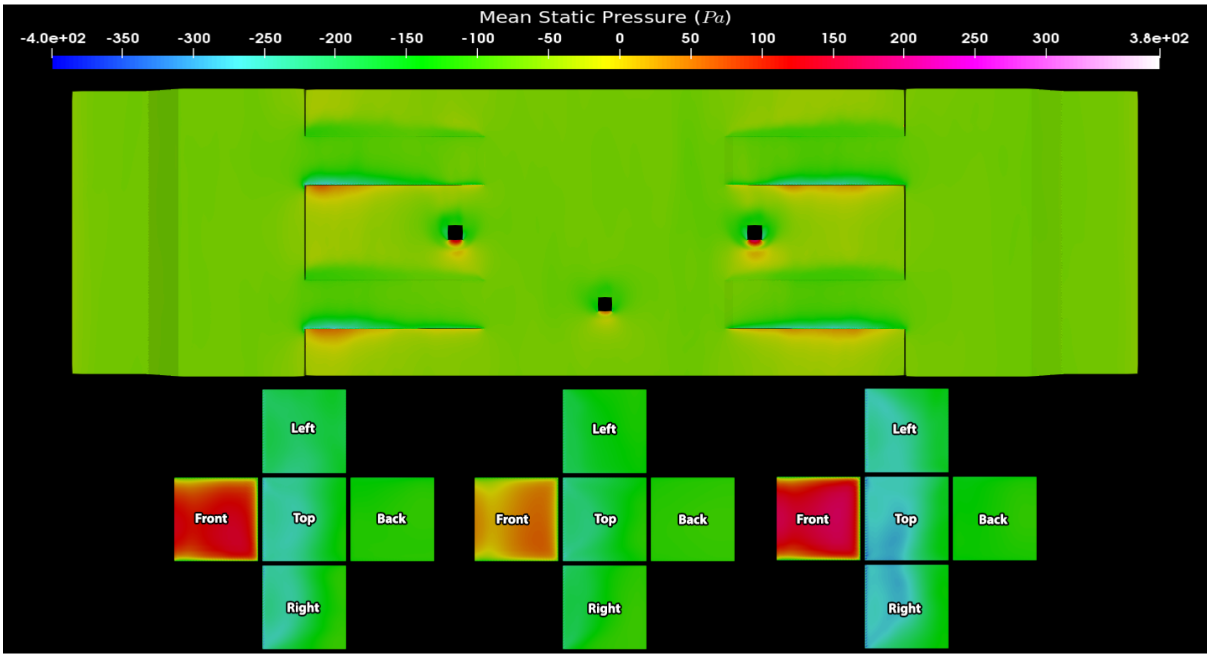

Figure 5.29: Mean static pressure distribution across the track section using mono-block sleepers. Ballast level: 20 mm above design with wall roughness on ballast bed.

The mean streamwise velocity plots in Figure 5.30 show large recirculation regions between the sleeper blocks at lower velocities. The flow re-attachment length from the sleeper is dependent on the depth of the cross-section. Owing to the physical roughness properties of the track, the mean streamwise velocity between the track and the train underbody is almost 25% of the moving wall speed, making the mass flow rate smaller.

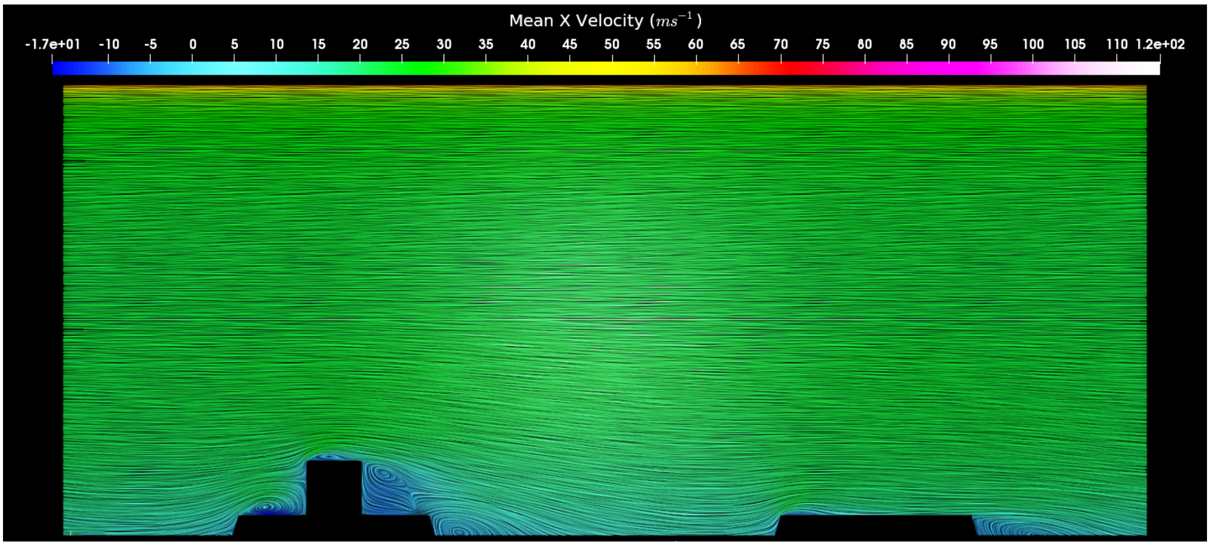

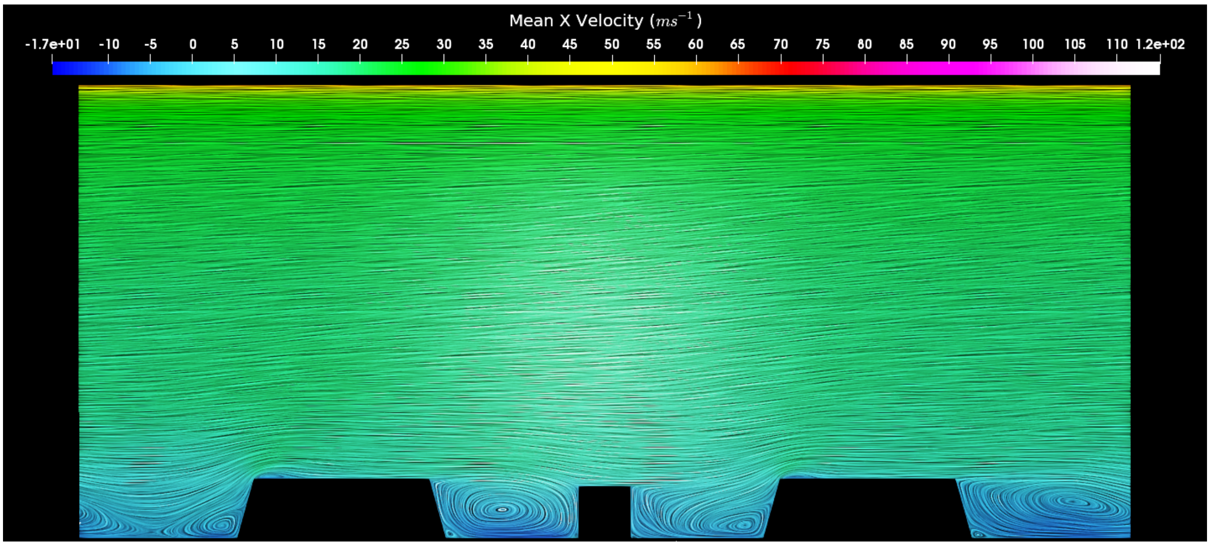

Figure 5.30: Streamwise velocity contour across the track section using mono-block sleepers. Z-plane at z/h = 0.0 (top) and z/h = 10.427 (bottom).

A spanwise plot (Figure 5.31), demonstrates how turbulent the flow is passing the track section.

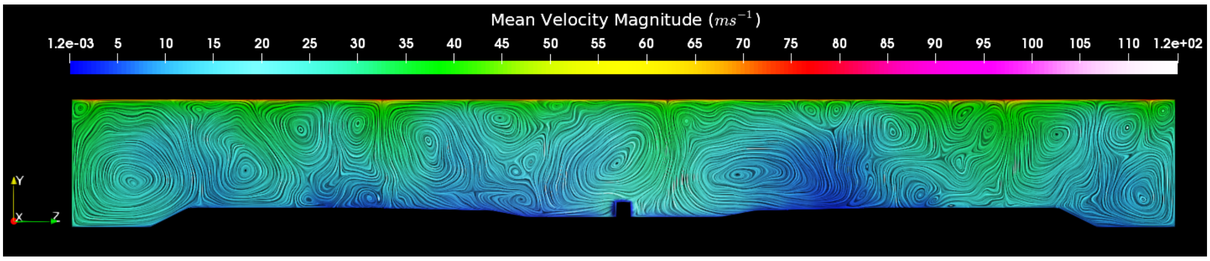

Figure 5.31: Streamwise velocity contour across the mono-block sleeper blocks using a z-plane at z/h = 0.0. Mono-block sleepers, with the ballast bed 40 mm below.

The streamwise velocities are quantified and normalised in Figure 5.32. When the ballast level is 40 mm below design, regardless of surface roughness, the freestream velocity rapidly drops from the underbody of the train from 120 ms^{-1} to speeds less than 24 ms^{-1}. The largest increase in velocity occurs when the separated flow from the sleeper passes the cube on top of the sleeper surface.

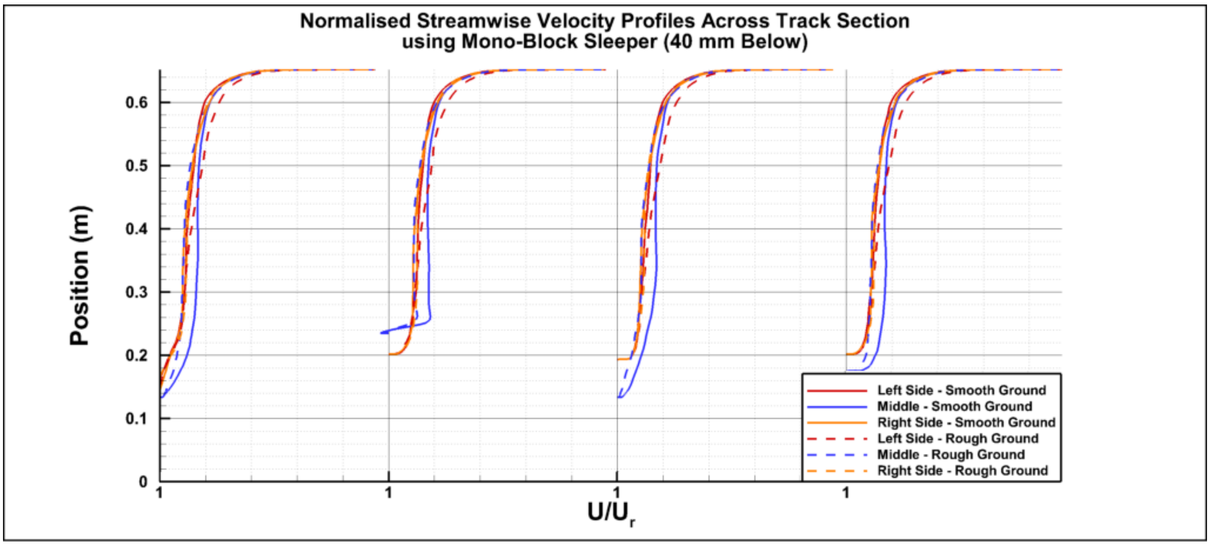

On raising the ballast level, the mass flow rate increases as the roughness effect has been reduced, which can cause recently packed ballast to move once loosened. Because the flow is unsteady, the profiles on the left and right sides of the sleeper are not symmetrical using the sampled flow time. This could be resolved by increasing the computed flow time from 2.0 seconds, at the expense of additional time and computing resources.

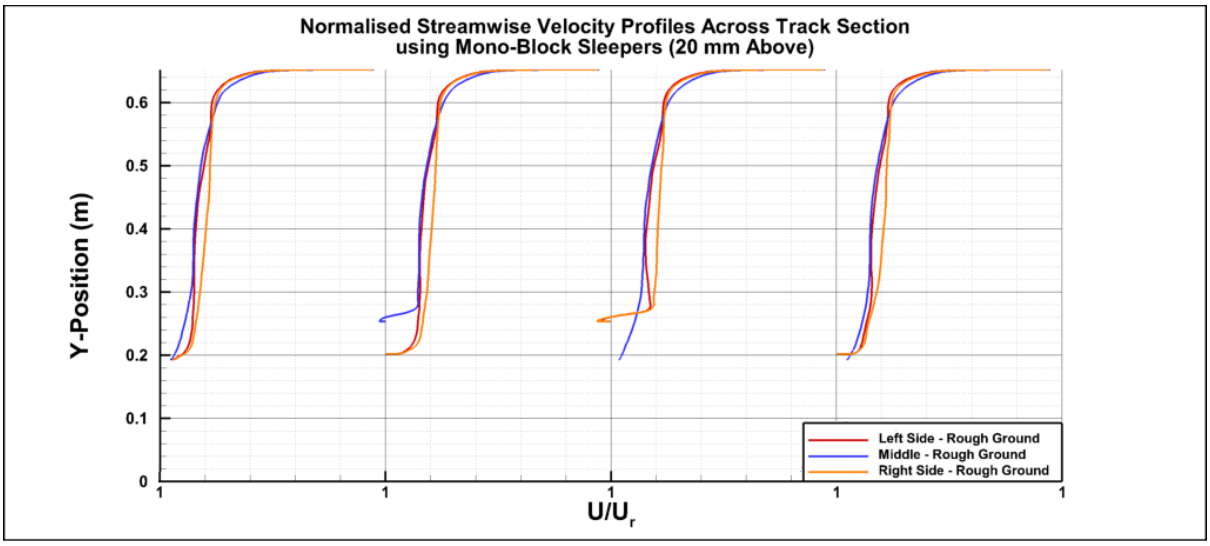

Figure 5.32: Normalised velocity profiles across the track section using G44 mono-block sleepers. When ballast level is 40 mm below design level (top), ballast level 20 mm above design level (bottom).

The changes in the mass flow rates have shown that the shape of the sleeper block affects the pressure forces more than the ballast bed surface roughness. Lowering the ballast bed would more likely prevent ballast movement by reducing the aerodynamic loads closer to its surface.

The iso-surface plot in Figure 5.33 shows two main zones in which vortices occur. The first is beneath the moving wall due to the constant shear flow generated by its movement. The other is between the track-sections and cubes at lower velocities where most of its turbulent kinetic energy is lost.

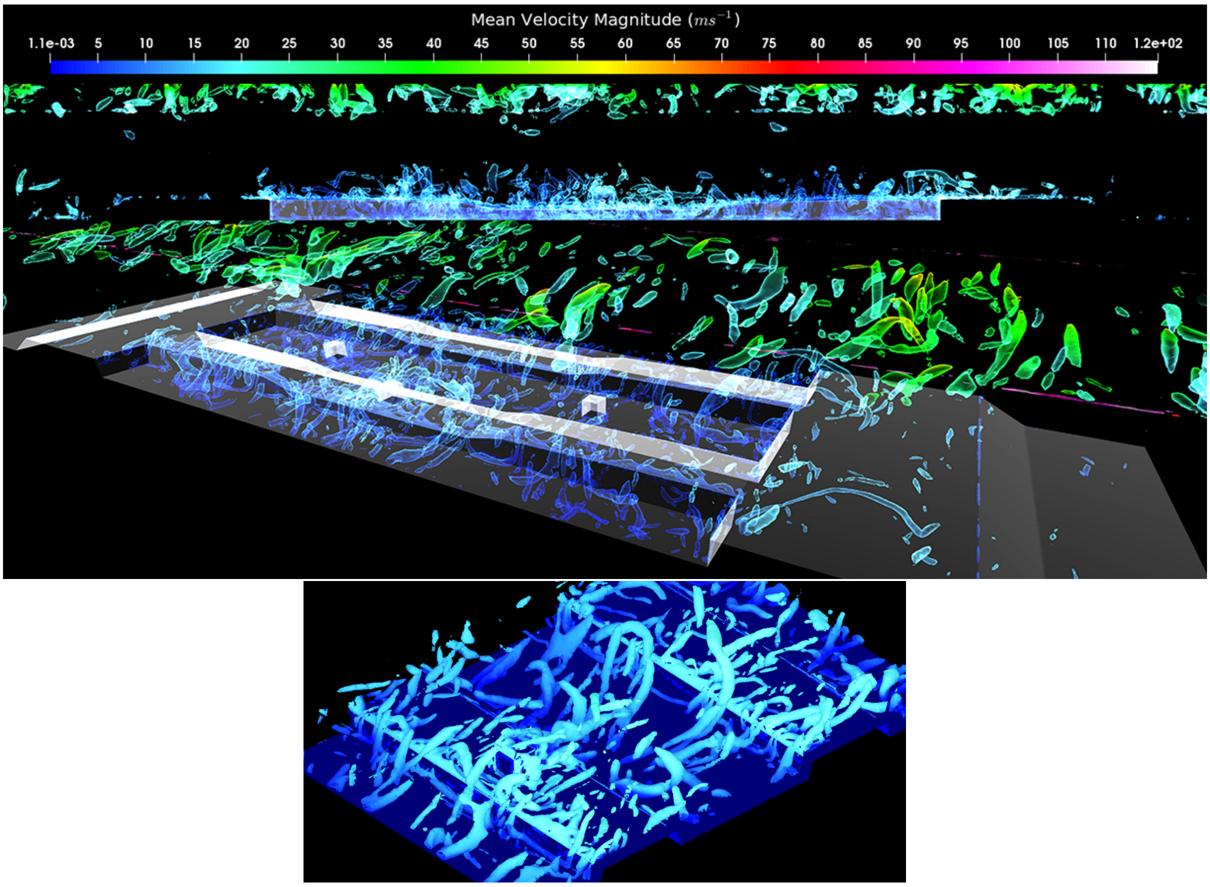

Figure 5.33: Iso-surface plot of the Q-Criterion (Q = 165,000) coloured by the mean velocity magnitude. Mono-block sleeper with a ballast depth 40 mm below design.

Figure 5.33 visualises the flow separation from the sleeper, which then clashes with the cube resting on top of the sleeper. By separating the flow using the sleeper blocks, the aerodynamic load on the ballast bed can be reduced but ballast resting on top of the sleeper block would then be prone to movement. The next phase is to repeat the study with different sleeper shapes starting with the aerodynamic sleeper.

5.4.2 Unsteady analysis using Aerodynamic sleepers

The second sleeper block considered is an aerodynamic sleeper that was developed by SENAR, known as the Aerotraviesa sleeper. No CAD files or dimensions were available to model the Aerotraviesa sleeper. The main dimensions of the sleeper block were obtained from Bazen (2012) and used to model it with the key features indicated in Figure 5.34.

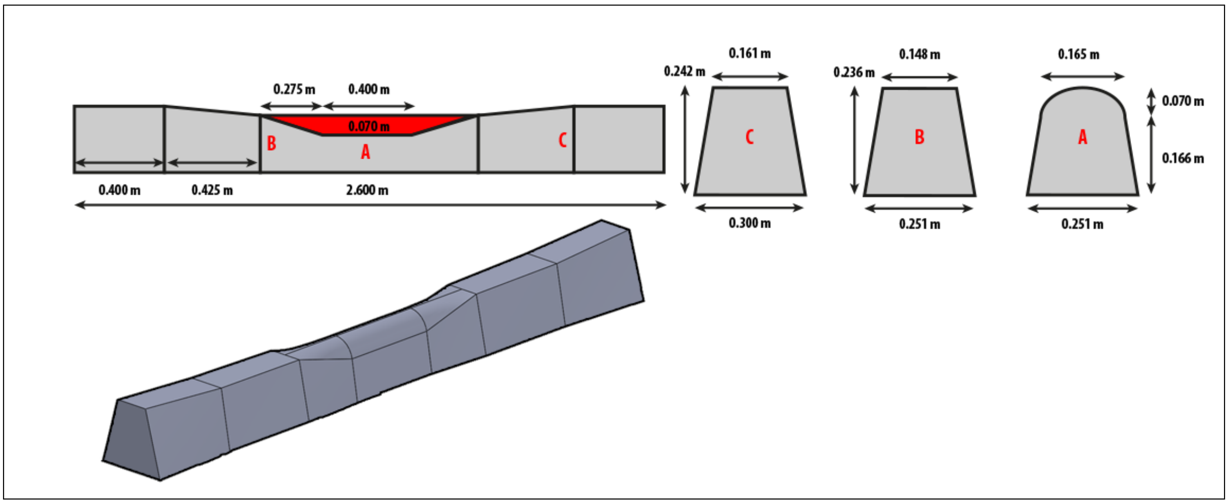

Figure 5.34: Measured dimensions of the Aerotraviesa sleeper with cross-sectional view and frontal view (top). Simplified 3D CAD model of the Aerotraviesa sleeper via Solidworks.

A simplified version of the Aerotraviesa sleeper was generated and then imported into AnSys for modelling and meshing in Figure 5.35.

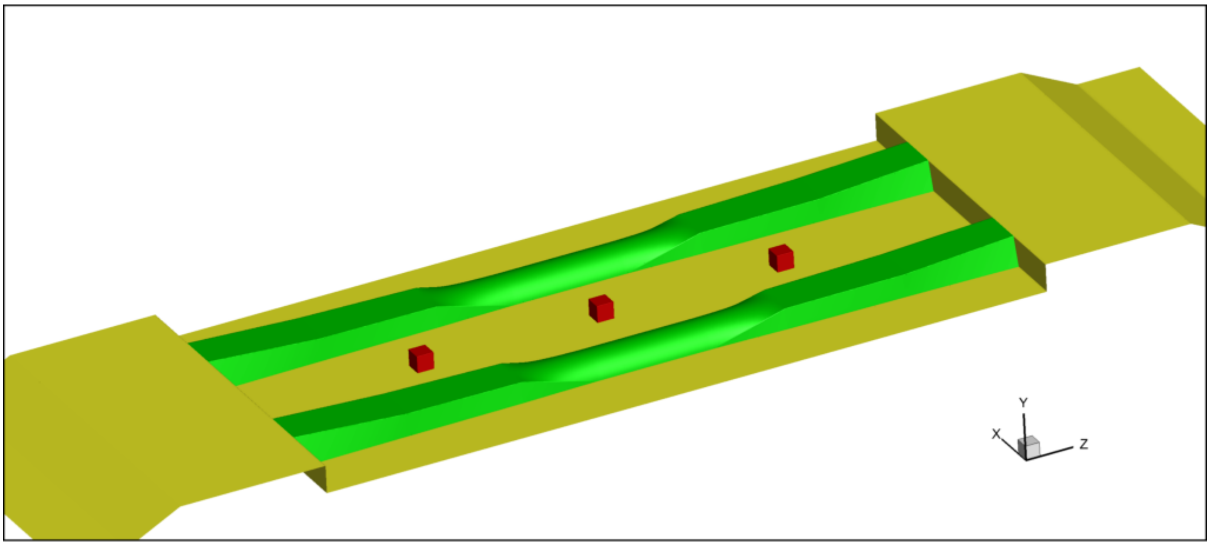

Figure 5.35: Geometry and mesh layout for the aerodynamic sleeper block study.

For this analysis, the centre cube was placed between the sleeper blocks since the design of the sleeper would prevent the ballast grain from settling on top of the sleeper. Therefore, the purpose of the analysis would be to see whether the cross-section of the sleeper block would have any influence on the separated flow that could affect the individual ballast grains.

Tables 5.8 and 5.10 summarise the statistical results for each cube from 1.5 to 2.0 seconds flow time.

Table 5.8: Calculated statistics of aerodynamics forces for each cube between the aerodynamic sleepers (40 mm below design).

		40 mm Below Smooth Wall				**40 mm Below Rough Wall**			
		Mean	**RMS**	**p10**	**p90**	**Mean**	**RMS**	**p10**	**p90**
Left Cube	**Drag (N)**	0.012	0.186	-0.200	0.247	0.046	0.234	-0.228	0.313
	Lift (N)	-0.004	0.148	-0.184	0.175	-0.065	0.172	-0.279	0.123
	Side (N)	-0.020	0.163	-0.200	0.167	0.006	0.204	-0.235	0.281
Middle Cube	**Drag (N)**	0.367	0.491	-0.032	0.848	0.162	0.229	-0.021	0.419
	Lift (N)	0.076	0.195	-0.130	0.314	0.052	0.136	-0.095	0.219
	Side (N)	-0.083	0.242	-0.344	0.198	-0.071	0.155	-0.244	0.069
Right Cube	**Drag (N)**	0.029	0.128	-0.106	0.176	0.037	0.210	-0.163	0.267
	Lift (N)	-0.009	0.121	-0.159	0.136	-0.039	0.140	-0.194	0.119
	Side (N)	0.026	0.107	-0.109	0.157	0.043	0.204	-0.165	0.242

Table 5.9: Calculated statistics of aerodynamics force coefficients for each cube between the aerodynamic sleepers (40 mm below design).

		40 mm Below Smooth Wall				**40 mm Below Rough Wall**			
		Mean	**RMS**	**p10**	**p90**	**Mean**	**RMS**	**p10**	**p90**
Left Cube	C_D	0.002	0.024	-0.026	0.032	0.006	0.030	-0.029	0.040
	C_L	-0.001	0.019	-0.024	0.022	-0.008	0.022	-0.036	0.016
	C_S	-0.003	0.021	-0.026	0.021	0.001	0.026	-0.030	0.036
Middle Cube	C_D	0.047	0.063	-0.004	0.109	0.021	0.029	-0.003	0.054
	C_L	0.010	0.025	-0.017	0.040	0.007	0.017	-0.012	0.028
	C_S	-0.011	0.031	-0.044	0.025	-0.009	0.020	-0.031	0.009
Right Cube	C_D	0.004	0.016	-0.014	0.023	0.005	0.027	-0.021	0.034
	C_L	-0.001	0.016	-0.020	0.017	-0.005	0.018	-0.025	0.015
	C_S	0.003	0.014	-0.014	0.020	0.005	0.026	-0.021	0.031

By preventing the cube from settling on top of the sleeper block, the aerodynamic forces on the centre cube have been greatly reduced in comparison to the mono-block sleeper. The left and right cubes between the sleeper blocks gave a similar results to the mono-block case, owing to under constant flow separation. Both of these have a lower surface pressure than the middle cube (Figure 5.36), hence lower aerodynamic forces.

Table 5.10: Statistics of aerodynamic forces for each cube between the aerodynamic sleepers (20 mm above the design).

		20 mm Above Rough Wall					**20 mm Above Rough Wall**			
		Mean	**RMS**	**p10**	**p90**		**Mean**	**RMS**	**p10**	**p90**
Left Cube	**Drag (N)**	0.660	0.709	0.364	0.969	C_D	0.084	0.091	0.047	0.124
	Lift (N)	0.465	0.497	0.271	0.705	C_L	0.060	0.064	0.035	0.090
	Side (N)	0.070	0.197	-0.173	0.284	C_S	0.009	0.025	-0.022	0.036
Middle Cube	**Drag (N)**	0.986	1.101	0.528	1.761	C_D	0.126	0.141	0.068	0.226
	Lift (N)	0.704	0.783	0.395	1.238	C_L	0.090	0.100	0.051	0.159
	Side (N)	0.051	0.289	-0.245	0.407	C_S	0.006	0.037	-0.031	0.052
Right Cube	**Drag (N)**	0.862	0.955	0.371	1.452	C_D	0.110	0.122	0.048	0.186
	Lift (N)	0.576	0.632	0.263	0.943	C_L	0.074	0.081	0.034	0.121
	Side (N)	-0.037	0.280	-0.388	0.285	C_S	-0.005	0.036	-0.050	0.037

Again, by raising the ballast bed increases the aerodynamic loads on each cube. In comparison with the mono-block study, the middle cube is more prone to ballast movement with the aerodynamic sleeper. This is because of the smaller presence of the sleeper cross-section above the ballast bed, causing minor flow separation. Therefore, for the aerodynamic sleeper to function properly, sufficient ballast depth is required.

In Figure 5.36, the pressure distributions across the track have changed because of the curved surface in the cross-section. The front surface of the middle cube encounters a larger surface pressure inducing drag force. The largest pressure magnitude is located at the curved surfaces of the sleeper, with a pressure distribution similar to a circular cylinder.

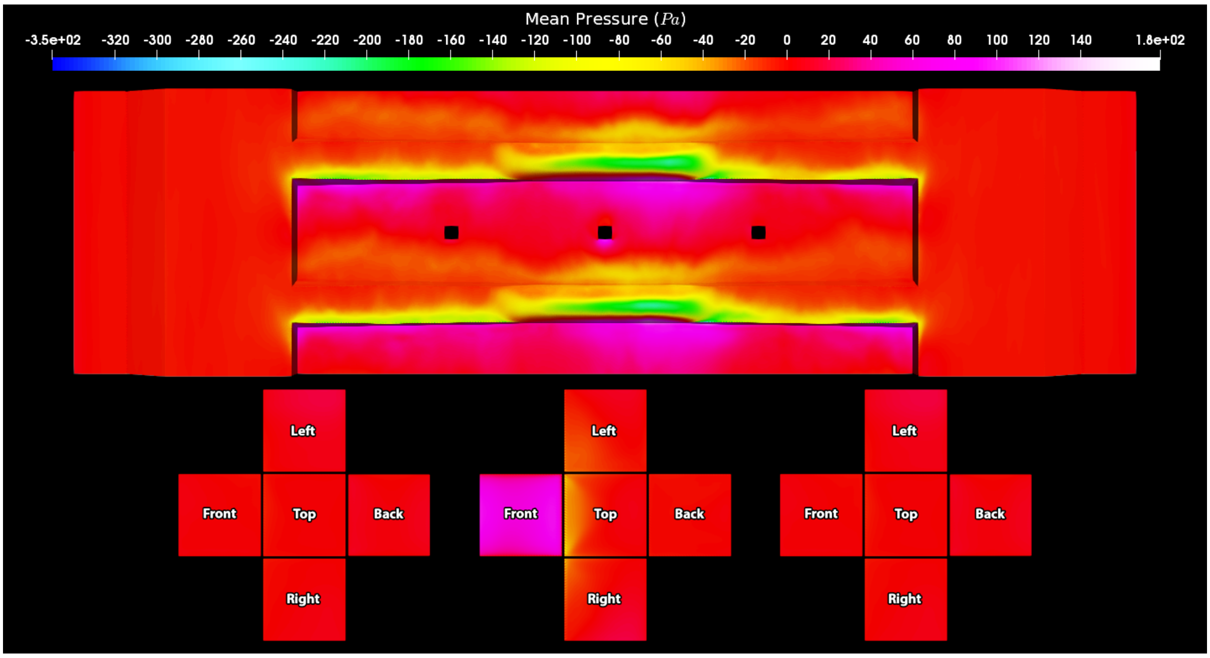

Figure 5.36: The mean static pressure across the aerodynamic sleeper. Ballast level 40 mm below design.

Owing to the smooth circular shape of the curved surface, the flow reattachment length was reduced meaning that the aerodynamic load on the ballast bed increase (Figure 5.37) compared with the mono-block shape. But given to the raised height of the aerodynamic sleeper cross-section to compensate, the aerodynamic load on the ballast bed has been reduced.

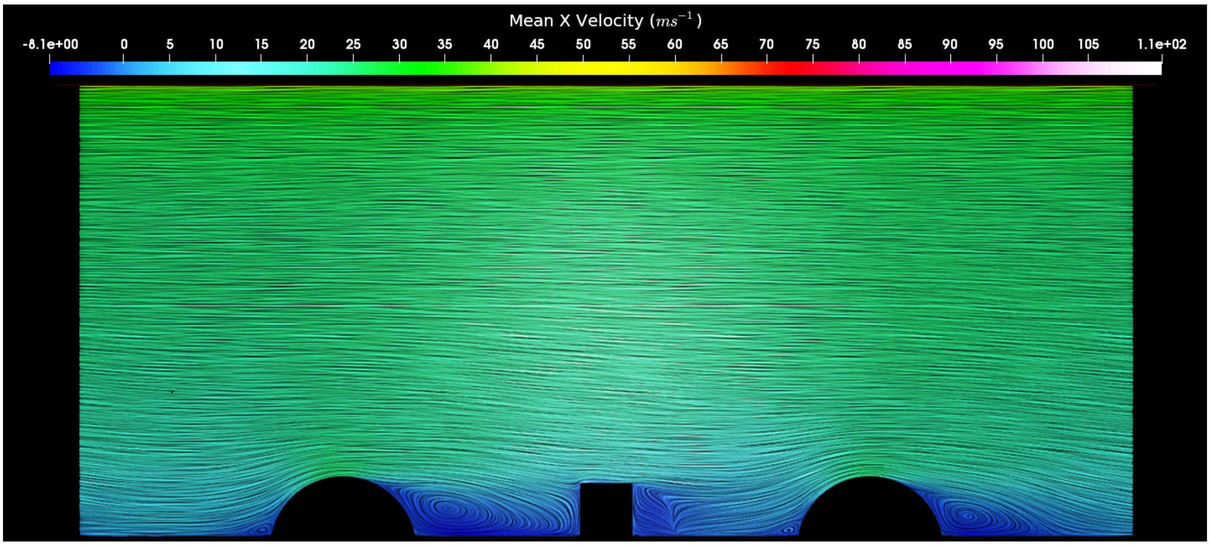

Figure 5.37: Streamwise velocity contour across the aerodynamic sleeper blocks using a z-plane at z/h = 0.0. Aerodynamic sleepers, with the ballast bed 40 mm below.

Comparing the time-averaged velocity profiles between both sleeper blocks shows small changes in the mass flow rate. It was expected that the profiles on the left and right side of the track would be similar but due to the unsteadiness of the turbulent flow, the profiles are asymmetrical.

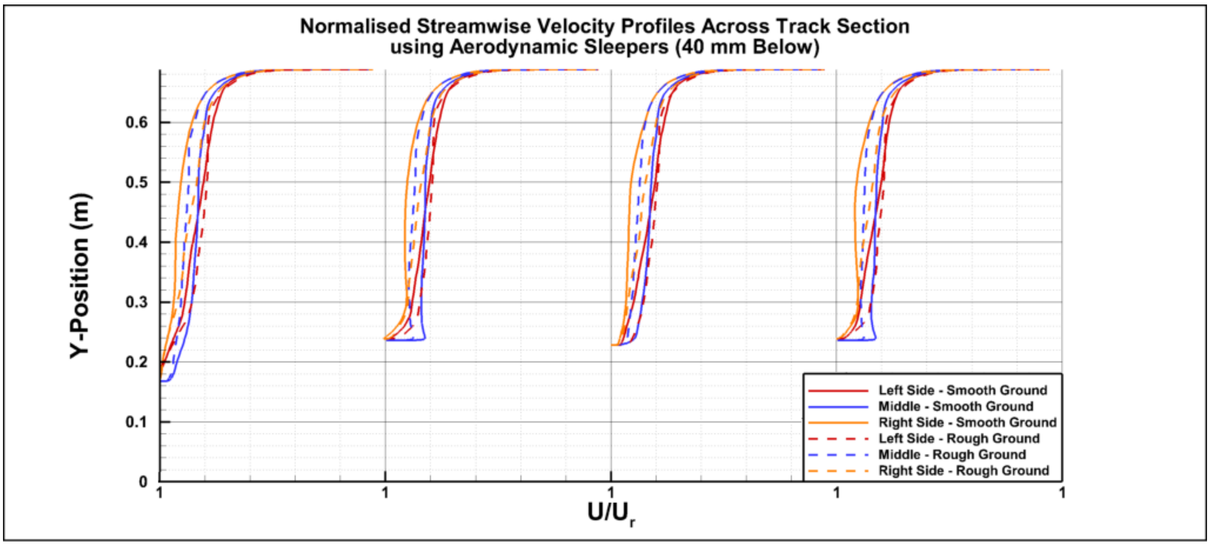

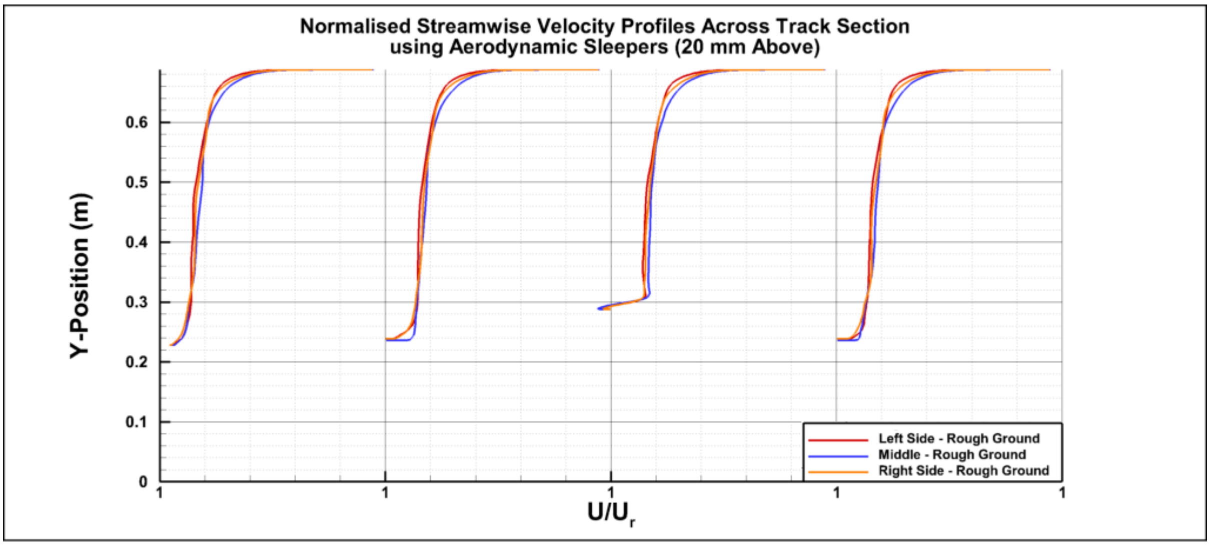

Figure 5.38: Normalised velocity profiles across the track section using aerodynamic sleeper blocks. Ballast level is 40 mm below design level (top), ballast level 20 mm above design level (bottom).

Again, with the raised ballast, the average streamwise velocity profiles (Figure 5.38) have increased. Due to the smooth shape of the sleeper block, the flow shows a shorter re-attachment length as visualised in Figure 5.37.

In Figure 5.39, the general vortices are similar except in the middle, where turbulent layers are formed across the front half of the cylindrical surface.

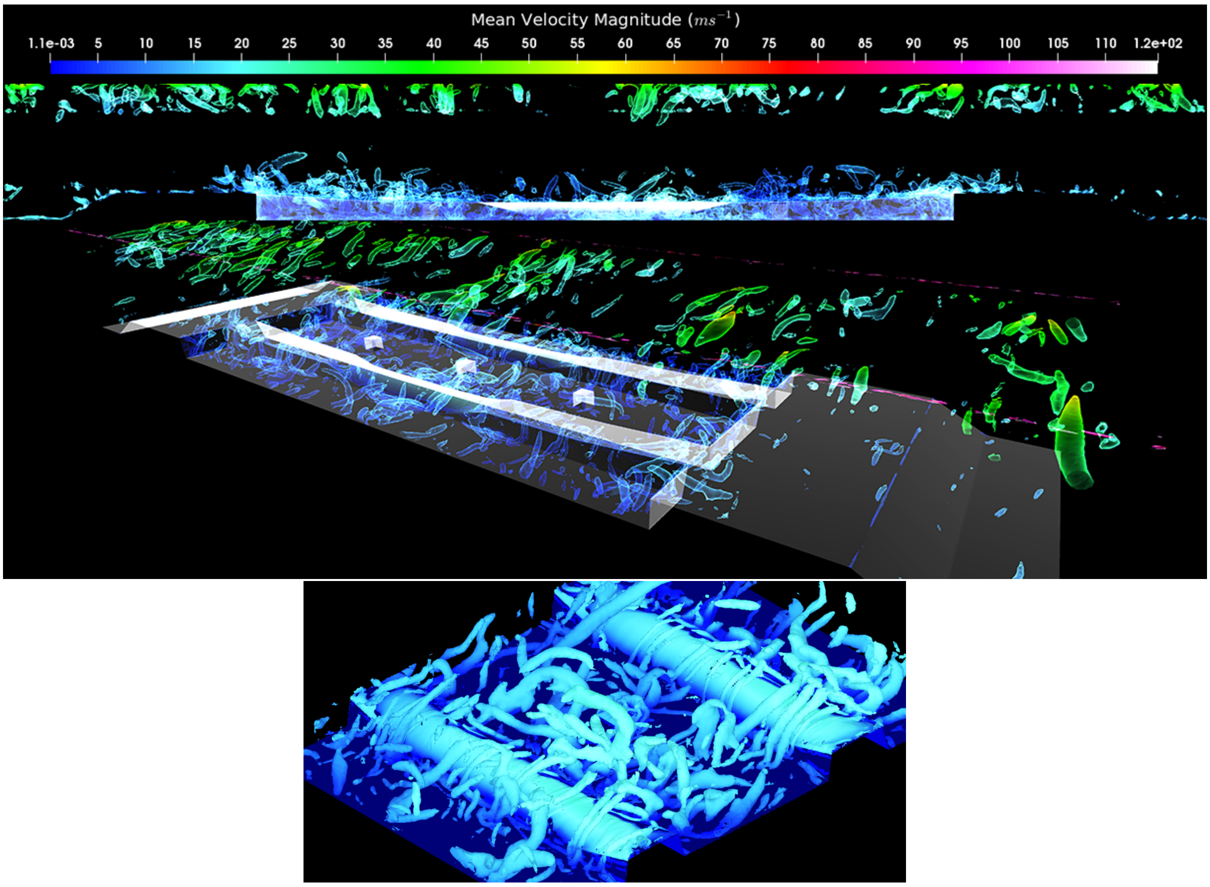

Figure 5.39: Iso-surface plot of the Q-Criterion (Q = 165,000) coloured by mean velocity magnitude. Aerodynamic sleeper with ballast depth 40 mm below design.

Following the analysis of the aerodynamic sleeper, it was concluded that the middle section of the sleeper had to be raised to counteract the smaller flow separation caused by the curved upper surface of the sleeper whilst preventing ballast from settling on top of the upper surface. Therefore, redesigning the shape of the middle section may improve the aerodynamics around the track. The curved upper surface was replaced with a sharp triangular shape in an attempt to increase the flow separation.

5.4.3 Unsteady analysis using Triangular sleeper blocks

Based on the previous results, the middle section of the simplified aerodynamic sleeper was replaced with a sharp edge of the same height and length of the curvature (Figure 5.40).

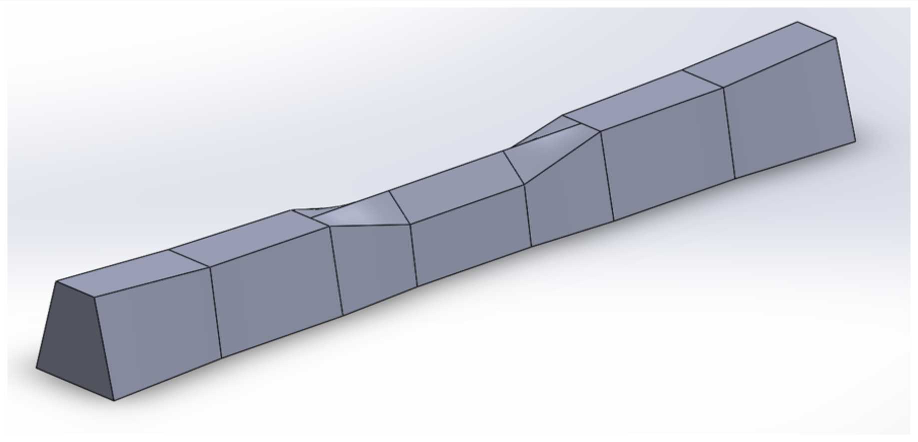

Figure 5.40: Simplified three-dimensional CAD model of the Triangular sleeper via Solidworks.

The cube placements were the same as the aerodynamic sleeper study, except that the case where the ballast was raised was neglected due to the exposed length of the middle section, which would likely produce a similar outcome as the aerodynamic sleeper block.

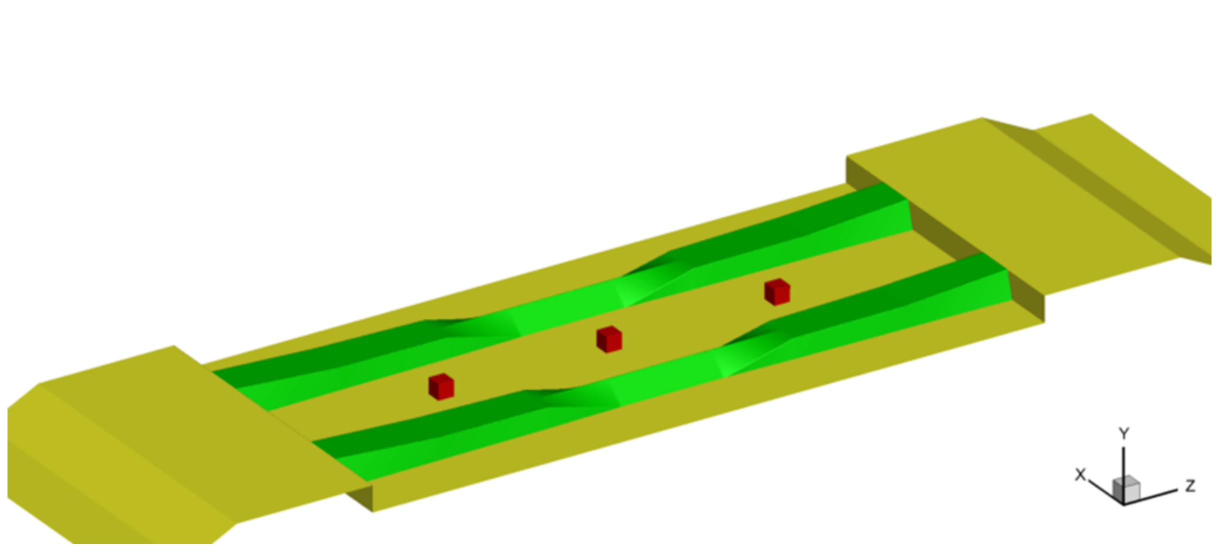

Figure 5.41: Geometry and mesh layout for the triangular sleeper block study.

Comparing the time-averaged force measurements for this sleeper (Table 5.11) and the aerodynamic sleeper. The average lift and drag forces for each cube have been reduced, which means that the risk of ballast movement should be smaller.

Table 5.11: Calculated statistics of aerodynamic forces for each cube between the triangular sleeper blocks (40 mm below design).

		40 mm Below Smooth Wall				**40 mm Below Rough Wall**			
		Mean	**RMS**	**p10**	**p90**	**Mean**	**RMS**	**p10**	**p90**
Left Cube	**Drag (N)**	0.055	0.239	-0.244	0.362	0.012	0.191	-0.219	0.249
	Lift (N)	-0.129	0.226	-0.363	0.108	-0.093	0.187	-0.293	0.109
	Side (N)	0.024	0.228	-0.221	0.322	0.033	0.229	-0.254	0.303
Middle Cube	**Drag (N)**	-0.017	0.097	-0.134	0.109	0.012	0.075	-0.075	0.108
	Lift (N)	-0.039	0.134	-0.204	0.117	-0.008	0.088	-0.122	0.089
	Side (N)	-0.007	0.086	-0.114	0.103	-0.004	0.060	-0.074	0.072
Right Cube	**Drag (N)**	0.090	0.222	-0.143	0.303	0.026	0.143	-0.126	0.215
	Lift (N)	-0.121	0.198	-0.322	0.059	-0.052	0.123	-0.201	0.077
	Side (N)	0.028	0.195	-0.213	0.259	0.012	0.158	-0.174	0.198

Table 5.12: Calculated statistics of aerodynamic force coefficients for each cube between the triangular sleeper blocks (40 mm below design).

		40 mm Below Smooth Wall				**40 mm Below Rough Wall**			
		Mean	**RMS**	**p10**	**p90**	**Mean**	**RMS**	**p10**	**p90**
Left Cube	C_D	0.007	0.031	-0.031	0.046	0.002	0.024	-0.028	0.032
	C_L	-0.017	0.029	-0.046	0.014	-0.012	0.024	-0.038	0.014
	C_S	0.003	0.029	-0.028	0.041	0.004	0.029	-0.033	0.039
Middle Cube	C_D	-0.002	0.012	-0.017	0.014	0.002	0.010	-0.010	0.014
	C_L	-0.005	0.017	-0.026	0.015	-0.001	0.011	-0.016	0.011
	C_S	-0.001	0.011	-0.015	0.013	0.000	0.008	-0.009	0.009
Right Cube	C_D	0.011	0.028	-0.018	0.039	0.003	0.018	-0.016	0.028
	C_L	-0.015	0.025	-0.041	0.008	-0.007	0.016	-0.026	0.010
	C_S	0.004	0.025	-0.027	0.033	0.002	0.020	-0.022	0.025

The static pressure distribution (Figure 5.42) changes in where the aerodynamic load is diverted in the spanwise direction, hence the frontal surfaces of the left and right cubes have larger pressure regions than the centre cube. This was due to the profile between the triangular mid section and the trapezoidal sections diverting the flow.

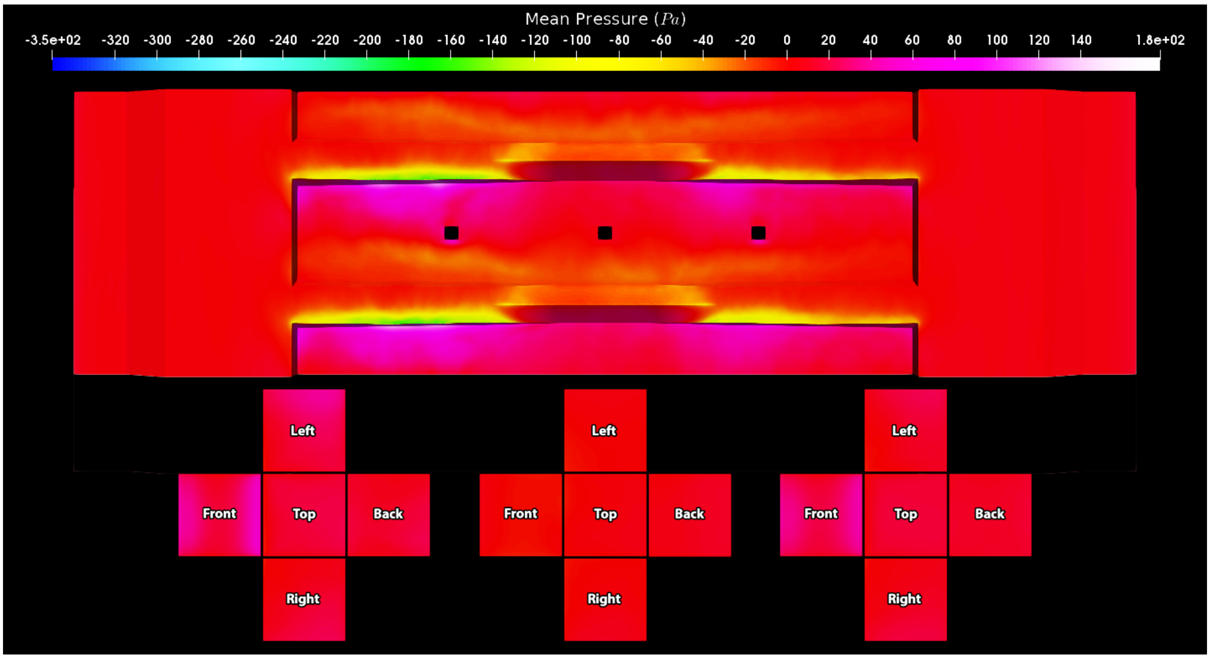

Figure 5.42: Time-averaged static pressure distribution across the track section using triangular sleepers. Ballast level 40 mm below design level.

The streamwise contour in Figure 5.43 features a stronger roughness effect than the aerodynamic sleeper because the average velocity between the triangular sleepers at the middle section is less than 10 ms^{-1}, whereas for the aerodynamic sleeper it was below 20 ms^{-1}.

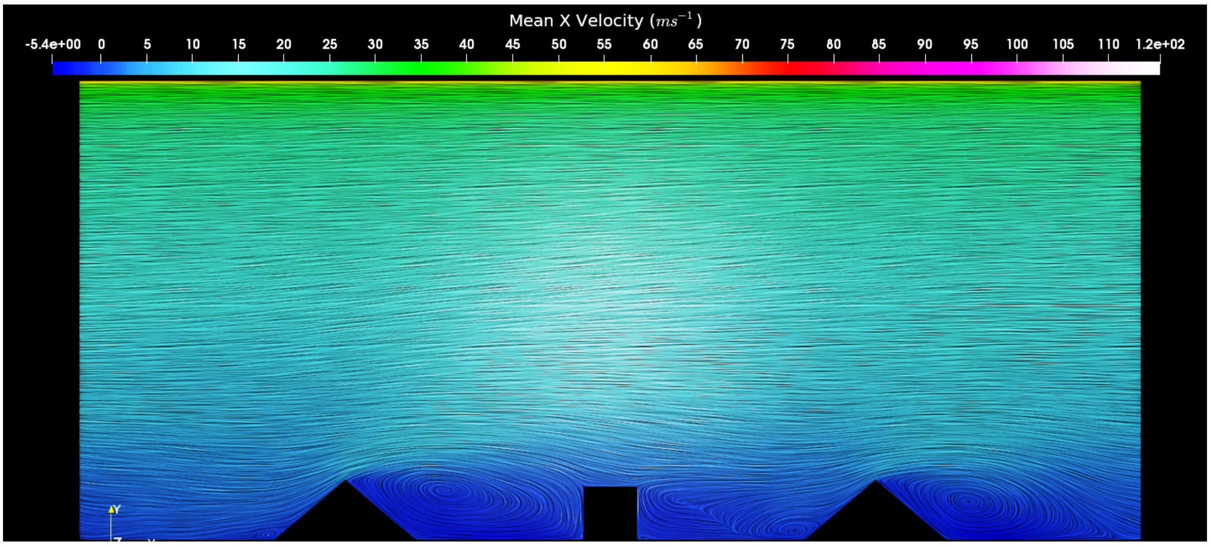

Figure 5.43: Streamwise velocity contour across the triangular sleeper blocks using a z-plane at z/h = 0.0. Triangular sleepers, with the ballast bed 40 mm below design.

This is confirmed by comparing the velocity profiles in Figure 5.44 with Figure 5.38, where the streamwise velocity near the ballast bed is smaller at the middle section when using the triangular sleeper.

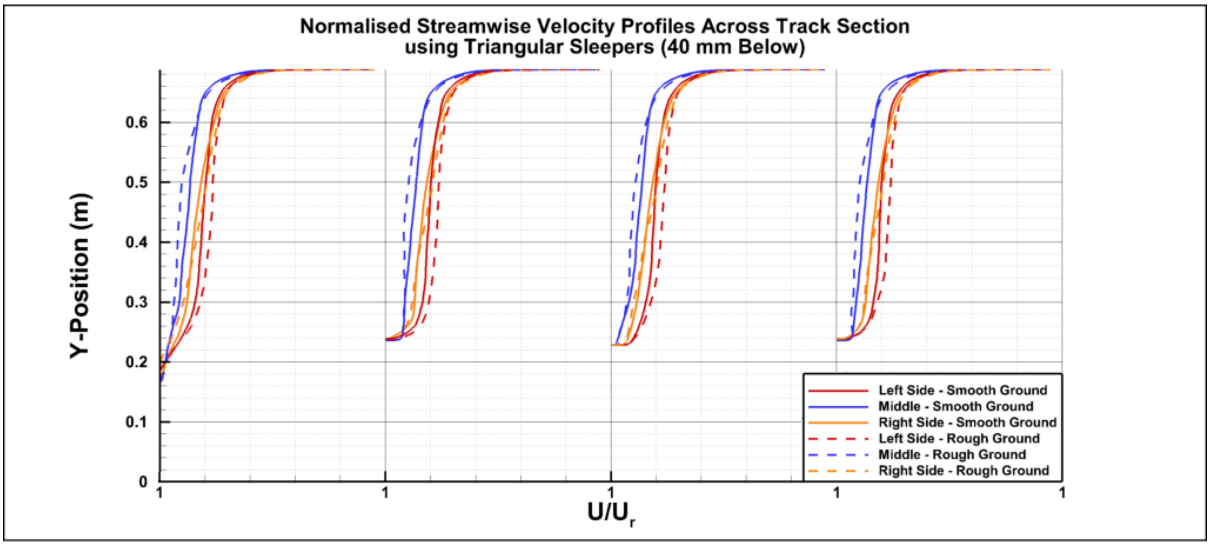

Figure 5.44: Normalised velocity profiles across the track section using triangular sleeper. When ballast level is 40 mm below design level.

The isosurface plot in Figure 5.45 features flow separation across the middle section. However, on closer inspection, the converging wedge from the middle section towards either side of the sleeper has caused some of the vortices to move in the spanwise direction, which could have been the cause of the side cubes' additional aerodynamic loads.

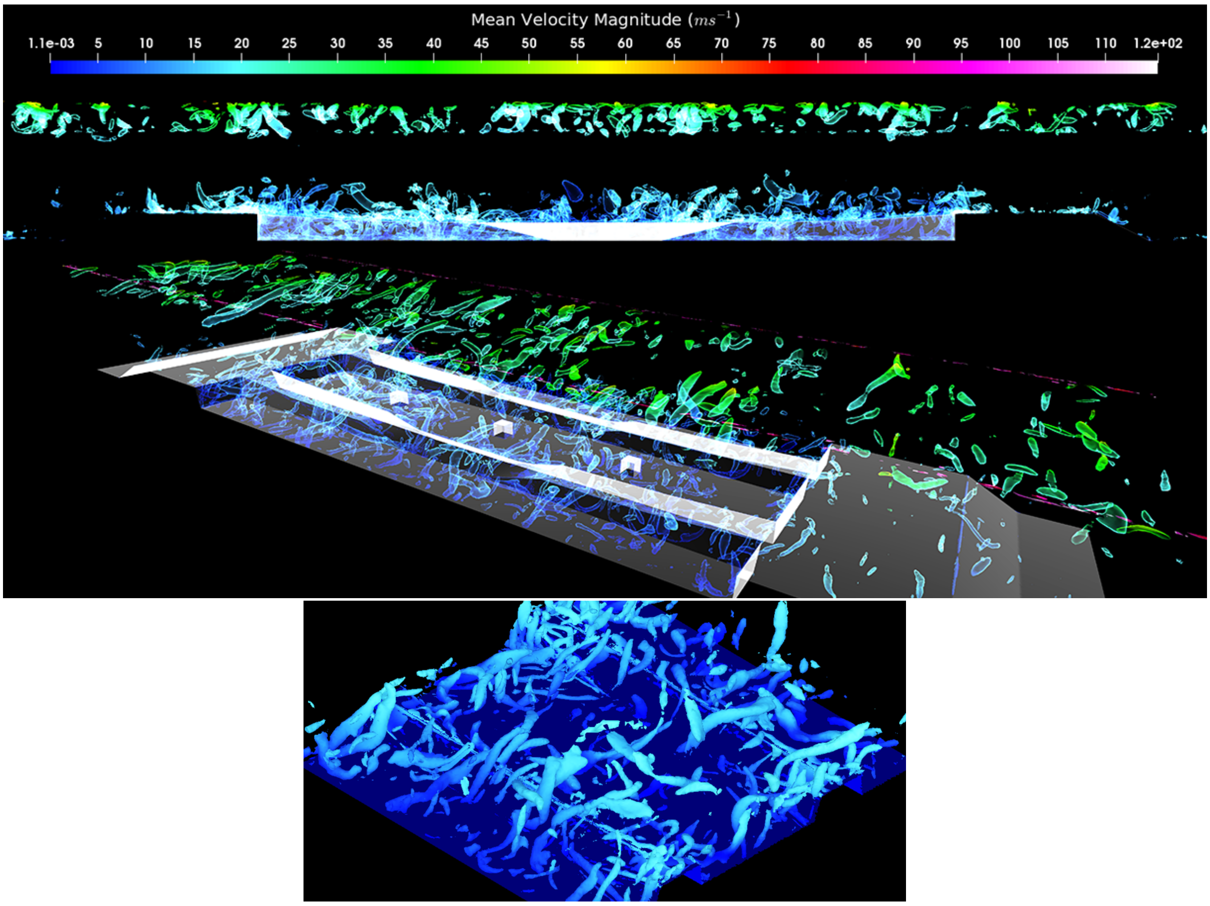

Figure 5.45: Iso-surface plot of the Q-Criterion (Q = 165,000) coloured by mean velocity magnitude. Triangular sleeper with ballast depth 40 mm below design.

The results for this sleeper have shown its potential to reduce ballast movement compared with the aerodynamic sleeper. But additional testing and modifications are required before doing so. Some suggestions may include a rounded edge on top of the sleeper to resist structural damage and to modify the face of the sleeper to provide additional surface roughness or ventilation to allow the pressure to escape. Doing so may bring additional manufacturing costs, depending on the required features.

5.5 Summary of flow over sleeper track case studies

These numerical results have provided some useful information relating to how the ballast bed and sleeper blocks can affect the movement of single particles. The results can be verified by building a small track section inside the wind tunnel and by placing isolated particles in similar locations as the CFD analysis. A full-scale track section would be ideal, but the track may need to be scaled down to accommodate the wind tunnels limitations, similarly to the 1:5 scale pictured in Figure 5.46. The ballast would also need to be glued together using resin to prevent ballast from flying across the wind tunnel or the ballast bed surface would need to be modelled and manufactured to replicate the ballast bed roughness.

Figure 5.46: Scaled model (1:5) of ballasted track using mono-block sleepers. University of Southampton.

Owing to the large cell count, these computational studies were time-consuming to establish sufficient flow to be generated from the moving wall above the sleeper. Only 2.0 seconds of flow time was simulated using DES k-ω, which showed convergence in the average mass-flow rate, which would suggest the sampled time-averaged results can provide sufficient information of its outcome.

It was found that raising the ballast bed 20 mm above the design level would cause the aerodynamic forces on cubes laying on top of the ballast bed to increase. This is because the roughness effect from the sleeper blocks is no longer applied, which means the only source of roughness to reduce the aerodynamic load would be the ballast bed surface. This was verified by comparing results with the same sleeper blocks but at a lower ballast level, reducing the mass flow rate. This is further supported by comparing the pressure distributions for each case.

However, the lateral strength between the sleepers would also decrease since the ballast holds the track in place when the sleepers are buried sufficiently. This can be solved by increasing the depth of the sleeper blocks but this would increase installation costs doing so.

In most cases, the centre cube on the sleeper experiences the largest lift and drag forces, which is why the design of the middle section of the cross-section is essential to prevent ballast movement, whilst preventing ballast from settling on top of the sleeper where it is prone to flight due to flow separation. The aerodynamic sleeper attempts to resolve this by making the cross-section a circular curve, which causes any displaced ballast to roll off its surface. But by doing so, it was found that the flow re-attaches at a shorter distance than the mono-block sleeper, which means that the height of the middle section would need to increase to increase flow separation.

Based on this analysis, a different sleeper was introduced in which the curved mid-section was replaced with an inclined slope on both sides, preventing ballast from settling while increasing the flow separation. Comparing the new sleeper results with the aerodynamic sleeper has shown a further reduction in the aerodynamic loads between the sleeper blocks, which may be worth considering for future projects (if successful in other aerodynamic tests). The current disadvantage of the sleeper geometry would be the sharp edge at the centre point, making it easier to fracture. This could be resolved by making the tip of the upper surface smoother.

In all computational analysis, it seems that the flat ballast shoulder has minimal effect on the track aerodynamics. However, this can change if the ballast shoulder has risen with a steeper incline near the track section.

Chapter 6

Conclusions and Recommended Future Research

6.1 Conclusions

A broad range of computational studies has been carried out using a range of CFD techniques, applied to simple shapes (i.e. cube and hemisphere) and more complex geometries including simplified ballast. It was found that:

- For most smooth and complicated cases, Delayed DES (SST k-ω) predicts the flow separation better than RANS and URANS, but requires a decent mesh and additional computational resources to get an accurate calculation.
- It was found that by increasing the Reynolds number, the measured force coefficients loses sensitivity.
- DES provides more realistic flow structures (visualised using Q-Criterion) than URANS since DES resolves smaller eddies whereas URANS resolves the general shape of turbulent flow.
- When the isolated particle is airborne, the side and drag forces remained the same whereas its lift force was reduced, allowing its weight and downforce to overtake the lift force. This would suggest that even in a steady flow, once the particle lifts off the ground, the particle would move freely in the streamwise direction but would also descend towards the ground.

This was shown in the cubic and hemisphere studies, where results were validated against observations made in different numerical and physical conditions. Based on the surface pressure measurements, the calculated forces were in good agreement with Castro & Robins (1977), particularly when using unsteady turbulence models with the cube wall-mounted at 90 degrees to the flow. Quantitatively results indicated that DES k-ω describes the flow separation better, especially in the spanwise direction when comparing with Castro & Robins (1977). Due to flow separation and vortex shedding, vortices are generated in the spanwise and streamwise direction around the wall mounted particle.

However, to represent the flow conditions better, the inlet flow was replaced with a moving wall condition above the cube, representing the speeding train. This meant the flow speed the particle would encounter would be a fraction of the moving wall speed depending on the location of the isolated particle.

Additional experimental analysis took place on the cube at two different angles by measuring aerodynamic forces using a force transducer. When comparing the force measurements with the calculated results using CFD it was found that the drag and side force coefficients had similar outcomes. However, the lift force was not in good agreement with the CFD results. The source of error was likely because the force transducer was pocketed inside the cube rather than wall mounted onto the test section and onto the cubic surface, which could have interfered with the force measurements in the vertical direction. The wind tunnel lab did not meet the exact flow conditions as the simulations including its Reynolds number but as stated earlier, the force coefficients at high Reynolds number should be similar. Therefore in future studies, the force transducer would need to be mounted onto the subjects bottom surface.

The computational analysis was then repeated onto a more complex geometry such as a hemisphere. By comparing results with Tavakol et al. (2014) the flow separation was more sensitive to the Reynolds number, which meant the study was repeated at different Reynolds numbers to validate before proceeding. It was noted that SST k-ω was able to calculate the flow separation correctly at a lower Reynolds number, unlike Realisable k-ε. At a higher Reynolds number, the profile shapes from each turbulence model showed similar outcomes but DES SST k-ω provided the most realistic outcome. The calculated lift and drag force coefficients of the hemisphere are lower than the cubic cases due to the smoothness of the shape. Comparing flow separation to the cube, the reattachment length is smaller, meaning its vortices is less likely to have any influence on nearby isolated particles. Therefore, SST k-ω would be ideal to calculate flow behaviour across complex geometries including ballast shapes and track sections.

The final set of computational studies took place on isolated ballast shapes, using a moving wall condition above the shape, to represent the train underbody. The shapes were simplified to reduce the difficulty in meshing, providing a flat bottom surface. Due to the complex geometries, an unstructured polyhedra mesh was defined with a greater mesh density closer to the object. Fourteen large ballast shapes was assessed in four different orientations, which meant at least 56 unsteady case analysis were carried out. The model used for these cases started with URANS (k-ω) as this requires less computational resources than DES. At a moving wall speed of 120 ms^{-1}, the calculated lift force for at least half of the cases exceeded its weight, implying lift off. Four of these cases exceeded two times its own weight and a few cases also experienced a large amount of drag force. The study implied that certain ballast shapes are more prone to movement at a certain angle, especially with a large projected area facing the incoming flow. The largest drag and lift forces were up to 3.5 N and 4.0 N respectively. Repeating the studying using DES, the force calculations changed by up to 20% due to additionally resolved eddies, which could alter the outcome in relation to movement. By reducing the volume of the ballast, the calculated drag forces on the selected ballast shapes was similar to its larger counterpart. However, the lift forces almost exceeded ten times the weight of the smaller ballast, which meant smaller ballast on the ballast bed surface is more likely to move/fly than larger ballast. On rotating the particle, the flow structure, vortices and distribution changes, which would affect other particles adjacent to it.

Using the ellipsoid approach from Ahmed et al. (2015) revealed the majority of the particles to be classified as Flat or Spherical. When comparing the results with the ballast information including its frontal area, it was difficult to relate the particle shape classification to the current aerodynamic results as only four angles were assessed and most results were similar. The current analysis indicated that ballast shapes classified as flat or columnar with a large projection area are more likely to move than any other shape. Shapes with a smaller projection area, on the other hand, are less likely to move owing to the boundary layer effect. The wind tunnel experiment measuring critical velocities showed similar trends.

However, a limitation of the study was that ballast stone was only rotated by one axis, and only four angles of attack meaning there might be insufficient data to make a certain conclusion. Also, the ballast shapes were smoothed to remove the angular edges and roughness, which would marginally affect the results. The lift forces for each stone exceeded the weight of each stone, but the simulation does not take into account the interlocking of particles and the fact the ballast is fully exposed to the flow. However, does not take the mechanical forces and damping mechanisms of the track into consideration that could affect the overall outcome.

The wavy channel study represents the ballast layer distribution and only steady RANS was used, which showed that k-ε was in better agreement than k-ω with the experimental results (Kuzan , 1986). Thus k-ω overestimates the flow separation and reattachment for this two-dimensional problem. But was decided for three-dimensional periodic track studies, SST k-ω was used due to rapid shear flow was predicted when passing through the sleepers and isolated particles.

For the track section studies, only DES SST k-ω was used owing to the unsteady and complex nature of the study. Only 2.0 seconds of flow time data were calculated to provide some meaningful results, which revealed that having the cube on top of the sleeper near the centre would make it more prone to movement than anywhere else. This was the likely motive behind the Aerotraviesa sleeper development. If the cube was placed in-between the track and the ballast level was low enough, the cubes would experience less lift and drag due to flow separation. If the ballast bed was raised due to ballast repacking, the cubes on the ballast bed are more likely to move due to additional aerodynamic loading. Replacing the cubes with a ballast particle at the same orientation would change the force outcome by a fraction. Comparing velocity profiles for each track section study showed that by having the ballast surface below the sleeper top surface would cause a larger roughness effect that would cause further reduction of turbulence flow energy before reaching the ballast bed. By applying surface roughness to the ballast bed reduces the effect even further, which means the calculated lift and drag forces are generally reduced due to lower static pressures.

The main disadvantage of the mono-block sleeper is to allow ballast grain to settle onto its upper surface. The Aerotraviesa sleepers resolved that issue by changing the shape of the middle section, to allow the ballast to roll of the sleeper block. However, changing the shape to a smooth geometry like a cylinder has caused the separated airflow to decrease, which means the aerodynamic load on the ballast bed would increase. This was resolved in their design by increasing the middle cross-sectional height allowing the flow to be separated further, while preventing ballast from coming to rest. Increasing the ballast depth to 20 mm above the design level would increases the probability of ballast movement compared with using a mono-block sleeper, as the majority of the cross-section is buried in ballast.

Therefore, to use the advantages of the Aerotraviesa sleeper, the ballast bed would need to be lower. Doing so may lead to additional costs to produce deeper sleepers to keep the track in place. The key feature seems to rely in flow separation and ballast depth, which was why the triangular sleeper was proposed. This increases the flow separation between the sleepers, which can decrease the potential for ballast movement even further. However, the aerodynamics dealt with only considers a moving wall study without any gusts or additional aerodynamic forces that may trigger a different outcome.

The calculated force coefficients of the cubes on the track section is significantly lower than the cubes when placed in open space for the isolated particle study. This is due to the roughness effects caused by the ballast bed surface and the sleeper blocks, making the flow more turbulent. This would suggest a similar outcome when realistic ballast is placed in the track section. Therefore, changes in the track section design (and train underbody design) is more likely to influence ballast movement than the shapes of individual ballast grain.

6.2 Recommended Future Research

Having established a large range of results throughout this study, there are still many factors to consider to establish a better understanding of ballast flight. Further studies include additional experimental/computational studies to try and identify key components to prevent ballast movement when the High-Speed Train is operating at its potential speed.

6.2.1 Isolated Ballast Future Research

For future studies from this report, it is recommended for the wind tunnel experiment to attached the force transducer to the shapes bottom surface to measure its forces more accurately starting with the cube and hemisphere before moving onto the ballast shapes. The cube or hemisphere can then be replaced with the aluminium ballast shapes by attaching them onto an adapter plate. The force measurements made can be compared with the aerodynamic forces from the CFD analysis. A better 3D scanner would be useful to scan the ballast shapes in greater detail, including the bottom surfaces to provide better CAD models than the simplified ballast.

Most of the ballast studies were focused on whether the ballast lift force would exceed the weight of the ballast with little consideration as to whether the ballast would slide across the surface, which was why additional studies would be required concerning the ballasts' interaction with the ground surface by calculating its frictional resistance. Realistically the granite ballast would only interact with either granite or concrete surfaces in wet and dry conditions. This could be done by using a pulley system with known masses to calculate its displacement horizontally.

Furthermore, for the critical velocity studies, additional aerodynamic techniques can be utilised such as using Pressure Sensitive Paint on the surfaces of ballast to observe the pressure distribution across its surfaces. Additionally, an accelerometer can be implanted into the ballast to measure changes in speed and acceleration in different situations. A simple model was designed and 3D printed for conceptional use (Figure 6.1).

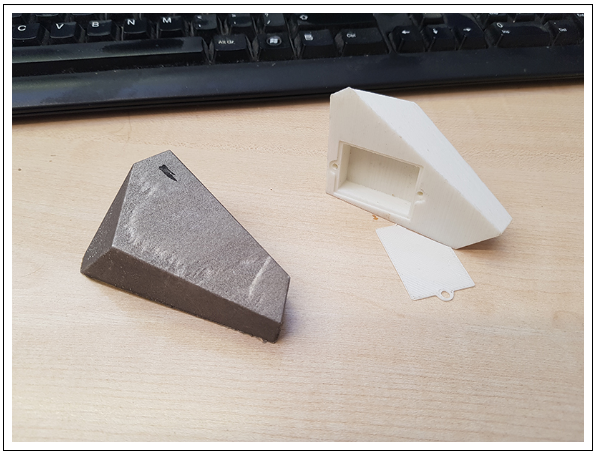

Figure 6.1: 3D printed ballast shape, allowing an accelerometer to be inserted into the ballast shape.

Also the effect of applying additional vertical forces on the test section should be considered as the current critical velocity studies only considers the aerodynamic effects towards ballast movement. This would represent the train passing in greater detail, which would likely reduce the critical velocity if nothing else is considered.

For the computational side of future studies, there are some areas of improvement or recommendations. For the ballast studies in particular, all 56 cases should run using DES instead of URANS as the change in force calculations was quite significant. Although the grid quality was reasonably good using unstructured polyhedra, an improvement would involve replacing with grid with a Hexisnap/Cutcell mesh that has excellent orthogonal quality and sub-divides towards the solid boundaries where required to do so. Furthermore, for shapes with complex detail such as ballast with surface roughness, Immersed Boundary Method should be utilised. Most commercial software does not have this feature, which would suggest the methodology would need to be developed through in-house coding. Finally, another area worth considering is the possibility of applying mass and frictional resistance onto each ballast shape and the visualise ballast movement when the aerodynamic load was applied. This would require the use of dynamic meshing that would change and adapt as the ballast begins to move in the CFD study.

6.2.2 Track Section Future Research

For the track section study, no experiments were carried out owing to space and weight limitations of the available wind tunnels and the complexity of the design. However, it is recommended to have the track section experiment scaled down to increase the Reynolds number and reduce the weight and space requirements of the experiment. It is debatable whether to apply an inlet flow across the track section using a model underbody of the train or to having a moving wall running at sufficient speed above the model track section.

There are multiple measurements of interest for each case including velocity profiles using hot-wire anemometer and flow visualisations using Particle Image Velocimetry. For specific isolated shapes, its movement and aerodynamic forces can be measured using accelerometers and force transducers. Each case would involve changes in ballast depths and sleeper geometry to observe which configure would most likely prevents any ballast movement. This approach may grant opportunities to generate additional sleeper designs with small modifications including the triangular cross section design to increase flow separation while preventing ballast from settling on top of the sleeper. If the experiment was to be scaled down, the ballast bed geometry could be artificially generated with use of 3D scanning and printing or another methodology to produce similar wall roughness, which can also be applied to the computational studies.

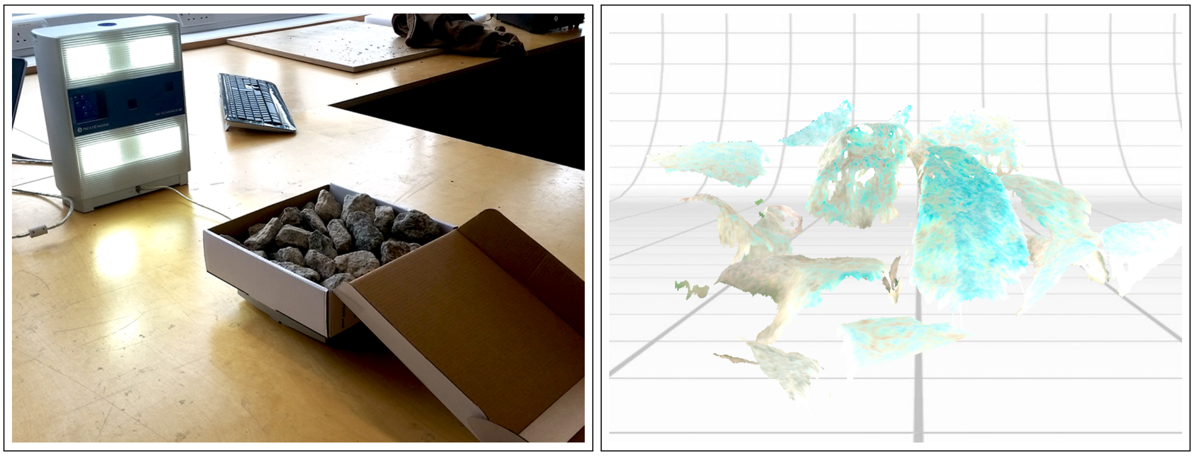

Figure 6.2: A box of granite ballast undergoing 3D scanning with the scanner normal to the ballast (left). Sample output of scanned ballast (right).

For computational analysis a dynamic mesh can be introduced to include a sliding mesh of different train models passing the track section. By doing so would mean the mesh resolution would either need to be reduced in certain areas or the cell count would need to increase further requiring additional resources to compensate. By changing the train models may prove that certain train designs are more likely to trigger ballast movement than others due to smaller distance between the underbody and ballast bed or certain components underneath the train can cause additional vortices and aerodynamic loading on the ballast bed.

Its noted that some assumptions were made throughout this studying including no void gaps in-between the ballast particles as it is difficult to model. Including voids at the ballast surface could potentially decrease the aerodynamic load on the ballast upper surface but could also lead to pressure forces underneath causing the ballast to lift up.

The complicated feature of this experiment would be applying a mechanical force underneath the track system representing the train movement or vibrations. Depending on the force output, the force transducer mentioned earlier may need to be replaced to avoid damaging the sensor. The amplitude of these forces can be collected from measured data and programmed onto a force generator that is installed underneath the wind tunnel platform. The vibration data can be complicated so an alternative would be to use a sinusoidal wave of a similar force magnitude to simplify the motion. Finding the correct equipment that would replicate this movement can be difficult and whether it could adapt to the wind tunnel design.

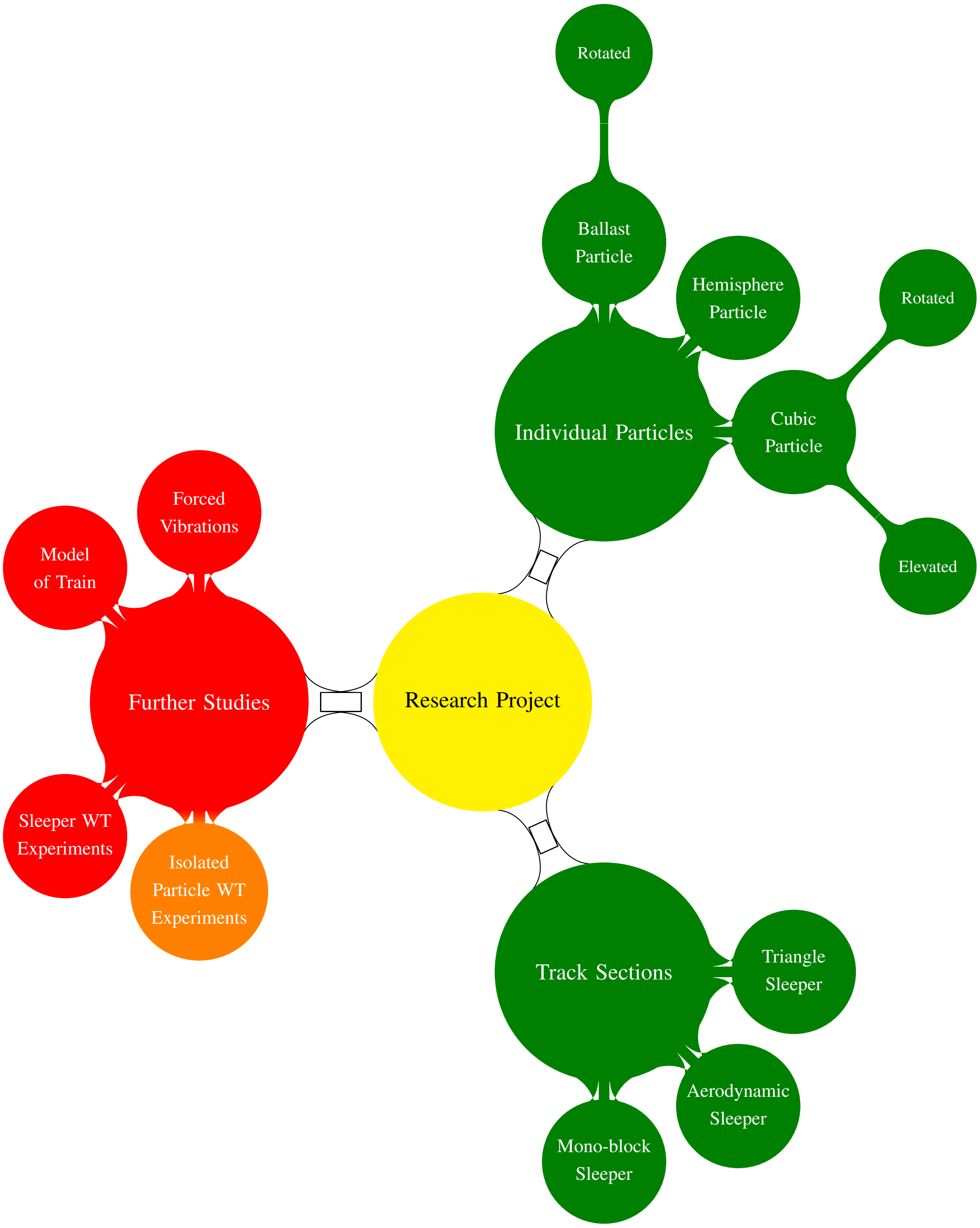
Rotated
Ballast Particle
Hemisphere Particle
Rotated
Cubic Particle
Individual Particles
Elevated
Forced Vibrations
Model of Train
Further Studies
Research Project
Sleeper WT Experiments
Isolated Particle WT Experiments
Track Sections
Triangle Sleeper
Aerodynamic Sleeper
Mono-block Sleeper

Appendix A

Wind Tunnel Apparatus Design to Measure Forces

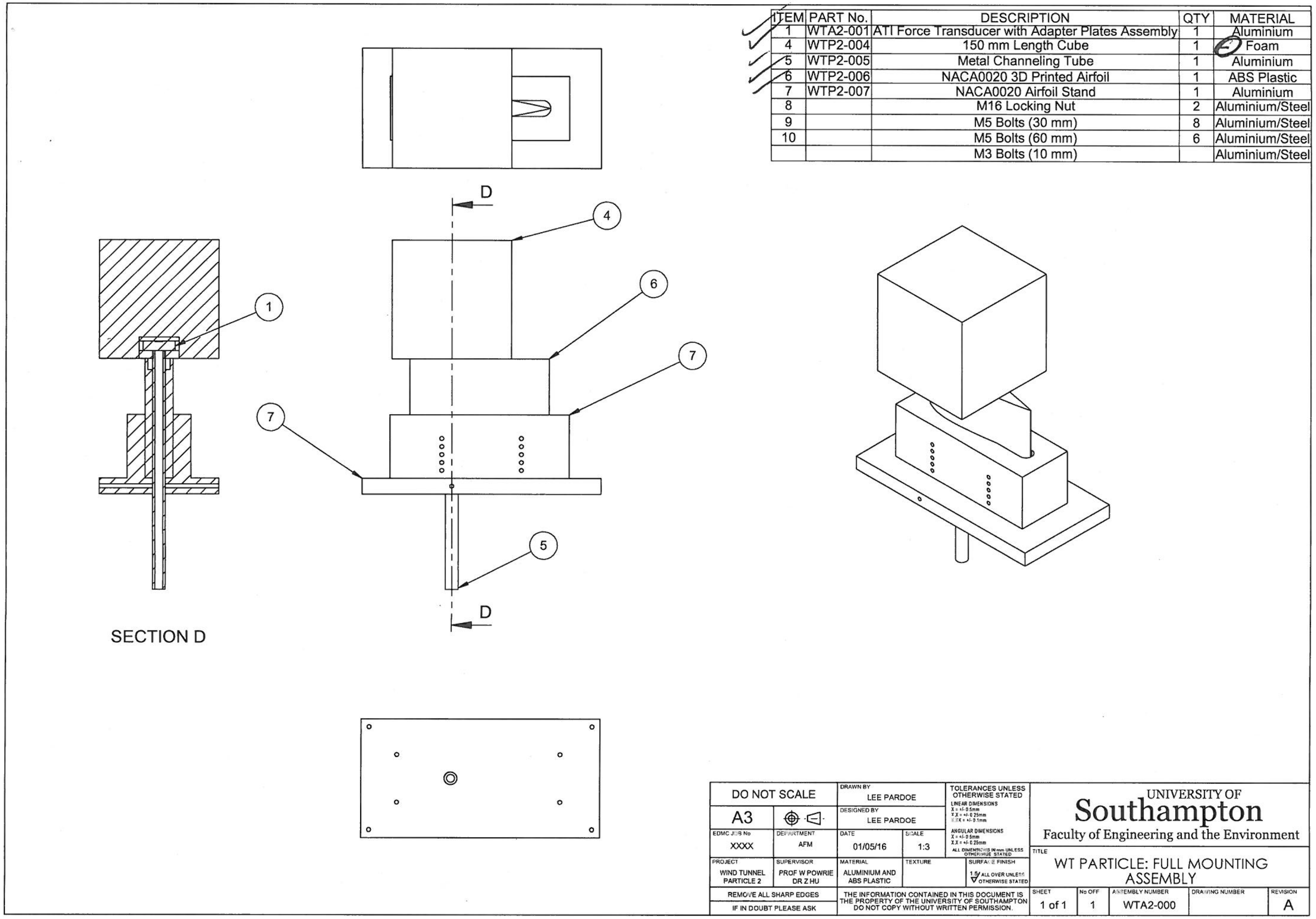

ITEM	PART No.	DESCRIPTION	QTY	MATERIAL
1	WTA2-001	ATI Force Transducer with Adapter Plates Assembly	1	Aluminium
4	WTP2-004	150 mm Length Cube	1	Foam
5	WTP2-005	Metal Channeling Tube	1	Aluminium
6	WTP2-006	NACA0020 3D Printed Airfoil	1	ABS Plastic
7	WTP2-007	NACA0020 Airfoil Stand	1	Aluminium
8		M16 Locking Nut	2	Aluminium/Steel
9		M5 Bolts (30 mm)	8	Aluminium/Steel
10		M5 Bolts (60 mm)	6	Aluminium/Steel
		M3 Bolts (10 mm)		Aluminium/Steel

DO NOT SCALE
A3
DRAWN BY LEE PARDOE
DESIGNED BY LEE PARDOE
EDMC JOB No XXXX
DEPARTMENT AFM
DATE 01/05/16
SCALE 1:3
TOLERANCES UNLESS OTHERWISE STATED
LINEAR DIMENSIONS
X = +/- 0.5mm
X.X = +/- 0.25mm
X.XX = +/- 0.1mm
ANGULAR DIMENSIONS
X = +/- 0.5mm
X.X = +/- 0.25mm
ALL DIMENSIONS IN mm UNLESS OTHERWISE STATED
PROJECT WIND TUNNEL PARTICLE 2
SUPERVISOR PROF W POWRIE DR Z HU
MATERIAL ALUMINIUM AND ABS PLASTIC
TEXTURE
SURFACE FINISH 1.6 ALL OVER UNLESS OTHERWISE STATED
REMOVE ALL SHARP EDGES
IF IN DOUBT PLEASE ASK
THE INFORMATION CONTAINED IN THIS DOCUMENT IS THE PROPERTY OF THE UNIVERSITY OF SOUTHAMPTON DO NOT COPY WITHOUT WRITTEN PERMISSION.

UNIVERSITY OF
Southampton
Faculty of Engineering and the Environment

TITLE WT PARTICLE: FULL MOUNTING ASSEMBLY
SHEET 1 of 1
No OFF 1
ASSEMBLY NUMBER WTA2-000
DRAWING NUMBER
REVISION A

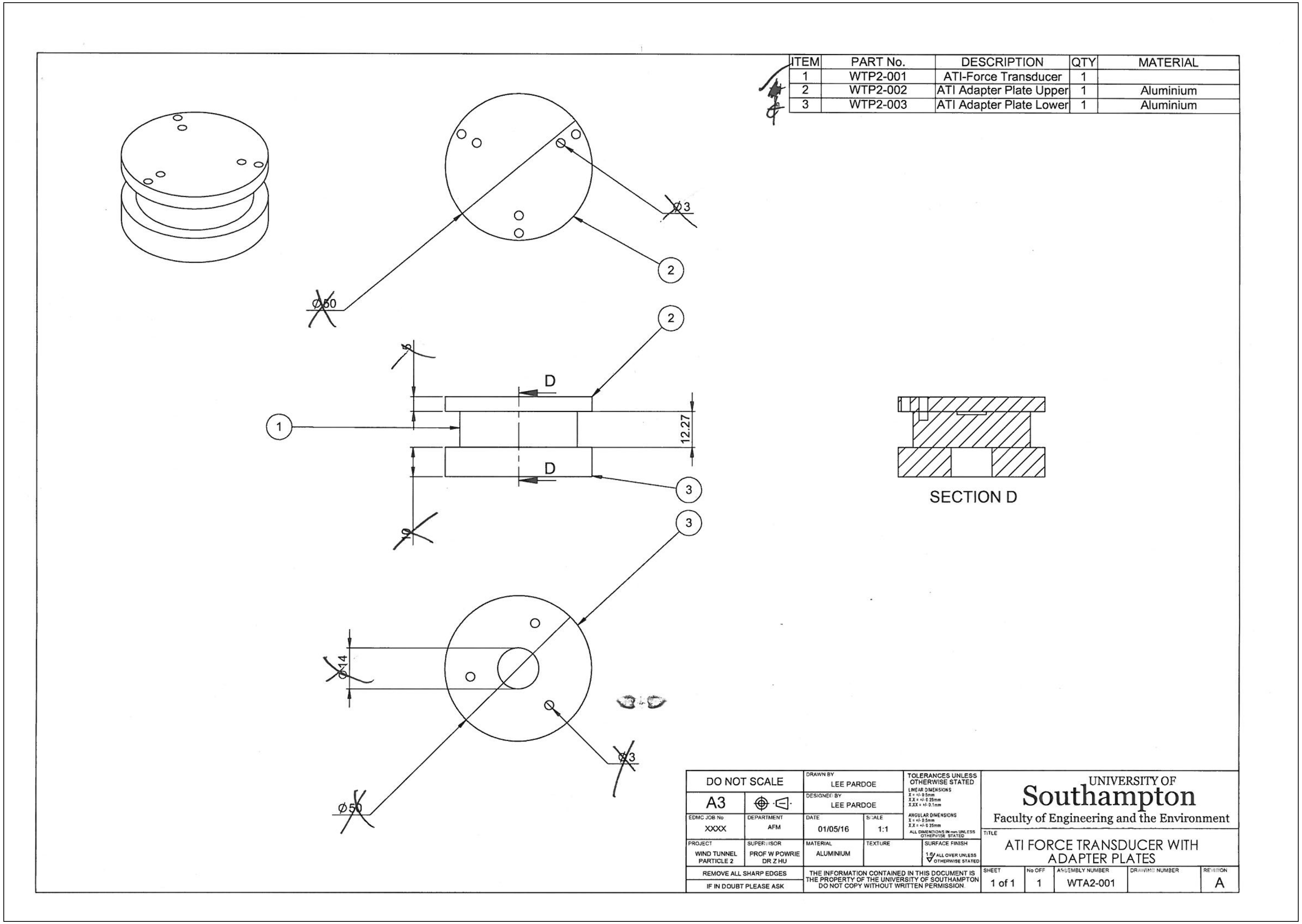

ITEM	PART No.	DESCRIPTION	QTY	MATERIAL
1	WTP2-001	ATI-Force Transducer	1	
2	WTP2-002	ATI Adapter Plate Upper	1	Aluminium
3	WTP2-003	ATI Adapter Plate Lower	1	Aluminium

DO NOT SCALE
A3
DRAWN BY LEE PARDOE
DESIGNED BY LEE PARDOE
EDMC JOB No XXXX
DEPARTMENT AFM
DATE 01/05/16
SCALE 1:1
TOLERANCES UNLESS OTHERWISE STATED
LINEAR DIMENSIONS
X = +/- 0.5mm
X.X = +/- 0.25mm
X.XX = +/- 0.1mm
ANGULAR DIMENSIONS
X = +/- 0.5mm
X.X = +/- 0.25mm
ALL DIMENSIONS IN mm UNLESS OTHERWISE STATED
PROJECT WIND TUNNEL PARTICLE 2
SUPERVISOR PROF W POWRIE DR Z HU
MATERIAL ALUMINIUM
TEXTURE
SURFACE FINISH 1.6 ALL OVER UNLESS OTHERWISE STATED
REMOVE ALL SHARP EDGES
IF IN DOUBT PLEASE ASK
THE INFORMATION CONTAINED IN THIS DOCUMENT IS THE PROPERTY OF THE UNIVERSITY OF SOUTHAMPTON DO NOT COPY WITHOUT WRITTEN PERMISSION.

UNIVERSITY OF Southampton
Faculty of Engineering and the Environment
TITLE ATI FORCE TRANSDUCER WITH ADAPTER PLATES
SHEET 1 of 1
No OFF 1
ASSEMBLY NUMBER WTA2-001
DRAWING NUMBER
REVISION A

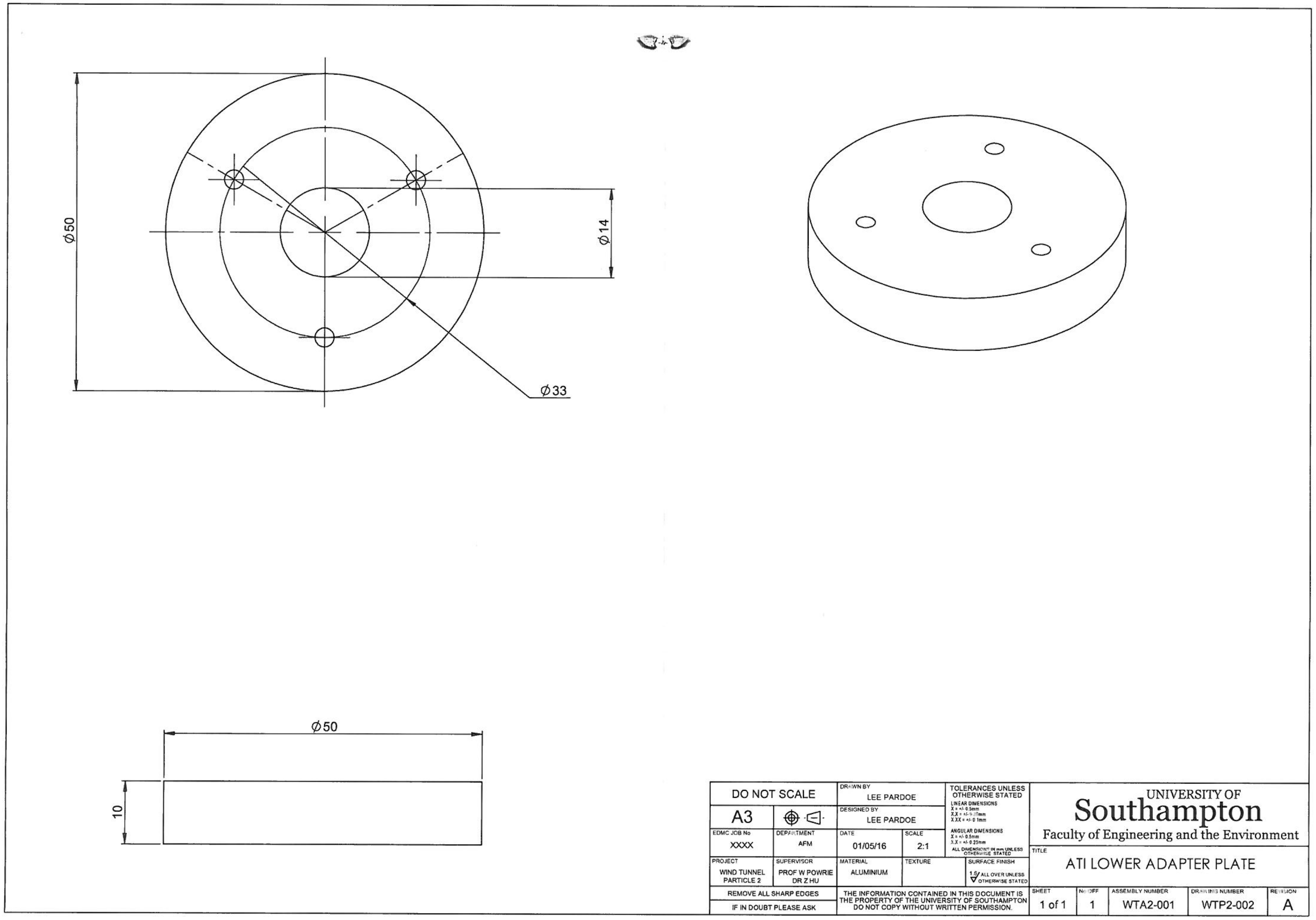
⌀50
⌀14
⌀33
⌀50
10
DO NOT SCALE
A3
DRAWN BY
LEE PARDOE
DESIGNED BY
LEE PARDOE
EDMC JOB No
XXXX
DEPARTMENT
AFM
DATE
01/05/16
SCALE
2:1
TOLERANCES UNLESS OTHERWISE STATED
LINEAR DIMENSIONS
X = +/- 0.5mm
X.X = +/- 0.25mm
X.XX = +/- 0.1mm
ANGULAR DIMENSIONS
X = +/- 0.5mm
X.X = +/- 0.25mm
ALL DIMENSIONS IN mm UNLESS OTHERWISE STATED
PROJECT
WIND TUNNEL PARTICLE 2
SUPERVISOR
PROF W POWRIE
DR Z HU
MATERIAL
ALUMINIUM
TEXTURE
SURFACE FINISH
1.6 ALL OVER UNLESS OTHERWISE STATED
REMOVE ALL SHARP EDGES
IF IN DOUBT PLEASE ASK
THE INFORMATION CONTAINED IN THIS DOCUMENT IS THE PROPERTY OF THE UNIVERSITY OF SOUTHAMPTON DO NOT COPY WITHOUT WRITTEN PERMISSION.
UNIVERSITY OF Southampton
Faculty of Engineering and the Environment
TITLE
ATI LOWER ADAPTER PLATE
SHEET
1 of 1
No OFF
1
ASSEMBLY NUMBER
WTA2-001
DRAWING NUMBER
WTP2-002
REVISION
A

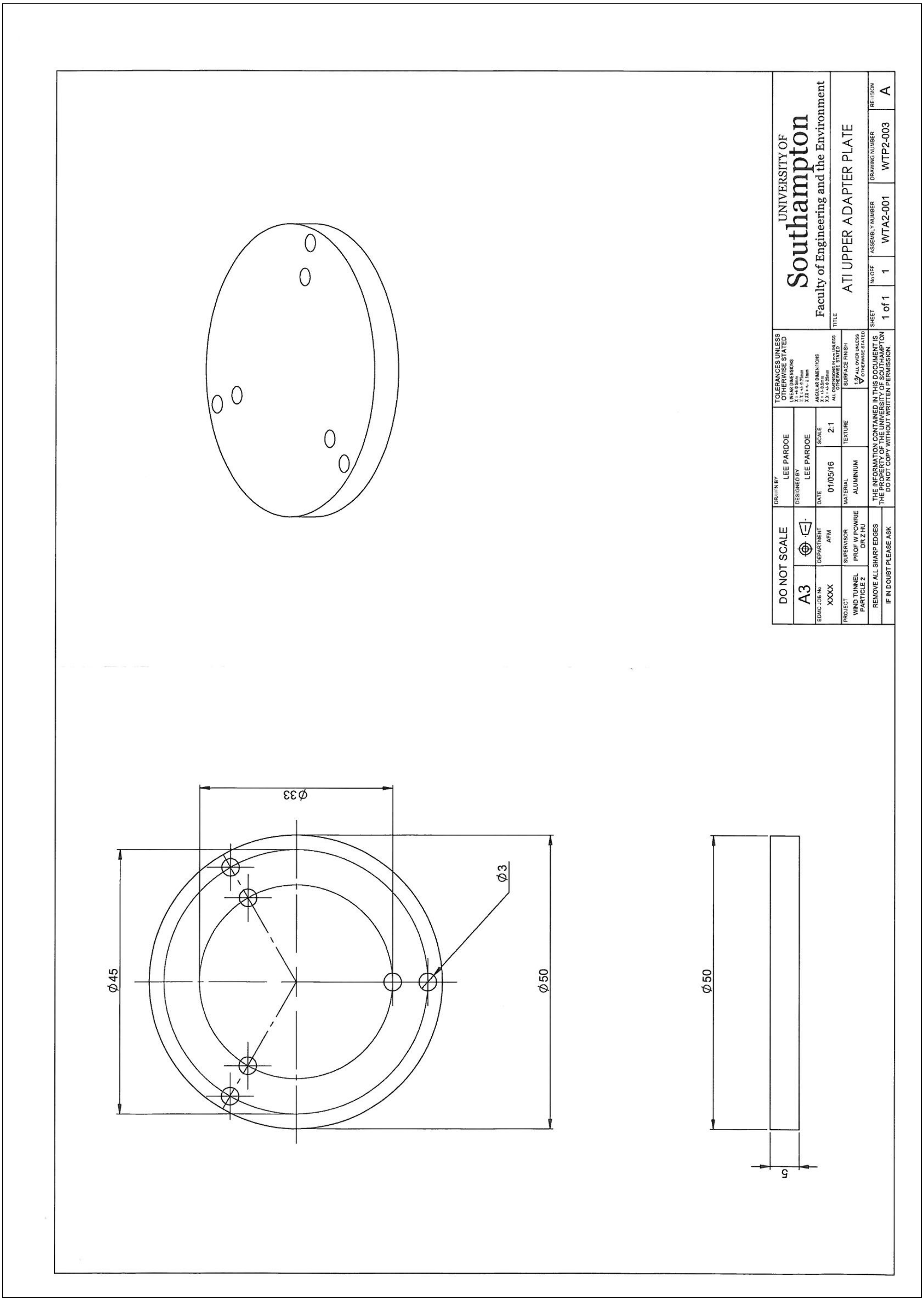
UNIVERSITY OF
Southampton
Faculty of Engineering and the Environment
TITLE
ATI UPPER ADAPTER PLATE
SHEET
1 of 1
No OFF
1
ASSEMBLY NUMBER
WTA2-001
DRAWING NUMBER
WTP2-003
REVISION
A
DO NOT SCALE
A3
EDMC JOB No
XXXX
DEPARTMENT
AFM
PROJECT
WIND TUNNEL PARTICLE 2
SUPERVISOR
PROF W POWRIE
DR Z HU
REMOVE ALL SHARP EDGES
IF IN DOUBT PLEASE ASK
DRAWN BY
LEE PARDOE
DESIGNED BY
LEE PARDOE
DATE
01/05/16
SCALE
2:1
MATERIAL
ALUMINIUM
TEXTURE
TOLERANCES UNLESS OTHERWISE STATED
LINEAR DIMENSIONS
X = +/-0.5mm
X.X = +/-0.25mm
X.XX = +/-0.1mm
ANGULAR DIMENSIONS
X = +/-0.5mm
X.X = +/-0.25mm
ALL DIMENSIONS IN mm UNLESS OTHERWISE STATED
SURFACE FINISH
1.6 ALL OVER UNLESS OTHERWISE STATED
THE INFORMATION CONTAINED IN THIS DOCUMENT IS THE PROPERTY OF THE UNIVERSITY OF SOUTHAMPTON DO NOT COPY WITHOUT WRITTEN PERMISSION
Ø33
Ø3
Ø45
Ø50
Ø50
5

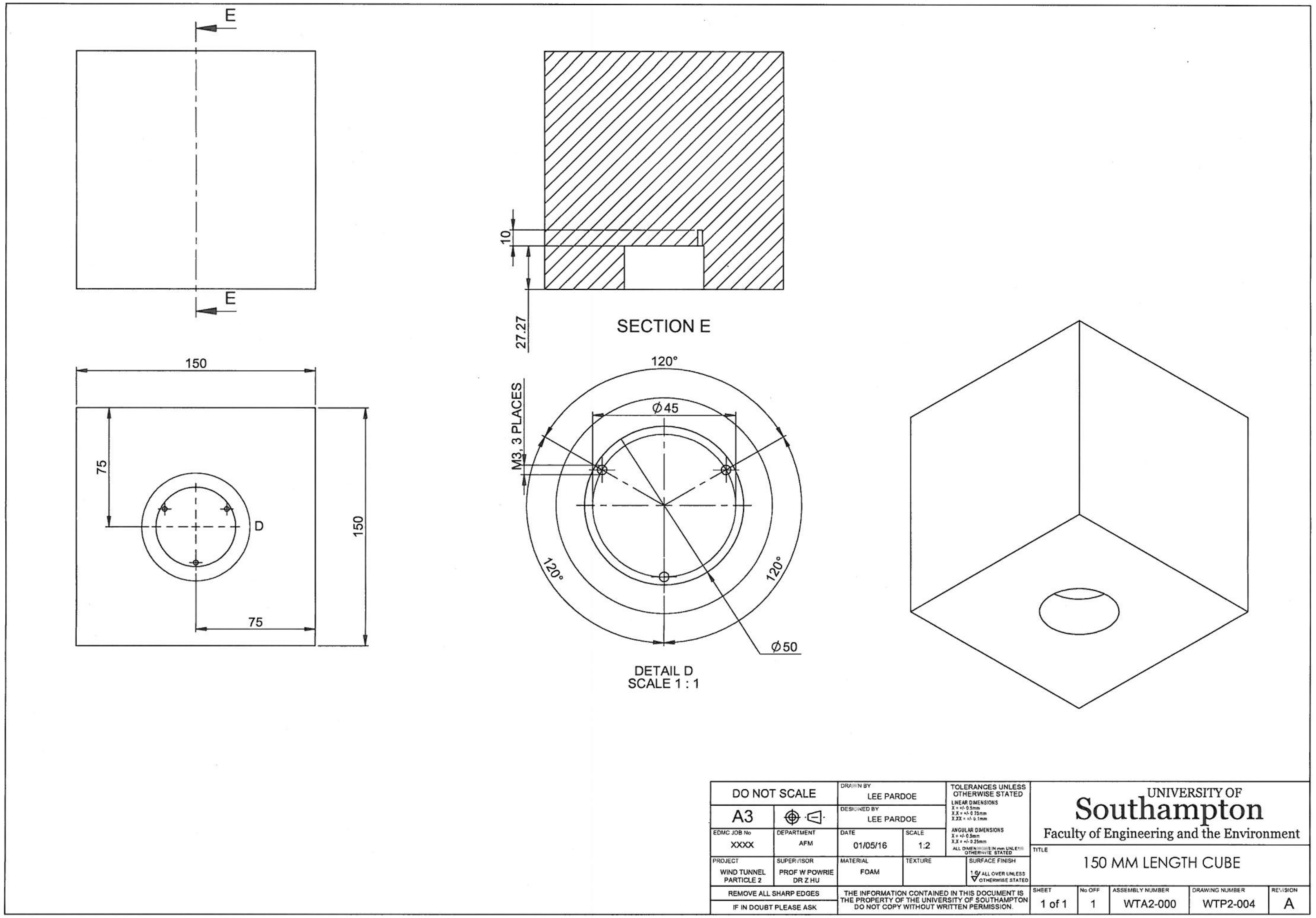
E
E
150
75
75
150
D
10
27.27
SECTION E
120°
Ø45
M3, 3 PLACES
120°
120°
Ø50
DETAIL D
SCALE 1 : 1
DO NOT SCALE
A3
DRAWN BY
LEE PARDOE
DESIGNED BY
LEE PARDOE
TOLERANCES UNLESS OTHERWISE STATED
LINEAR DIMENSIONS
X = +/- 0.5mm
X.X = +/- 0.25mm
X.XX = +/- 0.1mm
ANGULAR DIMENSIONS
X = +/- 0.5mm
X.X = +/- 0.25mm
ALL DIMENSIONS IN mm UNLESS OTHERWISE STATED
EDMC JOB No
XXXX
DEPARTMENT
AFM
DATE
01/05/16
SCALE
1:2
PROJECT
WIND TUNNEL PARTICLE 2
SUPERVISOR
PROF W POWRIE
DR Z HU
MATERIAL
FOAM
TEXTURE
SURFACE FINISH
1.6 ALL OVER UNLESS OTHERWISE STATED
REMOVE ALL SHARP EDGES
IF IN DOUBT PLEASE ASK
THE INFORMATION CONTAINED IN THIS DOCUMENT IS THE PROPERTY OF THE UNIVERSITY OF SOUTHAMPTON DO NOT COPY WITHOUT WRITTEN PERMISSION.
UNIVERSITY OF
Southampton
Faculty of Engineering and the Environment
TITLE
150 MM LENGTH CUBE
SHEET
1 of 1
No OFF
1
ASSEMBLY NUMBER
WTA2-000
DRAWING NUMBER
WTP2-004
REVISION
A

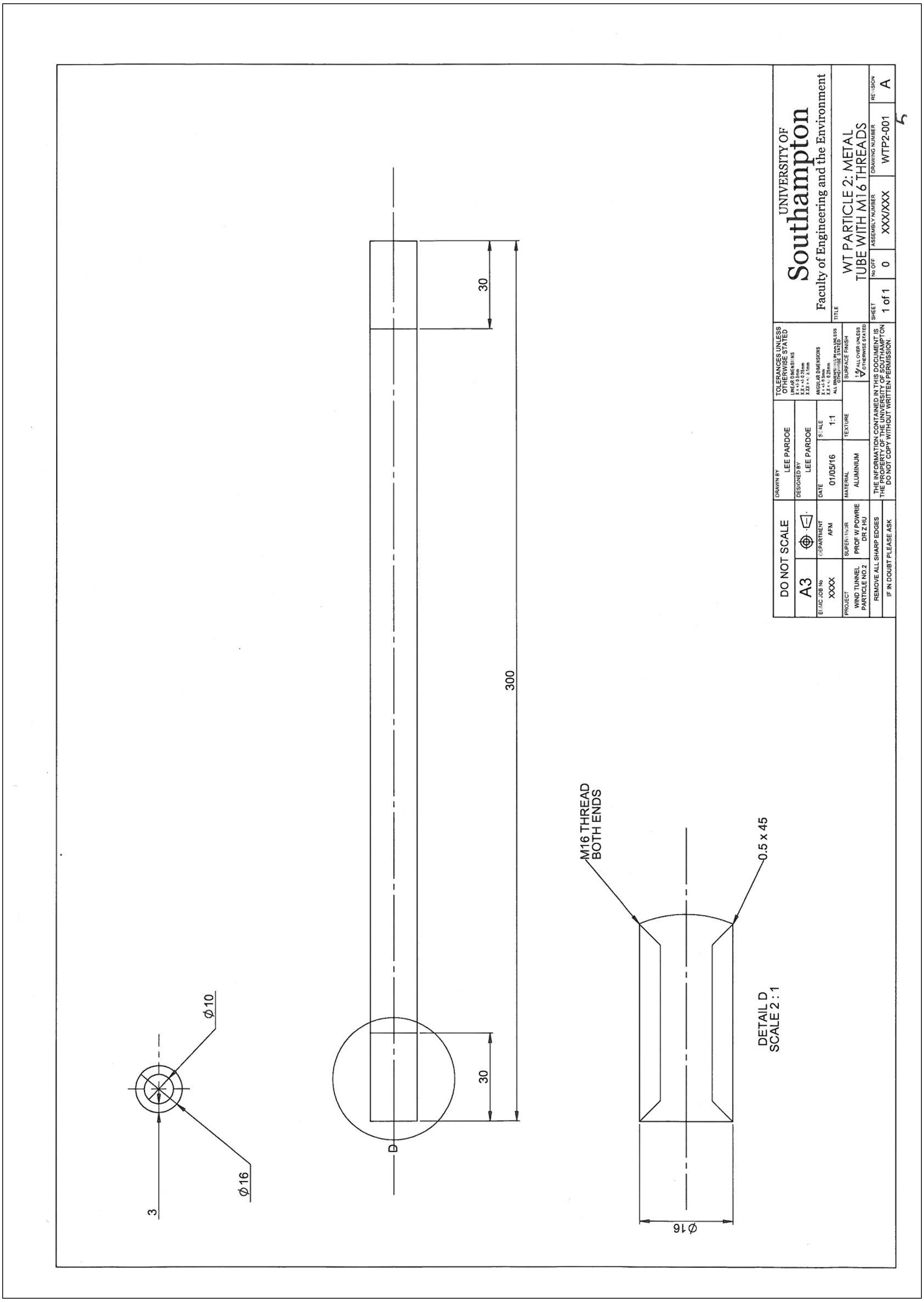
3
Ø16
Ø10
D
30
300
30
M16 THREAD
BOTH ENDS
Ø16
0.5 x 45
DETAIL D
SCALE 2 : 1
DO NOT SCALE
A3
EI/MC JOB No
XXXX
DEPARTMENT
AFM
PROJECT
WIND TUNNEL PARTICLE NO.2
SUPERVISOR
PROF W POWRIE
DR Z HU
REMOVE ALL SHARP EDGES
IF IN DOUBT PLEASE ASK
DRAWN BY
LEE PARDOE
DESIGNED BY
LEE PARDOE
DATE
01/05/16
SCALE
1:1
MATERIAL
ALUMINIUM
TEXTURE
SURFACE FINISH
1.6 ALL OVER UNLESS OTHERWISE STATED
THE INFORMATION CONTAINED IN THIS DOCUMENT IS THE PROPERTY OF THE UNIVERSITY OF SOUTHAMPTON DO NOT COPY WITHOUT WRITTEN PERMISSION.
TOLERANCES UNLESS OTHERWISE STATED
LINEAR DIMENSIONS
X = +/- 0.5mm
X.X = +/- 0.25mm
X.XX = +/- 0.1mm
ANGULAR DIMENSIONS
X = +/- 0.5mm
X.X = +/- 0.25mm
ALL DIMENSIONS IN mm UNLESS OTHERWISE STATED
UNIVERSITY OF
Southampton
Faculty of Engineering and the Environment
TITLE
WT PARTICLE 2: METAL TUBE WITH M16 THREADS
SHEET
1 of 1
No OFF
0
ASSEMBLY NUMBER
XXX/XXX
DRAWING NUMBER
WTP2-001
REVISION
A
5

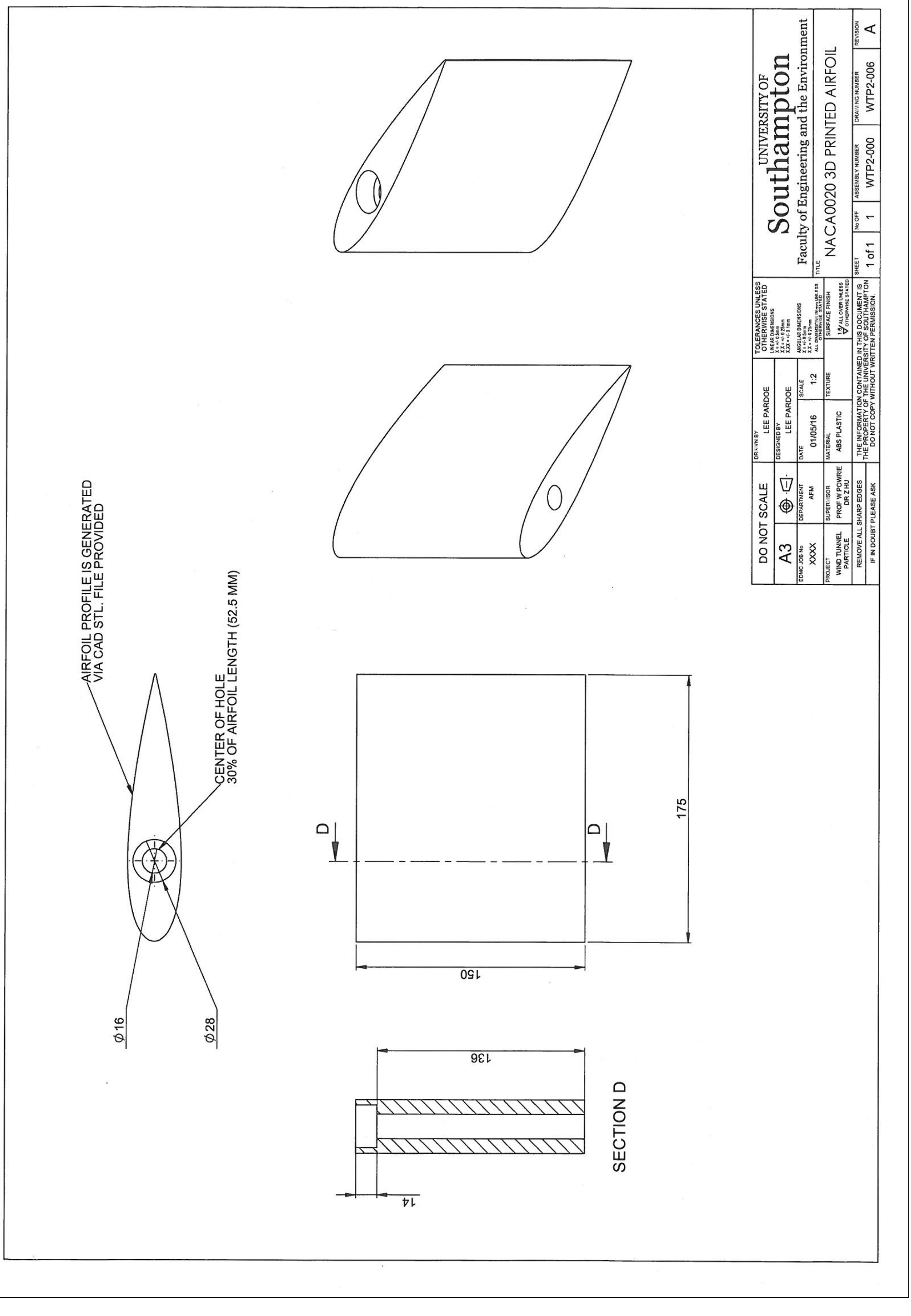
AIRFOIL PROFILE IS GENERATED
VIA CAD STL. FILE PROVIDED
CENTER OF HOLE
30% OF AIRFOIL LENGTH (52.5 MM)
Ø16
Ø28
D
D
175
150
136
14
SECTION D
DO NOT SCALE
A3
DRAWN BY
LEE PARDOE
DESIGNED BY
LEE PARDOE
TOLERANCES UNLESS OTHERWISE STATED
LINEAR DIMENSIONS
X = +/- 0.5mm
X.X = +/- 0.25mm
X.XX = +/- 0.1mm
ANGULAR DIMENSIONS
X = +/- 0.5mm
X.X = +/- 0.25mm
ALL DIMENSIONS IN mm UNLESS OTHERWISE STATED
EDMC JOB No
XXXX
DEPARTMENT
AFM
DATE
01/05/16
SCALE
1:2
PROJECT
WIND TUNNEL PARTICLE
SUPERVISOR
PROF W POWRIE
DR Z HU
MATERIAL
ABS PLASTIC
TEXTURE
SURFACE FINISH
1.6 ALL OVER UNLESS OTHERWISE STATED
REMOVE ALL SHARP EDGES
IF IN DOUBT PLEASE ASK
THE INFORMATION CONTAINED IN THIS DOCUMENT IS THE PROPERTY OF THE UNIVERSITY OF SOUTHAMPTON
DO NOT COPY WITHOUT WRITTEN PERMISSION.
UNIVERSITY OF
Southampton
Faculty of Engineering and the Environment
TITLE
NACA0020 3D PRINTED AIRFOIL
SHEET
1 of 1
No OFF
1
ASSEMBLY NUMBER
WTP2-000
DRAWING NUMBER
WTP2-006
REVISION
A

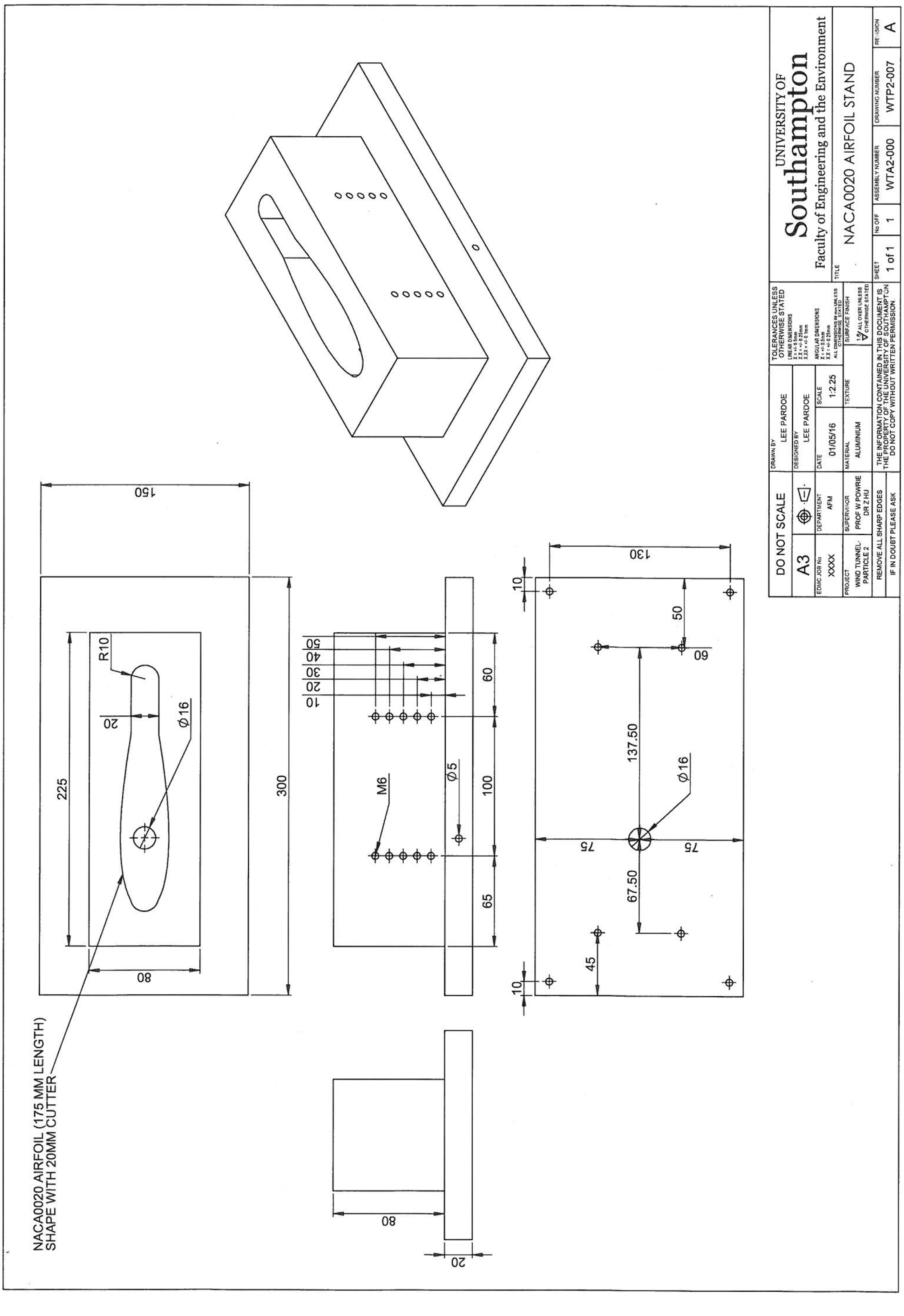
150
300
225
80
R10
20
Ø16
NACA0020 AIRFOIL (175 MM LENGTH)
SHAPE WITH 20MM CUTTER
50
40
30
20
10
60
100
65
M6
Ø5
80
20
130
10
50
60
137.50
Ø16
75
75
67.50
45
10
DO NOT SCALE
A3
EDMC JOB No
XXXX
DEPARTMENT
AFM
PROJECT
WIND TUNNEL-PARTICLE 2
SUPERVISOR
PROF W POWRIE
DR Z HU
REMOVE ALL SHARP EDGES
IF IN DOUBT PLEASE ASK
DRAWN BY
LEE PARDOE
DESIGNED BY
LEE PARDOE
DATE
01/05/16
SCALE
1:2.25
MATERIAL
ALUMINIUM
TEXTURE
TOLERANCES UNLESS OTHERWISE STATED
SURFACE FINISH
THE INFORMATION CONTAINED IN THIS DOCUMENT IS THE PROPERTY OF THE UNIVERSITY OF SOUTHAMPTON
DO NOT COPY WITHOUT WRITTEN PERMISSION
UNIVERSITY OF
Southampton
Faculty of Engineering and the Environment
TITLE
NACA0020 AIRFOIL STAND
SHEET
1 of 1
No OFF
1
ASSEMBLY NUMBER
WTA2-000
DRAWING NUMBER
WTP2-007
REVISION
A

Appendix B

Eureka Experimental Results

Table B.1: Eureka Can Trial 1 results.

	Trial 1			
	Large		**Small**	
Ballast No.	**Weight Dry (g)**	**Weight Wet (g)**	**Weight Dry (g)**	**Weight Wet (g)**
1	143.51	143.66	46.04	46.15
2	167.35	167.64	28.53	28.59
3	116.88	117	48.09	48.27
4	266.71	266.96	56.59	56.61
5	180.28	180.64	46.84	46.96
6	261.72	261.9	42.61	42.61
7	174.55	174.8	44.52	44.58
8	155.06	155.24	28.62	28.73
9	125.35	125.43	20.05	20.07
10	167.97	168.08	16.16	16.32
11	131.59	131.71	30.31	30.33
12	171.02	171.27	29.71	29.78
13	140.67	141.46	25.69	25.79
14	125.17	125.39	34.32	34.36
15	145.24	145.41	32.56	32.59
16	190.5	190.8	31.3	31.34
17	85.48	85.67	18.24	18.33
18	128.76	128.88	17.59	17.61
19	124.4	124.76	20.33	20.34
20	155.63	155.73	46.68	46.85
Bulk Ballast Mass (kg)	3.15784	3.16243	0.66478	0.66621

Correction Factor	0.9982	0.9982
Water Density (kg/m^3)	998.2	998.2
Beaker Mass Empty (kg)	0.39428	0.3942
Beaker Mass Filled (kg)	1.58525	0.64461
Water Mass (kg)	1.19097	0.25041
Water Volume (m^3)	0.001193118	0.000250862
Bulk Ballast Volume (m^3)	0.001193118	0.000250862
Bulk Ballast Density (kg/m^3)	2646.713089	2649.987604

Table B.2: Eureka Can Trial 2 results.

	Trial 2			
	Large		**Small**	
Ballast No.	**Weight Dry (g)**	**Weight Wet (g)**	**Weight Dry (g)**	**Weight Wet (g)**
1	143.51	143.69	46.07	46.21
2	167.35	167.59	28.55	28.76
3	116.88	116.97	48.16	48.43
4	266.69	267.02	56.59	56.64
5	180.27	180.63	46.88	46.99
6	261.71	261.91	42.6	42.62
7	174.54	174.77	44.53	44.59
8	155.06	155.2	28.64	28.75
9	125.34	125.44	20.06	20.08
10	167.96	168.09	16.18	16.35
11	131.59	131.77	30.33	30.37
12	171.00	171.47	29.73	29.84
13	140.6	141.52	25.73	25.86
14	125.17	125.37	34.34	34.42
15	145.24	145.46	32.57	32.61
16	190.49	190.85	31.31	31.32
17	85.48	85.62	18.27	18.34
18	128.76	128.91	17.59	17.6
19	124.39	124.86	20.38	20.39
20	155.64	155.8	46.72	46.9
Bulk Ballast Mass (kg)	3.15767	3.16294	0.66523	0.66707

Correction Factor	0.9982	0.9982
Water Density (kg/m^3)	998.2	998.2
Beaker Mass Empty (kg)	0.39479	0.39442
Beaker Mass Filled (kg)	1.58879	0.64568
Water Mass (kg)	1.19399	0.25126
Water Volume (m^3)	0.001196143	0.000251713
Bulk Ballast Volume (m^3)	0.001196143	0.000251713
Bulk Ballast Density (kg/m^3)	2639.876543	2642.810579

Table B.3: Eureka Can Trial 3 results.

	Trial 3			
	Large		**Small**	
Ballast No.	**Weight Dry (g)**	**Weight Wet (g)**	**Weight Dry (g)**	**Weight Wet (g)**
1	143.51	143.72	46.01	46.24
2	167.35	167.73	28.51	28.62
3	116.88	116.99	48.04	48.38
4	266.69	267.08	56.58	56.65
5	180.28	180.76	46.74	46.89
6	261.71	261.84	42.59	42.68
7	174.54	174.82	44.43	44.55
8	155.06	155.27	28.59	28.76
9	125.34	125.46	20.04	20.08
10	167.97	168.12	16.13	16.33
11	131.58	131.71	30.30	30.35
12	171.02	171.2	29.69	29.78
13	140.57	141.38	25.69	25.82
14	125.16	125.33	34.29	34.41
15	145.24	145.38	32.53	32.62
16	190.5	190.77	31.28	31.36
17	85.49	85.58	18.23	18.40
18	128.77	128.84	17.57	17.65
19	124.39	124.79	20.37	20.41
20	155.63	155.8	46.62	47.02
Bulk Ballast Mass (kg)	3.15768	3.16257	0.66482	0.66723

Correction Factor	0.9982	0.9982
Water Density (kg/m^3)	998.2	998.2
Beaker Mass Empty (kg)	0.39419	0.39614
Beaker Mass Filled (kg)	1.58867	0.64403
Water Mass (kg)	1.19446	0.24984
Water Volume (m^3)	0.00119661	0.000250291
Bulk Ballast Volume (m^3)	0.00119661	0.000250291
Bulk Ballast Density (kg/m^3)	2638.854765	2665.82207

Table B.4: Average results for the Eureka Can experiment.

	Average (Last 3 Trials)			
	Large		**Small**	
Ballast No.	**Weight Dry (g)**	**Volume** (m^3)	**Weight Dry (g)**	**Volume** (m^3)
1	143.51	0.00005432	46.04	0.00001743
2	167.35	0.00006335	28.53	0.00001080
3	116.88	0.00004424	48.10	0.00001821
4	266.70	0.00010095	56.59	0.00002142
5	180.28	0.00006824	46.82	0.00001773
6	261.71	0.00009907	42.60	0.00001613
7	174.54	0.00006607	44.49	0.00001684
8	155.06	0.00005869	28.62	0.00001083
9	125.34	0.00004745	20.05	0.00000759
10	167.97	0.00006358	16.16	0.00000612
11	131.59	0.00004981	30.31	0.00001147
12	171.01	0.00006473	29.71	0.00001125
13	140.61	0.00005323	25.70	0.00000973
14	125.17	0.00004738	34.32	0.00001299
15	145.24	0.00005498	32.55	0.00001232
16	190.50	0.00007211	31.30	0.00001185
17	85.48	0.00003236	18.25	0.00000691
18	128.76	0.00004874	17.58	0.00000666
19	124.39	0.00004709	20.36	0.00000771
20	155.63	0.00005891	46.67	0.00001767

Average Volume (m^3)	0.00005976	0.00001258
Average Bulk Ballast Density (kg/m^3)	2641.81	2648.88

Bibliography

Abbireddy, C.O.R., Clayton, C.R.I. & Schiebel, R. *A method of estimating the form of coarse particulates.* Geotechnique Vol. **59**(6), pp. 493–501.

Adif 2012 *AeroTraviesa: New design of sleeper for High Speed lines* http://www.adif.es/en_US/compromisos/doc/PT_13-Aerotraviesa_Eng.pdf

Ahmed S., Harkness J., Le Pen L, Powrie W. & Zervos A. *Numerical modelling of railway ballast at the particle scale.* International Journal for Numerical and Analytical Methods in Geomechanics 2015.

AnSys Inc. 2009 *AnSys Fluent User Guide 12.0.*

Baker C.J. 2001 *Flow and dispersion in vehicle wakes.* Journal of Fluids and Structures, Vol. **15** (7), pp. 1031-1060.

Baker C.J. 2010 *The flow around high speed trains.* Journal of Wind Engineering and Industrial Aerodynamics, Vol. **98**.

Baker C.J. 2014a *A review of train aerodynamics Part 1 - Fundamentals.* The Aeronautical Journal. Vol. **118**, pp. 201-228.

Baker C.J. 2014b *A review of train aerodynamics Part 2 - Applications.* The Aeronautical Journal. Vol. **118**, pp. 345-382.

Baron A., Mossi M. & Sibilla S. 2001 *The alleviation of the aerodynamic drag and wave effects of high-speed trains in very long tunnels.* Journal of Wind Engineering and Industrial Aerodynamics, Vol. **89** (5), pp. 365-401.

Bazan L. 2012 *Aerotraviesa Combats Flying Ballast* EU Rail Mag, Focun Spain, Vol. **26**, pp. 144.

Blocken, B.J.E. 2014 *50 Years of computational wind engineering : past, present and future.* Journal of Wind Engineering and Industrial Aerodynamics. Vol. **129**, pp. 69-102.

BS 1377-2:1990 *BS 1377-2:1990 Methods of test for soils for civil engineering purposes. Compressibility, permeability and durability tests. Part 2*

BS 1377-5:1990 *BS 1377-5:1990 Methods of test for soils for civil engineering purposes. Compressibility, permeability and durability tests. Part 5*

Diaz-Daniel C., Laizet S., Vassilicos J.C. 1977 *Direct Numerical Simulations of a wall-attached cube immersed in laminar and turbulent boundary layers.* International Journal of Heat and Fluid Flow. Vol. **68**, pp. 269-280.

Castro I.P. & Robins A.G. 1977 *The flow around a surface-mounted cube in uniform and turbulent streams.* Journal of Fluid Mechanics. Vol. **79**, part 2.

CHANDRA S. & AGARWAL M.M (2013). *Railway Engineering, Second Edition* Oxford University Press.

China to increase high-speed rail network to 30,000 km by 2020 http://indianexpress.com/article/business/business-others/china-to-increase-high-speed-rail-network-to-30000-km-by-2020/

Consolis: Famous trains are running on Consolis sleepers http://www.consolis.com/focus/famous-trains-are-running-on-consolis-sleepers/

Dantec Dynamics, probes for hot-wire anemometry. https://www.dantecdynamics.com/split-fiber-probes

DANIELS S.J., CASTRO I.P. & XIE Z.T. 2013 *Peak loading and surface pressure fluctuations of a tall model building.* Journal of Wind Engineering and Industrial Aerodynamics, Vol. **120**.

GARCIA J., CRESPO A., BERASARTE A. & GOIKOETXEA J. 2011 *Study of the flow between the train underbody and the ballast track.* Journal of Wind Engineering and Industrial Aerodynamics, Vol. **99**.

HADAVAND M., YAGHOUBI M., EMDAD H. 2008 *Thermal analysis of vaulted roofs.* Energy Build. Vol. **40**, pp. 265-275.

HEARST R.J., GOMIT G. & GANAPATHISUBRAMANI B. 2016 *Effect of turbulence on the wake of a wall-mounted cube.* Journal of Fluid Mechanics, Vol. **804**, pp. 513-530.

HOEFENER L. 2012 *DB Mobility Newtwork Logistics: Turkish Republic State Railway.* T.TVI32 (2), Aerodynamics and HVAC.

HUNT, J.C.R., ABBEL, C.J., PETERKA, J.A., WOO, H. 1978 *Kinematic studies of the flows around free or surface-mounted obstacles; applying topology to flow visualization.* Journal of Fluid Mechanics, Vol. **86**, pp. 179-200.

HUR N., WON C., KIM S.R. & CHOI C. W. 2008 *Wind load simulation for high-speed train stations.* Journal of Wind Engineering and Industrial Aerodynamics, Vol. **96**.

INDRARATNA B. 2011 *Advanced Rail Geotechnology - Ballasted Track.* CRC Press.

JACOBINI F.B., TUTUMLUER E. & SAAT M.R. 2013 *Identification of High-Speed Rail Ballast Flight Risk Factors and Risk Mitigation Strategies.* 10th World Congress on Railway Research.

JANG D.S., JETLI R., & ACHARYA S. (1986). *Comparison of the PISO, SIMPLER, and SIMPLEC Algorithms for the Treatment of the Pressure-Velocity Coupling in Steady Flow Problems.* Numerical Heat Transfer **19**, pp. 209-228.

JING G.Q., LIU G.X., LIN J., MARTINEZ J. & YIN C.T. (2014). *Aerodynamic Characteristics of Individual Ballast Particle by Wind Tunnel Tests.* Journal of Engineering Science and Technology, Review **7**, pp. 137-142.

KALTENBACH H. 2008 *DeuFraKo Project - Aerodynamics in Open Air (AOA).* Deutsche Bahn AG. Munich: DeuFraKo.

KUZAN, J.D. 1986 *Velocity Measurements for Turbulent Separated and Near-Separated Flows Over Solid Waves.* Ph.D. thesis, Dept. Chem. Eng., Univ. Illinois, Urbana, IL, 1986.

KWON H.B., PARK C.S. 2004 *Substructure flow analysis and experiments of high speed train for researching the mechanism of ballast dispersion.* Proceeding of Korean Society for Railway 2003. Vol. **3**, pp. 275-280.

KWON H.B., PARK C.S. 2006 *An experimental study on the relationship between ballast-flying phenomenon and strong wind under high-speed train* Proceedings of the World Congress on Rail Research, Montreal, Canada.

LE PEN L.M., POWRIE W., ZERVOS A., AHMED S., AINGARAN A. 2013 *Dependence of shape on particle size for a crushed rock railway ballast.* Granular Matter. Vol. **15** (6).

LUBKE H., SCMIDT ST., RUNG T., THIELE F. 2001 *Comparison of LES and RANS in bluff-body flows.* Journal of Wind Engineering Industry Aerodynamics. Vol. **89**, pp. 1471-1485.

MERONEY R.N., LETCHFORD C.W., SARKAR P.P. 2002 *Comparison of numerical and wind tunnel simulation of wind loads on a smooth, rough and dual domes immersed in a boundary layer.* Journal of Wind and Structural. Vol. **91**, pp. 219-228.

MILNE D., LE PEN L., THOMPSON D., POWRIE W. 2016 *Measurement of ballast grain acceleration at track level.* Permanent Way Institution Journal. Vol. **134** (4).

PETERS J.L. 1983 *Aerodynamics of high speed trains and Maglev vehicles. In Impact of Aerodynamics on Vehicle Design* MA Dorgham, pp. 308–41.

POWRIE W. 2013 *Soil Mechanics Concepts and Applications, Third Edition.* CRC Press.

PREMOLI A., ROCCHI D., SCHITO P., SOMASCHINI C. & TOMASINI G. 2015 *Ballast flight under high-speed trains: Wind tunnel full-scale experimental tests, Third Edition.* Journal of Wind Engineering and Industrial Aerodynamics. Vol. **145**, pp. 351-361.

QUINN A.D., HAYWARD M., BAKER C.J., SCHMID F., PRIEST J.A. & POWRIE W. 2010 A full-scale experimental and modelling study of ballast flight under high-speed trains. IMechE Journal. Vol. **224**, part F.

RAGHUNATHANA R.S., KIM H.D., SETOGUCHI T. 2002 *Aerodynamics of high-speed railway train.* Progress in Aerospace Sciences, Vol. **38**, pp. 469-514.

RODI W., 1997 *Comparison of LES and RANS calculations of the flow around bluff bodies.* Journal of Wind Engineering and Industrial Aerodynamics. Vol. **69**, pp. 55-75.

SAKAMOTO H., MORIYA M., TANIGUCHI S., & ARIE M. (1982) *The Form Drag of Three-Dimensional Bluff Bodies Immersed in Turbulent Boundary Layers.* Journal of Fluids Engineering, Vol. **104**, pp. 326-333.

SAKAMOTO, H., & OIWAKE, S. (1984) *Fluctuating Forces on a Rectangular Prism and a Circular Cylinder Placed Vertically in a Turbulent Boundary Layer.* Journal of Fluids Engineering, Vol. **106**, pp. 160-166.

SANDBERG R. 2014 *Turbulence 2: Modelling and Simulation Course Material.* University of Southampton.

SALIM S.M., ONG K.C. & CHEAH S.C. 2011 *Comparison of RANS, URANS and LES in the Prediction of Airflow and Pollutant Dispersion.* Proceedings of the World Congress on Engineering and Computer Science **2**, WCECS, San Francisco, USA, October 19-21, 2011.

SAUSSINE G., ALLAIN E., PARADOT N., GAILLOT V. 2009 *Railway ballast flying phenomenon: from numerical computations towards risk assessment.* Euromech Colloquium **50**, Vehicle Aerodynamics of Railway Vehicles, Trucks, Buses and Cars, Berlin, March 24-25, 2009.

SAVORY E., TOY N. 1986 *The flow regime in the turbulent near wake of a hemisphere.* Experimental Fluids. Vol. **4**, pp. 181-188.

SAVORY E., TOY N. 1986 *Hemisphere and hemisphere-cylinders in turbulent boundary layers.* Journal of Wind Engineering and Industrial Aerodynamics. Vol. **23**, pp. 345-364.

SCHETZ J.A. 2001 *Aerodynamics of High-Speed Trains.* Journal of Fluid Mechanics. Vol. **33**, pp. 371-414.

SOPER D., BAKER C., JACKSON A., MILNE D.R., LE PEN L., WATSON G., POWRIE W. 2017 *Full scale measurements of train underbody flows and track forces.* Journal of Wind Engineering and Industrial Aerodynamics. Vol. **69**, pp. 251-264.

SPALART P.R., JOU W.H. STRELETS M. AND ALLMARAS S.R. 1997 *Comments on the Feasibility of LES for Wings, and on a Hybrid RANS/LES Approach.* Advances in DNS/LES. Greyden Press, Columbus, OH.

STANTON-BONNA LIMITED *Railway Sleepers and Bearers* http://www.stanton-bonna.co.uk/rail-products/railway-sleepers-and-bearers [Accessed: 05/07/2016]

SYSTRA 2013 *Systra Report on Ballasted Track at High Speed Tracks.* Systra Report.

TAMURA T., KUWAHARA K., SUZUKI M. 1990 *Numerical study of wind pressure on a domed roof and near wake flows.* Journal of Wind Engineering and Industrial Aerodynamics. Vol. **36**, pp. 1001-1010.

TANIGUCHI F.J., SAKAMOTO H., KIYA M., ARIE M. 1982 *Time averages aerodynamic forces acting on a hemisphere immersed in a turbulence boundary layer.* Journal of Wind Engineering and Industrial Aerodynamics. Vol. **91**, pp. 257-273.

TAVAKOL M.M., YAGHOUBI M., MASOUDI MOTLAGH M. 2009 *Air flow aerodynamic on a wall-mounted hemisphere for various turbulent boundary layers.* Experimental Thermal and Fluid Science. Vol. **34**, pp. 538-553.

TAVAKOL M.M., ABOUALI O., YAGHOUBI M. 2014 *Large eddy simulation of turbulent flow around a wall mounted hemisphere.* Applied Mathematical Modelling, Iran.

TAYLOR T.J. 1990 *Wind pressures on a hemispherical dome.* Journal of Wind Engineering and Industrial Aerodynamics. Vol. **40**, pp. 199-213.

TOY N., MOSS W.D., SAVORY E. 1983 *Wind tunnel studies on a dome in turbulent boundary layers.* Journal of Wind Engineering and Industrial Aerodynamics. Vol. **11**, pp. 201-212.

TUTAR M., HOLDO A.E. 2001 *Computational modelling of flow around a circular cylinder in sub-critical flow regime with various turbulence models.* International Journal for Numerical Methods in Fluids. Vol. **35** (7), pp. 763-784.

TARMAC (2016) *Tarmac: Sustainable construction solutions* http://www.tarmac.com/

UPBOX (2016) *UpBox Tech-Specs.* http://up3dprinters.co.uk/up-box-tech-specs/

VERSTEEG H.K., MALALASEKERA W. 2007 *An Introduction to Compuational Fluid Dynamics The Finite Volume Method (Second Edition)* Pearson Prentice Hall.

WADELL H. 1932 *Volume, shape and roundness of rock particles.* The Journal of Geology. Vol. **40** (5), pp. 443-451.

WILCOX D.C. 1998 *Turbulence Modelling for CFD, Second Edition.* DCW Industries, La Canada, California.

WILCOX D.C. 2006 *Turbulence Modelling for CFD, Third Edition.* DCW Industries, La Canada, California.

WILLIAMSON C.H.K. 1996 *Vortex dynamics in the cylinder wake.* Annual Reviews Fluid Mechanics. Vol. **28**, pp. 477-539.

XU C., CHEN L., LU X. (2007) *Large-eddy and detached-eddy simulations of the separated flow around a circular cylinder.* Journal of Hydrodynamics. Vol. **19** (5), pp. 559-563.

YOSHIDA M., UCHIDA M., YAGUCHI N. (1992). *Countermeasures for ballast-flying phenomena caused by high-speed trains.* RTRI Report. Vol. **6** (6), pp. 27-36.

YOKOYAMA A. 2000 *Infrastructure for high speed lines in Japan.* American Public Transportation Association